A SYNOPTIC VIEW OF THE UPSCALE ENERGY CASCADE

A Dissertation

by

DAVID A. COATES

Submitted to the Office of Graduate and Professional Studies of
Texas A&M University
in partial fulfillment of the requirements for the degree of

DOCTOR OF PHILOSOPHY

Chair of Committee,	John Nielsen-Gammon
Committee Members,	Istvan Szunyogh
	Robert Korty
	Ping Chang
Head of Department,	Ramalingam Saravanan

May 2021

Major Subject: Atmospheric Sciences

ABSTRACT

Moist processes can produce kinetic energy at subsynoptic scales, traditionally regarded as part of the -5/3 inertial subrange. Atmospheric kinetic energy cascades to both smaller and larger scales, so moist dynamics at the subsynoptic scales should in part cascade inversely into the synoptic scales. This process has heretofore been examined statistically using simplified models. In this study, for the first time, we examine this process using a case study approach with simulations of amplifying jet stream waves by the WRF mesoscale model. Pairs of simulations are carried out, with standard initial conditions and with subsynoptic-scale energy suppressed in the initial conditions. We make use of a two-dimensional wavelet filter to both remove subsynoptic scale incoherent constituents of the instantaneous stream function and velocity potential and to diagnose the resulting differences in the evolution of the scales and structures of simulated features.

Synoptic analysis of filtered and control simulation output shows that moist dynamics project onto the synoptic scales via the development of new PV gradients in the upper troposphere, altering the amplification rate and phase of the mid-latitude baroclinic waves. Differences in the location and magnitude of PV gradients depend largely on precipitation intensity and spatial coverage. Filtered simulations were observed to produce greater precipitation maxima and larger corresponding enstrophy maxima than the unfiltered simulations. These filtered enstrophy maxima emerged from areas with generally lower enstrophy than in the unfiltered simulations. Perturbation kinetic energy typically shifts back and forth between zonally elongated features and meridionally elongated features over the course of the multiday simulations. The onset of high

amplitude jet stream waves and wave breaking coincides with a rapid increase in the perturbation kinetic energy of all subsynoptic and synoptic scales. The distribution of energy among perturbation scales and orientations follows patterns that coincide with common stages of cyclone development. Ensemble members with moist dynamics that produced different PV gradients aloft followed different pattern progressions that may reflect systematic life cycle differences, but additional case studies would be necessary to determine whether these differences are systematically determined by the energy differences of the initial states.

DEDICATION

For my wife, Augustina, for her endless support, who believes in me when I don’t believe in myself.

ACKNOWLEDGEMENTS

I would like to thank my committee chair, Dr. John Nielsen-Gammon, and my committee members Drs. Istvan Szunyogh, Robert Korty, and Ping Chang, for their time and effort in helping me complete my dissertation.

I would also like to thank my friends, both from the Texas A&M Atmospheric Sciences graduate program and my alma mater, for always assuring me that, in spite of how long it took, they believed I could finish.

Finally, I'd like to thank my mom for her faith in me specifically and all the support she provided, and my wife, who never gave up on me despite my protestations.

CONTRIBUTORS AND FUNDING SOURCES

Contributors

This work was supervised by a dissertation committee consisting of Professors John Nielsen-Gammon, advisor and committee chair; Professors Istvan Szunyogh and Robert Korty of the Atmospheric Sciences Department; and Professor Ping Chang of the Atmospheric Sciences and Oceanography Departments.

All work for the dissertation was completed independently by the student.

Funding Sources

Graduate study was supported in part by funding from the Office of the Texas State Climatologist.

TABLE OF CONTENTS

Page

LIST OF FIGURES

Page

Page

Page

Page

Page

Page

CHAPTER I

INTRODUCTION

The kinetic energy spectrum of the atmosphere, theorized by Kolmogorov (1941) and calculated from observations in Nastrom and Gage (1985), depicts a broad, wavenumber-dependent range of slopes across the typical scales of atmospheric motion—k^{-3} between the planetary/synoptic injection scales and the large mesoscales (500 km and greater) and $k^{-5/3}$ from the small mesoscales (1-500 km) to the microscales making up the inertial subrange. Stratification has been shown to cause flow to deviate from the $k^{-5/3}$ power law as the flow ceases to be isotropic (Gage, 1979; Lilly, 1983). Early studies suggested that there was an inverse energy cascade from large wavenumbers to small wavenumbers responsible for the difference between the theorized isotropic turbulence of Kolmogorov and stratified anisotropic turbulence of the mesoscales (Charney, 1972). However, theories arguing the opposite, that the difference between the theorized and observed spectra was due to the downscale cascade of kinetic energy (Merilees and Warn, 1975), also existed, and there were decades of debate over this question. More recent modeling studies (Tung and Orlando 2002; Lindborg, 2006; Pouquet and Marino 2013; among many others) have provided evidence that quasi-geostrophic turbulence produces a kinetic energy cascade that radiates energy up- and down-scale from the scale at which it is injected, suggesting that the kinetic energy spectrum at the mesoscales is more strongly influenced by kinetic energy cascading forward from the synoptic wavenumbers than inversely from large wavenumbers.

These studies made use of simplified, dry dynamical models. Hamilton et al. (2008) and Augier and Lindborg (2013) used GCMs that accounted for moist processes in the mesoscales and found that the mesoscales are energized by latent heat release below the synoptic scales, as the dry dynamical core versions of those GCMs produced shallower slopes in the mesoscales than the dynamical cores with moist conditions. Latent heat release has been shown to increase the isotropic, higher-order contributions to turbulent energy flux, including solenoidal and pressure-dilatation, while having little influence on anisotropic, turbulent Reynolds stress (Eschenroeder, 1964; Jaberi and Madnia, 1998; Livescu et al., 2001; and Livescu, 2004). Latent heat release also increases the production of enstrophy. Waite and Snyder (2012) found that moist dynamics affect the upper-level mesoscales by inducing gravity waves that contract and cascade energy downscale. These studies provide various sources of latent heat release in the atmosphere at various scales, which must transform partly to kinetic energy at those scales. Waite and Snyder noted that there is a peak injection of kinetic energy in the mesoscales at 800 km.

It is known that energy will radiate, in part, upscale, so if latent heat can be released in the upper mesoscale wavenumbers, then kinetic energy should cascade upscale into the synoptic scales. However, the transformation of kinetic energy across spatial orientations for a typical synoptic scale wave is not well studied.

Waite and Snyder used the Advanced Research WRF model (WRF-ARW; hereafter just WRF) for their study, and this study will do the same. Input data for WRF will be filtered to suppress incoherent components of the flow residing at subsynoptic scales and a comparative analysis of pairs of filtered and unfiltered simulations will be carried out in a case-oriented approach to identify the role of subsynoptic scale components of flow on synoptic scale development. A case-oriented approach is a novel method for studying the turbulent energy cascade, and provides a synoptic view of the transformation of small-scale kinetic energy injection onto the larger scales. Case selection involves choosing mid-latitude weather events that follow typical baroclinic development, which allows for generalizability among cases. The cases will include wave breaking, which is a physical manifestation of the forward energy cascade and is both sensitive to small-scale perturbations and acts to generate small-sale perturbations of its own.

Chapter 2 will discuss the wavelet transform in general: what wavelets are, what their properties are, and how they facilitate multi-resolution analysis. Chapter 3 will introduce wavelet filtering by a recursive algorithm and will identify a dynamical framework that constrains the wavelet filter applied to the WRF input data to suppress incoherent features at subsynoptic scales. Chapter 4 will present the selected model environment for all cases to be investigated, which includes the domain configuration, parameterizations, and input data, as well as the output of the wavelet filter. Chapter 5 will discuss the first case, establishing the dynamical and statistical methods with which the comparative analysis of the base and filtered simulations will be carried out. Chapters 6 and 7 will expand upon the conclusions presented in Chapter 5, with two more cases with very different atmospheric conditions than Case 1 to highlight how the upscale energy cascade manifests in different conditions. Finally, Chapter 8 will present overall conclusions for this study.

CHAPTER II

WAVELET TRANSFORM

2.1 Wavelet transform basics

The majority of the mathematics of this section follows Blatter's (1998) notation, with some exceptions as noted below. The discrete wavelet transform was developed over the course of the 1980s, with notable contributions from Yves Meyer (1990), Stephanie Mallat (1989), Ingrid Daubechies (1988), and many others. In the geophysical sciences, it is often used for denoising data sets, particularly in studies of turbulence (Farge 1992). When considering the wavelet transform, it is useful to compare and contrast it with the more familiar Fourier transform, which takes an input signal $f(x)$ and transforms it to a function $\hat{f}(\nu)$, where ν is frequency and f maps from the domain of real numbers to complex, $f: \mathbb{R} \to \mathbb{C}$. The Fourier transform's resolution in wavenumber space is very high, but the function in wavenumber space lacks locality.

For applications requiring locality in their spectral transforms, the windowed and short-time Fourier transforms are a means of adding locality to the Fourier transform; the Gabor transform is a famous example of this (Blatter 1998). The advantages such modified transforms afford is that, for an input signal with a continuously changing power spectrum, one can identify not only the peaks in wavenumber power but also the time or location at which changes in the frequency or wavenumber power occur. The addition of locality to the transformed signal allows a variety of analysis techniques can allow for targeting specific frequencies and wavenumbers in specific times or locations (Mallat 1989) at the cost of resolution in wavenumber space.

The major difference between the windowed Fourier transform and the wavelet transform is the choice of wavelets as the analyzing function. The windowed Fourier transform, while having some locality, is still carried out via the integral that defines the Fourier transform. In contrast, a generic wavelet is finitely compacted, *i.e.* it exists within some closed interval and is zero elsewhere, and its integral in L^1 space converges to zero:

$$\int_{-\infty}^{\infty} \psi \, dt = 0 \, . \tag{2.1}$$

A mother wavelet is a function that specifically exists in the Hilbert space $\psi \cap L^1 \cap L^2$ whose norm is 1. What this means is that the mother wavelet is a function that is square integrable (finitely valued and locally compacted) and whose norm is defined as the L^2 norm, or the Euclidean norm. Most of the well-known wavelets, such as the Debauchies, Haar, or Mexican Hat wavelets are functions that exhibit both of these characteristics, which make them convenient for signal processing.

A wavelet ψ has parameters a and b that define its size and position: a is the dilation parameter, which determines the amplitude of the wavelet function, and b is the translation parameter, which determines the location of the peak of the wavelet along the transform axis. The dilation and translation parameters function similarly to the parameters that determine the window shape for the windowed Fourier transform, and are defined such that $(a, b) \in \mathbb{R}^+ \times \mathbb{R}$ and that $Wf: \mathbb{R}^+ \times \mathbb{R} \to \mathbb{C}$, where (Blatter 1998):

$$Wf = \langle f, \psi \rangle = \frac{1}{|a|^{0.5}} \int_{-\infty}^{\infty} f(t) \overline{\psi\left(\frac{t-b}{a}\right)} dt. \tag{2.2}$$

The wavelet transform for a wavelet function and a given input signal *f* is the inner product of the wavelet function and the input signal across the input domain using translations of *b* and with *a* scaling. The above definition is the continuous form, but hereafter the primary transform described will be the discrete transform, and as a result the dilation and translation parameters *a* and *b* will be replaced with *j* and *k*.

However, equation 2.2 alone does not allow for multiresolution analysis—the separation of the wavelet space into spectral bins at sequential transformation levels. The continuous wavelet transform does not necessarily map back onto itself when scaled, so we want to find a transform that reproduces itself when subject to a scaling operator:

$$D_a \psi(t) \equiv \psi\left(\frac{t}{a}\right) \to D_2 \psi(t) \equiv \sum_{k=0}^{n} c_k \, \psi(t-k) \,, \tag{2.3}$$

For that, the *scaling function* is needed. It is defined with similar properties to that of the mother wavelet, but with a few other considerations that allow for dilations of scale $a > 1$

to have interesting properties. Consider a series of subspaces V_j that are all contained within the L^2 space that contains $\psi_{j,k}$:

$$\cdots \subset V_{j+1} \subset V_j \subset V_{j-1} \subset \cdots \subset L^2 \tag{2.4}$$

where larger j indicates a smaller subspace, $j \in \mathbb{Z}$, and that have the properties

$$\cap V_j = \{0\}, \quad \cup V_j = L^2, \quad \forall j. \tag{2.5}$$

The result of the above constraints is that the portions of the input signal f that are contained in a given subspace V_j, $f \in V_j$, are of the scale 2^j or larger. The subspaces can be related via the scaling property

$$V_{j+1} = D_2\left(V_j\right), \tag{2.6}$$

where c_k is a transform coefficient of a given level at location $t - k$. For a function ϕ whose translations form an orthonormal basis with the V_0 subspace of L^2, the subspace V_0 can be defined as a linear combination of signal components

$$V_0 = \left\{ f \in L^2 \mid f(t) = \sum_k c_k \phi(t-k) \right\}. \tag{2.7}$$

The scaling function can be defined in the form

$$\phi_{j,k}(t) \coloneqq 2^{-\frac{j}{2}}\phi\left(\frac{t}{2^j} - k\right). \tag{2.8}$$

However, while these are sufficient criteria for a multiresolution analysis, more is needed to establish the spectral bins, or filter banks, that allow for spectral analysis using the transform. The scaling equation is a means of achieving this:

$$\phi(t) = \sqrt{2}\sum_{k=-\infty}^{\infty} h_k \phi(2t - k) \tag{2.9}$$

where h_k is a coefficient vector. The coefficient vector h_k must satisfy a few constraints of its own to ensure that $\phi_{0,k}$ is orthonormal to V_0, namely that

$$\langle \phi_{0,n}, \phi \rangle = \delta_{0n} = \sum_k h_k \overline{h_{2n+k}}, \qquad \forall n \in \mathbb{Z}. \tag{2.10}$$

Fortunately, if the scaling function has compact support then the number of coefficients that are nonzero are bounded by the upper and lower limits of the scaling function in real space, which are themselves integers. This is because the scaling equation can be re-written in the form

$$\phi = \sum_k h_k \phi_{-1,k} \tag{2.11}$$

based on the formulation of the spaces V_j in Equation 2.7, which allows for the re-writing of the coefficient vector h_k as the inner product of the two scaling functions $\langle \phi, \phi_{-1,k} \rangle$. This ensures that the scaling function—and by extension the coefficient vectors—have compact support, which provides further constraints on possible scaling functions. To ensure completeness, the absolute value of the integral of the scaling function must be one.

The last major hurdle is connecting the scaling function to the wavelet function to complete the filter banks. The scaling equation can be transformed to Fourier space to yield

$$\hat{\phi}(\xi) = \frac{1}{\sqrt{2}} \sum_k h_k e^{-\frac{ik\xi}{2}} \hat{\phi}\left(\frac{\xi}{2}\right) = H\left(\frac{\xi}{2}\right) \hat{\phi}\left(\frac{\xi}{2}\right) \tag{2.12}$$

where H is known as the generating function, and is the sum of the coefficient vectors and the exponentials. Transforming the input signal $f(t)$ into Fourier space as well produces:

$$\hat{f}(\xi) = m_f\left(\frac{\xi}{2}\right) \hat{\phi}\left(\frac{\xi}{2}\right) \tag{2.13}$$

where m is a function analogous to H. H and m are periodic and form an orthogonal basis in $\mathbb{C}^2$, allowing for $\hat{f}$ and $\hat{\phi}$ to be directly related:

$$\hat{f}(\xi) = e^{\frac{i\xi}{2}} \nu(\xi) \overline{H\left(\frac{\xi}{2} + \pi\right)} \hat{\phi}\left(\frac{\xi}{2}\right). \tag{2.14}$$

The function ν is 2π-periodic and relates the functions H and m together. Its presence in the above equation is a necessary condition to ensure that the input signal f belongs to the wavelet subspace W_0, which is the wavelet equivalent to the V_0 subspace. As a result, the scaling and wavelet functions can be related directly:

$$\hat{\psi}(\xi) = e^{\frac{i\xi}{2}}\overline{H\left(\frac{\xi}{2}+\pi\right)}\,\hat{\phi}\left(\frac{\xi}{2}\right) \tag{2.15}$$

$$\rightarrow \psi(t) = \sqrt{2}\sum_{k} g_k \phi(2t-k) \tag{2.16}$$

where $g_k \coloneqq (-1)^{k-1}\overline{h_{-k-1}}$. Note that, while there is now a wavelet function that is built directly off of the scaling function, the scaling function does not uniquely determine the wavelet function. A given scaling function $\phi(t)$ could produce a variety of wavelet functions depending on the leading factors in the Fourier space relationship, but this does link the two functions together.

Consider then the projection of the scaling function onto the V_j space, P_j:

$$P_j f = \sum_{k=-\infty}^{\infty} \langle f, \phi_{j,k}\rangle\, \phi_{j,k} \tag{2.17}$$

which follows from orthogonality. Recall that the scaling function, by design, exists in chained subspaces of L^2 that are comprised of the components of f that are of span 2^j or larger. Moving from one subspace to the next largest—$V_{j+1} \rightarrow V_j$—gains space, which the scaling function *by itself* cannot fill. Thus, the chain of wavelet subspaces,$\cdots \subset W_{j+1} \subset W_j \subset W_{j-1} \subset \cdots \subset L^2$, which are pairwise orthogonal to the scaling subspaces, make up the components of their corresponding V_j subspaces remaining from lifting the $j-1$ space to the j space, meaning

$$V_{j-1} = V_j \oplus W_j, \;\; V_j \perp W_j, \;\; \forall j \in \mathbb{Z}\,. \tag{2.18}$$

Or, put another way, the projection of the wavelet subspaces $Q_j f = \sum_k \langle f, \psi_{j,k} \rangle \psi_{j,k}$ forms a quadrature pair filter bank with the equivalent scaling subspace:

$$Q_j = P_{j-1} - P_j, \qquad P_{j-1} = P_j + Q_j \tag{2.19}$$

Multiresolution analysis is possible because of the coupling of the wavelet function to a scaling function. The scaling function acts as the low pass filter of the pair while the wavelet function acts as the high pass filter.

Starting with the scaling equation and the wavelet function equivalents,

$$\phi(t) = \sqrt{2} \sum_k h_k \phi(2t-k)$$

$$\psi(t) = \sqrt{2} \sum_k g_k \phi(2t-k)\,,$$

where h_k and g_k are the coefficient vectors of the generating functions of the scaling and wavelet functions, respectively, Equation 2.8 and the alternate form of the scaling Equation 2.11 can be used to formulate the relationship

$$2^{-\frac{j}{2}}\phi\left(\frac{t}{2^j}-n\right)=2^{-\frac{j-1}{2}}\sum_k h_k\phi\left(\frac{t}{2^{j-1}}-2n-k\right),$$

where the n has replaced k as the translation parameter from Equation 2.8. An equivalent form for the wavelet function exists, both of which can be simplified to the following forms:

$$\begin{aligned}\phi_{j,n}&=\sum_k h_k\phi_{j-1,2n+k},\quad \forall j,\forall n\,,\\ \psi_{j,n}&=\sum_k g_k\phi_{j-1,2n+k},\quad \forall j,\forall n\,.\end{aligned}\tag{2.20}$$

This recursive formula for calculating the n-th position at the j-th dilation level based on the sum of the entire k-length array of the generating functions forms the backbone of the fast wavelet transform. If we refer to the wavelet transform as

$$A_{j,k}=\langle f,\phi_{j,k}\rangle=\int f(t)\overline{\phi(t-k)}dt$$

then Equation 2.20 can be extended to determine any given set of transform coefficients $A_{j,k}$:

$$A_{j-1,k} = \langle f, \phi_{j-1,k} \rangle \, ,$$

$$\rightarrow A_{j,n} := \langle f, \phi_{j,n} \rangle = \sum_k \overline{h_k} \langle f, \phi_{j-1,2n+k} \rangle = \sum_k \overline{h_k} A_{j-1,2n+k} \, . \tag{2.21}$$

The set of transform coefficients A at the j-th dilation level and n-th position is given by the sum of the product of the generating function coefficients h_k and the set of coefficients at the $(j-1)$-th dilation level. Recall from Equation 2.3 that the scaling function subspaces are contained within each other sequentially, meaning that the first transform level contains all information of each subsequent level. If we take the minimum level to be j=1, then levels $j = 2,3, \dots, J$ are all contained in and determined from the maximum transform level as given by Equation 2.21. As the coefficients here are from the low pass filter, the coefficient array A is known as the *Approximation* set.

The same calculations can be done with the wavelet function as well, yielding

$$D_{j,k} = \langle f, \psi_{j,k} \rangle = \int f(t) \overline{\psi_{j,k}} dt \, ,$$

$$D_{j-1,k} = \langle f, \psi_{j-1,k} \rangle \, ,$$

$$\rightarrow D_{j,n} := \langle f, \psi_{j,n} \rangle = \sum_k \overline{g_k} \langle f, \phi_{j-1,2n+k} \rangle = \sum_k \overline{g_k} A_{j-1,2n+k} \, . \tag{2.22}$$

Like Equation 2.21, Equation 2.22 demonstrates that every j-th set of transform coefficients contains the $(j-1)$-th set of coefficients, which means the transform is highly redundant.

However, unlike Equation 2.21, Equation 2.22 shows that the set of coefficients from the wavelet component of the transform can be calculated from the previous level's approximation set. The sets $D_{j,n}$ are known as the *Detail* sets, and they contain what remains of the transform coefficients after stepping from one dilation level to the next.

The wavelet transform does not have a single defined inversion formula, owing to the fact that the transformed function $\mathcal{W}f$ is a function of two parameters *j* and *k*. This means that the inversion formula can take many forms and that many of those forms are equally valid to use. The general formula used in the methods for this project take the following form: let C_ψ be the integral of the Fourier transform of a generic mother wavelet ψ as depicted

$$C_\psi := 2\pi \int_{\mathbb{R}^+} \frac{\left|\hat{\psi}(a)\right|^2}{|a|} da\ ,$$

which converges by necessity. The input signal $f(t)$ can be found via

$$f(t) = \frac{1}{C_\psi} \int_{\mathbb{R}^2} \mathcal{W}f(a,b)\psi_{a,b}(t) \frac{dadb}{|a|^2} \tag{2.23}$$

in the case of the continuous wavelet transform. In the discrete case, it can be noted that Equation 2.17 already demonstrates a similar calculation.

Prior to this point, much time has been spent focusing on the theoretical background of the wavelet transform and multiresolution analysis. Previously, the wavelet and scaling subspaces have used index notation $j, j-1, j-2, \dots, J$ to indicate higher dilation levels and, consequently, higher resolution in wavenumber space with a reduced resolution in physical or temporal space. Hereafter, $j = 1$ will be considered the first level of the transform, with level 0 being the input signal, and progressively larger j values indicating higher dilation, which is more in line with common software packages that perform the wavelet transform. Likewise, individual coefficient sets at each level are hereafter referred to by the sequence of filters that produced them—*i.e.* the first transform level contains sets A and D, the second transform level contains sets AA and DA, the third containing sets AAA and DAA, and so on. Figure 2.1a depicts the banking of the coefficient arrays at each level, referred to as *nodes* hereafter.

Before moving on to of the wavelet transform in two dimensions, a brief discussion of the cardinality of the coefficient nodes is warranted. The fast wavelet transform takes advantage of the fact that resolvable wavenumbers are redundantly sampled and that each node generated by the transform can be downsampled. As a result, each node is decimated by 2^{-j}. For example, a one-dimensional signal $f(t)$ with 360 data points would be transformed into A and D arrays containing 180 points in the first transform level. Subsequent levels would have fewer by half as well, with AA and DA having 90 points, AAA and DAA having 45 points, and so forth. Conversely, while the temporal or spatial resolution is reduced for every dilation level, the wavenumber resolution becomes finer as each transform level is constructed from the inner product of the scaling function and the previous level's approximation node. For a wavenumber space $\mathcal{V}$ with a maximum resolvable wavenumber V:

$$\{\nu_A \in \mathcal{V} \mid 1 \leq \nu_A \leq 0.5V\}, \qquad \{\nu_D \in \mathbb{N} \mid 0.5N < \nu_D \leq V\}$$

$$\{\nu_{AA} \in \mathcal{V} \mid 1 \leq \nu_{AA} \leq 0.25V\}, \qquad \{\nu_{DA} \in \mathbb{N} \mid 0.25N < \nu_{DA} \leq 0.5V\}$$

$$\{\nu_{AAA} \in \mathcal{V} \mid 1 \leq \nu_{AAA} \leq 0.125V\}, \qquad \{\nu_{DAA} \in \mathbb{N} \mid 0.125N < \nu_{DAA} \leq 0.25V\}$$

The traditional wavelet transform does nothing with the detail coefficients when transforming to higher levels, but for many data sets the detail coefficients contain wavenumbers that are of interest. The wavelet packet transform can be used if one wants to include the detail coefficients in subsequent levels with minimal change in process. This transform is depicted in Figure 2.1b. Downsampling results in aliasing in the detail nodes, however, and needs to be accounted for. In Figure 2.1b, the tree is shown using *natural* order, but the *frequency* ordering is *AAA*, *DAA*, *DDA*, *ADA*, *AAD*, *DAD*, *DDD*, and *ADD*, effectively reversing the order of the nodes built from the $(j-1)$-th level's detail node.

2.2 The two-dimensional wavelet transform

The wavelet transform is separable, so the two-dimensional wavelet transform is two one-dimensional transforms along two different axes. Mathematically, this doesn't change what the transform does or what the coefficients represent at any level, but it does warrant a brief discussion of the banking involved. Figure 2.2 is a schematic of the coming discussion.

For an input signal $f(x, y)$, the scaling and wavelet functions can be applied to the x and y axes in succession in four combinations: low pass in x and y; low pass in x, high pass in y; high pass in x and low pass in y; and high pass in both x and y. This can be written as the sum of four tensor products (Misiti et al. 2007)

$$V_{j-1}^{2D} = \overline{(V_j \otimes V_j)} \oplus (\overline{V_j \otimes W_j)} \oplus (\overline{W_j \otimes V_j)} \oplus (\overline{W_j \otimes W_j)}\,, \tag{2.24}$$

where V and W are the subspaces of the scaling and wavelet functions mentioned previously. The effect of the above is that there are now three wavelet functions and one scaling function derived from the products, given by

$$\begin{aligned}
\phi_{j,n}(x, y) &= \phi_{j,n}(x)\phi_{j,n}(y)\,, \\
\psi_{j,n}^{H}(x, y) &= \psi_{j,n}(x)\phi_{j,n}(y)\,, \\
\psi_{j,n}^{V}(x, y) &= \phi_{j,n}(x)\psi_{j,n}(y)\,, \\
\psi_{j,n}^{D}(x, y) &= \psi_{j,n}(x)\psi_{j,n}(y)\,.
\end{aligned} \tag{2.25}$$

The family of Equations 2.25 represent the four combined two-dimensional scaling and wavelet functions for the two-dimensional wavelet transform. As the transform is a sequence of one-dimensional transforms, the general transform Equations 2.21 and 2.22 still describe the individual transforms. Here the verbiage can be a bit tricky: the superscripts on the wavelets are no longer simply A and D for approximation and detail; A remains the approximation, but H is the horizontal wavelet and node, V is the vertical wavelet and node, and D is the diagonal wavelet and node. The three new wavelet functions

$\psi^H_{j,n}$, $\psi^V_{j,n}$, and $\psi^D_{j,n}$ are short-hand representations of the low- and high-pass filter combinations. The inverse of the two-dimensional transform is like that of the one-dimensional transform.

Finally, the rules that govern node cardinality and wavenumber resolution that were discussed for the one-dimensional transform still apply to the two-dimensional transform, with the only complication being that each node is now a combination of frequencies in two dimensions, such that the A node contains both low wavenumber subsections, the D node contains both high wavenumber subsections, and the H and V nodes contain one low wavenumber subsection and one high wavenumber subsection. In physical space, this corresponds to the horizontal node containing a subset of flow components elongated in the zonal direction and the vertical node containing a subset of flow components elongated in the meridional direction. For this reason, the coefficients in the approximation and diagonal nodes represent the power of the roughly isotropic constituents of the input signal, while the horizontal and vertical nodes represent the power of the roughly anisotropic constituents of the input signal. For a wavenumber space $\mathcal{V}$ with maximum resolvable wavenumbers K and L, each node would contain wavenumbers k and l that fall within the intervals:

$$V_A\colon \{k_A \in \mathcal{V} \mid 1 \le k_A \le 0.5K, l_A \in \mathcal{V} \mid 1 \le l_A \le 0.5L\}$$

$$W_H\colon \{k_H \in \mathcal{V} \mid 1 \le k_H \le 0.5K, l_H \in \mathcal{V} \mid 0.5L < l_H \le L\}$$

$$W_V\colon \{k_V \in \mathcal{V} \mid 0.5K < k_V \le K, l_V \in \mathcal{V} \mid 1 \le l_V \le 0.5L\}$$

$$W_D\colon \{k_D \in \mathcal{V} \mid 0.5K < k_D \le K, l_D \in \mathcal{V} \mid 0.5L < l_D \le L\}$$

Beyond the first level, the two-dimensional transform shapes up quite similarly to the node structure of the one-dimensional form with the exception of there being many more nodes in the filter bank. The number of nodes in each levels' filter banks in the two-dimensional transform is equal to 2^{2a}. The naming convention for two-dimensional nodes mentioned above is consistent with the conventions for higher levels in the one-dimensional transform: at level 2, the A node is used to calculate the AA, HA, VA, and DA nodes; the H node is used to calculate the AH, HH, VH, and DH nodes, and so on for the V and D nodes. Each node at each subsequent level would contain a subsection of the node that it was calculated from as is the case in the one-dimensional transform. With this established, we can move on to using wavelets as a filter basis and the dynamical framework we use to justify the target of our filter.

Figures

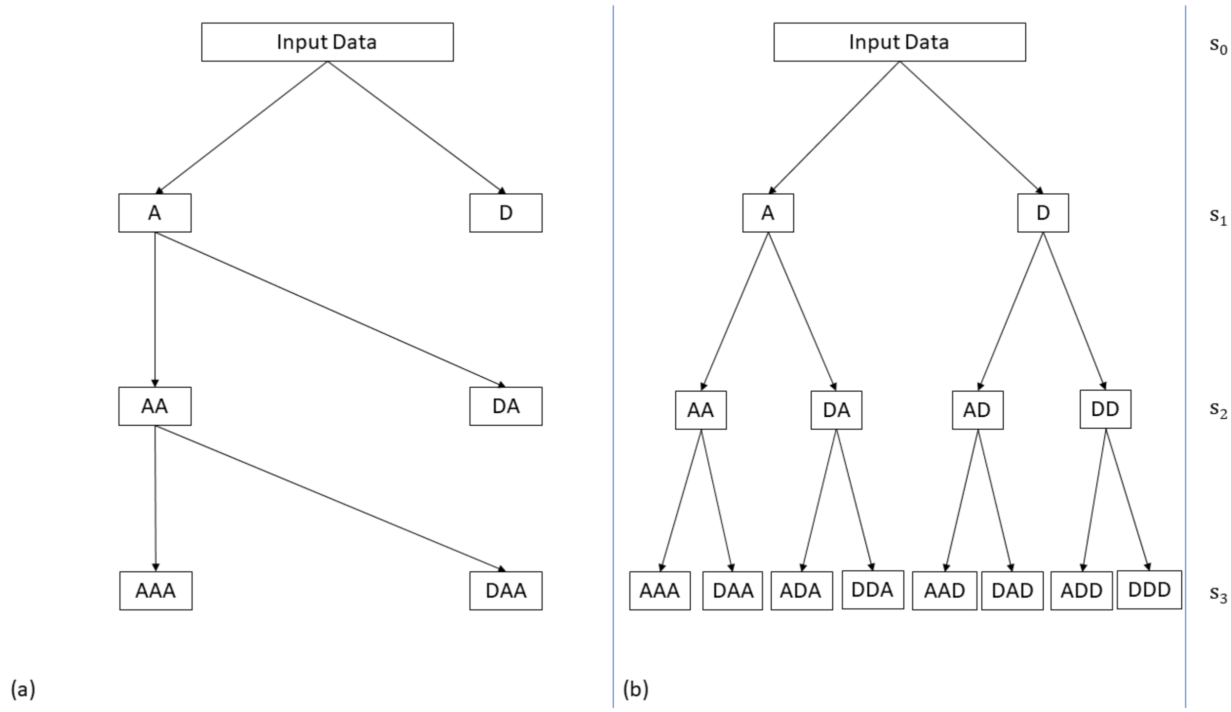

Figure 2.1: Schematic of the wavelet transform (left) and wavelet packet transform (right) in one dimension. Transform levels are indicated by the rightmost column, and node by the lettering in each box.

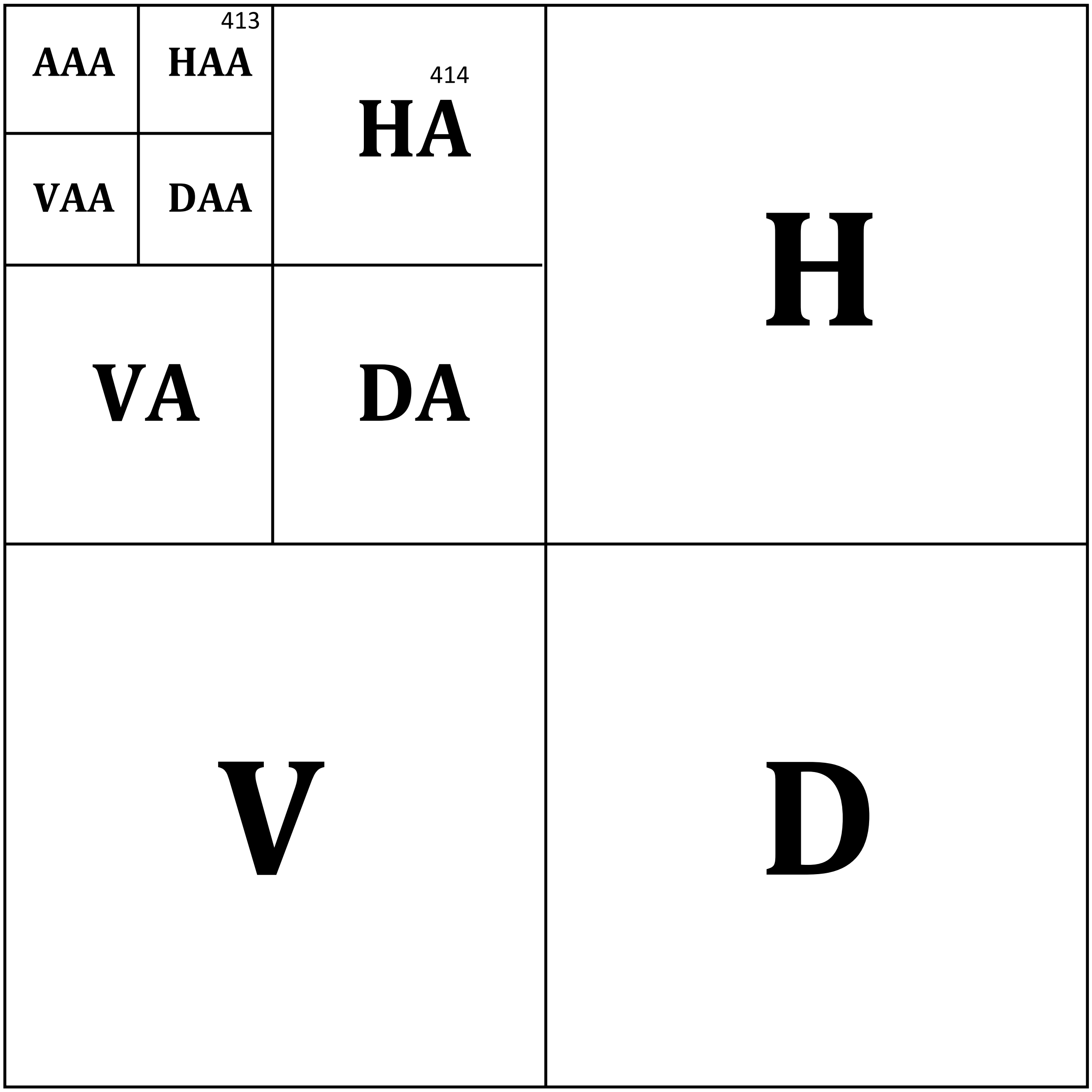

Figure 2.2: Schematic diagram of the two-dimensional wavelet transform. Nodes and level are indicated by the letters and length of labels, respectively.

CHAPTER III

FILTER ALGORITHM AND DYNAMIC BASIS

3.1 Coherence and turbulence

A method for removing nonlinear noise from instantaneous flow fields was the subject of a wealth of research in the early to mid-1990s. It was found that the wavelet transform compared favorably to other forms of filtering such as those using the two-dimensional Fourier transform, as it was as effective at identifying and removing noise while remaining lossless; the latter property is highly desirable as it ensures the inverse of the filtering method does not negatively alter the input fields. A recursive filter method is described in Azzalini et al. (2005), which uses a threshold based on the input signal's variance and cardinality:

$$s_0 = \left(\frac{1}{2}\,\langle f \rangle \ln[N]\right)^{\frac{1}{2}} \tag{3.1.1}$$

where $\langle f \rangle$ is the input signal variance and N is the number of grid points in the input signal. Each coefficient magnitude, $|h_k|$, in every node is compared against the threshold value and is set to zero if it is greater than the threshold value:

$$A_{j,n} = 0 \leftrightarrow |A_{j,n}| > s_0\,. \tag{3.1.2}$$

After every node has been checked in this way, the remaining coefficients are used for the inverse transform and the resulting signal is the noisy, “incoherent” field $f_<$. As the wavelet transform is lossless, the relationship between the incoherent signal and the input signal can be described thus:

$$f \equiv f_> + f_< , \tag{3.1.3}$$

where f is the input signal, $f_>$ is the coherent portion of the signal, and $f_<$ is the incoherent portion of the signal. To ensure that all of the constituent noise is removed from the input signal, the process in Equation 3.1.2 is repeated with the threshold value calculated from the remaining incoherent field:

$$s = \left(\frac{1}{2}\langle f_< \rangle \ln[N]\right)^{\frac{1}{2}} , \tag{3.1.4}$$

where the input signal variance $\langle f \rangle$ has been replaced with the incoherent signal variance $\langle f_< \rangle$. The algorithm passes over the remaining coefficients again to see if any more need to be removed, and then produces a new $f_<$. The algorithm eventually converges to $s_{new} = s_{old}$, and the result is the final incoherent field.

The term “noise” is used to describe the incoherent components discarded after the filtering, but this is a bit of a misnomer for our purposes. Farge et al. (1999) used the filter threshold calculation described in Equation 3.1.1 to target Gaussian white noise using the input signal variance, arguing that Gaussian white noise present in the input signal contributed a small fraction of the input signal variance. The n iterations of the threshold calculation used the incoherent component variance $\langle f_{<,n-1} \rangle$, which is necessarily constructed with fewer and fewer wavelet coefficients as the number of iterations n increases, until the iteration N results in the variance $\langle f_{<N} \rangle$ that converges to the Gaussian variance. If the incoherent component one is seeking to remove from an input dataset is not the Gaussian noise as described by Farge et al., the thresholding needs to be adjusted and there needs to be some justification given for why those components are being targeted at all if they are not simply "noise." That justification is the focus of this section.

Because we are interested in the kinetic energy cascade between the synoptic and upper-mesoscale wavenumbers, we want to retain the synoptic-scale components of the flow. These motions are quasi-balanced according to quasi-geostrophic balance, and so when we define "coherent" components of flow, these are the components we mean. Our goal, then, is to remove constituents of flow below the synoptic scales that are unbalanced, have high variability, and contribute weakly to the total kinetic energy of the troposphere. Energy and enstrophy concepts allow us to analytically define the ideal target for the wavelet filter.

From Merilees and Warn (1975), the vorticity equation for a two-dimensional QG inviscid flow can be solved via a Fourier expansion of a horizontally periodic flow in the form

$$\psi(x, y) = \sum_{\boldsymbol{K}} \psi_{\boldsymbol{K}} e^{i\boldsymbol{K}\cdot\boldsymbol{R}}$$

(3.1.5)

where $\boldsymbol{K}$ is total wavenumber $\boldsymbol{K} = k\hat{\boldsymbol{\imath}} + l\hat{\boldsymbol{\jmath}}$, $\boldsymbol{R}$ is the position vector $\boldsymbol{R} = x\hat{\boldsymbol{\imath}} + y\hat{\boldsymbol{\jmath}}$, and ψ is the streamfunction. Because viscous molecular dissipation is not being considered, the total energy

$$E = \sum_{\boldsymbol{K}} (\boldsymbol{K} \cdot \boldsymbol{K}) \psi_{\boldsymbol{K}} \psi_{\boldsymbol{K}}^{*} \tag{3.1.6}$$

must be conserved. As the total energy is the sum of the superposition of the many wavenumber components of the flow (and thus components of the stream function), one can consider a triad of waves interacting with one another such that their energies are being passed amongst one another. If the constituent wavenumbers ***K*, *L*,** and ***M*** are defined such that $\boldsymbol{K} \leq \boldsymbol{L} \leq \boldsymbol{M}$, then

$$\delta E_K + \delta E_L + \delta E_M = 0 \tag{3.1.7}$$

$$(\boldsymbol{K} \cdot \boldsymbol{K})\delta E_K + (\boldsymbol{L} \cdot \boldsymbol{L})\delta E_L + (\boldsymbol{M} \cdot \boldsymbol{M})\delta E_M = 0 \tag{3.1.8}$$

as from Lorenz (1960). Defining A to be the ratio of the differentials of the K and L waves and B to be the ratio of the differentials of the L and M waves,

$$A = \frac{\delta E_K}{\delta E_L} = \frac{\boldsymbol{M} \cdot \boldsymbol{M} - \boldsymbol{L} \cdot \boldsymbol{L}}{\boldsymbol{K} \cdot \boldsymbol{K} - \boldsymbol{M} \cdot \boldsymbol{M}} \tag{3.1.9}$$

$$B = \frac{\delta E_M}{\delta E_L} = \frac{\boldsymbol{L} \cdot \boldsymbol{L} - \boldsymbol{K} \cdot \boldsymbol{K}}{\boldsymbol{K} \cdot \boldsymbol{K} - \boldsymbol{M} \cdot \boldsymbol{M}} \tag{3.1.10}$$

means both A and B must be negative due to the denominator $\boldsymbol{K} \cdot \boldsymbol{K} - \boldsymbol{M} \cdot \boldsymbol{M}$ being negative definite. As they are both ratios of the change in energy between one wave and another and since they're both defined in terms of wave $\psi_{\boldsymbol{L}}$, that means that any interaction between wave $\psi_{\boldsymbol{L}}$ and waves $\psi_{\boldsymbol{K}}$ and $\psi_{\boldsymbol{M}}$ results in a cascade of energy away from $\psi_{\boldsymbol{L}}$. The ratio of A to B

$$S = \frac{X}{Y} = \frac{\boldsymbol{K} \cdot \boldsymbol{K} + \boldsymbol{2L} \cdot \boldsymbol{K}}{\boldsymbol{L} \cdot \boldsymbol{L} - \boldsymbol{K} \cdot \boldsymbol{K}} \tag{3.1.11}$$

produces an inverse cascade $S > 1$ for situations where the norms of K and L are related via $|\boldsymbol{K}| = |\boldsymbol{L}|(1 - \varepsilon)$, and a normal energy cascade $S < 1$ when $|\boldsymbol{K}| = \varepsilon|\boldsymbol{L}|$. $\psi_{\boldsymbol{L}}$ does not preferentially cascade energy toward one end of the spectrum over the other, but the net cascade of energy was suggested to be primarily toward small wavenumbers, because small wavenumber elements of the flow tended to have more energy than large wavenumbers innately.

Unlike the energy cascade, the enstrophy cascade is primarily toward large wavenumbers. Taking the potential enstrophy

$$\mathcal{Z} = \frac{1}{2} \sum_{\boldsymbol{K}} (\boldsymbol{K} \cdot \boldsymbol{K})^2 \psi_{\boldsymbol{K}} \psi_{\boldsymbol{K}}^* \tag{3.1.12}$$

the same operation used for Equation 3.2.7 to determine the ratio of the enstrophy cascade from one wave to another yields

$$Q = \frac{\boldsymbol{K} \cdot \boldsymbol{K}}{\boldsymbol{M} \cdot \boldsymbol{M}} S \, .$$

The result is that, in addition to the energy spectrum, there is an enstrophy spectrum that is effectively reversed: high wavenumbers tend to be enstrophy dominated, and they both produce higher enstrophy and have more enstrophy cascade toward them (Merilees and Warn 1975).

This, of course, is not particularly surprising given what is known about the formulations of large-scale flow. For flow at the synoptic scales, part of the QG approximation dictates that the relative vorticity of the flow tends to be much smaller than the planetary vorticity, indicated by the smallness of the Rossby number. As a result, the enstrophy of the flow at large scales will also be dominated by the planetary enstrophy. This makes intuitive sense when you consider that the enstrophy is the square of the relative vorticity in physical space:

$$\mathcal{Z} = \int_{p_0}^{P_T} \zeta_r^2 \, dp \, , \tag{3.1.13}$$

$$\zeta_r = \left(\frac{\partial v}{\partial x} - \frac{\partial u}{\partial y}\right),$$

such that the order of the vorticity is the characteristic flow velocity over the characteristic length scale, U/L. Comparing the characteristic velocities across scales, the subsynoptic and mesoscales tend to have flow velocity variations that don't differ significantly from those of the synoptic scales. However, the characteristic length scales decrease by several orders of magnitude between the synoptic and mesoscales. As a result, the relative vorticity at the mesoscales tends to be as large or larger than the planetary vorticity.

When considering the kinetic energy across scales, it is clear that most of the kinetic energy is concentrated at the higher wavenumbers in the form of zonal jets, which are characterized by the highest flow velocities. Because kinetic energy does not depend on length scale, reducing the spatial scale of the fluid motions does not have any effect on the kinetic energy, and thus there is no preference for the concentration of kinetic energy at small scales like there is with enstrophy. From this, we can say that the flow at large scales is *energy dominated*. Conversely, flow at subsynoptic, mesoscale, and microscales are *enstrophy dominated*.

This is the second characteristic of the model input data that we seek to target with the wavelet filter. As discussed in section 3.1, the wavelet filter shouldn't target the synoptic scales and mean flow. We want the incoherent wind to be that which is enstrophy dominated—high frequency components with small length scales that don't perturb the background flow and thus ensure that the total kinetic energy of the model data is largely unchanged. It is likely that the eddy perturbations would be altered, but to order ε at most. This will reduce the enstrophy of the input data with minimized suppression of the kinetic energy and the synoptic scales.

3.2 Nonlinear wavelet filter

Now that some constraints on the filter target have been established, determining the filter threshold is needed. According to Helmholtz' Theorem, a flow field can be decomposed into two components, the irrotational and the non-divergent flows. Those components are given by

$$\boldsymbol{V_{nd}} = \mathbf{k} \times \nabla\psi, \qquad \nabla \cdot \boldsymbol{V_{nd}} = 0 \tag{3.2.1}$$

$$\boldsymbol{V_{ir}} = \nabla\chi, \qquad \nabla \times \boldsymbol{V_{ir}} = 0 \tag{3.2.2}$$

where ψ is the stream function and χ is the velocity potential. Globally, winds in the mid to upper troposphere mid-latitudes are typically more strongly determined by the curl of the stream function than they are by the gradient of the velocity potential; the reverse is generally true for the tropics. As the name implies, the contribution of the irrotational wind to the vertical component of the relative vorticity vector is zero, and the contribution of the nondivergent wind to the divergence field is zero. Helmholtz's Theorem also states that:

$$\boldsymbol{V} = \boldsymbol{V_{ir}} + \boldsymbol{V_{nd}} = \boldsymbol{V} = \boldsymbol{\nabla}\chi + \mathbf{k} \times \boldsymbol{\nabla}\psi \tag{3.2.3}$$

or, in component form:

$$u = \frac{\partial\chi}{\partial x} - \frac{\partial\psi}{\partial y} \tag{3.2.4}$$

(3.2.5)

$$v = \frac{\partial\psi}{\partial x} + \frac{\partial\chi}{\partial y}$$

such that the wind is the sum of partial derivatives of the stream function and velocity potential. Filtering the irrotational wind only could be seen as a way to target subsynoptic components of the flow because they are higher order contributors at the synoptic scales, but doing so would not produce an incoherent field that reduces the enstrophy of the input field. Instead, the filter would be applied to both the stream function and velocity potential in a way that limits the reduction of the stream function power.

First, the filter threshold 3.1.1 is calculated from the input velocity potential

$$s_\chi = \left(\frac{1}{2}\langle\chi\rangle \ln(N)\right)^{\frac{1}{2}}$$

The magnitude of the nondivergent wind tends to be larger than the irrotational wind, and thus the variance of ψ tends to be higher than the variance of χ. This is important because ψ and χ are not filtered with different thresholds; s_χ is used as the filter threshold for both variables. The relative smallness of the variance of χ allows for the filter to only remove the components of ψ that contribute weakly to the total variance of ψ, a goal set out by the analysis above.

At this point in the filter process there are two possible methods that can be used. One method, the conventional method set out in Equation 3.1.2, is to set all coefficients larger than the threshold to zero, invert the transform, and calculate a new threshold using the incoherent field produced by the inverse transform (Equation 3.1.2). This filter is referred to as the *fine filter*. The other filter, referred to as the *coarse filter*, is carried out by setting all transform coefficients that are *smaller* than the threshold to zero and inverting the transform, and is new to this study. This produces the coherent field, and its variance is used on the next iteration of the threshold calculation.

The coarse filter produces much stronger filtering than the fine filter because the incoherent field has a much smaller variance than the coherent field. The two methods are arguably the maximum and minimum acceptable threshold limits, and produce the maximum and minimum “noisy” constituents of the total flow. The coarse filter is the only filter to produce an incoherent field that is large enough that it approaches the scale of the synoptic scale flow, and thus the fine filter is not used in this study. The effects of the coarse filter on the simulation input data are discussed in the following chapter.

CHAPTER IV

EXPERIMENTAL PROCEDURES

The case studies are simulated using the Advanced Research Weather Research Forecasting Model (WRF-ARW, WRF hereafter) version 4.1, compiled in realistic data mode. The WRF Pre-processing System (WPS), which takes input grib data and formats it such that WRF can ingest it, is version 4.1 as well. There is no data assimilation used in any model runs for this study: no analysis nudging, observation nudging, or spectral nudging is carried out. Boundary conditions are updated every six hours using WRF's initialization routines.

The model is configured for synoptic-scale events. Each model simulation makes use of a large outer domain (d01) covering a large portion of the Northern Hemisphere mid-latitudes. Nested within that outer domain is a smaller, higher-resolution domain (d02). This inner domain is positioned such that much of the upstream dynamics is contained within the outer domain, minimizing potential boundary effects. A sample domain, from the January 2000 case, can be seen in Figure 4.1. The model uses two-way nesting for its domains. The inner domain is initialized 6 hours after the outer domain, so there is no WPS input for the inner domain; rather, the outer domain 6-hour forecast is used for initialization instead. The domains are built on a Lambert Conformal grid, with the outer domain having a nominal *dx* and *dy* of 60 km; the inner domain is one-third the scale of the outer domain and has a nominal *dx* and *dy* of 20 km. The model has 40 vertical sigma levels and 4 soil levels. The dynamical core has a time step of 2 minutes for the outer domain and 40 seconds for the inner domain.

The simulation makes use of the WSM 5 microphysical scheme (Hong et al., 2004). The long and shortwave parameterization schemes are both New Goddard (Chou and Suarez, 1999) with a radiative Δt of 20 minutes. This scheme also allows for cloud effects on the radiation optical depth. The surface layer physics model is the revised MM5 Monin-Obukhov scheme (Jimenez et al. 2012) for WRF models, with surface heat and moisture fluxes and a snow cover effect. The land surface model is the Unified Noah land-surface model (Tewari et al. 2004). The planetary boundary layer physics model is the YSU planetary boundary layer model (Hong et al. 2006), called every time step. The cumulus physics model is the Grell-Freitas ensemble scheme (Grell and Freitas 2014) which is likewise called every time step.

Turbulence and mixing uses the second order diffusion term along with the horizontal Smagorinksy first order closure. Upper-level damping uses w-Rayleigh damping with a larger inverse time scale suited for real data cases. The parent domain uses a sixth order numerical diffusion with a 0.12 rate factor, while the child domain does not make use of this damping.

Input data are from the NCEP FNL Operational Global Analysis data set (NCEP 2000) in GRIB1 format with forecasts every 6 hours. WRF is configured to update its boundary conditions for each of these forecast times. The GFS FNL dataset used in this study has a grid resolution of 1° by 1°; the 0.25° by 0.25° FNL dataset does not have temporal coverage that includes the dates of this case study. The data is global and includes a volumetric inventory of many atmospheric variables on isobaric levels from 1000 hPa to 10 hPa; the WRF model initialization requires temperature, horizontal wind components, relative humidity, and geopotential height on isobaric levels. WRF also requires volumetric soil moisture and temperature at multiple ground depths, surface geography, surface pressure, mean sea-level pressure, and various other surface condition flags to properly build the model surface grid.

The filter algorithm is implemented in Python using the PyWavelets wavelet transform module (Lee et al. 2006). FNL files are converted to netCDF using UCAR's Python grib wrapper module. The wavelet family chosen for the filter algorithm is the Coiflet 4, based on the work of Yano et al. (2004) and Plu et al. (2008), the latter describing the general guidelines for choosing a wavelet family for filtering atmospheric data. The Coiflet family of wavelets, unlike many discrete wavelet families such as the Haar or Daubechies wavelets, is symmetric about its peak amplitude at zero and the Coiflet 4 specifically has 4 vanishing moments (Figure 4.1). Unlike Plu et al., filtering was carried out on the original data's grid. This was done primarily for ease of interpretation: filtering the data after it has been pre-processed and mapped to the WRF grid has the combined issues of the WRF pre-processing system interpolating data to a higher resolution grid, which can influence the power of the high wavenumber bands, while also making filtering along lines of latitude and longitude much more difficult. If the input signal is aligned with latitude and longitude, the transform allows for wavenumber bins in each coefficient node to contain easily separable subsets of either the zonal or meridional wavenumbers.

Edge effects pose a problem for the filter. There is no completely developed wavelet family that is orthogonal on the sphere; there are biorthogonal wavelet families that aim to fill this need, but were not considered for this project during the filter design phase. As a result, the wavelet transforms utilized do not account for variations in grid spacing in the input signal grid, nor are they able to account for the collapse of atmospheric data to a single harmonic at the poles. This results in systematic erroneous filtration occurring at around the 10 most poleward latitude lines. To avoid this problem, events chosen take place mainly equatorward of 70 °N.

Another edge effect that needs to be addressed is signal extension. While periodic signal extension is a sensible choice in the latitudinal direction, the stream function and velocity potential are not periodic across the poles. In order to account for the discrepancy in extension mode needs, the input data was mirrored across both poles. There is still some false periodicity near the poles introduced by this process that unfortunately cannot be avoided (this is shown in Chapter 8). Diagonal effects are the most pronounced here, and the combination of the two filter extensions produce the most systematic, erroneous transform errors. For each of the cases chosen, this is diminished by selecting model domains that do not entrain that erroneous data (Figure 4.2 for Case 1, Figure 4.3 for Case 2, and Figure 4.4 for Case 3). Each of these domains are chosen such that the troughs and vorticity signatures of interest are almost entirely contained in the inner domains for as much of the model time as possible, and that initial and boundary conditions do not include erroneous periodicity.

The Case 1 unfiltered stream function power spectrum for all input isobaric levels in log-base 10 units is shown in Figure 4.5, calculated via the square of the transform coefficients divided by their wavelet space transform scale (Liu et al. 2007). The axes of Figure 4.5 are the zonal and meridional wavenumbers, with the largest, planetary scale flow components at the upper left and the smallest, mesoscale flow components at the lower right; the largest wavenumber is 180 since the input data has a 1° resolution. As expected, the largest scales have more energy than smaller spatial scales. One can also note that there is a bias toward the zonally elongated constituents, which hold slightly more energy than their meridional counterparts. The unfiltered velocity potential (Figure 4.6) also shows much more energy at the large scales than the small scales, however there is no bias in orientation. Additionally, the power spectrum falls off more quickly in the velocity potential, with the smallest scales seeing about an order of magnitude less energy than in the stream function. The filtered stream function for Case 1 has energy reduced by several orders of magnitude at the subsynoptic scales (Figure 4.7). The filtered velocity potential shows a similar outcome (Figure 4.8) but with an even stronger reduction in subsynoptic node energy.

The reduction in stream function energy via filtering results in a reduction of total stream function variance of around 1-2%, and the reduction in the velocity potential energy results in a reduction of total velocity potential variance of around 2-6%. Reductions in variance are typically higher near the surface than at the upper levels. Cases 2 and 3’s filtered results (not shown) are virtually identical, with weak variation in variance reduction in time. The resulting wind fields achieve our goal: reducing the components of wind that weakly contribute to the total energy of the atmosphere while reducing the enstrophy more strongly.

Figures

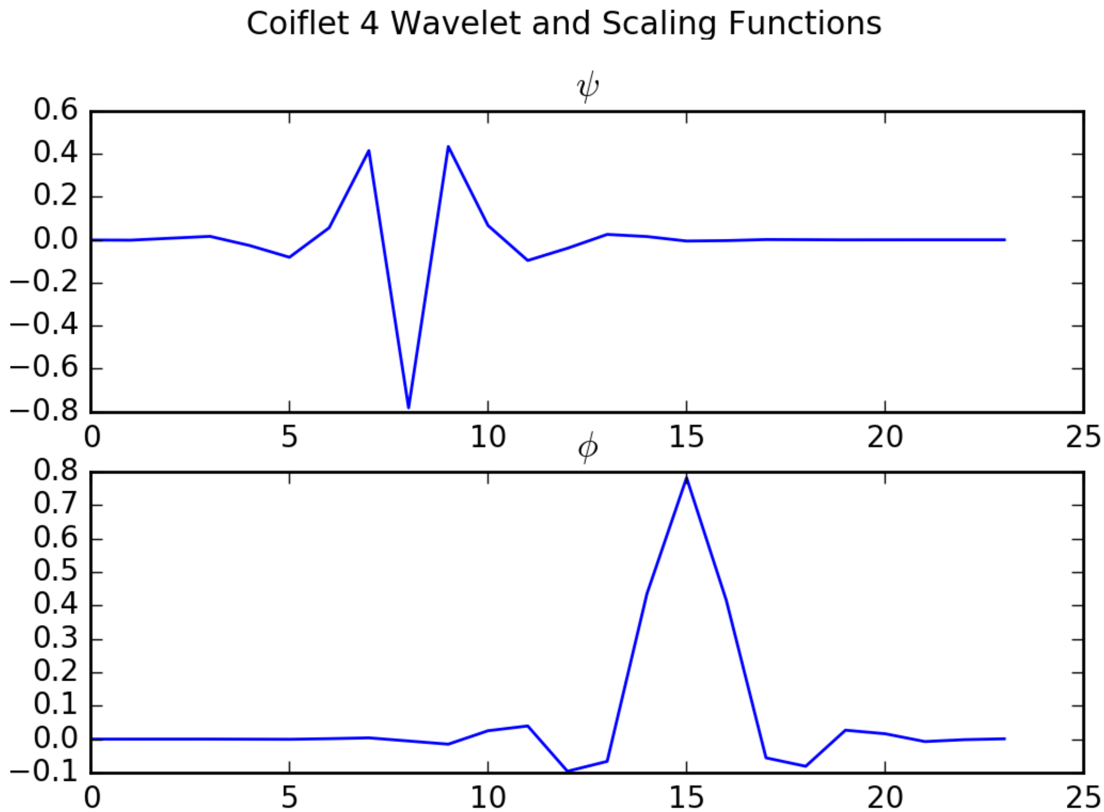

Figure 4.1: The Coiflet 4 Wavelet (top) and Scaling (bottom) Function.

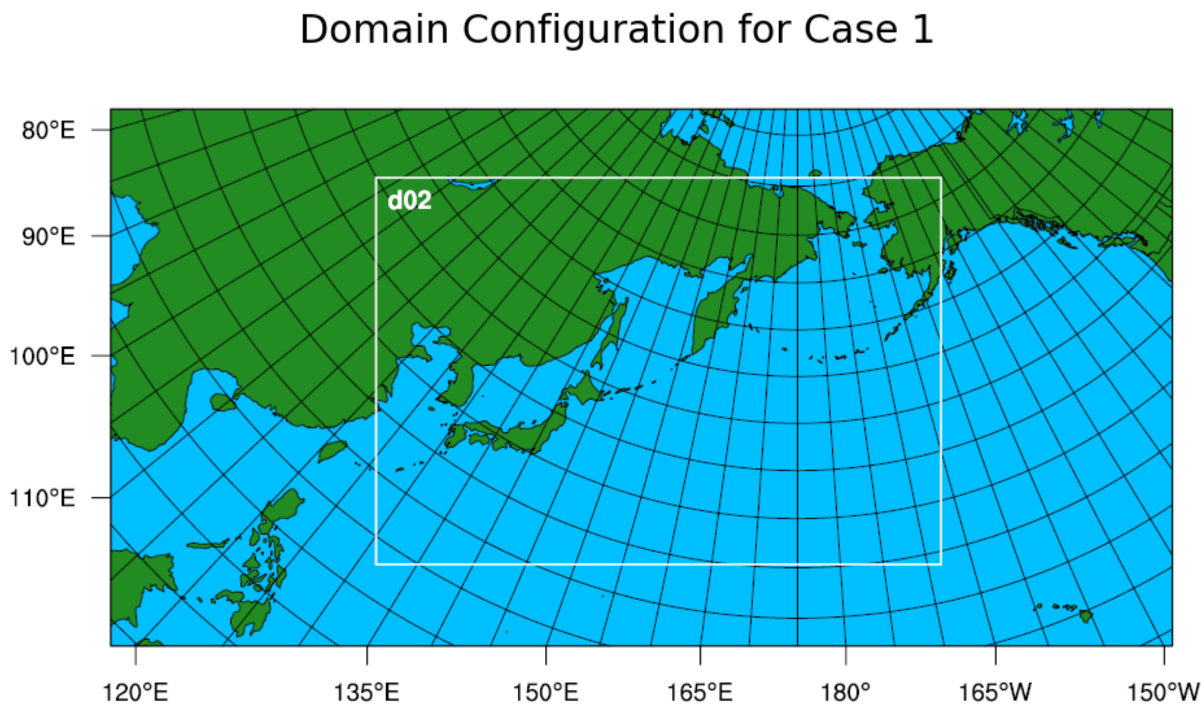

Figure 4.2: Domain Configuration for Case 1. The outer domain (d01) has a grid size of 190 by 110 grid points at a grid spacing of 60 km. The inner domain (d02) has a grid size of 301 by 229 grid points with a grid spacing of 20 km.

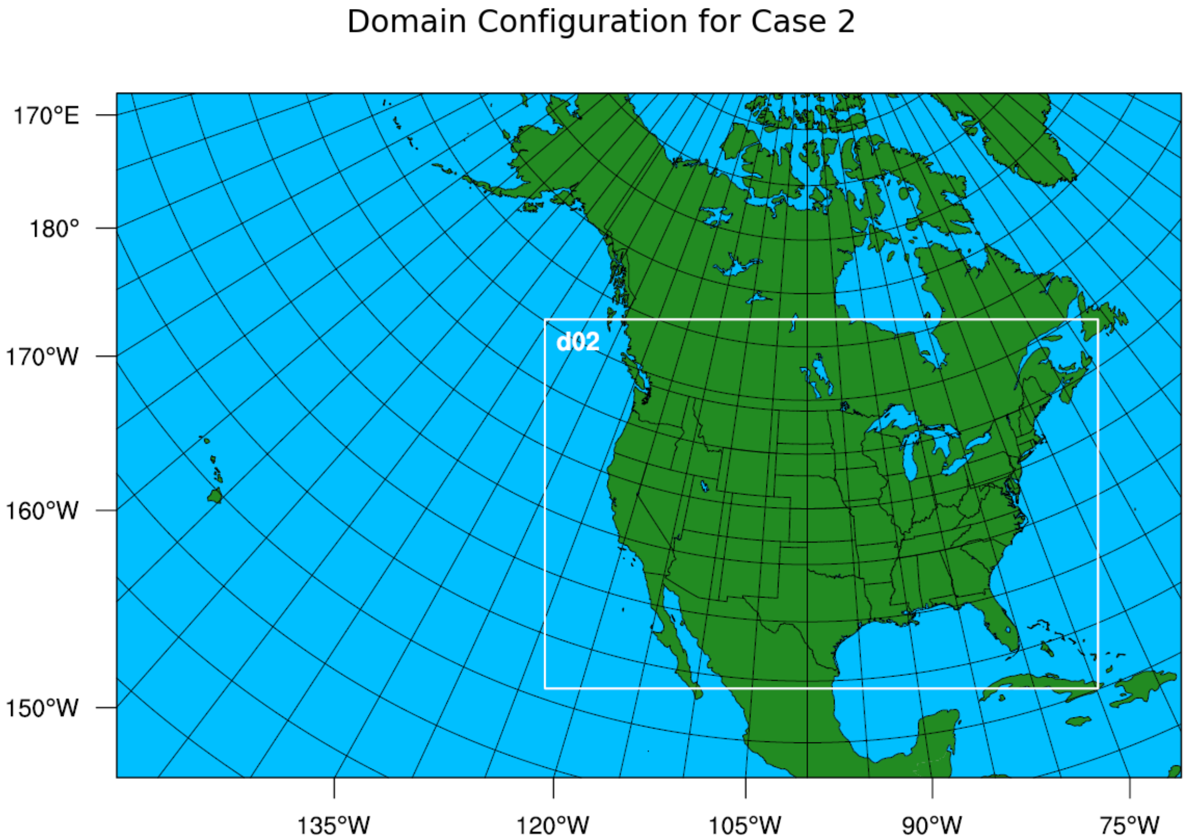

Figure 4.3: WRF model domains for the Case 2. The grid spacing is the same as that of Case 1. The outer domain has a 183x113 grid and the inner domain has a 274x184 grid.

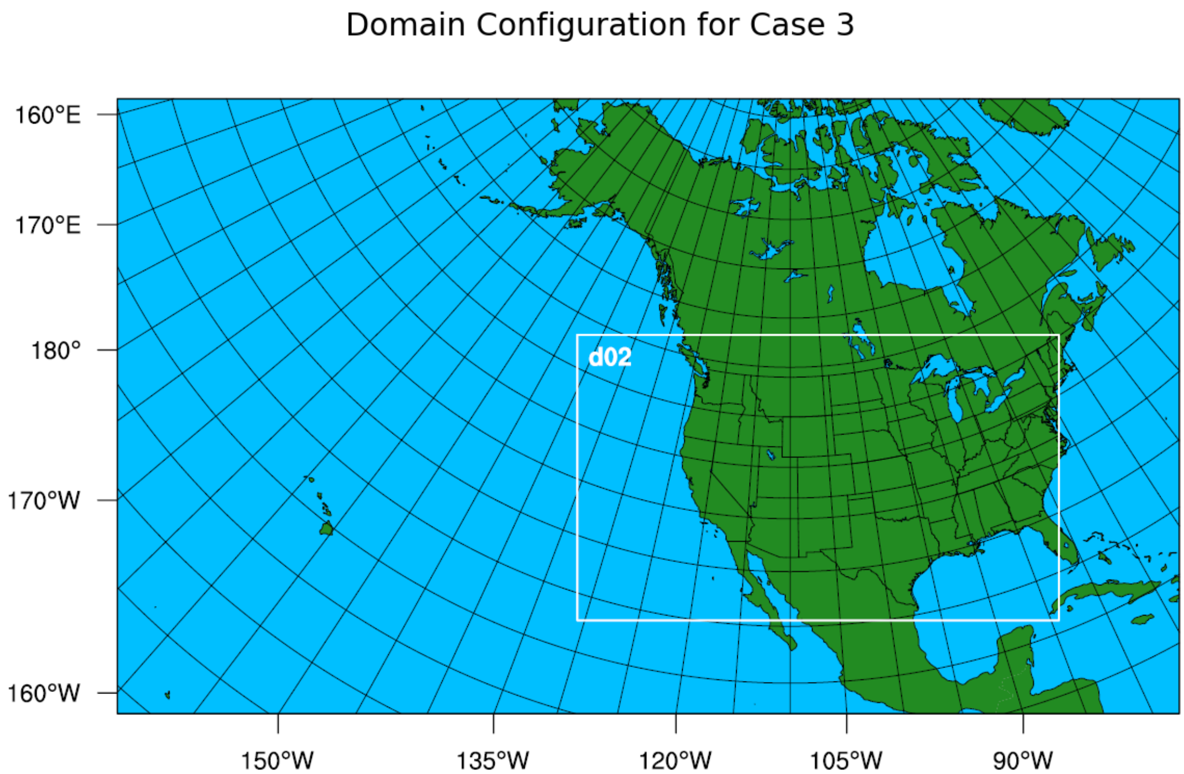

Figure 4.4: WRF model domains for Case 3. The grid spacing is the same as the other cases. The outer domain has a 195x113 grid and the inner domain has a 195x1113 grid.

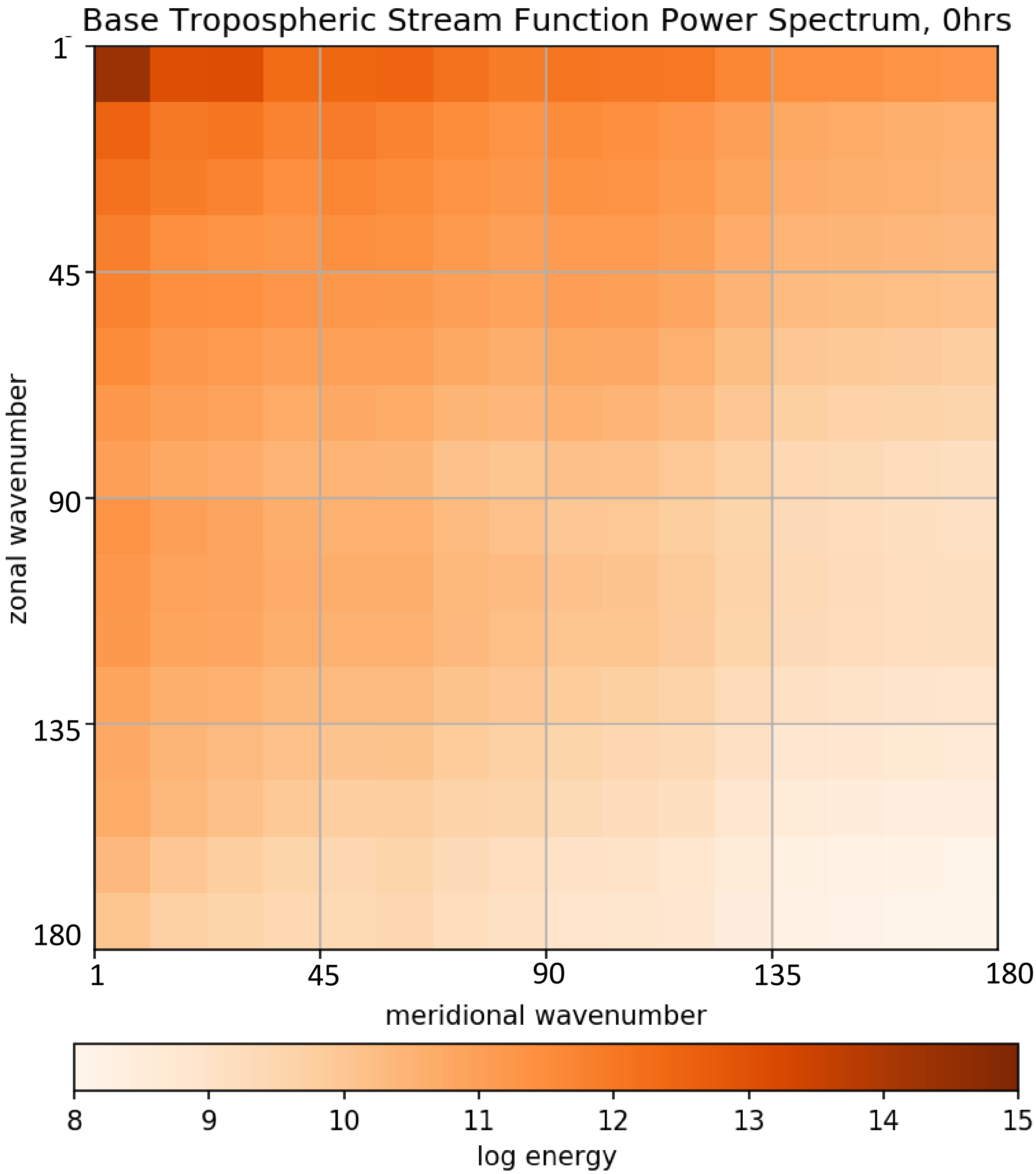

Figure 4.5: Case 1 Base Tropospheric Stream Function Power Spectrum at 0 Hours. Axes are wavenumber, and the colorbar represents the log base 10 energy of the nodes.

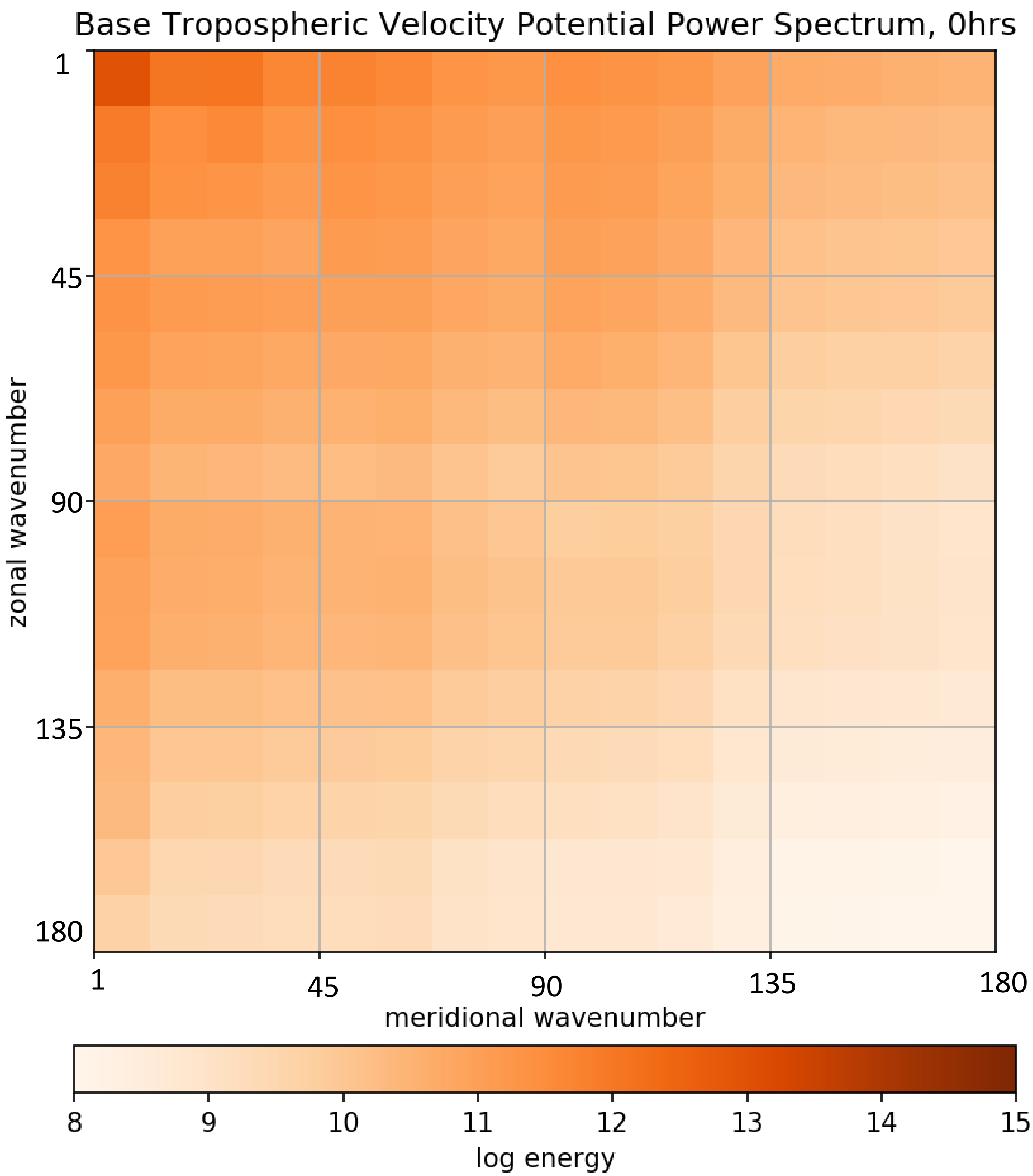

Figure 4.6: Case 1 Base Tropospheric Velocity Potential Power Spectrum at 0 Hours.

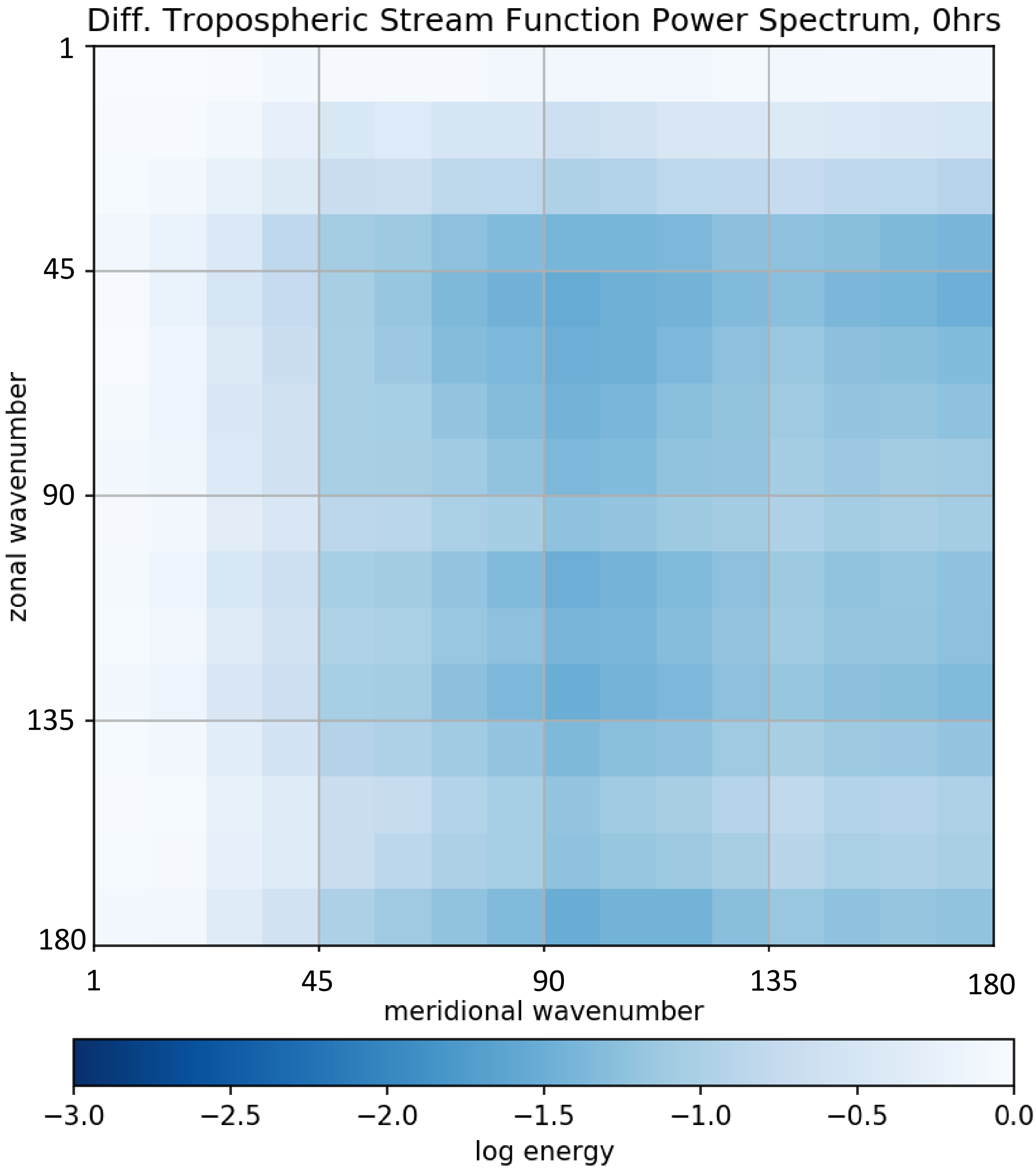

Figure 4.7: Case 1 Differential Tropospheric Stream Function Power Spectrum at Model Initialization.

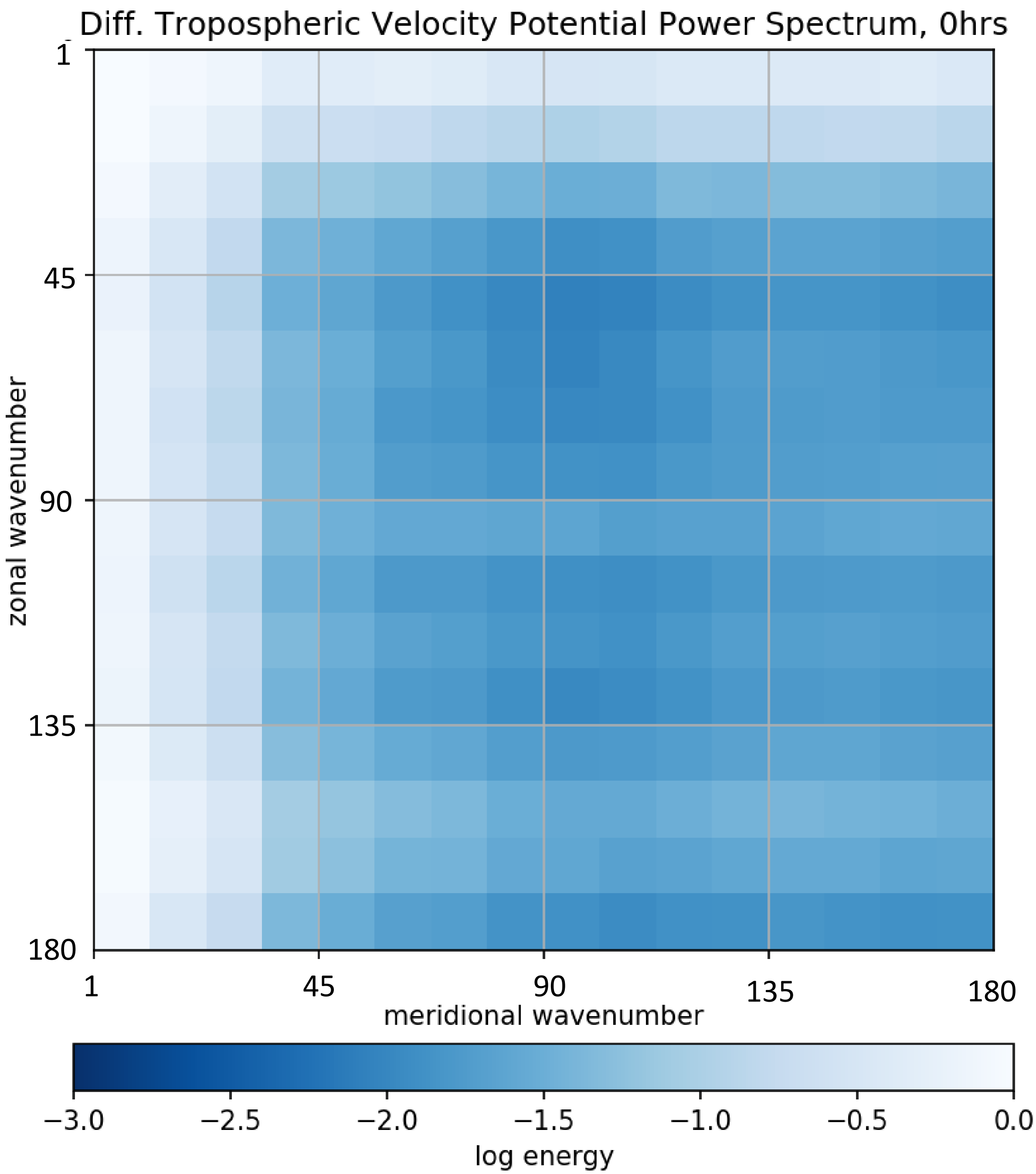

Figure 4.8: Case 1 Differential Tropospheric Velocity Potential Power Spectrum at Model Initialization.

CHAPTER V

CASE 1: JANUARY 2000

Case 1 features a baroclinic wave that deepens in the north central Pacific from late January into early February 2000. It is a representative example of a common type of upper-tropospheric feature during this time of year for the Pacific (Martius et al. 2007).

5.1 Day 1

Figure 5.1 shows the 300 hPa instantaneous geopotential height perturbation and potential vorticity (PV) fields during the first 18 hours of the inner domain simulation, which initializes 6 hours after the outer domain's initialization; geopotential height perturbation is defined as the departure from the mean along the *x*-axis Already present in the north Pacific is a broad, shallow trough extending south to around 30° N. At 6 hours, the tropopause PV gradient (PVU 1-3) is wavelike. Figure 5.2 shows the mean sea level pressure (MSLP) and 1000-500 hPa thickness for the same times as Figure 5.1. There are pressure minima near and downshear of the upper-level height minima at the 300 hPa level. From this, mutual amplification of the upper-level trough and surface lows in the central Pacific would be expected, and indeed this can be observed in both fields. Over time, the negative geopotential height anomalies become less anticyclonically tilted, broader, and larger in magnitude.

The PV in the coarse simulation (Figure 5.3) is higher at the southern edge of the wave and northern edge of the ridge at initialization and lower in the wave interior (Figure 5.4). As expected, higher (lower) PV is correlated spatially with lower (higher) geopotential height anomalies from the coast of Hokkaido to the southern Bering Sea. The coarse MSLP is broadly higher over the central Pacific and lower over Siberia and the east Pacific (Figure 5.5, difference field Figure 5.6). Figure 5.2 and 5.5 indicate that there is little difference in the large-scale thermal structure of the troposphere during the first day. Figure 5.4 shows that, at initialization, the PV field aloft differs between the two simulations, but by 18 hours the two are more similar, and differences appear to be caused by advection of initialization differences and not from amplification. The relative humidities at 700 hPa of the two simulations are shown in Figures 5.7 and 5.8. Both simulations show RH values of 90% or greater in the vicinity of the developing surface low after 18 hours, suggesting that both simulations' large-scale conditions permit precipitation. All of the above suggests that differences in MSLP during the early simulation may be tied less to the large-scale flow and more to perturbations and small-scale variability.

Figure 5.6 suggests there is also a small difference in the surface pressure near Hokkaido at 24 hours, though this is not associated with any particular PV anomaly or height minimum aloft. Because the RH indicates favorable conditions for precipitation in both simulations, differences between the simulations' moist dynamics may be the cause of the differential development. Examining the differential 6-hour precipitation between the two simulations at 12 hours (Figure 5.9), it is clear there is precipitation occurring southwest of Hokkaido that is stronger in the base simulation. From this arises a question: do differences in small-scale variability between the two simulations beget differences in precipitation or *vice versa*? Filtering the input data removes small-scale variability, so a reduction in precipitation in the coarse simulation could be an indicator that precipitation at this time is driven by small structures. To identify the differences in small scale variance between the simulations, we look to the enstrophy. High values of column-integrated enstrophy suggest that stronger perturbations or higher small-scale variability are present at a given location. Additionally, using an envelope function such as a Gaussian filter can tell us the neighborhood in which higher small-scale variability is present and the overall magnitude of that variability. Figure 5.10 shows the column-integrated enstrophy for both simulations at 18 hours. Some small-scale variance exists southwest of Hokkaido, co-located with the high relative humidity seen in Figure 5.7. The coarse simulation enstrophy shows similar behavior, but the two simulations' maxima are displaced (Figure 5.11). Six hours later (Figures 5.12 and 5.13), in addition to having higher enstrophy maxima over Hokkaido, the coarse simulation has a broad region of higher precipitation accumulation farther north (Figure 5.14), co-located with the region of the maximum MSLP difference; this becomes more prominent at 30 hours (Figure 5.15 and 5.16). This would suggest that differential development of small-scale variability causes heavier precipitation in the microphysics scheme of the model and not the other way around, and the injection of latent heat provides a differential surface pressure change through small-scale latent heat release.

5.2: Interpretation using wavelet energy and cluster analysis

We now look to the spectral components of the simulations to investigate more quantitatively how the simulations differ statistically. We can define a nodewise kinetic energy partition by starting with the wavelet node energy, P_n' (Liu et al. 2007):

$$P_n' = \sum_{p=p_0}^{P} 2^{-j} \left\| U_{p,n}' \right\|^2$$

where $U_{p,n}'$ is the perturbation from the zonal mean of the total wind on a given pressure level p in node n and j is the transform level. The nodewise energy is normalized using the ensemble mean—with the first day excluded— and divided by the standard deviation to create the ensemble energy partition:

$$P_n^* = \frac{P_n' - \overline{P_n'}}{\sigma_{\overline{P_n'}}}$$

Here, the ensemble is the combination of base and coarse simulations for a given case. This internal nodewise energy partition for the simulation wind does not include interactions between nodes. We are limiting ourselves to using the largest spatial scales only because spatial scales contained in nodes smaller than these would not cascade energy up into the synoptic scales. Upscale effects at the synoptic scales would be driven primarily by injection of energy from subsynoptic and largest mesoscales. The two-dimensional wavelet packet transform at the fourth transform level for our domain size and grid spacing provides convenient breakpoints between synoptic and subsynoptic spatial scales. Only the 16 largest nodes are used in the energy partition visualization, so the minimum resolvable wavelength is roughly 200 km meridionally and zonally. The fourth level approximation node (the *AAAA* node; see Figure 3.2) is a domain-wide synoptic-planetary node, meaning the bin of spatial components has a maximum extent of the entire model domain and has a minimum extent near the synoptic injection scales. Nodes filtered using only low-pass filters in the x-direction have zonal extents long enough to be considered synoptic but have subsynoptic meridional extents. The opposite is true for purely vertical nodes which have been filtered with low-pass filters in the y-direction. Purely diagonal nodes lack elongation so only the largest diagonal node is synoptic scale while the rest are subsynoptic. The remaining nodes are some combination of low and high pass filters in zonal and meridional directions, so they all have various degrees of anisotropy in the subsynoptic ranges.

Figures 5.17 and 5.18 are time series of the normalized nodewise energy partitions P_n^*. Line thickness represents spatial scale, with thicker lines representing greater wavelengths; line color represents anisotropy, with red (blue) lines representing zonal (meridional) elongation; and line saturation represents the degree of anisotropy, with higher (lower) saturation representing greater (weaker) elongation. Black lines represent isotropic nodes, and the thickest black line is the fourth level approximation node. Before discussing specific times, we can quickly note a few general trends in the simulations. First is that both simulations begin with substantially below average perturbation wind energy at initialization in almost all nodes, and total energy steadily increases for the first 12-24 hours with small-scale energy increasing most rapidly within the first 4-6 hours. This is due to the inner domain initializing from the forecast time of the outer domain: there is a 3:1 grid ratio between the inner and outer domain, and thus the resolvable features at 6 hours are limited by the grid resolution of the outer domain. Both simulations also exhibit an upward trend in the meridionally elongated nodes at the expense of the zonally elongated nodes; this trend is smaller in the coarse simulation. Finally, both simulations share very similar domain-wide synoptic energy partition behavior, which is expected given the maps shown earlier.

The coarse simulation has significantly less energy in its perturbation energy partition at initialization than the base simulation across all nodes except for the largest approximation node. As mentioned, both simulations have very low small-scale perturbation wind energy at initialization, which increases quickly after 6-10 hours; Figures 5.19-5.22 show the development of that energy in the nodewise energy spectra for each simulation. The mechanism is intuitive: there is conversion of background energy to eddy energy through synoptic injection via baroclinic growth at the largest spatial scales, and a direct injection of energy through radiative and cloud parameterizations in the simulations at the smallest resolvable spatial scales. That the mid-range nodes receive energy last is most evident in Figure 5.22, where the coarse simulation, having less initial energy due to the filter process, lags behind the base simulation in the mid-range spatial bands.

In the first 12 hours it is noticeable how much more perturbation wind energy the base simulation has than the coarse simulation. Figure 5.23 shows 850 hPa and 300 hPa winds reconstructed from the largest zonally elongated nodes as well as the largest subsynoptic isotropic nodes at 16 hours simulation time in the base simulation. Perturbation winds are stronger at the lower level than at the upper level in the northern part of the trough in the center of Figure 5.1c, though at the southern edge of the wave the perturbations are comparable. Though zonally aligned perturbations appear throughout the domain at this time, they are strongest in the mid-latitudes and near the subtropics. Figure 5.24, depicting the same spatial scale of perturbations but replacing the zonally elongated nodes with meridionally elongated nodes, shows the differences in typical locations for different elongated flow components: meridionally elongated flow tends to be closer to the polar regions of the mid-latitudes, with almost none farther south. As the wave is only weakly meridional, there is very little meridional elongation in the wave as a whole, and there is significantly more meridional elongation in the perturbation winds in the lower level than upper level. Figures 5.25 and 5.26 show the zonally and meridionally elongated components, respectively, of the coarse simulation at the same time as Figure 5.23 and 5.24. The coarse simulation exhibits the same behavior as the base simulation: weak meridionality in the southern mid-latitudes and stronger elongation in the lower levels. The magnitude of the perturbations is less in the coarse simulation for both types of elongation as well as the isotropic perturbations in the southern end of the wave, and there are some locational differences between the two sets of components, but these fit firmly within the broad observations made earlier in this section. The two simulations differ statistically in that the coarse simulation perturbations have much lower variance than the base simulation, both in terms of their hour-to-hour change but also their across-node spread (not shown).

The energy partition time series (Figs. 5.17 and 5.18) can be difficult to parse and we would like a simpler view into how the nodes vary collectively. We can use clustering to do this using P_n^*; for our purposes, we will make use of a k-means clustering algorithm. Each simulation forecast time's similarity with a given cluster is measured by determining the root-mean-square difference between the normalized cluster energy and forecast time energy across all sixteen nodes. This can be represented as:

$$D_k = \left(\sum_{n=1}^{N}\left(P_n^* - C_{k,n}\right)^2\right)^{\frac{1}{2}}$$

where $C_{k,n}$ is the normalized energy for a given cluster k and node n. The k-means clustering algorithm seeks to identify K clusters (the number of clusters K is specified by the user) such that, averaged over all times, the L^2 distance from the energy state to the nearest cluster is minimized. The cluster with the smallest associated D_k for a given forecast time describes that forecast time most accurately. Differences between the simulations' associated clusters indicates that the two simulations have different spectral configurations.

Figure 5.27 depicts the clusters for the "ensemble." We have chosen to use 6 clusters due to a combination of explanatory power and robustness— using fewer clusters makes transitions between clusters harder to interpret and using more clusters causes them to not be robust to different first guesses for cluster patterns. Only clusters one and four describe states whose synoptic scale energy partition tends to be greater than the temporal mean. Cluster one represents a simulation state where there is a large amount of energy across most of the largest and intermediate spatial scales and only the smallest zonally elongated spatial scales lack energy, while cluster four represents a simulation state where energy is concentrated in the zonally elongated and weakly isotropic nodes with less energy in the meridionally elongated nodes. Of those remaining, clusters two and five describe simulation states with energy below the temporal mean for the majority of their nodes. Cluster six is like clusters one and four in that it is an excited state with many nodes above their temporal means but lacks in the large-scale synoptic energy of the other two. Lastly, cluster three is a weak perturbation cluster, where no centroids have magnitudes much greater than the ensemble mean.

Now, with the clusters described, we can discuss the simulation D_k. Figure 5.28 depicts D_k for the base simulation, including a line for the “null cluster,” an artificial cluster representing D_k for the mean state (e.g., P_n^* is zero). At initialization, there is a very large spike in D_k for all clusters, a result of the steps we took calculating the energy partition. Since the first 24 time steps do not contribute to the ensemble mean, and there are no other times where the perturbation energy partition is as negative as it as at initialization, no cluster comes particularly close to representing its variance state. As mid-range flow components populate—a process that completes approximately 12 hours or so after the inner domain’s initialization—there is a steady reduction in D_k for all nodes. Afterward, there is an increase in D_k that is associated with the large reduction in nodewise partition energy as seen in Figure 5.17. This occurs because there is a large amount of both zonal and meridionally elongated flow components near the northeastern edge of the simulation domain which migrate out of the domain and cease to contribute energy to those nodes. The coarse simulation (Figure 5.29) shows similar behavior, with a smaller bump in D_k due to the coarse simulation having less total node energy within the first day, and the migration of perturbation energy out of the domain affects the coarse D_k to a lesser degree.

5.3 Day 2

Figures 5.28 and 5.29 show that both simulations transition from the mean variance state to cluster state four around 30-36 hours (the coarse simulation transitions later), suggesting the troposphere as a whole is broadly defined by large-scale synoptic and zonally-elongated flow. By the time day 2 begins, the upper-level trough ceases deepening (base: Figure 5.30, coarse: Figure 5.32, and difference field Figure 5.33). The southernmost minimum maintains its intensity for most of the day, but becomes decoupled from the surface low by the end (base: Figure 5.31, coarse: Figure 5.34). In the base simulation at hour 48, the height minimum over the Bering Strait has descended southward and the height minimum over the central Pacific that developed 24 hours previously has filled in. In the coarse simulation, the southernmost upper-level trough remains intense longer, and the northernmost height minimum, while extending equatorward during the second day, does not weaken on its north edge. It ends the day much more elongated than in the base simulation. In Figures 5.17 and 5.18, at both the synoptic and subsynoptic scales, the meridionally elongated nodes' energy is increasing, meaning there would be a net increase in tropospheric north-south winds throughout both simulations. Both simulations during day 2 have a large portion of their total perturbation energy in the domain-wide isotropic node,. It follows from both of these observations that differences between the two simulations would not be in the upper levels but rather in the middle and lower troposphere where smaller scale constituents of flow have higher amplitudes.

The base MSLP and 1000-500 km thickness during day 2 (Figure 5.31) shows three cyclones over the North Pacific. The southernmost has moved away from its associated 300 hPa low after 36 hours as the latter stagnated, and the two do not interact further. The northernmost has been migrating equatorward for the entirety of the simulation, and retained favorable baroclinic tilt with its associated upper-level height minimum and maintains itself. This brings us to the westernmost low. At that time, the upper-level wave is still largely meridionally confined, showing a local minimum in geopotential height aligned with a zonal streak of PV. The total precipitation of the simulations (Figure 5.35 and 5.36) shows, in the middle of day 2, there is precipitation occurring on the eastern and northern sides of the low minimum; the former is rain and the latter is snow. Precipitation is less concentrated in the coarse simulation than the base simulation, and by proxy there would be less concentrated latent heat release from condensation in the coarse simulation. The background conditions in both simulations are favorable for precipitation for the majority of the area surrounding the low in both simulations (very high RH, not shown), so, like during day 1, there must be some perturbation-based cause for the differences in the convective outcomes.

Figure 5.37 is a plot of the domain-scale 350 hPa divergence and 850 mb geopotential height anomalies for the base simulation at 36 hours. There is a region of upper-level divergence southeast of the 850 hPa low near Japan aiding in the reduction of surface pressure and producing favorable conditions for upward motion; the region of divergence is in the same location that the MSLP low develops during the next 6 hours. Figure 5.38 shows the same fields as 5.37, but the upper-level divergence is constructed using the zonally elongated nodes only. The divergence and convergence regions are much smaller, as would be expected, but there is some overlap between the large isotropic and zonally elongated nodes' divergences in the downstream region of the lower level low. To the northeast of the low, isotropic upper-level divergence is approximately offset by small-scale upper-level convergence. Conversely, to the southeast upper-level isotropic divergence is enhanced by upper-level zonally elongated divergence. This produces a net divergence to the south, causing the low to migrate southeast quickly. Figures 5.39 and 5.40 show the coarse large-scale isotropic and zonally elongated spectral divergences, respectively, along with the 850 hPa height perturbation. The coarse synoptic scale perturbations' contribution to the 350 hPa divergence is similar in location and intensity to the base, but there is a smaller contribution from the zonally elongated features. The lack of mutual amplification ahead of the low could explain the heaver precipitation in the base simulation during this time. It also provides a mechanism, though indirect, that the subsynoptic flow can project onto the synoptic scales.

By the end of the day, the coarse simulation's meridionally elongated perturbation energy partition has grown larger than the large-scale synoptic components, and the cluster variance state of the coarse simulation transitions from cluster state five to cluster state two. Figure 5.29 shows that the D_k for cluster state one is steadily declining throughout the day, matching the general increase in meridionally elongated nodes. This is in contrast to the base simulation which does not undergo a transition in associated clusters. The base simulation maintains a consistent level of zonally elongated flow components while seeing a reduction in meridionally elongated components by the end of day 2.

5.4 Day 3

Between days 2 and 3, the largest perturbation node's contribution to the perturbation energy declines after 48 hours. This decline persists throughout day 3, and both simulations have similar variance in the large-scale isotropic flow by the end of day 3. This decline is concurrent with the expansion of the PV hole at 300 hPa (base: Figure 5.41, coarse: Figure 5.42, and difference field Figure 5.43) which splits the upper-level wave. Midway through day 3, both simulations undergo transitions in their associated clusters: the base simulation transitions from cluster four to cluster three, and the coarse simulation transitions from cluster one to cluster six. Both new variance states are characterized by large-scale synoptic perturbation energy below ensemble temporal mean and meridionally elongated flow components being generally above the ensemble temporal mean. At a glance, one would expect that the two simulations would vary primarily in the zonally elongated nodes—cluster state six is associated with greater small-scale zonal energy than cluster state three, and thus the coarse simulation should have greater zonality. This, however, is not the case. Figures 5.44 and 5.45 show the base and coarse simulation zonally elongated nodes, respectively, at 66 hours when each variance state's D_k is minimized. The base simulation actually appears to have more energy at these levels, and a quick glance at the spectral time series suggests that this is entirely plausible. This helps to remind us that the describing clusters are not exact matches for the simulation data but approximates of the nodal distributions.

Knowing that the zonally elongated features are not the reason for the differing cluster identifications, we turn to the meridional nodes, plotted in Figures 5.46 and 5.47. Here it is clear that the coarse simulation has more meridionally aligned perturbation energy than the base simulation. Also, the coarse simulation, having had persistent above-ensemble-mean meridional elongation, produced a northern wavetrain of 300 hPa PV with eastward propagation of almost 10° that is largely separated from the wave to its south. Congruence between zonally and meridionally elongated flow constituents is likely an indicator of wave amplification. Between 54 and 66 hours rapid amplification of the 300 hPa wave begins. This is concurrent with overlapping zonal and meridional elongation in the storm track, which has not occurred prior to this time. Transition from an assigned cluster with a large, domain-wide feature and strong zonality to a cluster with small-scale zonal elongation and the intensification of meridional flow components occurs as a result.

The rapid transition from the excited cluster three to the low energy partition cluster two in both simulations at hour 70 (Figure 5.28 and 5.29) arises due to the rapidity of the transformation of the PV trough shape and the transfer of energy downscale. Both simulations are exhibiting nonlinear behavior as the 300 hPa wave amplitude grows to be very large and the PV begins to deform into thin filaments. Transition from large-scale energy to subsynoptic scale energy is quick and lasts briefly before the energy is then cascaded downscale further.

5.5 Day 4

The vorticity and PV fields continue to filament and stretch through the end of the simulation (Figure 5.48). The latitudinal span of the trough does not change, but the downstream ridge in both simulations extends farther northward until the end of the simulation; the coarse simulation sees a lesser northward extent of the ridge (Figure 5.50) than the base simulation, which is concurrent with a slower migration of the surface low (Figures 5.49, 5.51).

During this day, both models experience a transition from cluster one to cluster four (see Figure 5.28 and 5.29). The filamentation of the vorticity in both the zonal and meridional directions by the flow during day 4 are the kind of self-organization of PV gradients often seen in the atmosphere. During day 3 and 4, there is a high amount of deformation of the PV along the southern edge of the upper-level trough, and without any destruction occurring this allows the very thin zonal and meridional flow components to accumulate PV, resulting in a surge in that scale’s perturbation energy; the transition to a state described by cluster five results.

Finally, there is one final transition very late in the simulation time to cluster six in the base simulation. This is due to the fact that the coarse simulation has had persistently strong meridionally elongated flow components in the northern Pacific that has propagated energy southeast along the northern edge of the ridge. The base simulation does not exhibit this behavior, and much of the north Pacific low's energy remains in the model domain. Figure 5.48 shows the amplification of the wave height continues during this time. It is probable that the 300 hPa wave in the base simulation would go on to break if the simulation extended beyond 90 hours.

Figures

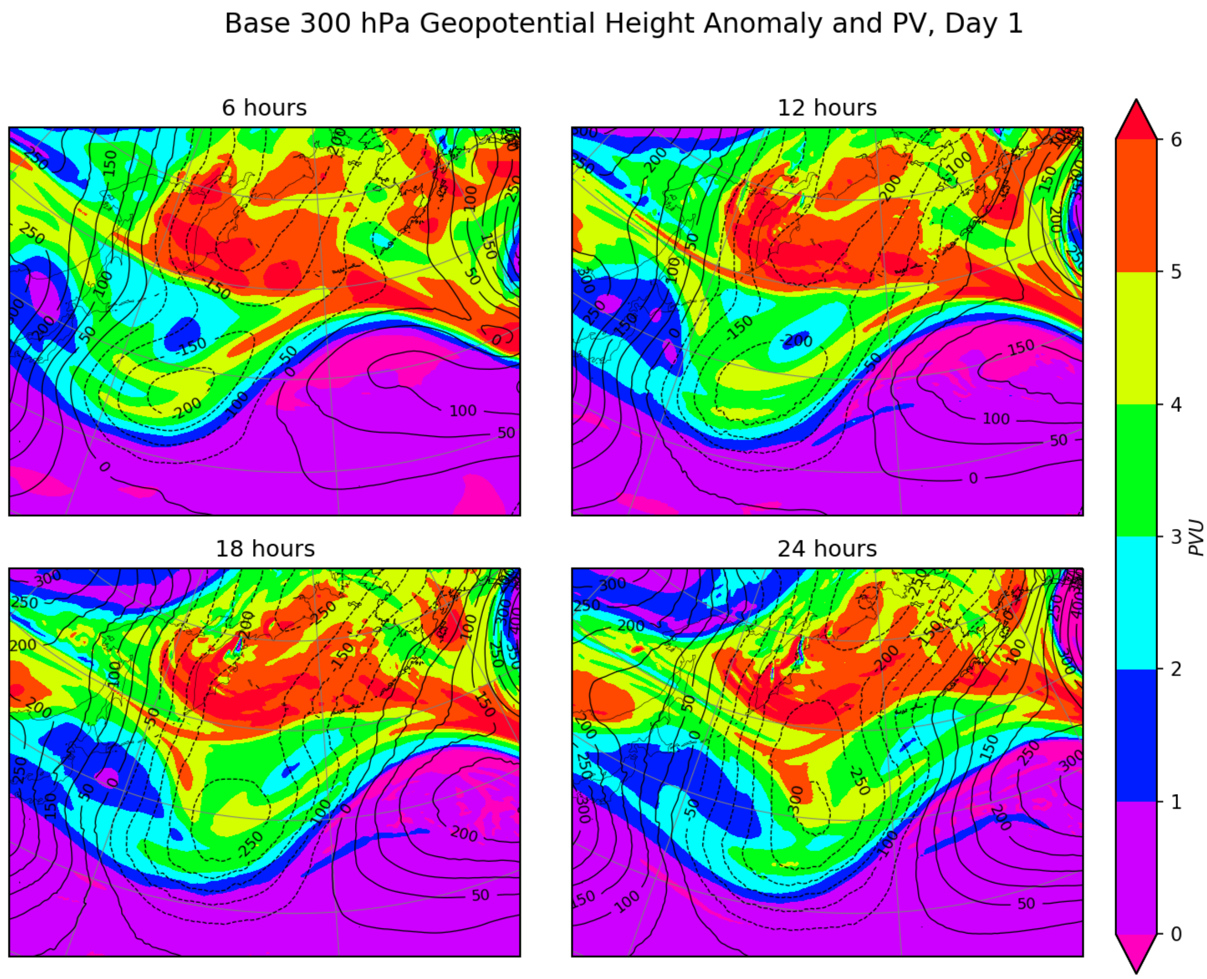

Figure 5.1: Case 1 Base 300 hPa Geopotential Height Anomaly (contours, dashed negative) and PV (filled contours), Day 1. Contour intervals are 50 gpm for height anomaly and 1 PVU for PV. From here on, unless otherwise noted, figures are of the simulation inner domains.

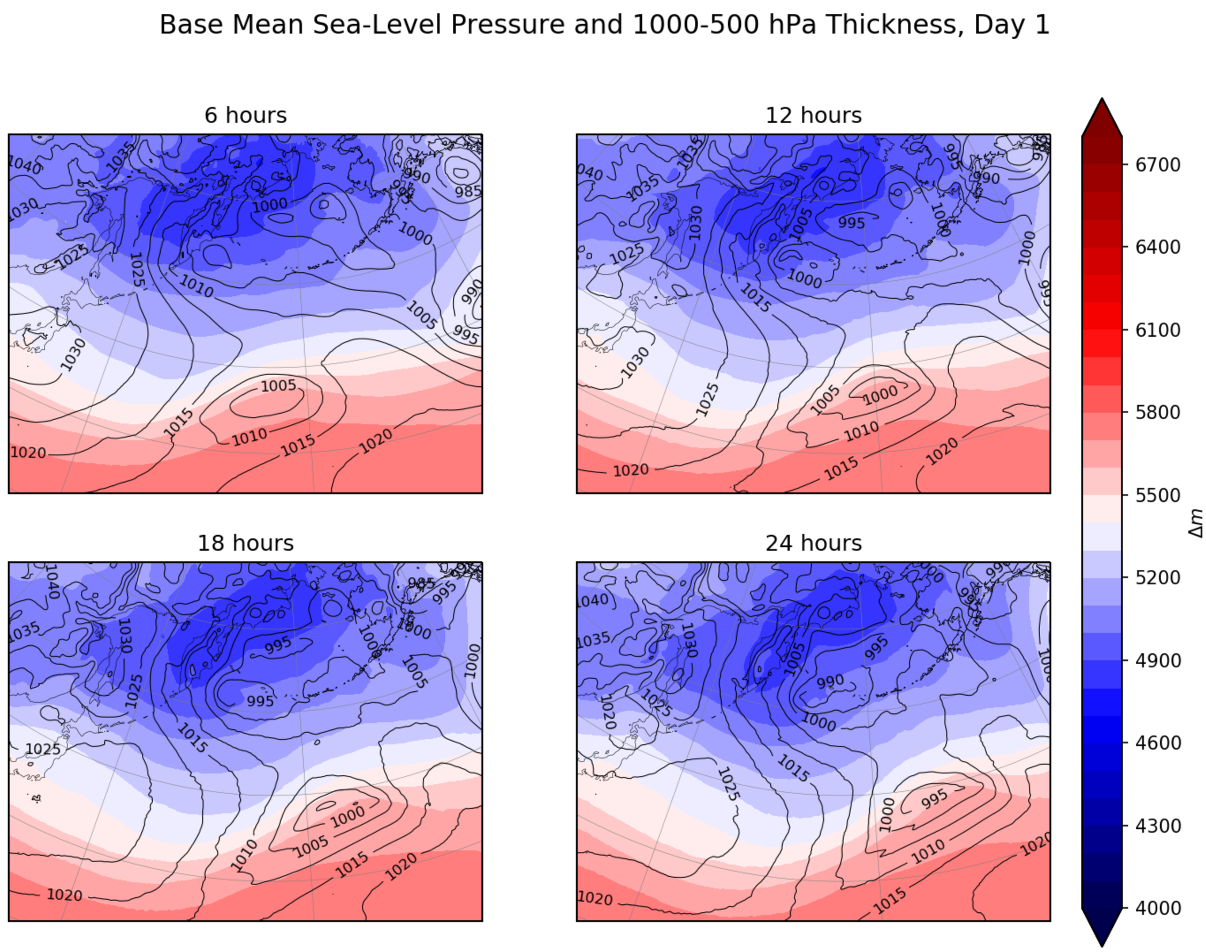

Figure 5.2: Case 1 Base Mean Sea-Level Pressure and 1000-500 hPa Thickness, Day 1. Contour intervals are 5 hPa for pressure and 100 m for thickness.

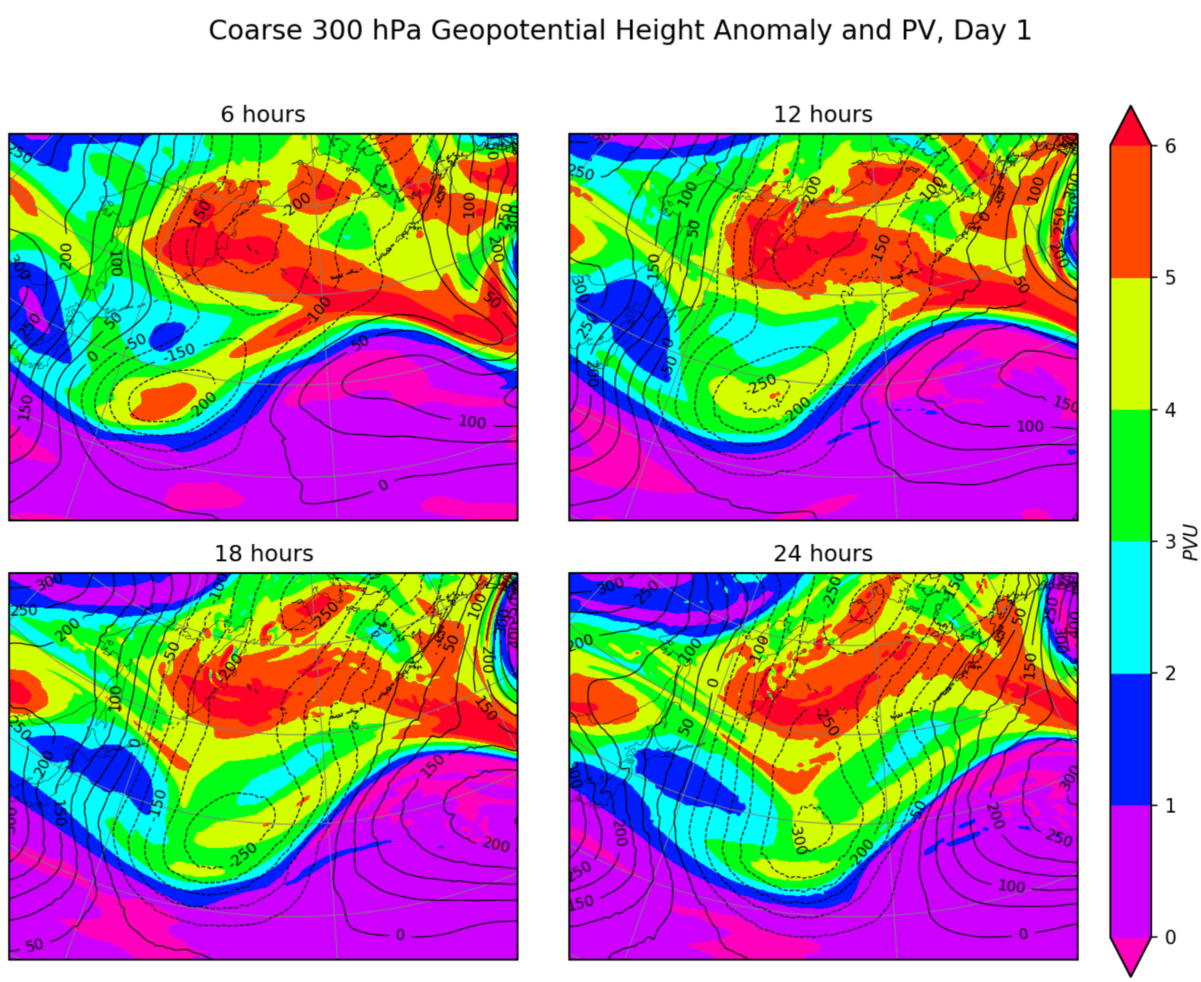

Figure 5.3: Case 1 Coarse 300 hPa Geopotential Height Anomaly and PV, Day 1. Contour intervals are 50 gpm for height anomaly and 1 PVU for PV.

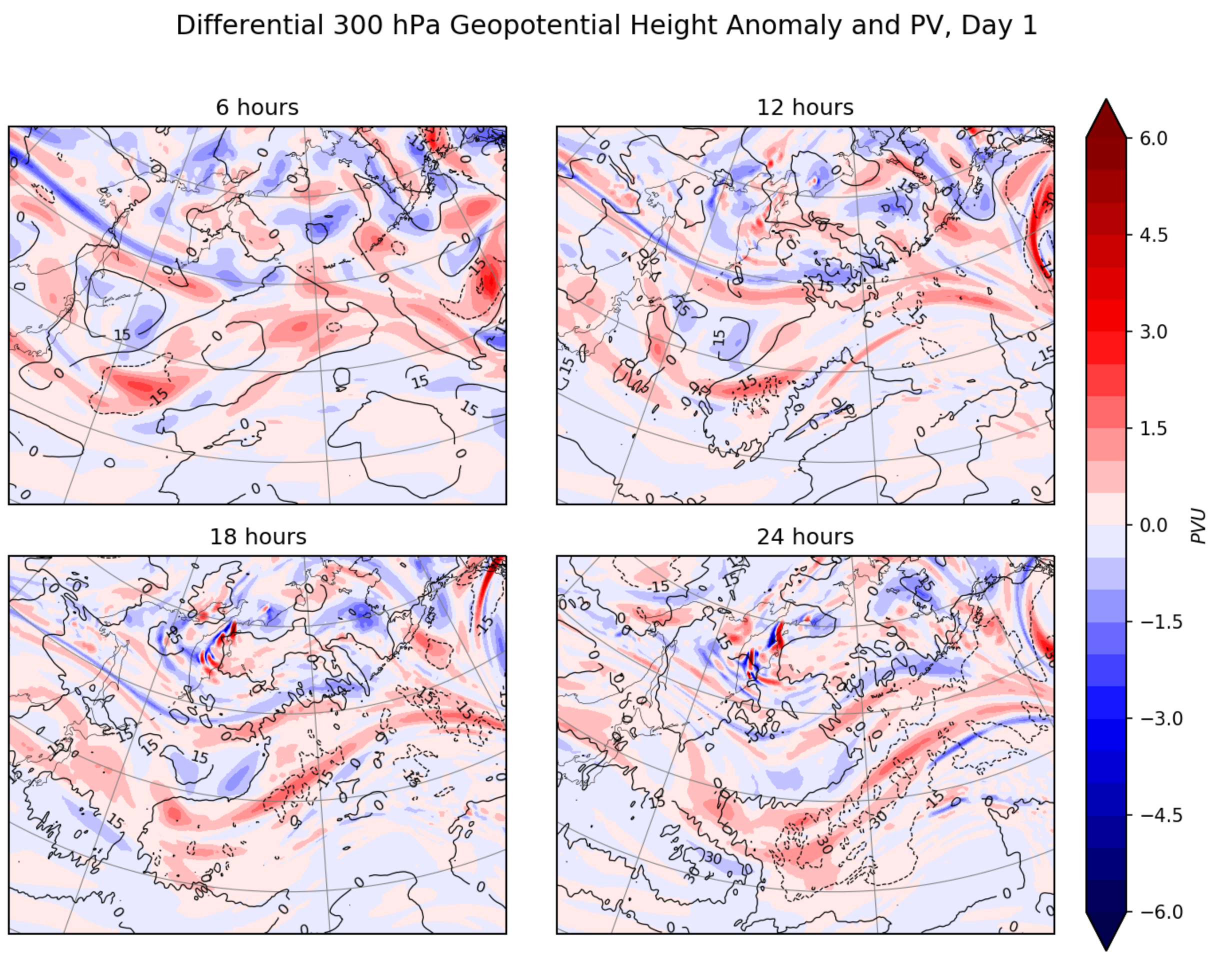

Figure 5.4: Case 1 Differential 300 hPa Geopotential Height Anomaly and PV, Day 1. Contour intervals are 15 gpm for differential height and 0.5 PVU for differential PV. Here and elsewhere, a positive difference indicates higher values in the coarse simulation.

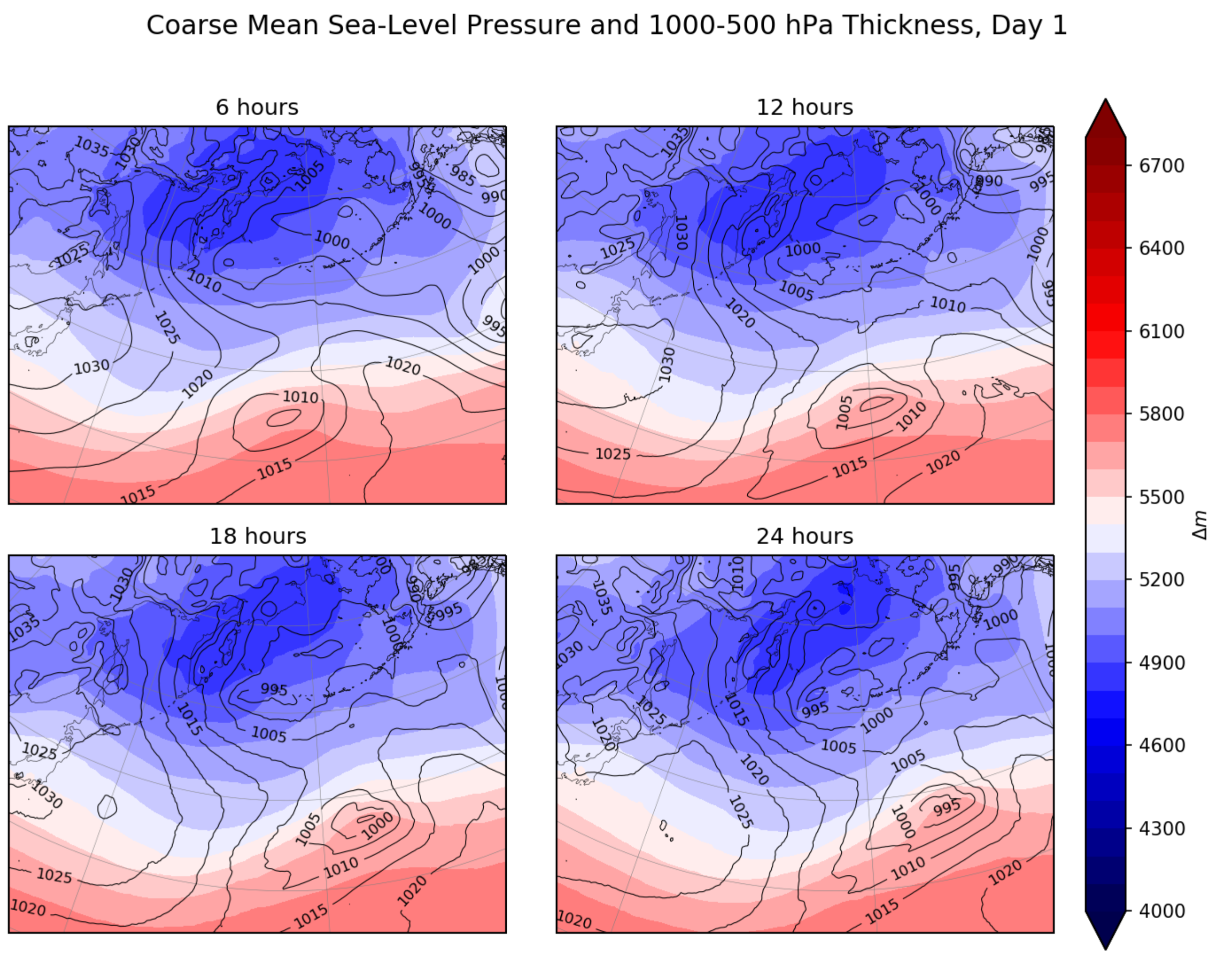

Figure 5.5: Case 1 Coarse Mean Sea-Level Pressure and 1000-500 hPa Thickness, Day 1. Contour intervals are 5 hPa for pressure and 100m for thickness.

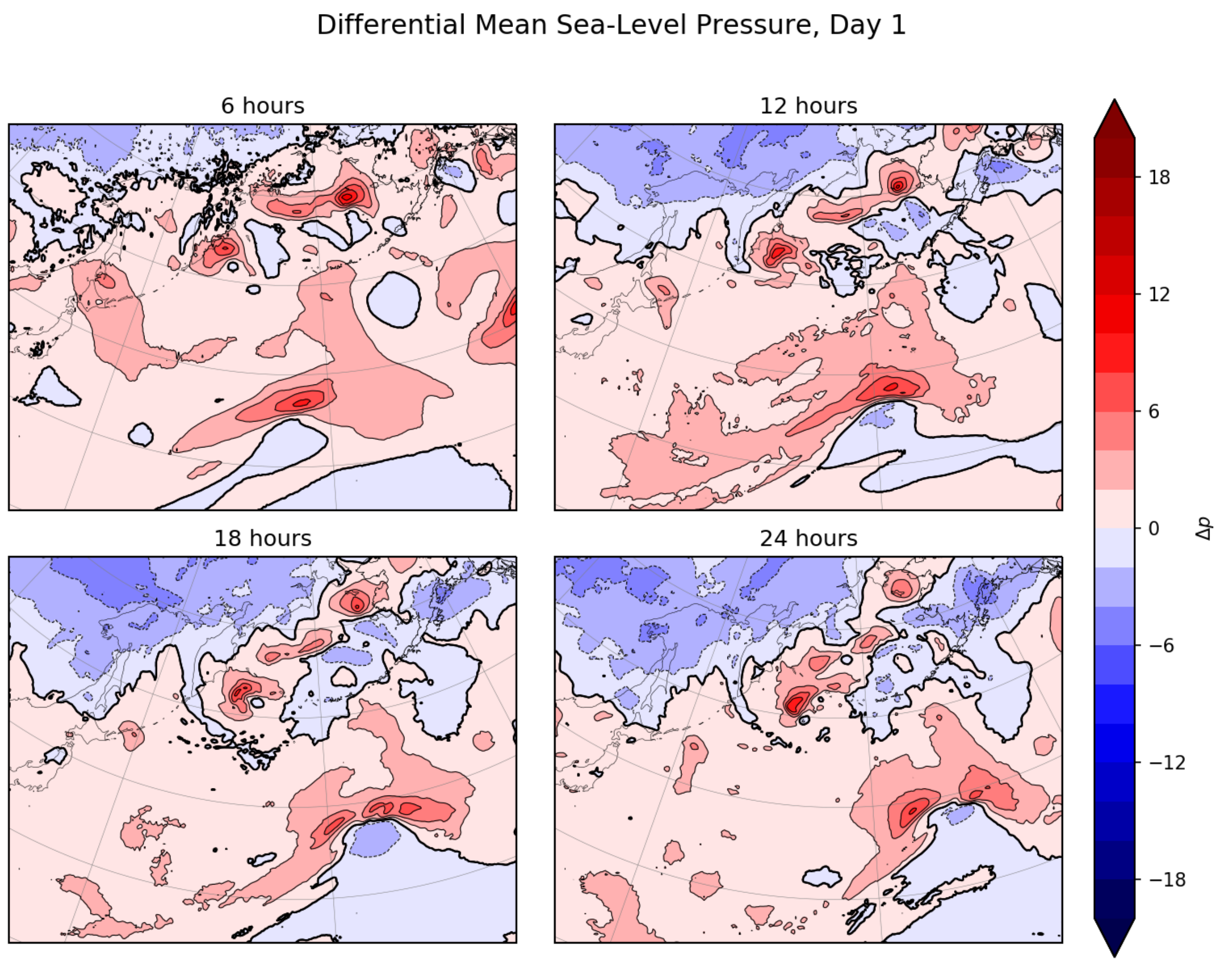

Figure 5.6: Case 1 Differential Mean Sea-Level Pressure, Day 1. Contour intervals are 2 hPa with the 0 hPa contour bolded.

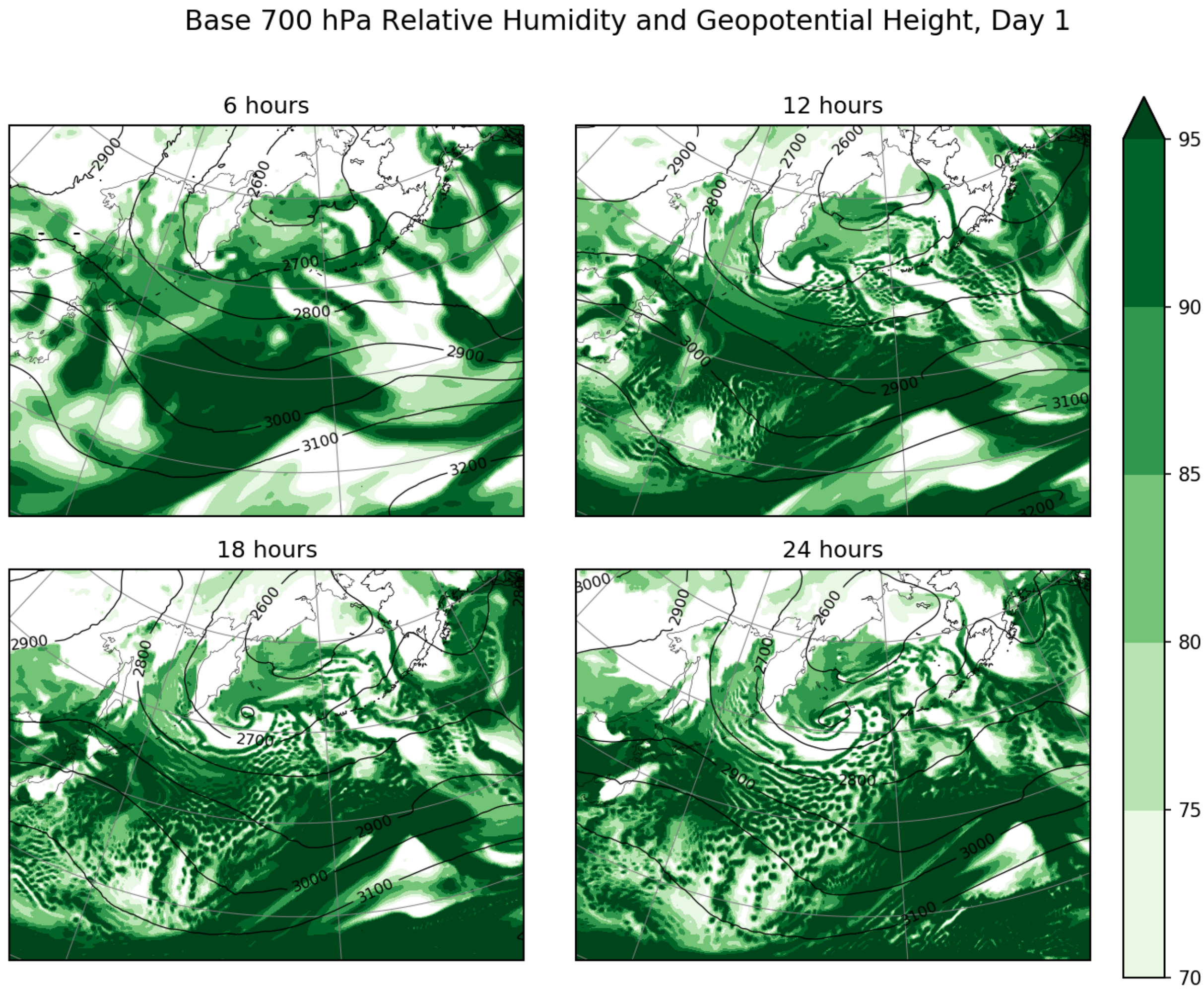

Figure 5.7: Case 1 Base 700 hPa Relative Humidity and Geopotential Height, Day 1. Contour intervals are 100 gpm for height and 5% for RH.

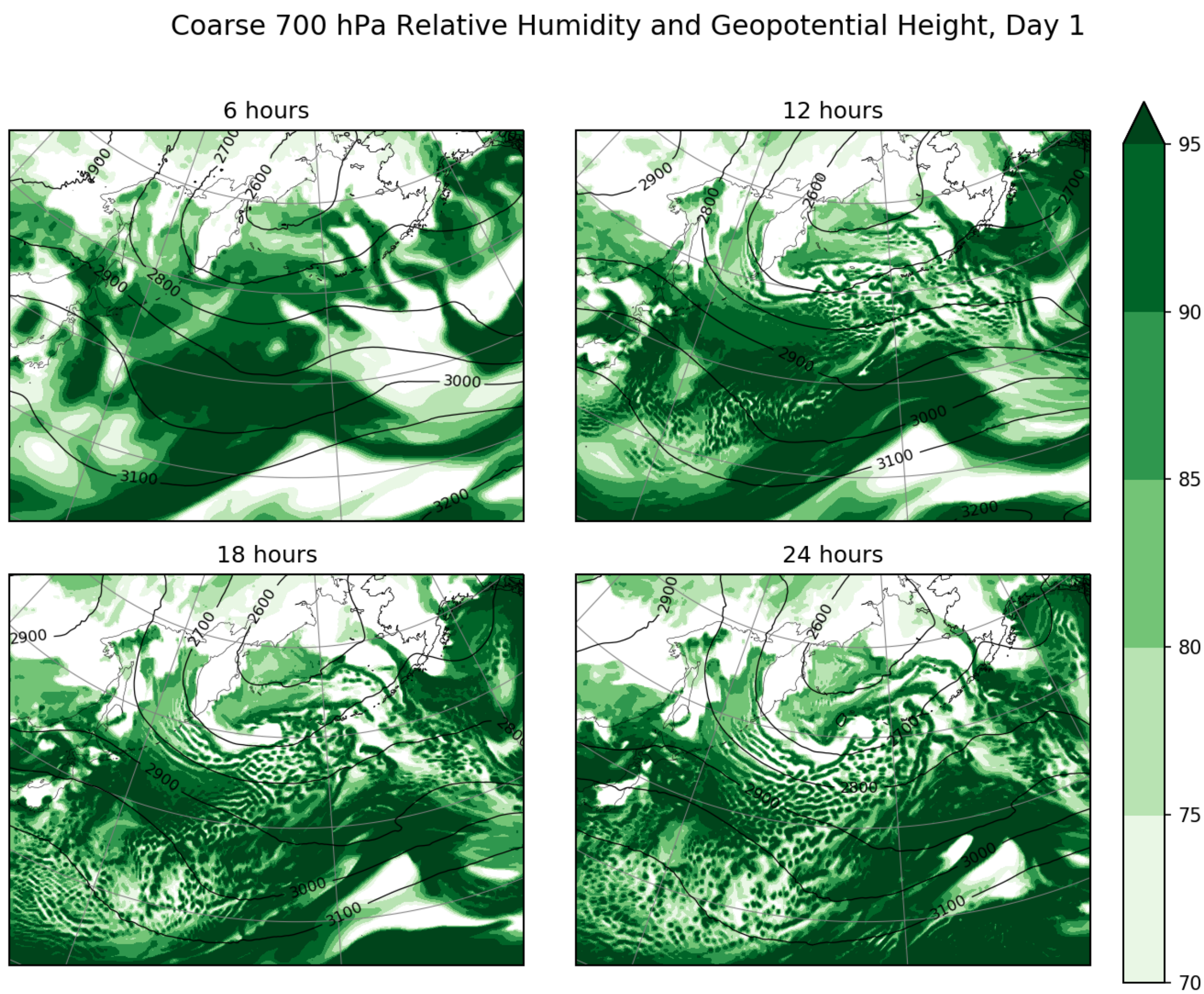

Figure 5.8: 7 Case 1 Coarse 700 hPa Relative Humidity and Geopotential Height, Day 1. Contour intervals are 100 gpm for height and 5% for RH.

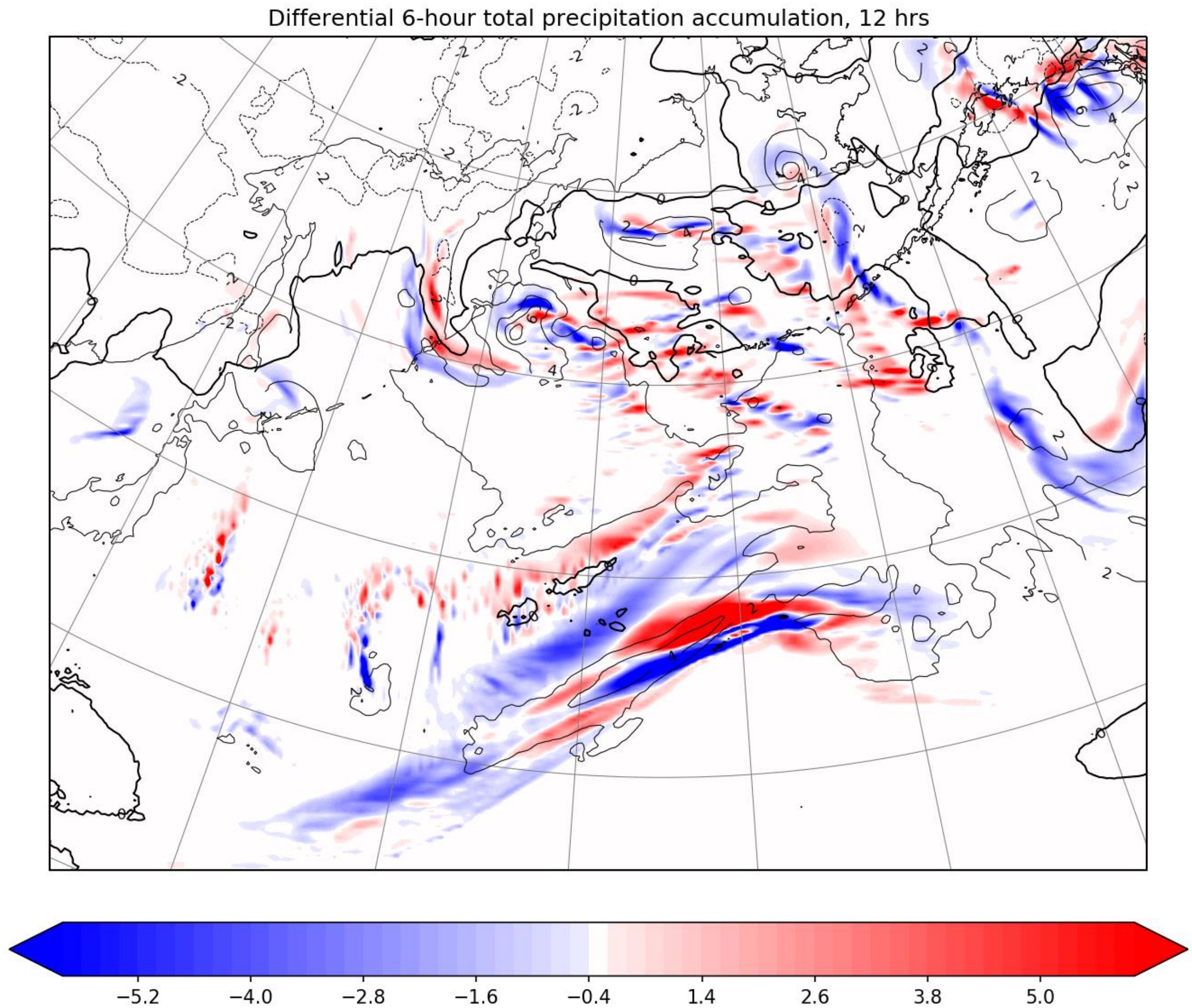

Figure 5.9: Case 1 Differential 6-hour Total Precipitation Accumulation at 12 Hours. Contours are differential MSLP with a 2 hPa interval. Differential precipitation contours are 0.4 mm with the interval -0.4 to 0.4 appearing white.

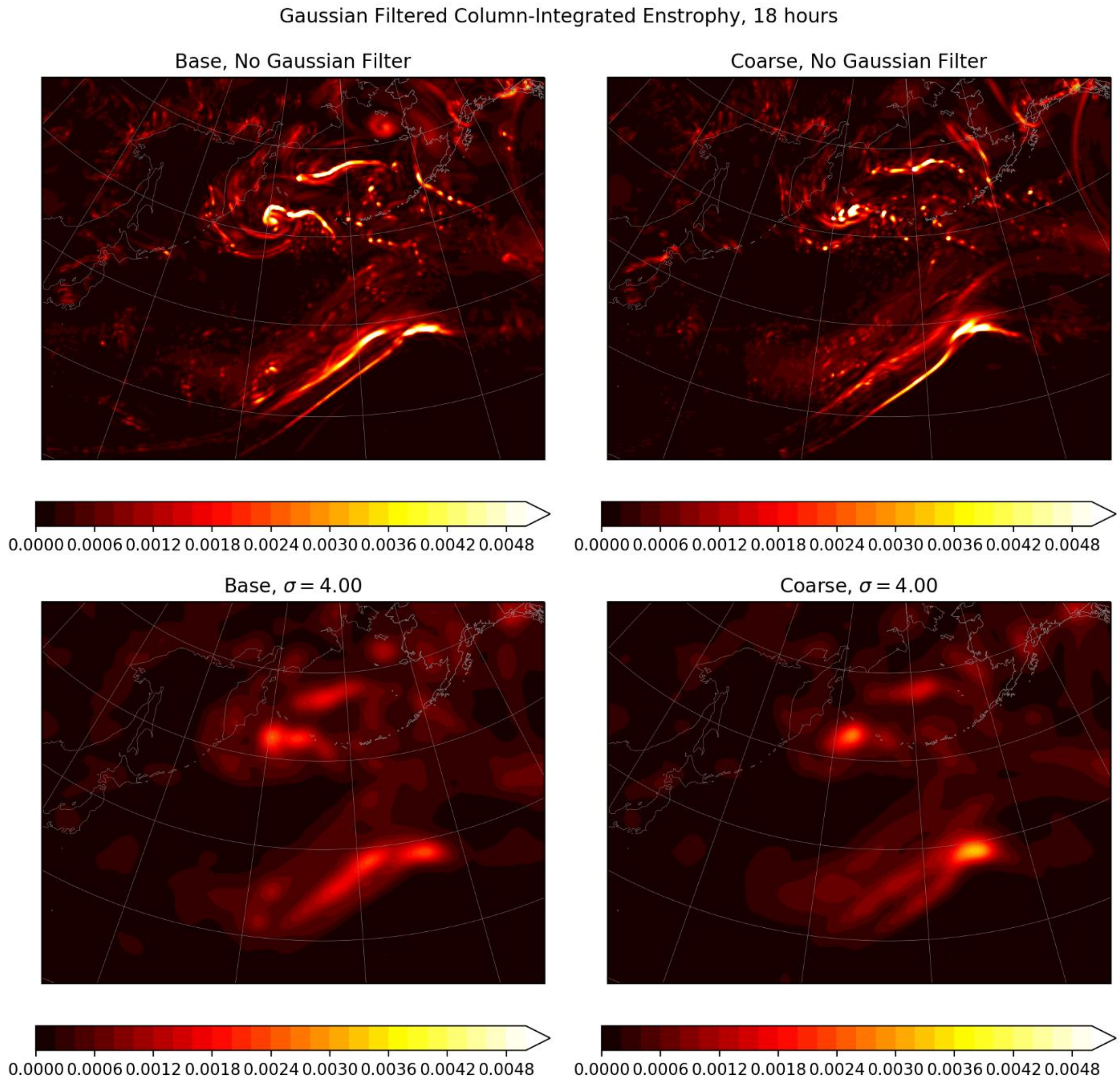

Figure 5.10: Case 1 Column-Integrated Enstrophy at 18 Hours. Panel titles indicate the standard deviation of the envelope function and, by proxy, the half-width. Top panels are with no envelope function. The left column panels are the base simulation and the right column panels are the coarse simulation. Contour intervals are 0.2×10^{-4} hPa s^{-1}.

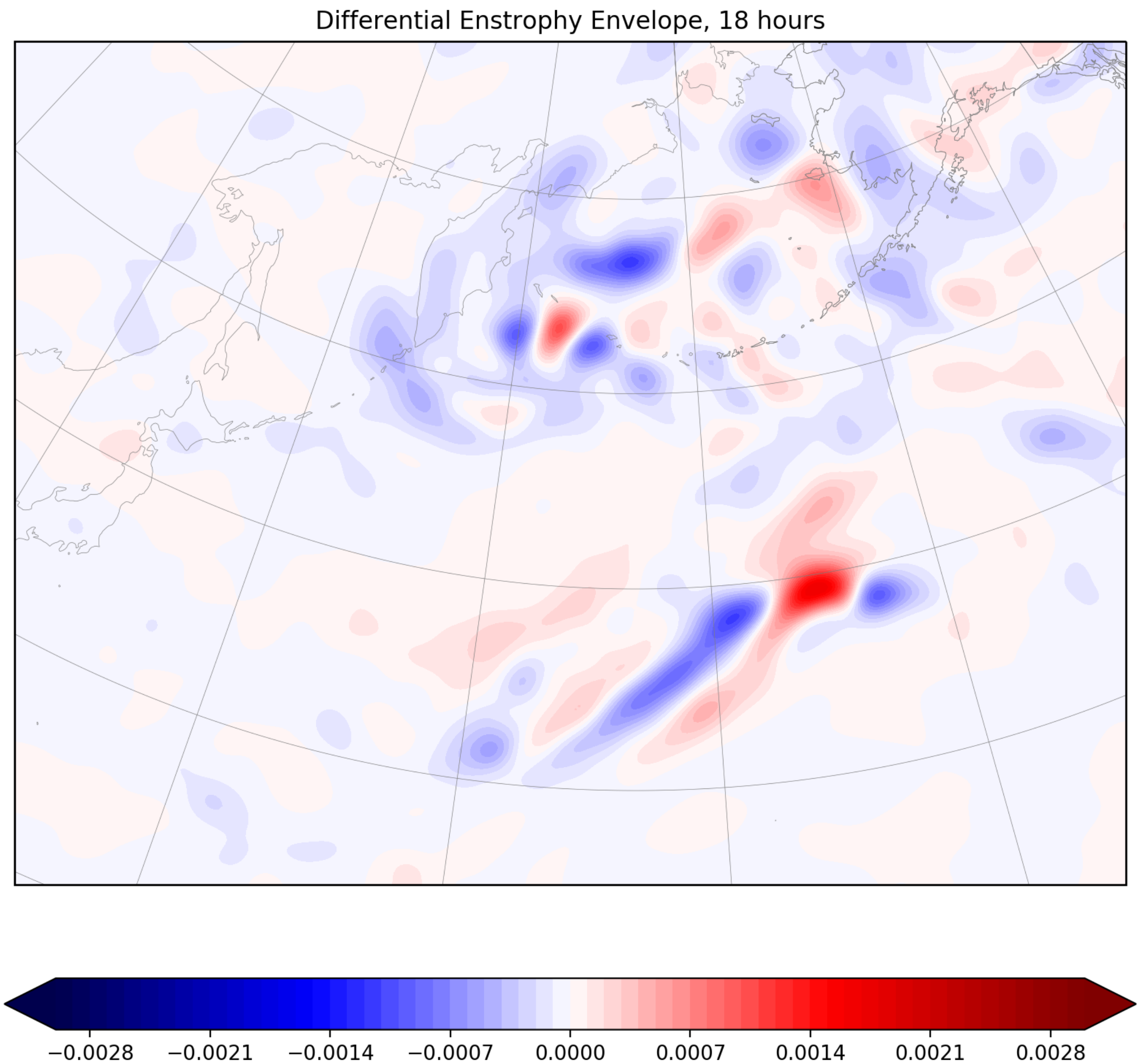

1167

1168 Figure 5.11: Case 1 Differential Enstrophy Envelope at 18 Hours. Contour intervals are 10^{-4} hPa s^{-1}.

1169

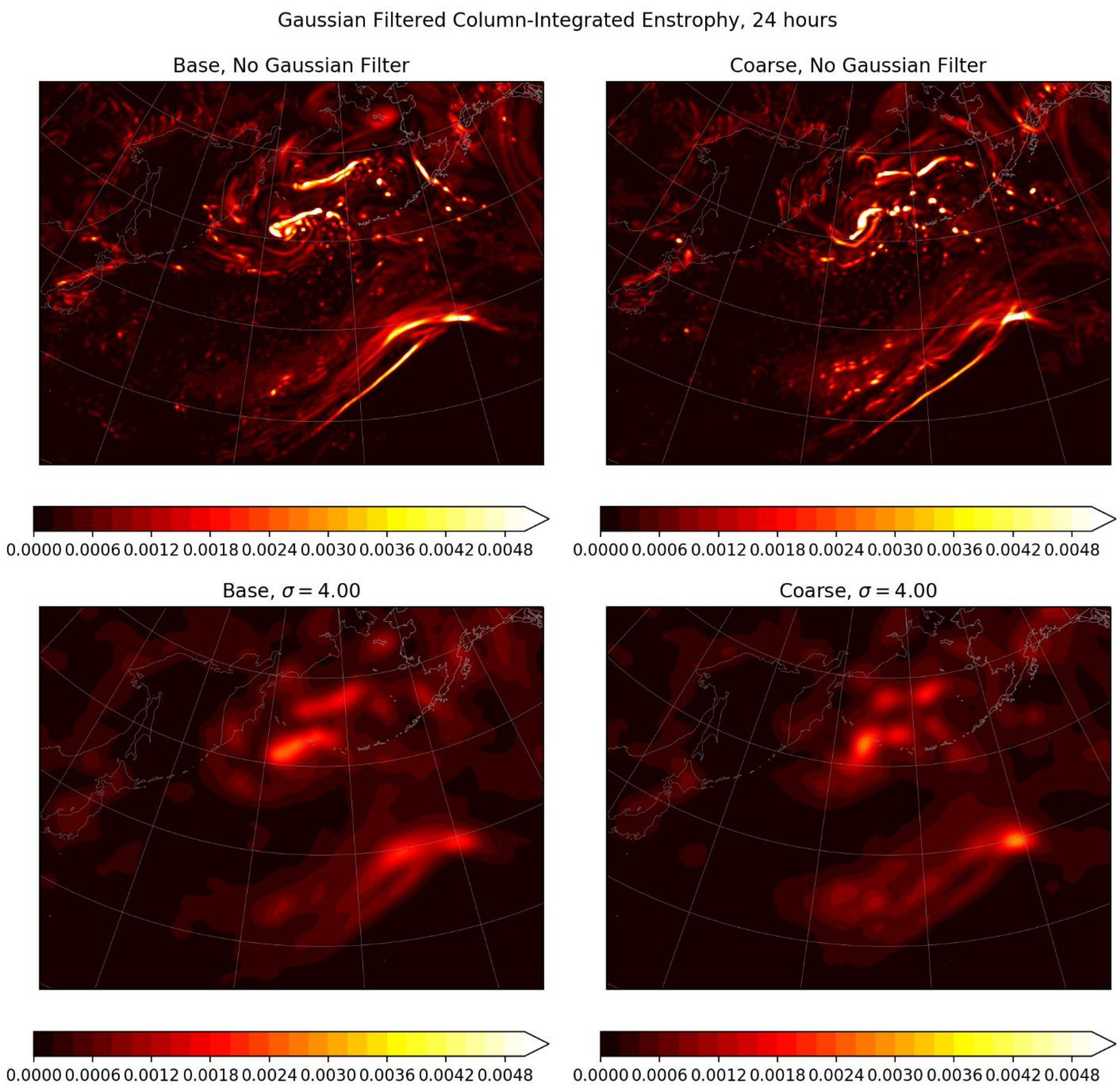

Figure 5.12: Case 1 Column-Integrated Enstrophy at 24 Hours. Contour intervals are $2x10^{-4}$ hPa s^{-1}.

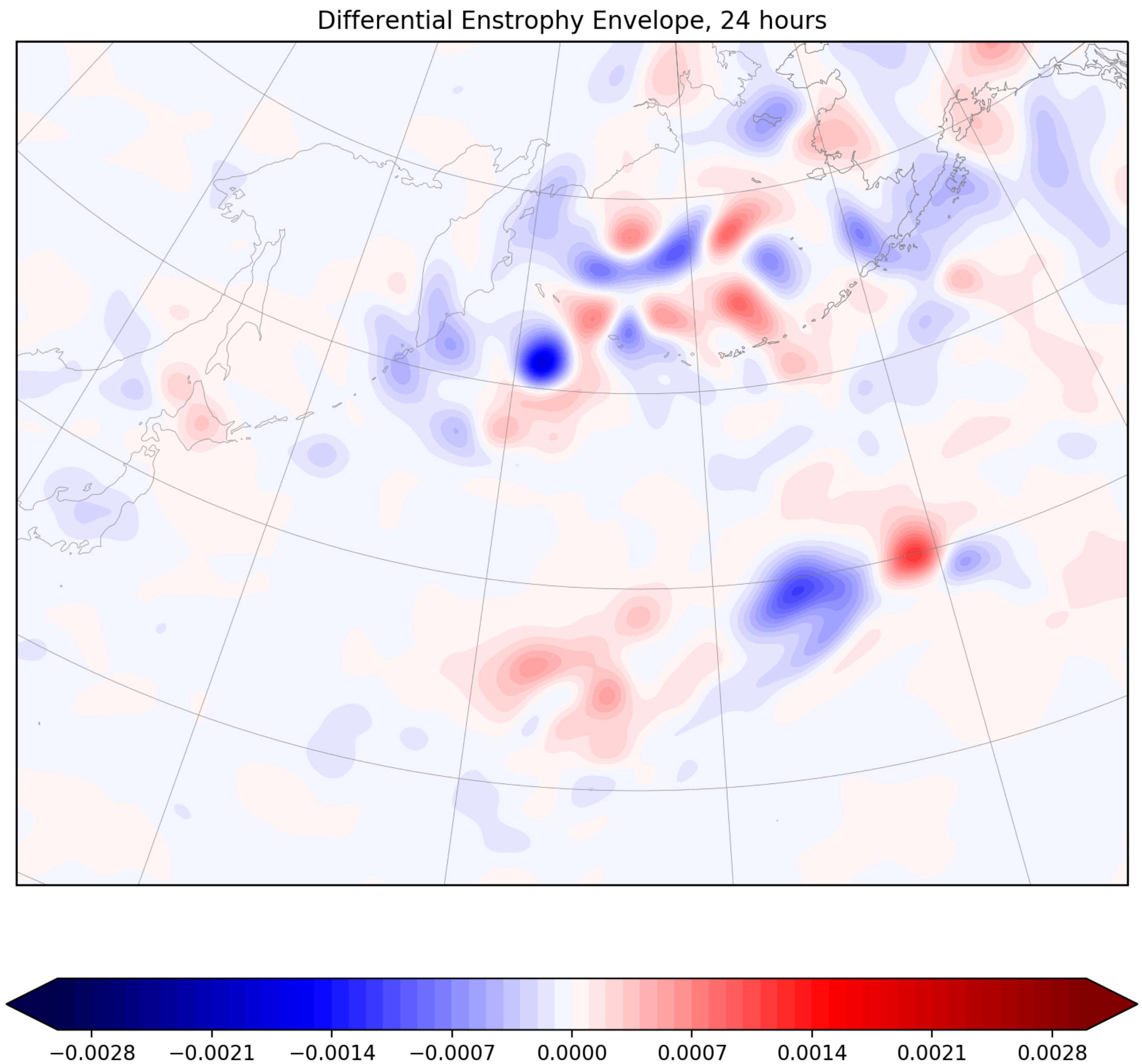

Figure 5.13: Case 1 Differential Enstrophy Envelope at 24 Hours. Contour intervals are 10^{-4} hPa s^{-1}.

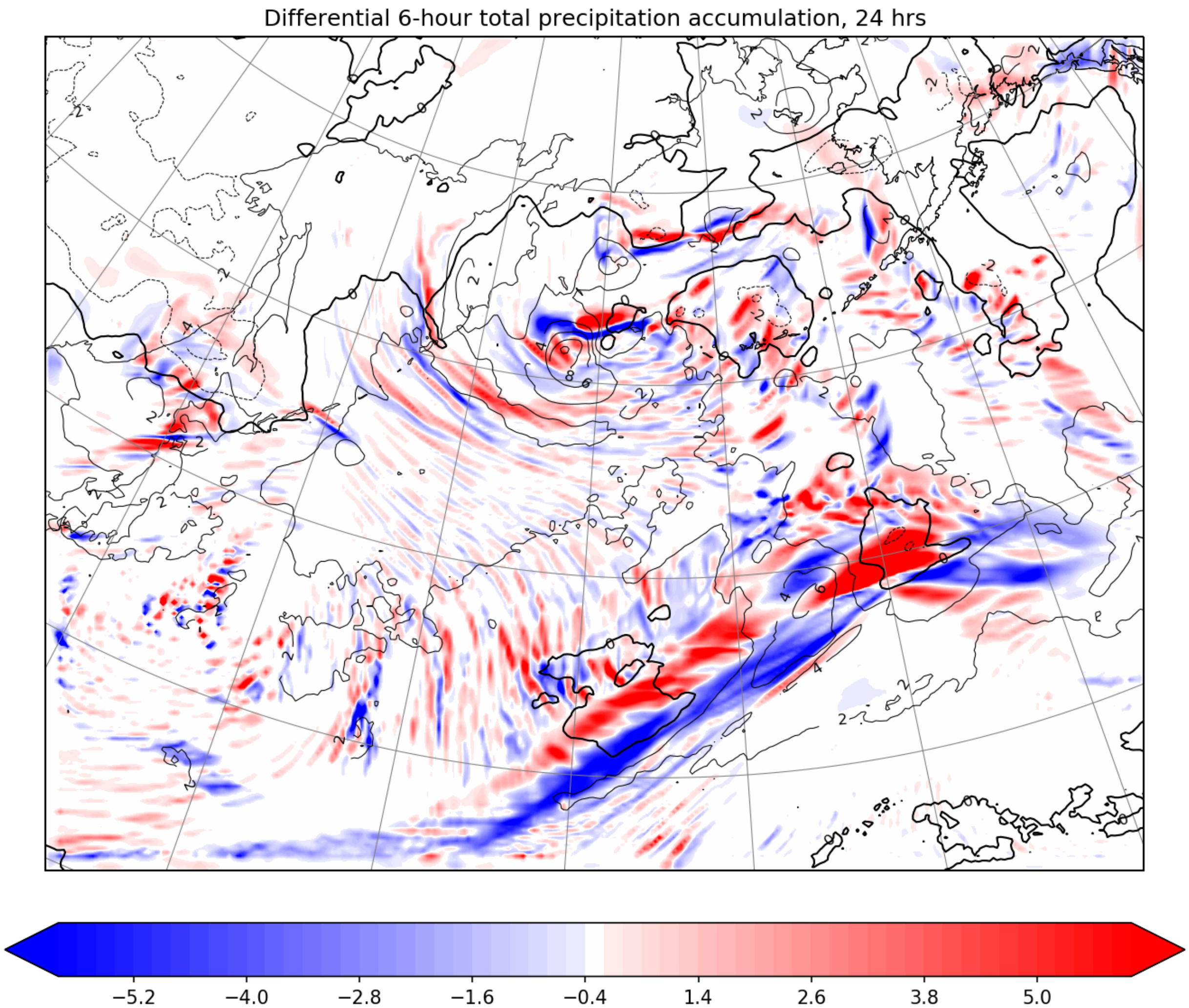

1176

1177 Figure 5.14: Case 1 Differential 6-hour Total Precipitation Accumulation at 24 Hours. Contours are differential

1178 MSLP with a 2 hPa interval. Differential precipitation contours are 0.4 mm with the interval -0.4 to 0.4

1179 appearing white.

1180

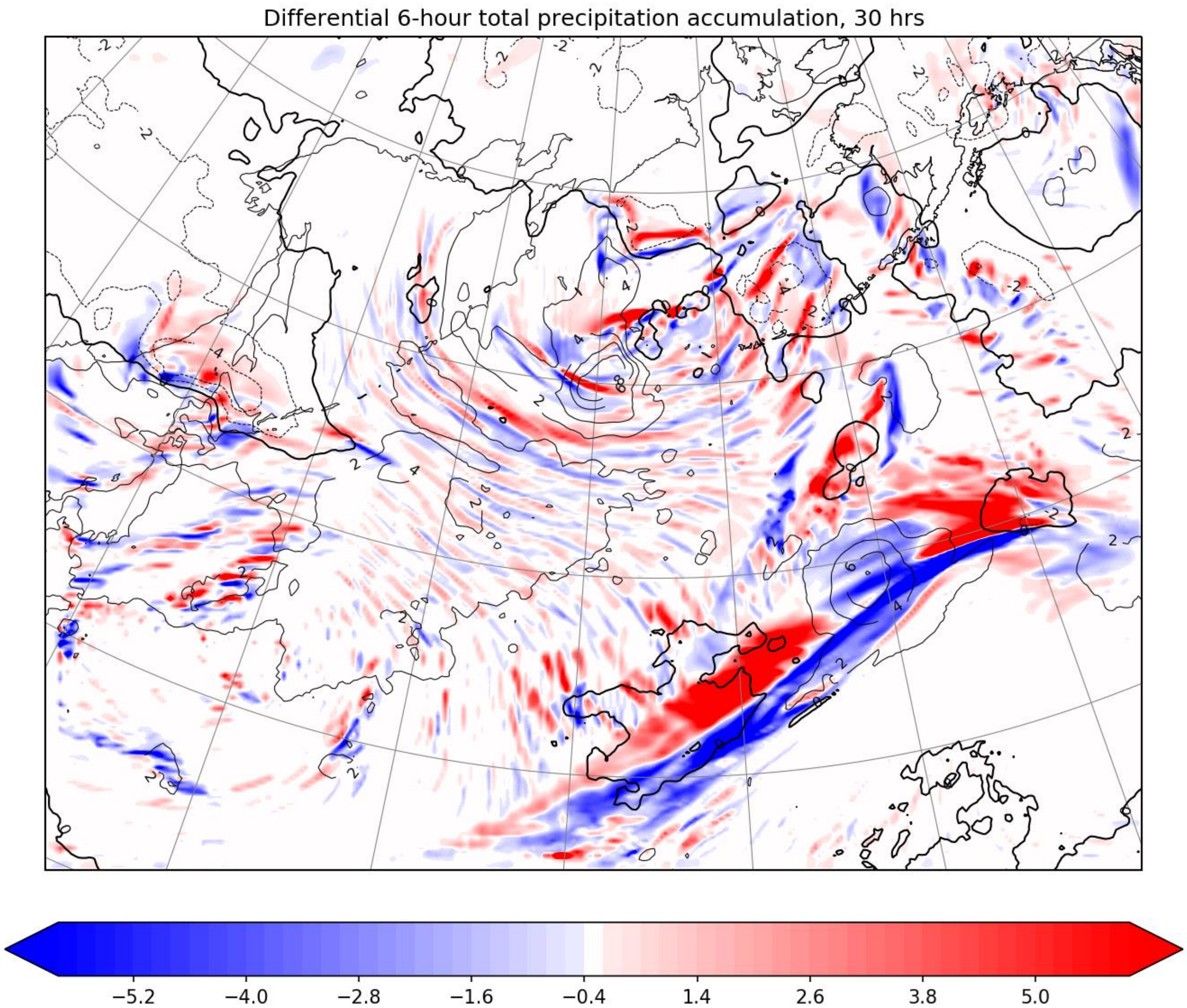

Figure 5.15: Case 1 Differential 6-hour Total Precipitation Accumulation at 30 Hours. Differential precipitation contours are 0.4 mm with the interval -0.4 to 0.4 appearing white.

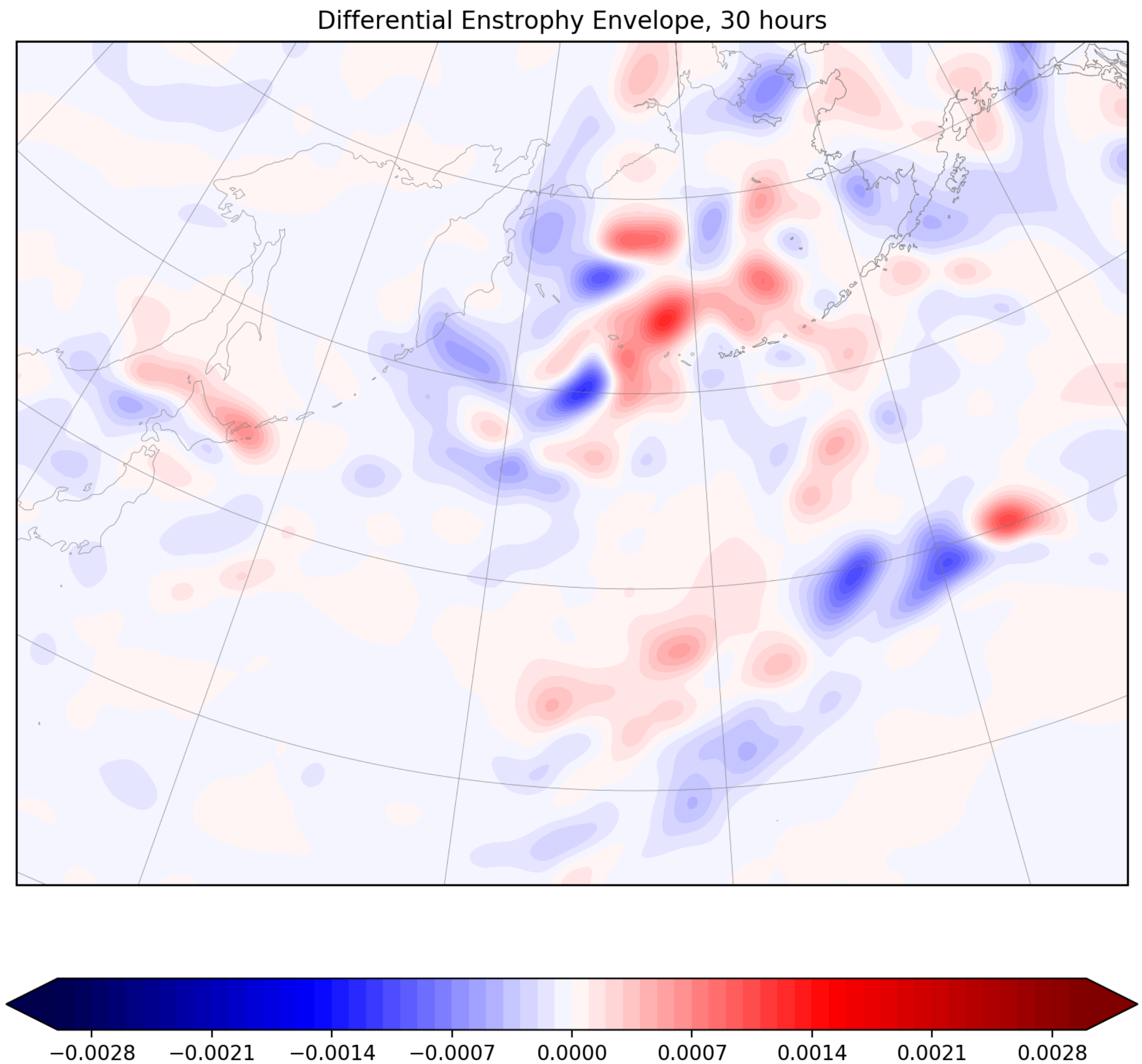

Figure 5.16: Case 1 Differential Enstrophy Envelope at 30 Hours. Contour intervals are 10^{-4} hPa s^{-1}.

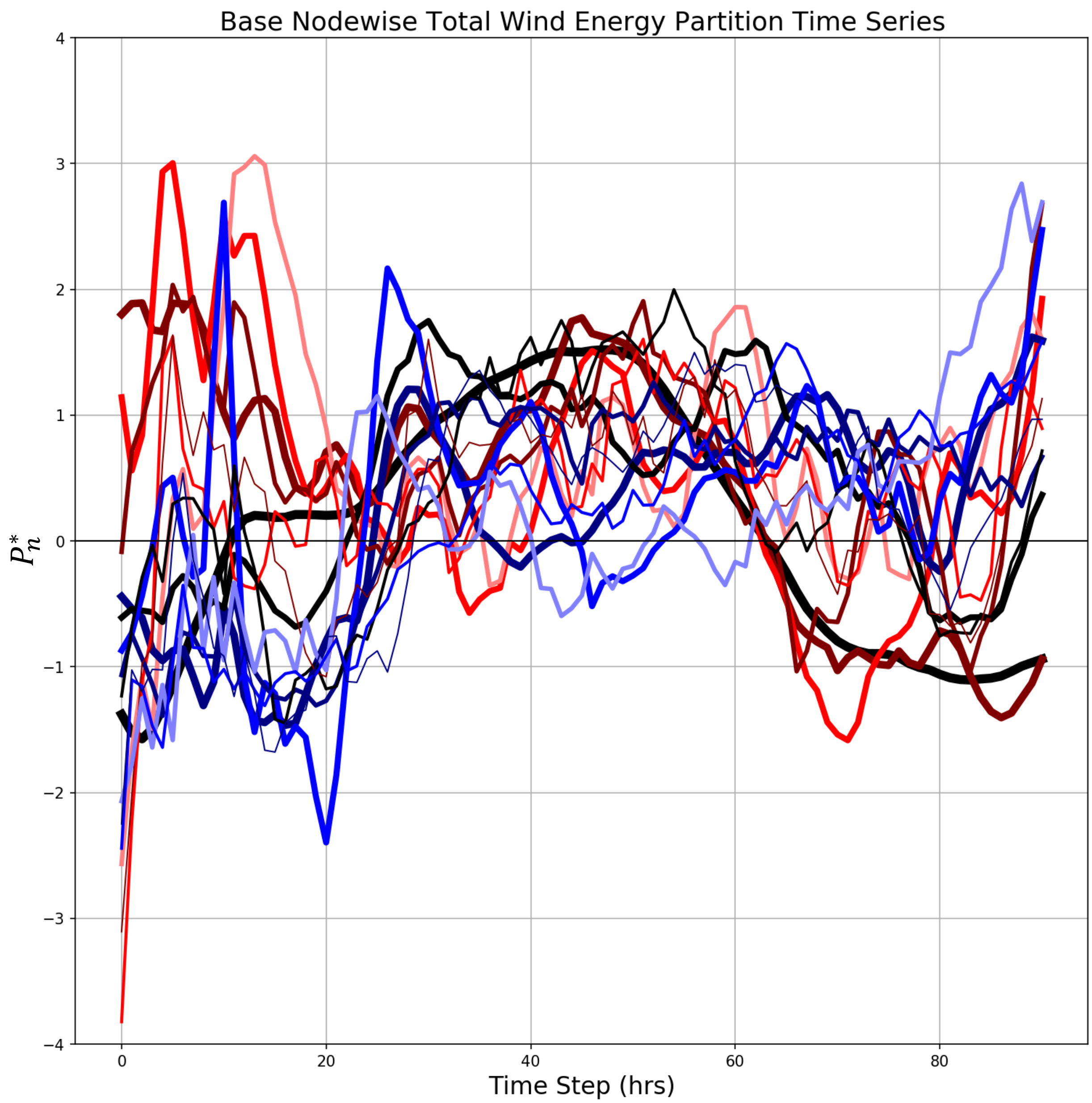

Figure 5.17: Case 1 Base Nodewise Total Wind Energy Partition Time Series. Red (blue) lines represent zonal (meridional) elongation, with line thickness indicating constituent scale and hue representing degree of elongation.

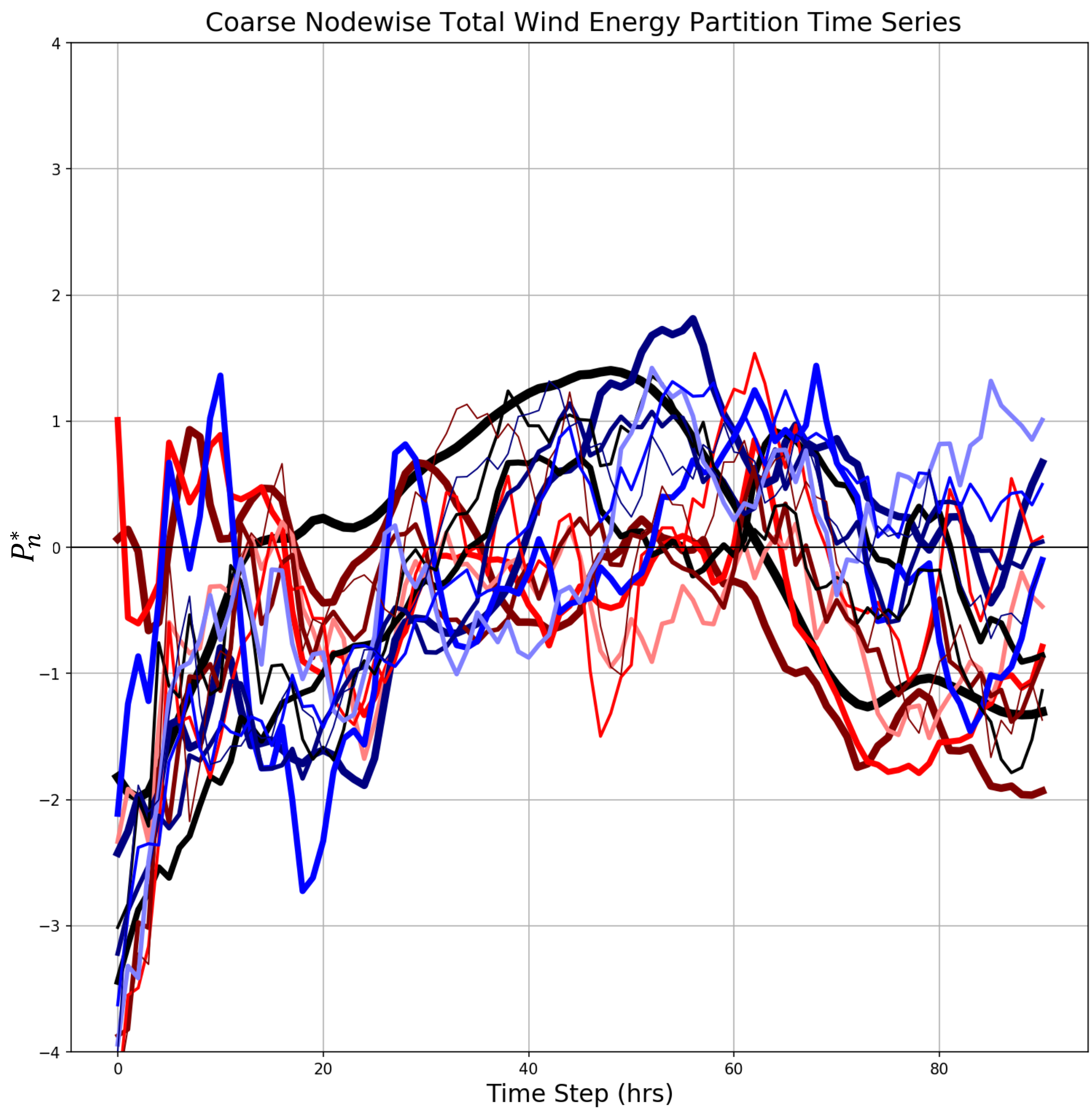

Figure 5.18: Case 1 Coarse Nodewise Total Wind Energy Partition Time Series. Line color, hue, and thickness are the same as in Figure 5.17.

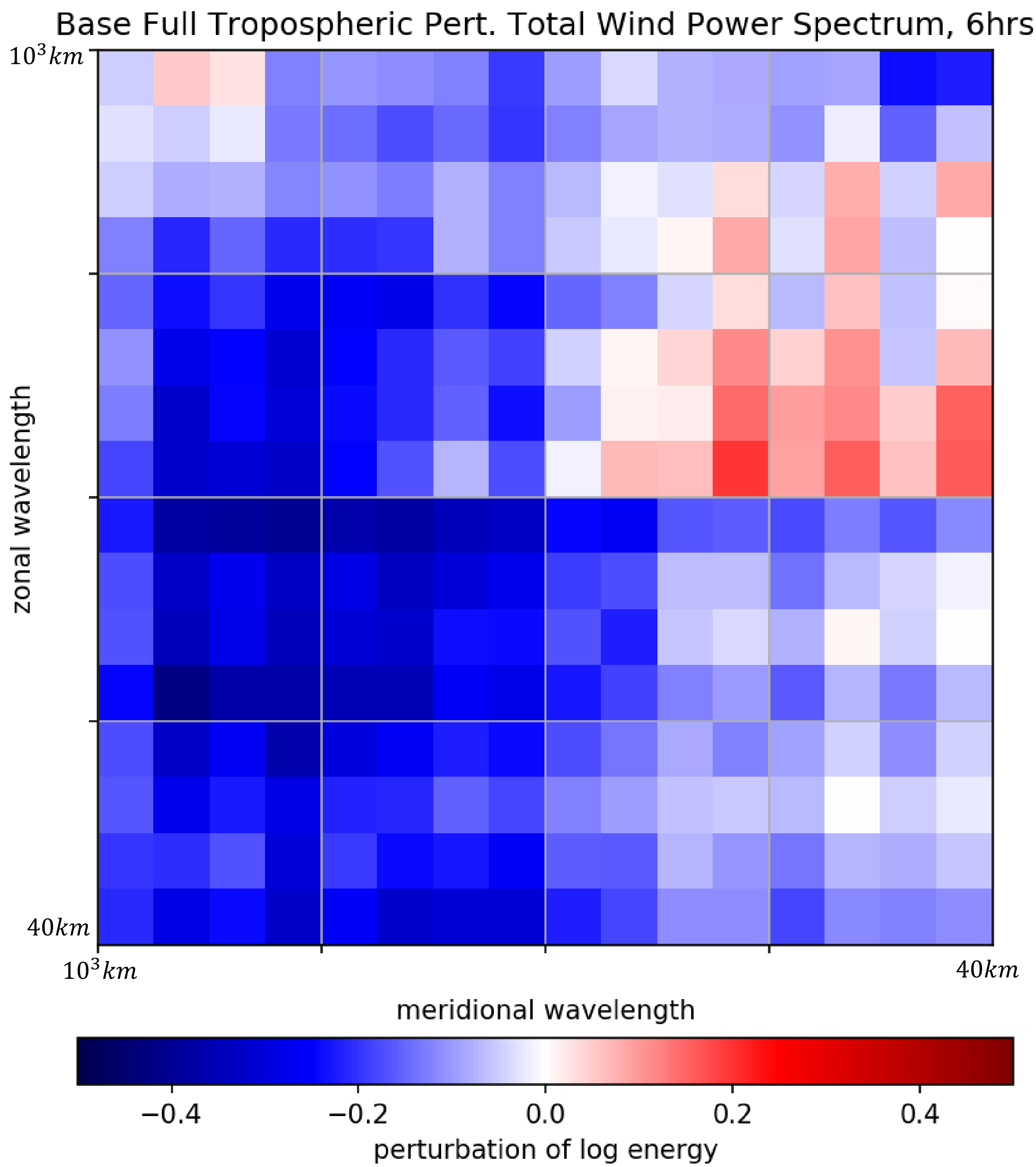

Figure 5.19: Case 1 Base Tropospheric Perturbation Total Wind Power Spectrum at 6 Hours. Axes highlight the maximum and minimum wavelengths resolvable by the model.

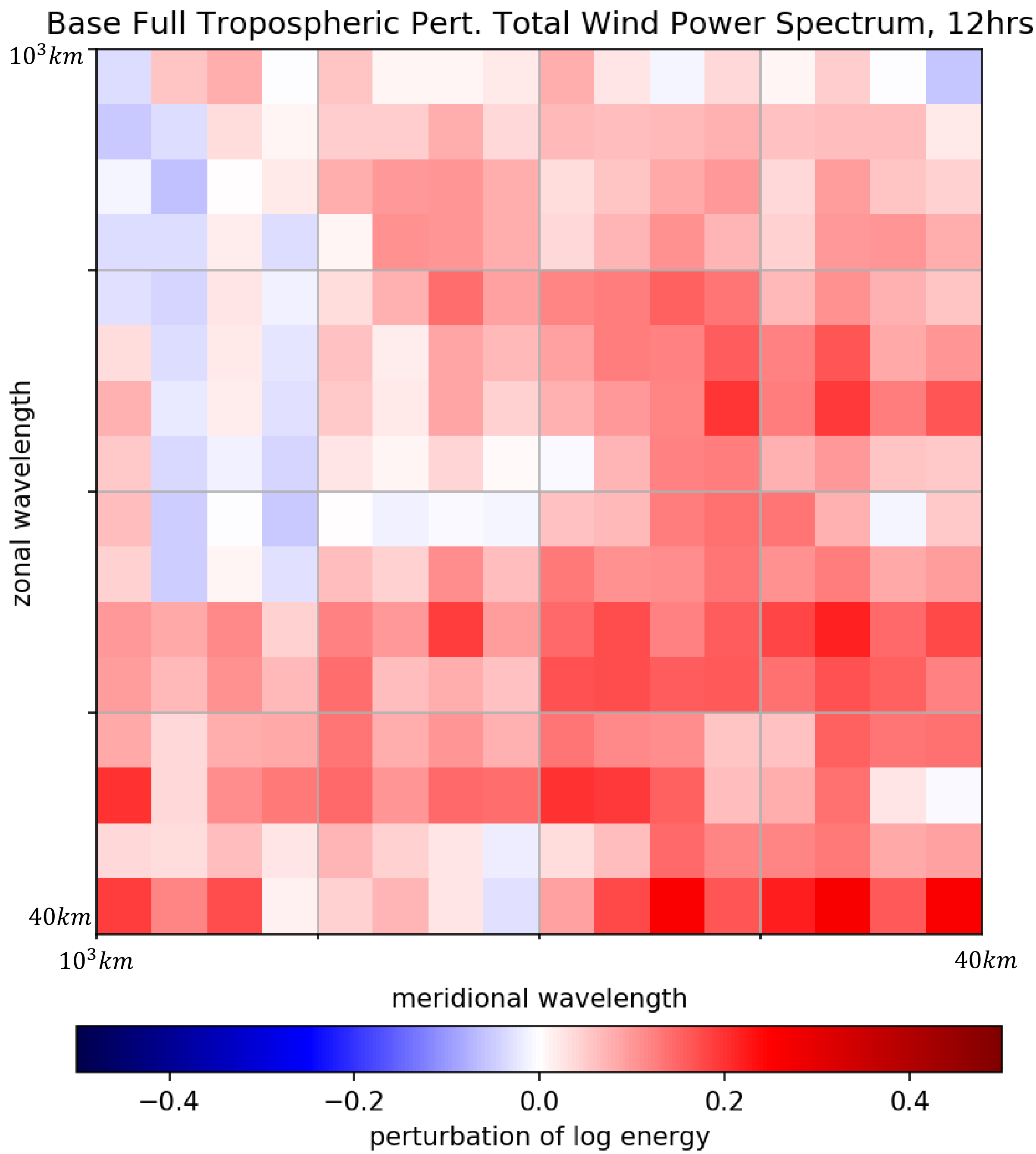

Figure 5.20: Case 1 Base Tropospheric Perturbation Total Wind Power Spectrum at 12 Hours.

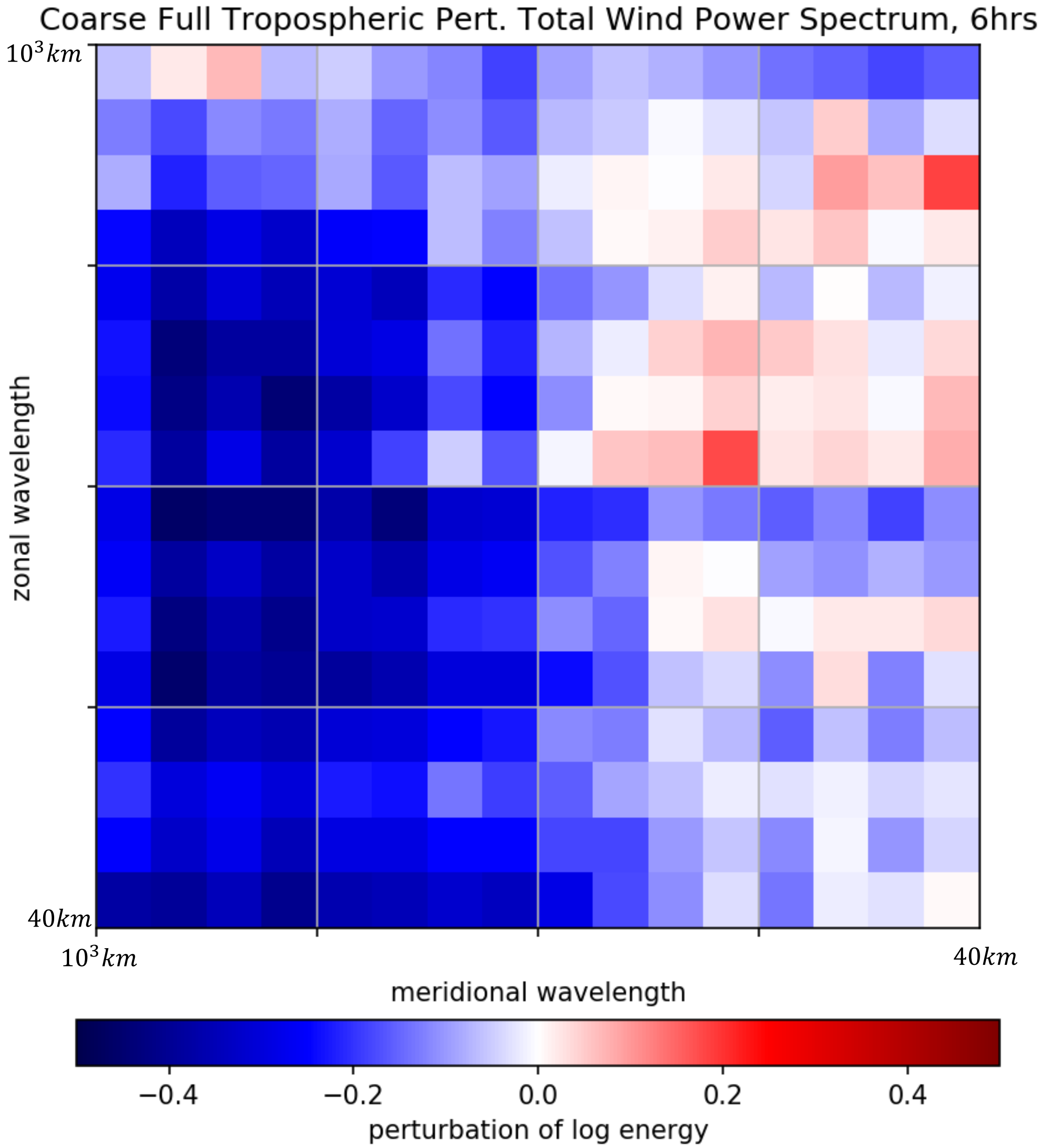

1204

1205 Figure 5.21: Case 1 Coarse Tropospheric Perturbation Total Wind Power Spectrum at 6 Hours.

1206

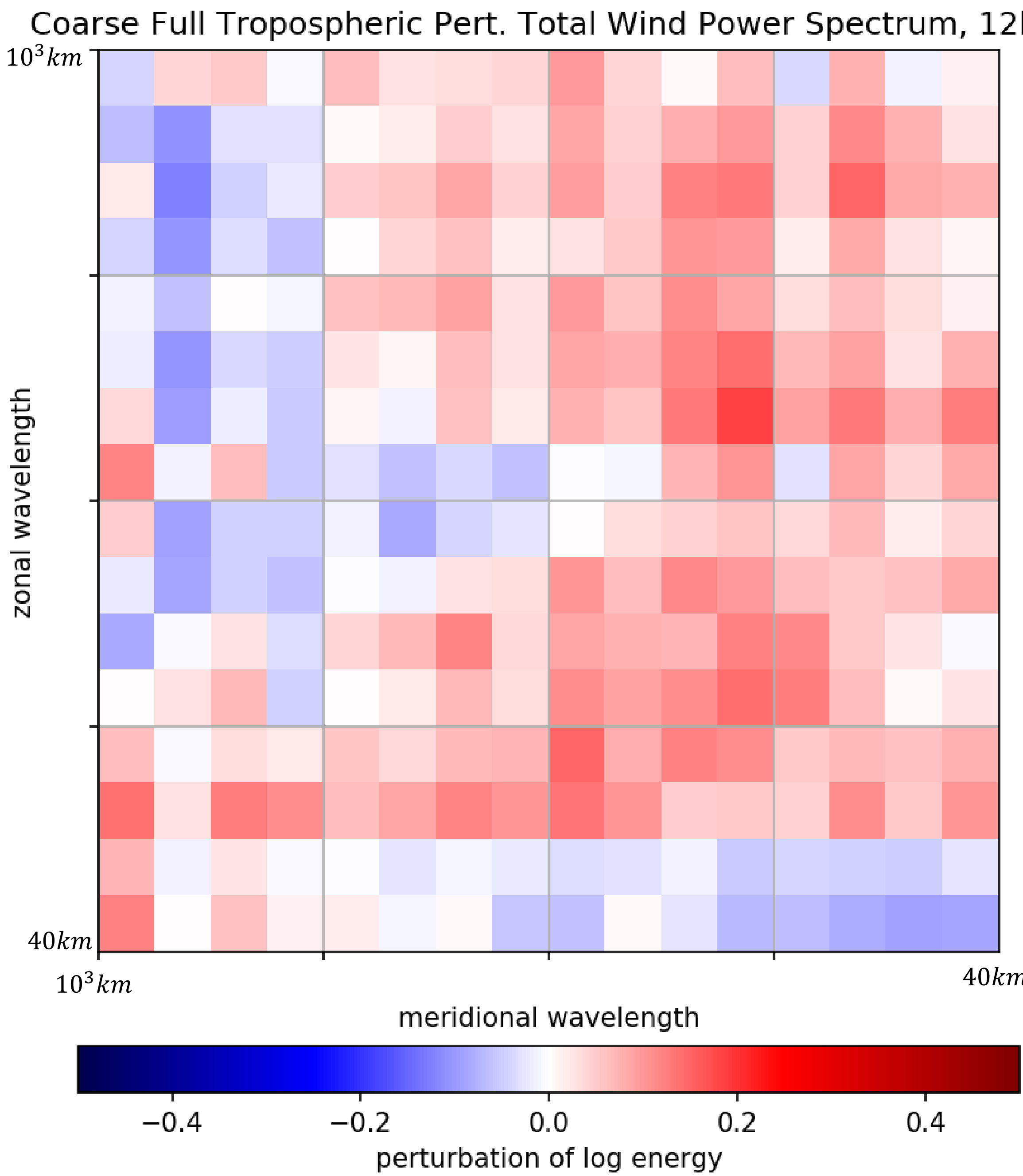

1207

1208 Figure 5.22: Case 1 Coarse Tropospheric Perturbation Total Wind Power Spectrum at 12 Hours.

1209

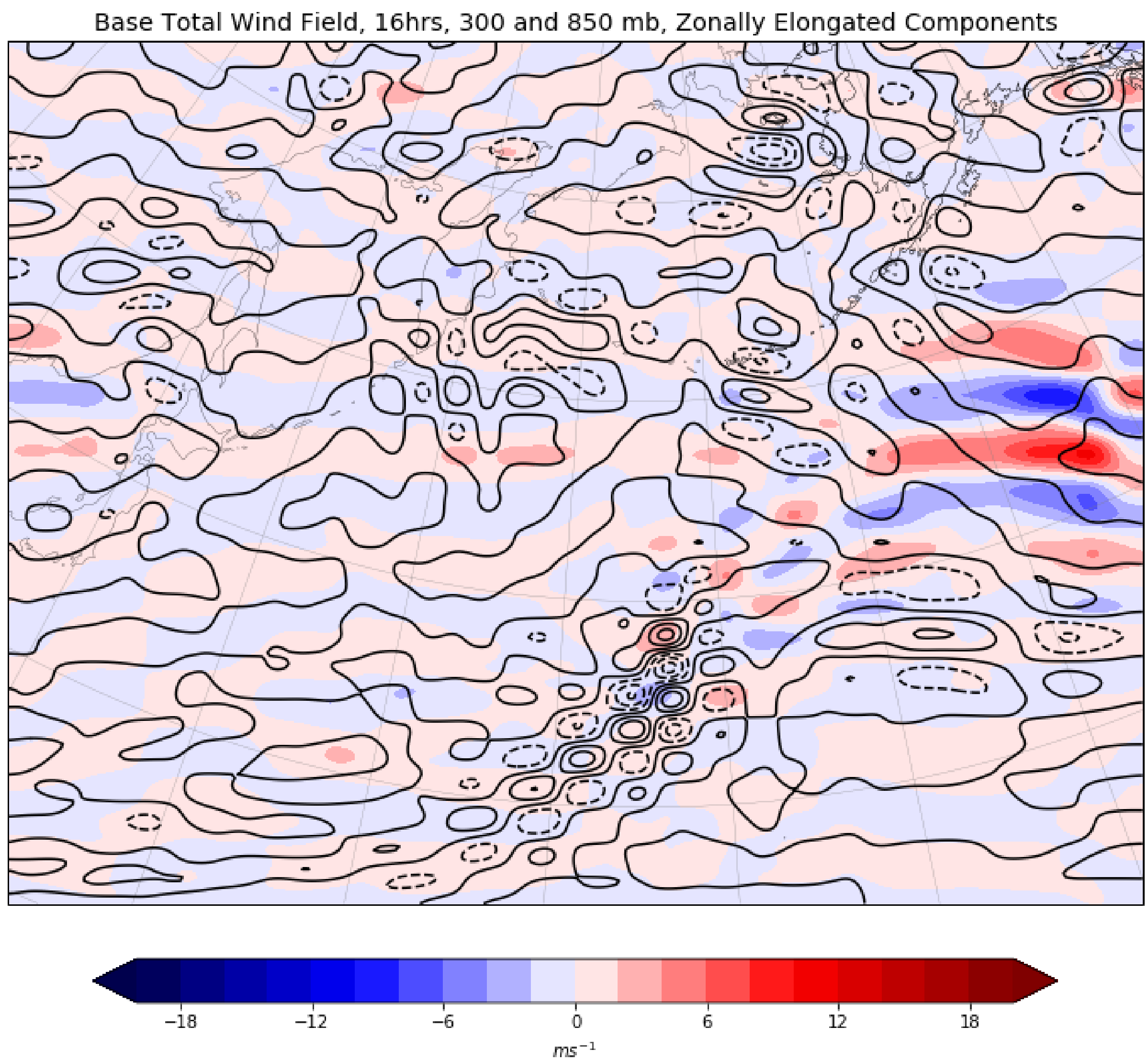

Figure 5.23 Case 1 Base Total Wind at 300 (filled) and 850 hPa (contours), Zonally Elongated Spectral Components. Contour intervals for both are 2 ms^{-1}

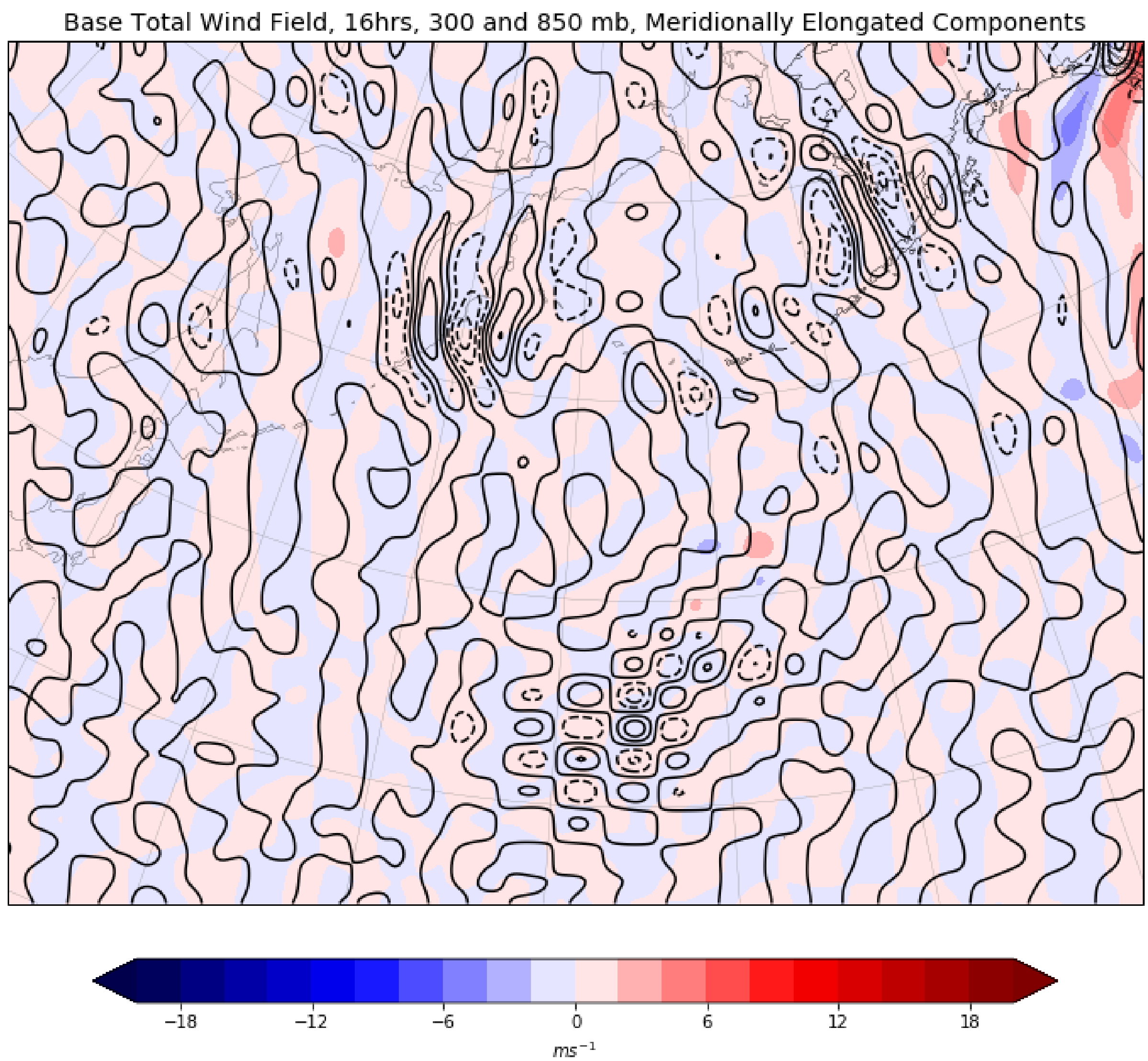

Figure 5.24: Case 1 Base Total Wind at 300 (filled) and 850 hPa (contours), Meridionally Elongated Spectral Components. Contour intervals for both are 2 ms^{-1}.

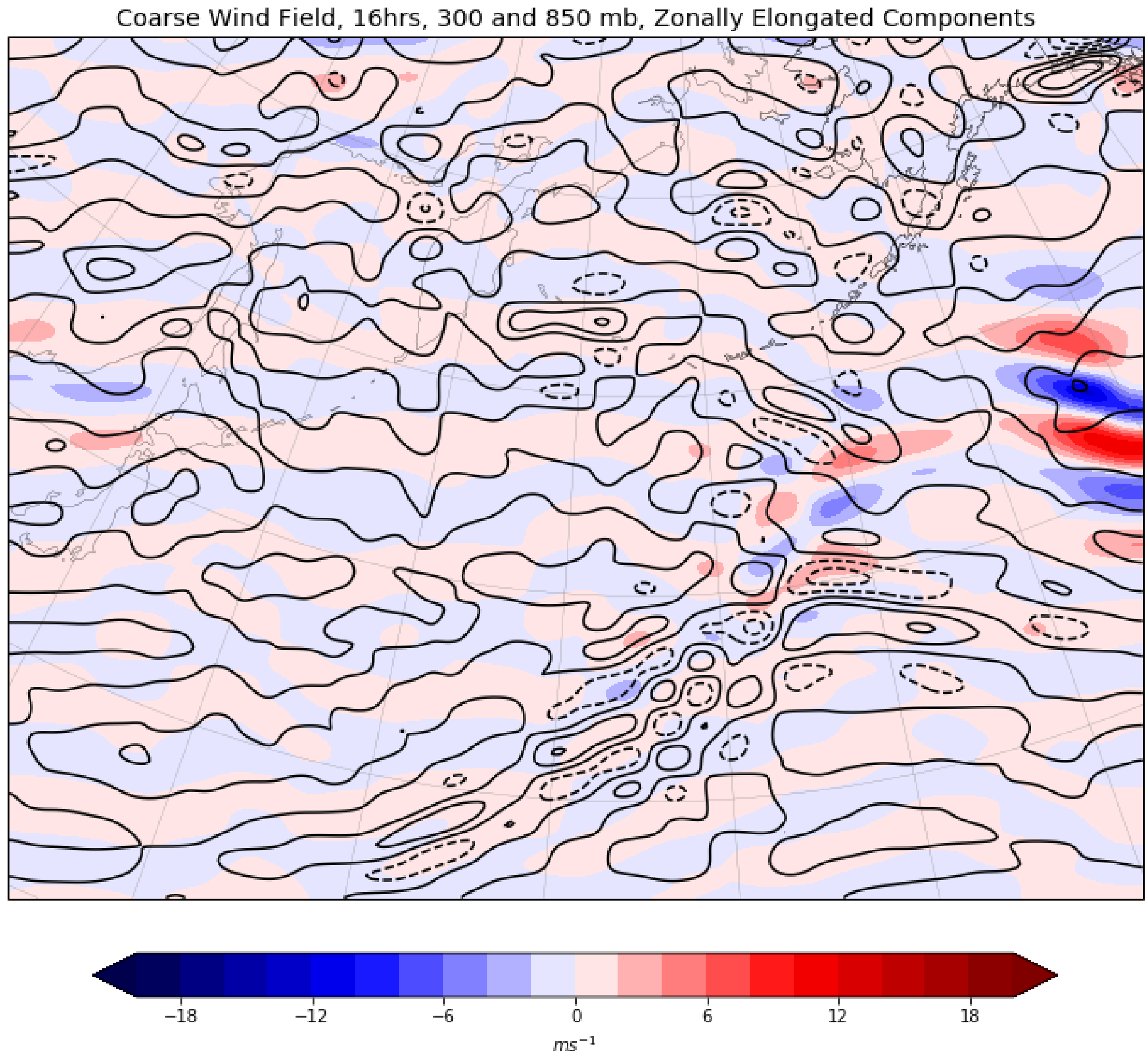

Figure 5.25: Case 1 Coarse Total Wind at 300 (filled) and 850 hPa (contours), Zonally Elongated Spectral Components. Contour intervals for both are 2 ms^{-1}

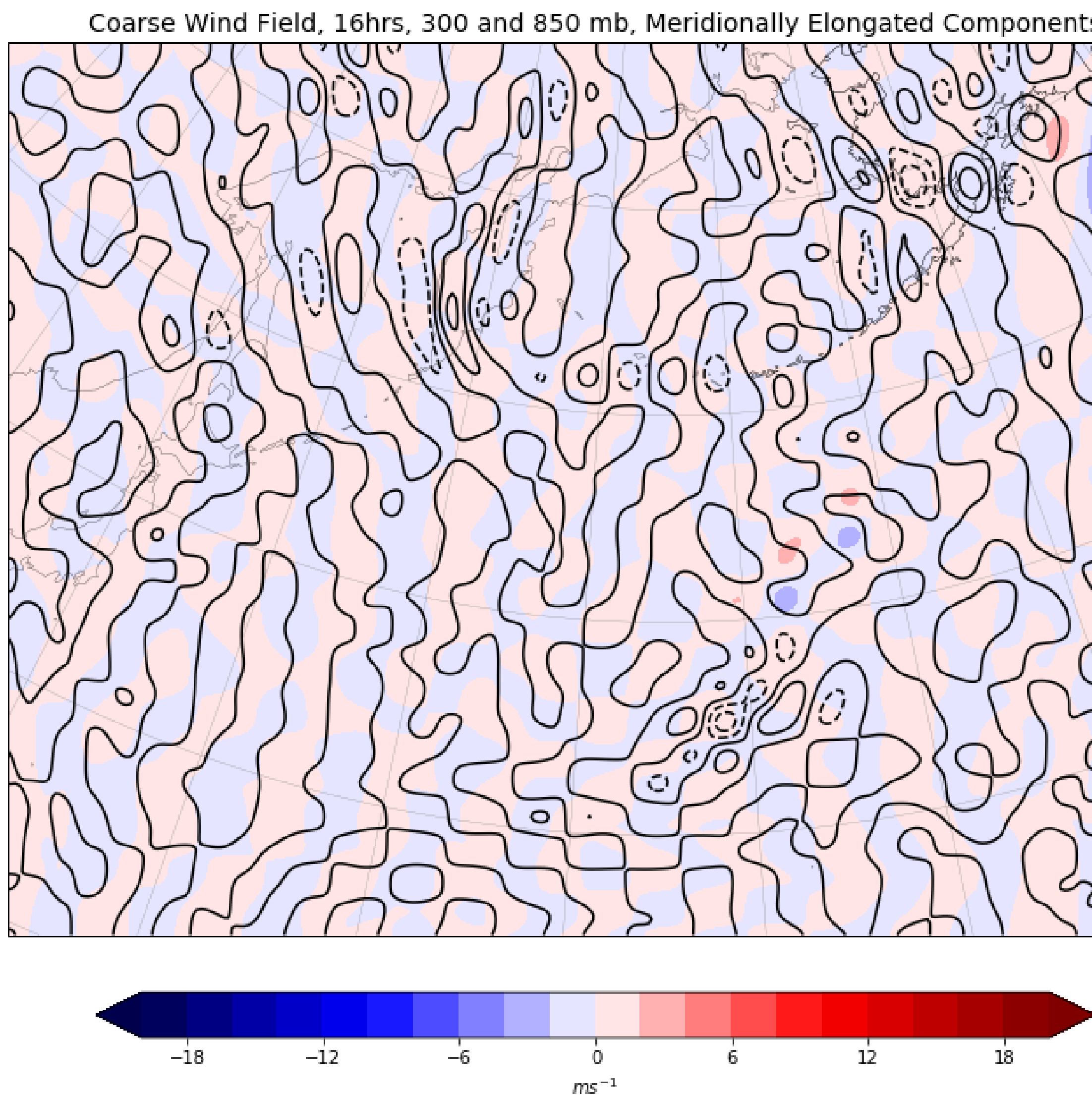

Figure 5.26: Case 1 Coarse Total Wind at 300 (filled) and 850 hPa (contours), Meridionally Elongated Spectral Components. Contour intervals for both are 2 ms^{-1}

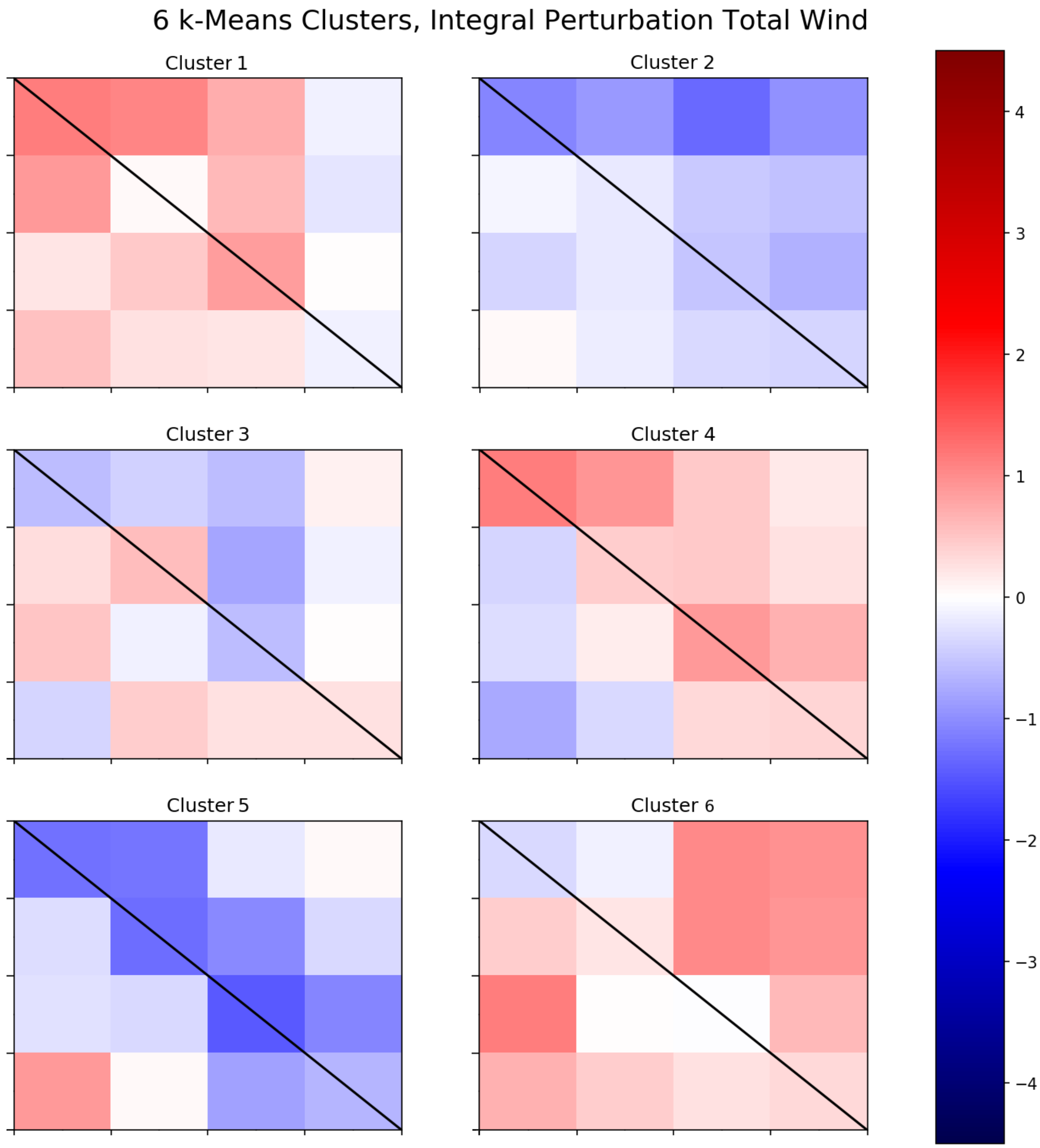

1227

1228 Figure 5.27: Case 1 k-Means Cluster Centroids, Integral Perturbation Total Wind. The black line represents a

1229 line of isotropy across, with nodes above the line zonally-elongated and those below meridionally elongated.

1230

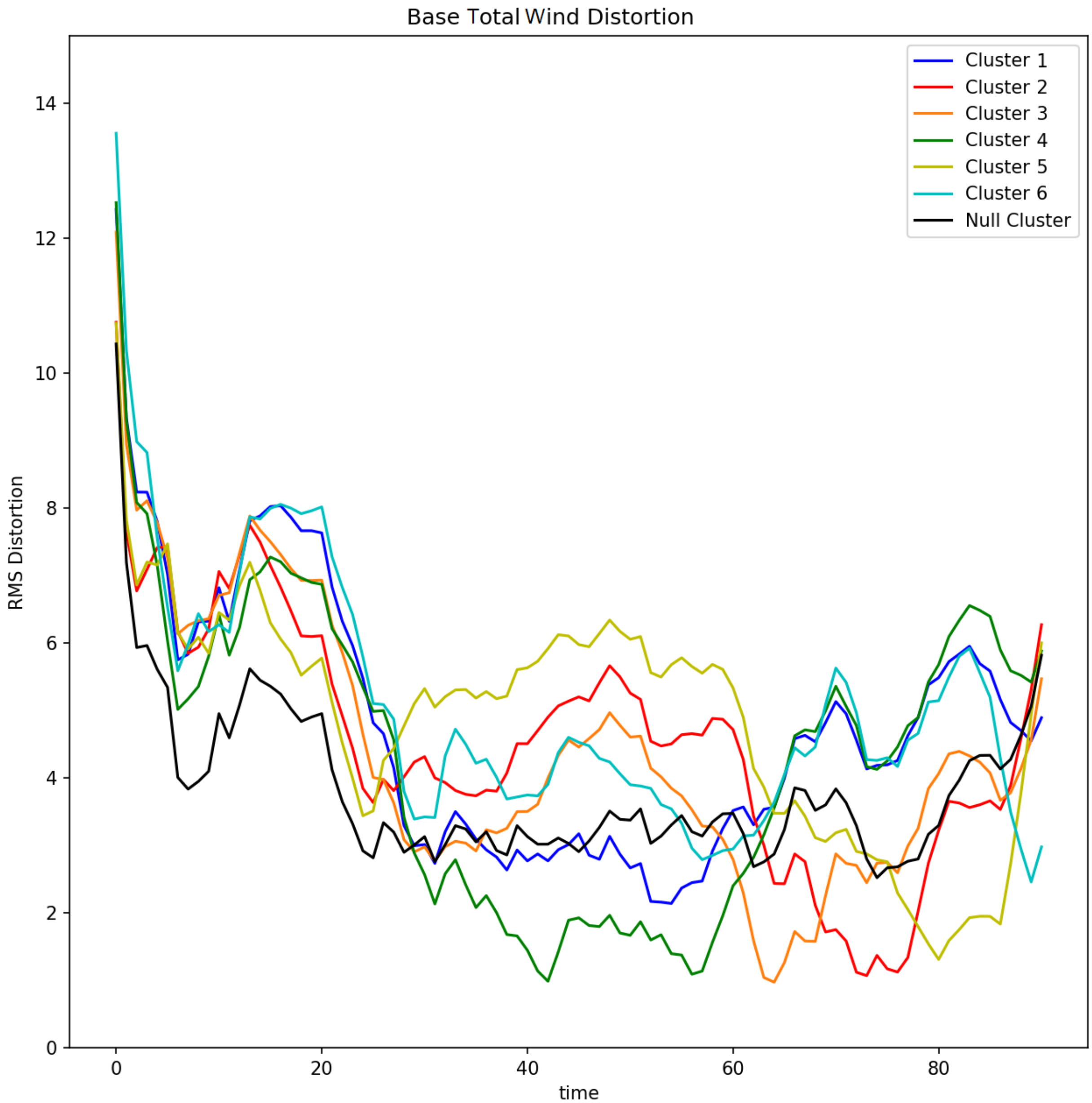

Figure 5.28: D_k for the Case 1 base simulation.

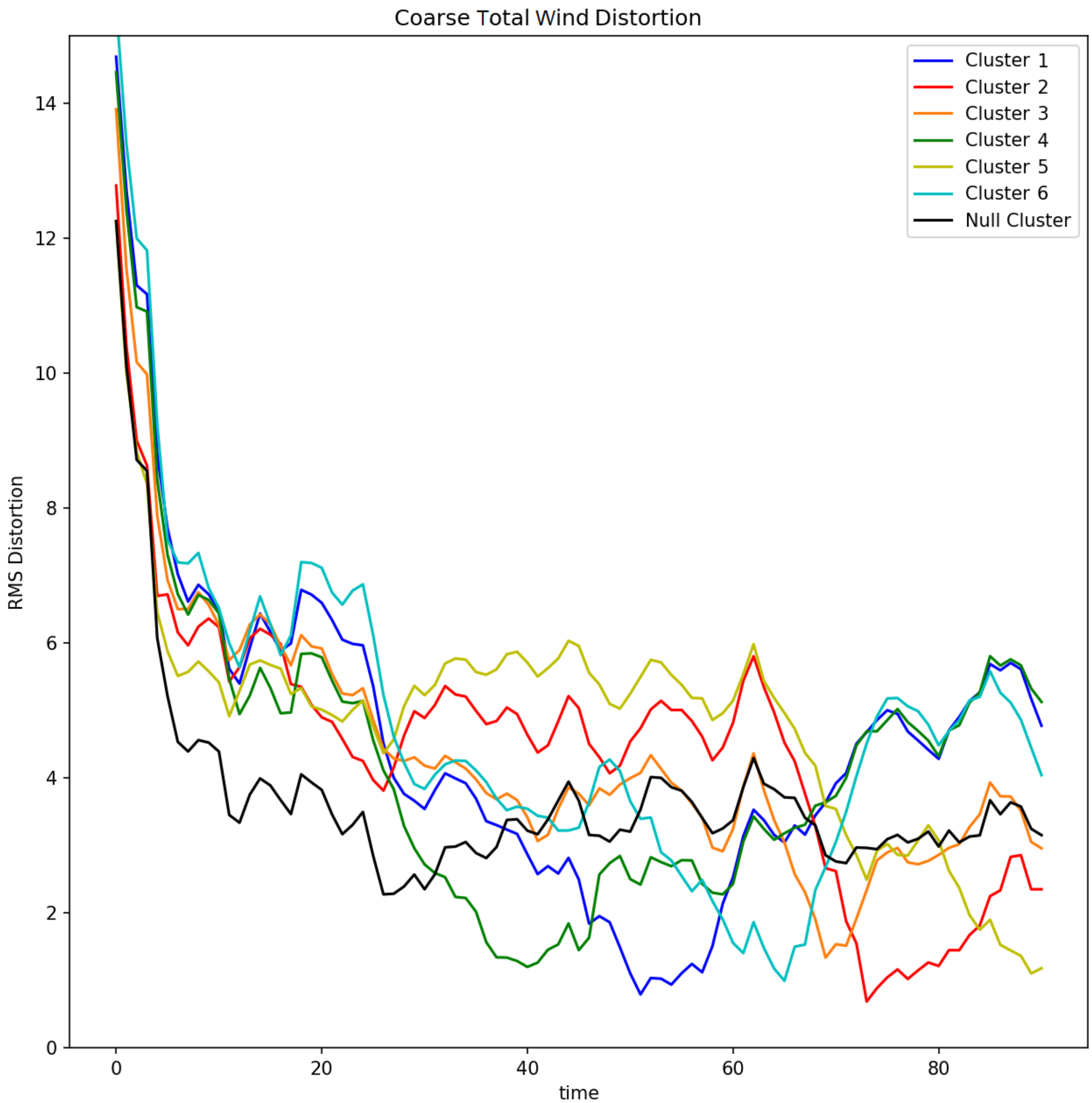

Figure 5.29: D_k for the Case 1 coarse simulation.

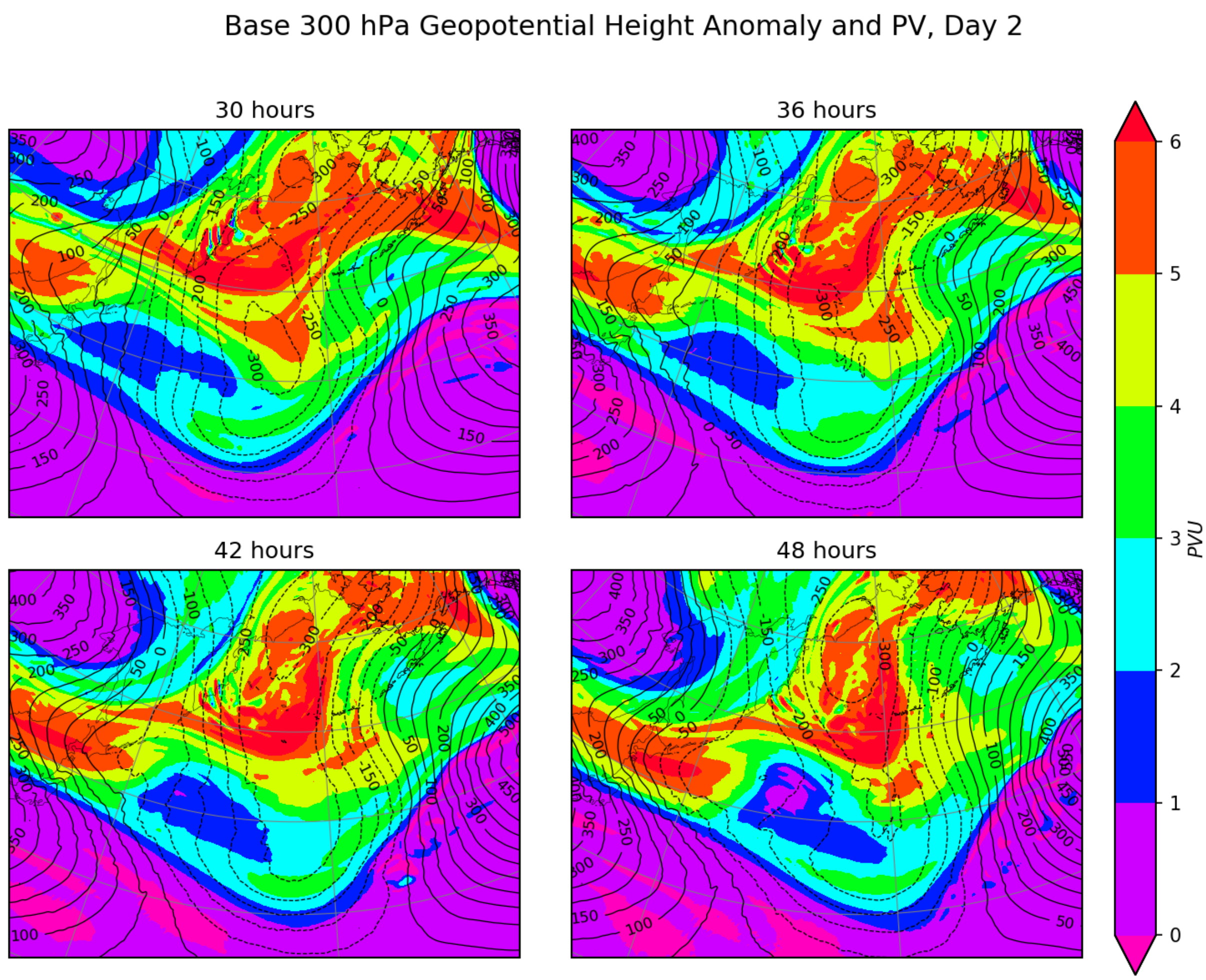

Figure 5.30: Case 1 Base 300 hPa Geopotential Height Anomaly and PV, Day 2. Contour intervals are 50 gpm for height anomaly and 1 PVU for PV.

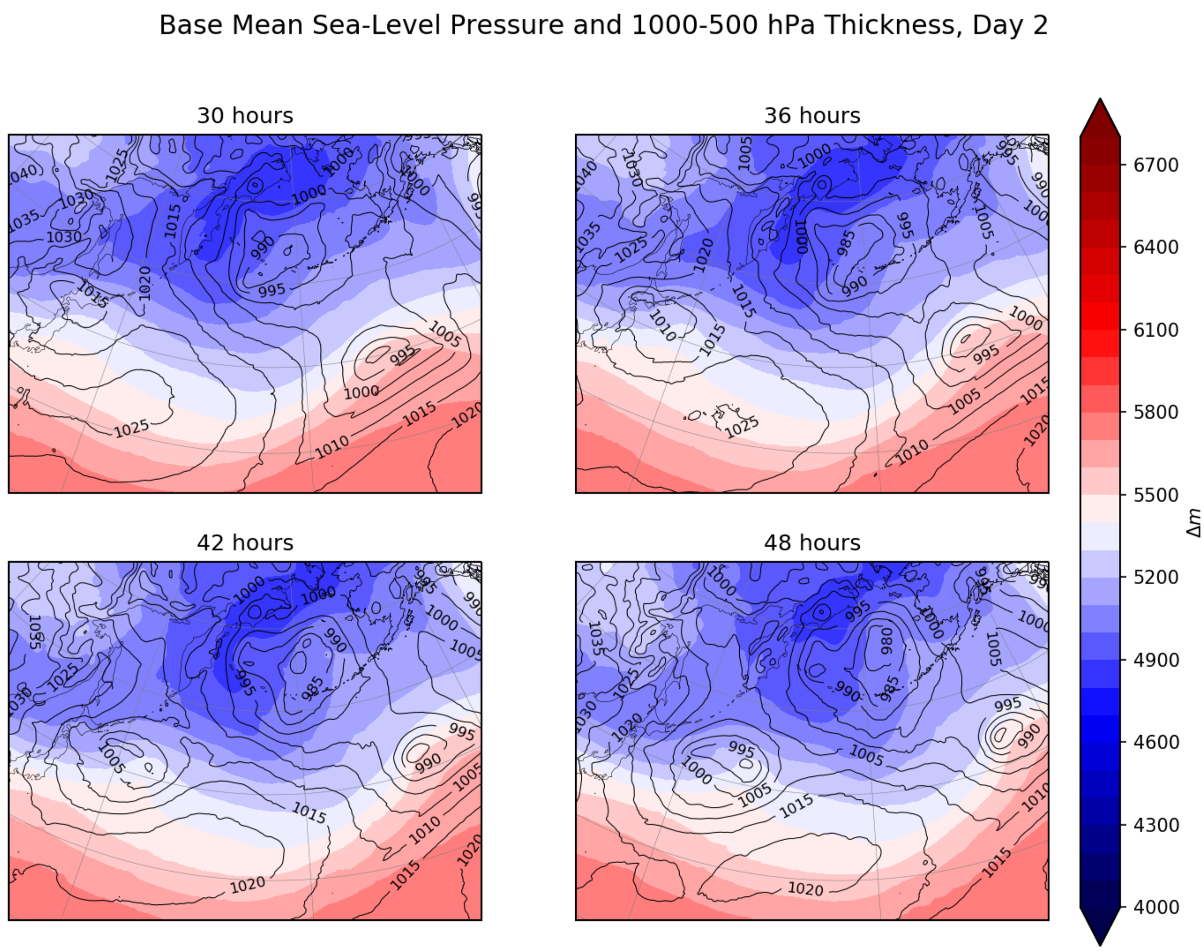

Figure 5.31: Case 1 Base Mean Sea-Level Pressure and 1000-500 hPa Thickness, Day 2. Contours are 5 hPa for pressure and 10m for thickness.

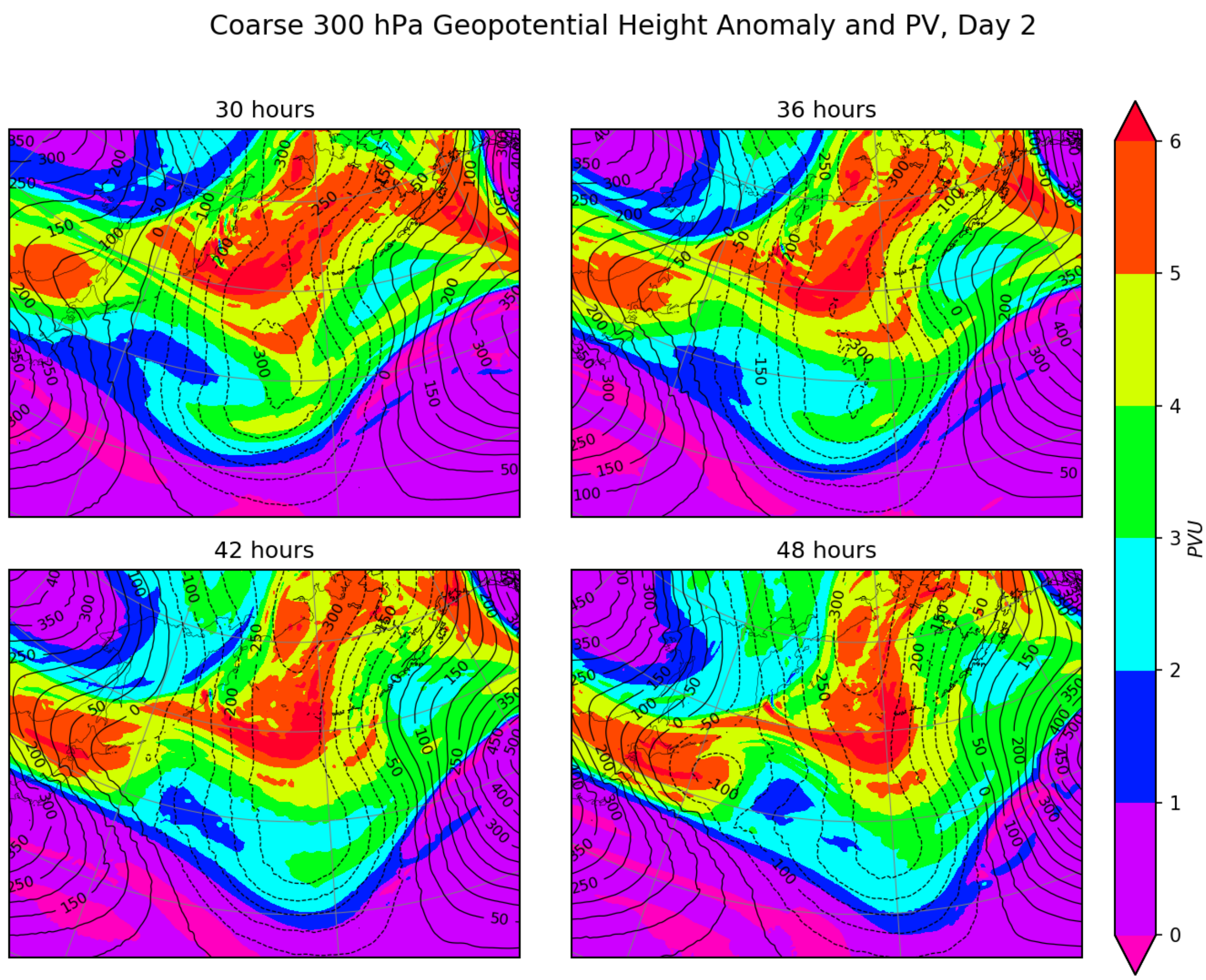

Figure 5.32: Case 1 Coarse 300 hPa Geopotential Height Anomaly and PV, Day 2. Contour intervals are 50 gpm for height and 1 PVU for PV.

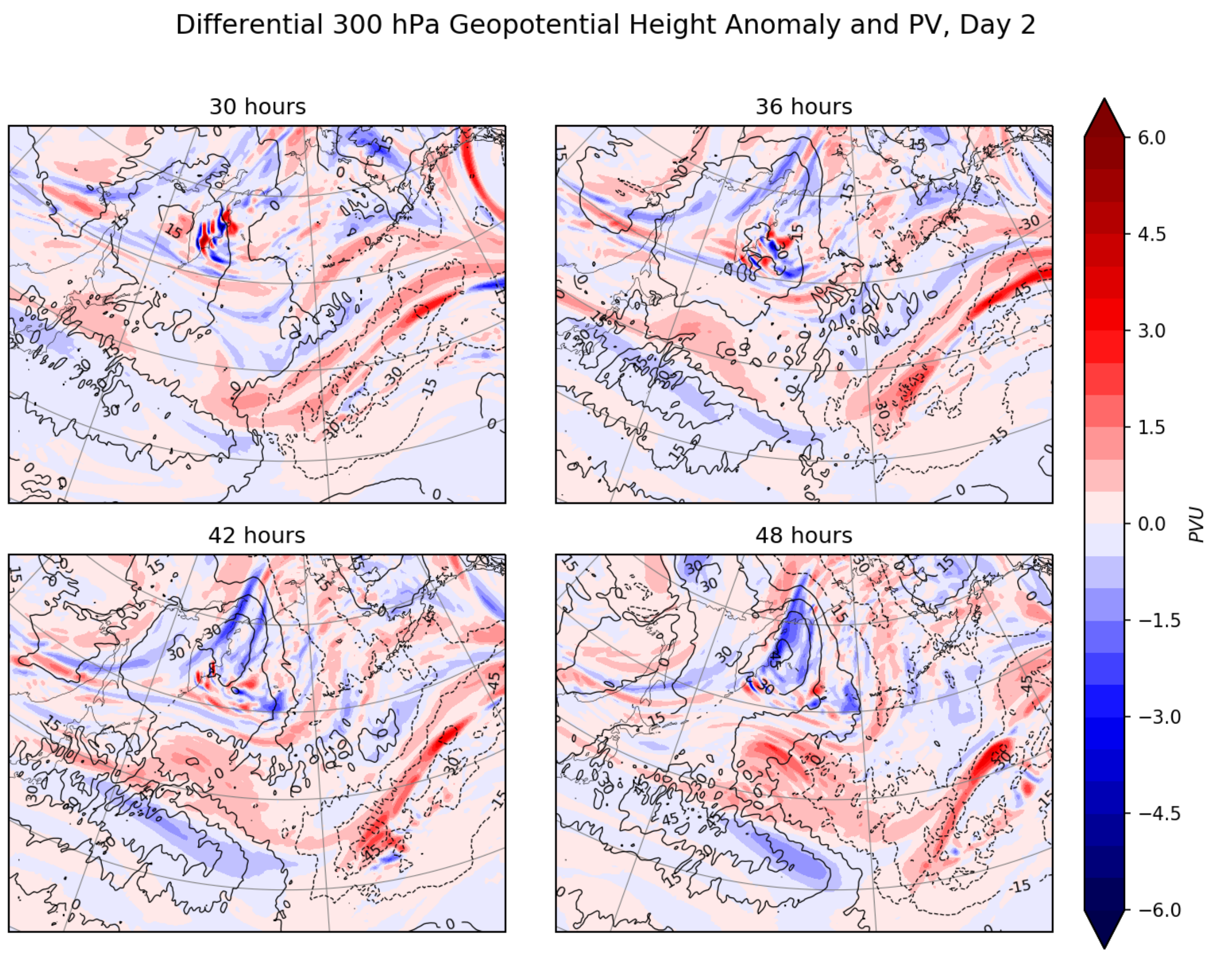

Figure 5.33: Case 1 Differential 300 hPa Geopotential Height Anomaly and PV, Day 2. Contour intervals are 15 gpm for differential height and 0.5 PVU for differential PV.

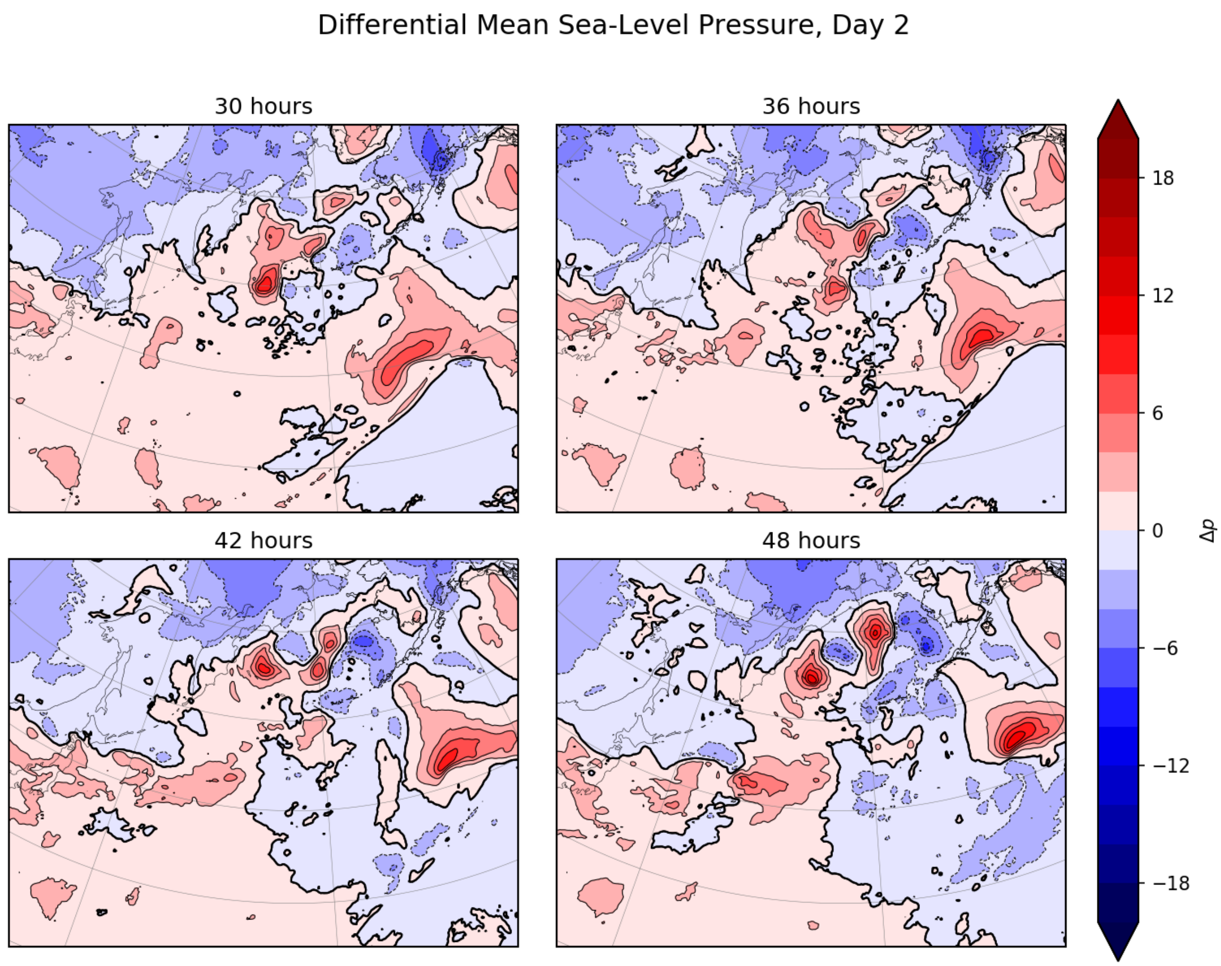

Figure 5.34: Case 1 Differential Men Sea-Level Pressure, Day 2. Contour intervals are 2 hPa with the 0 hPa line bolded.

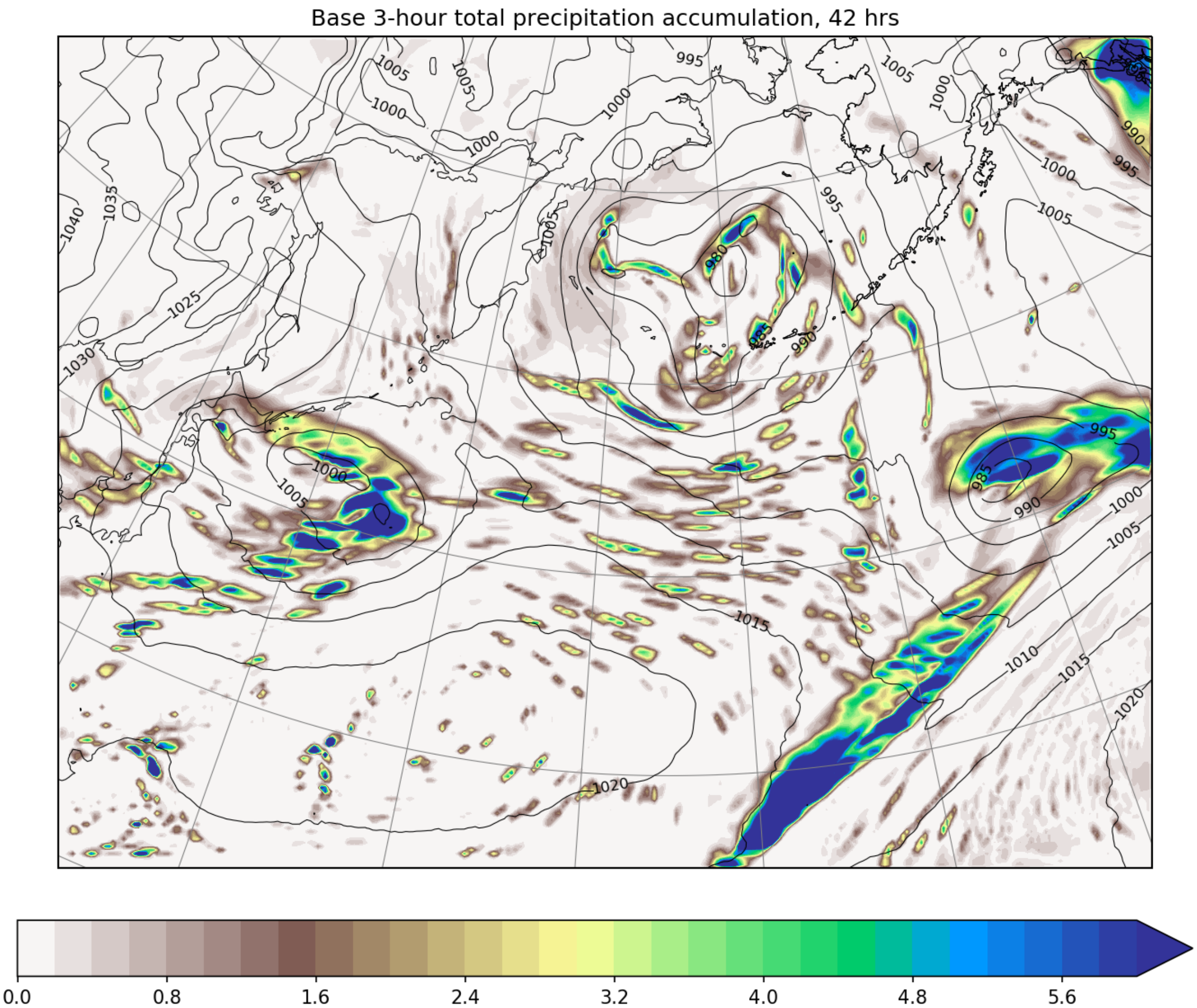

Figure 5.35: Case 1 Base 3-hour Total Precipitation Accumulation at 42 Hours. Units are mm.

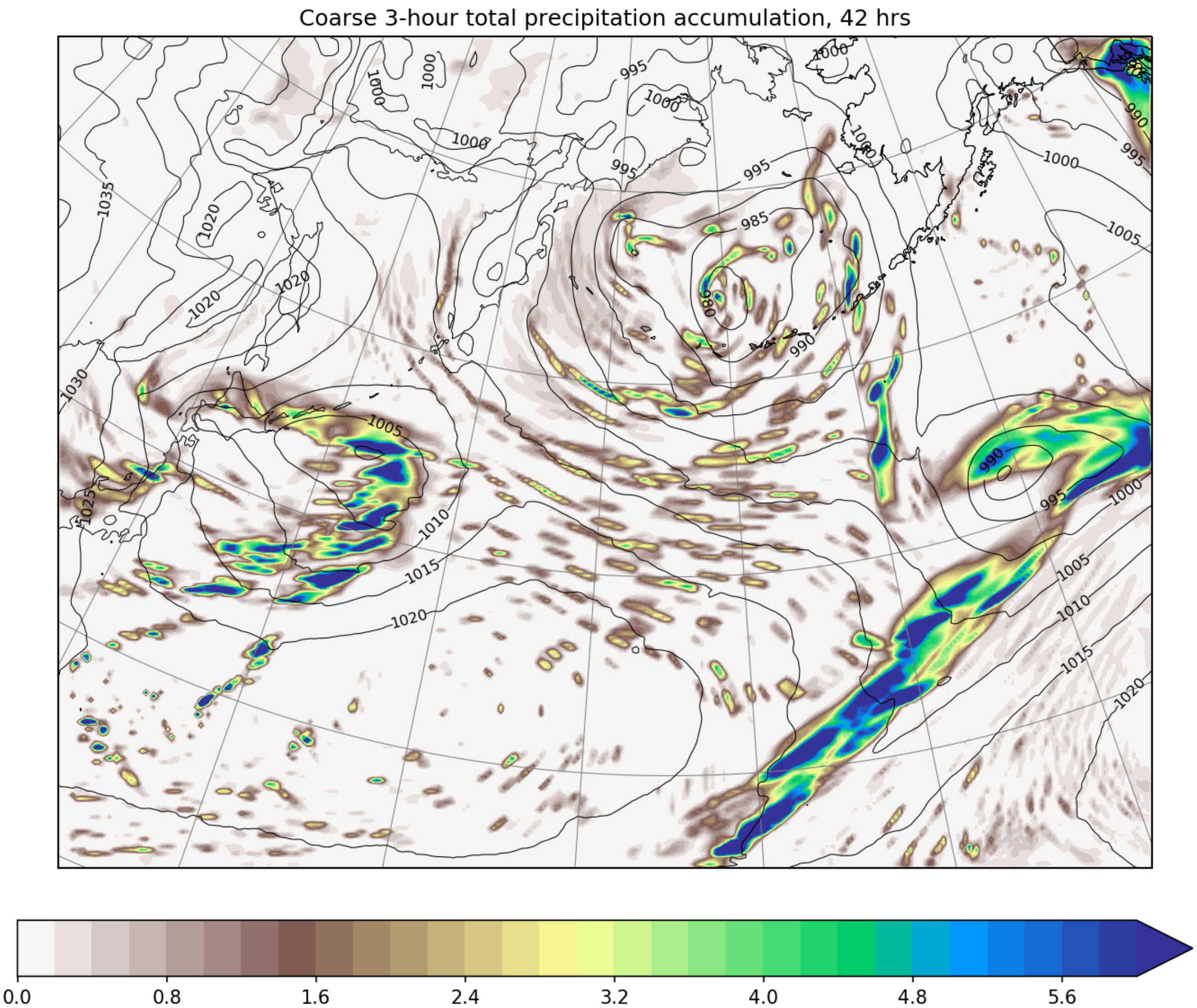

Figure 5.36: Case 1 Coarse 3-hour Total Precipitation Accumulation at 42 Hours. Units are mm.

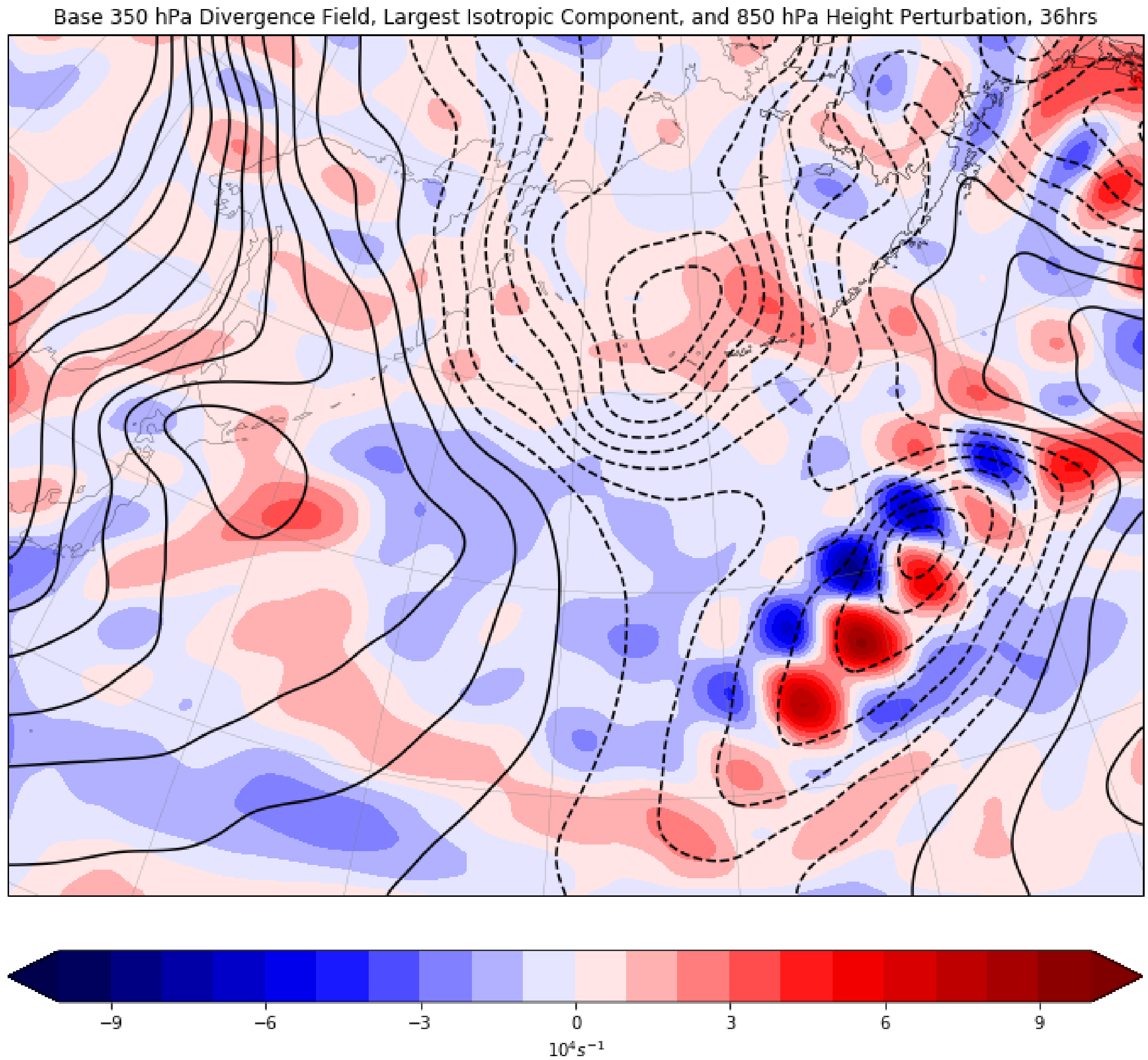

Figure 5.37: Case 1 Base 350 hPa Divergence (filled), Largest Isotropic Spectral Component, and 850 hPa Height Anomaly (contours) at 36 Hours. Intervals are 10^{-4} s^{-1} for divergence and 20 gpm for height.

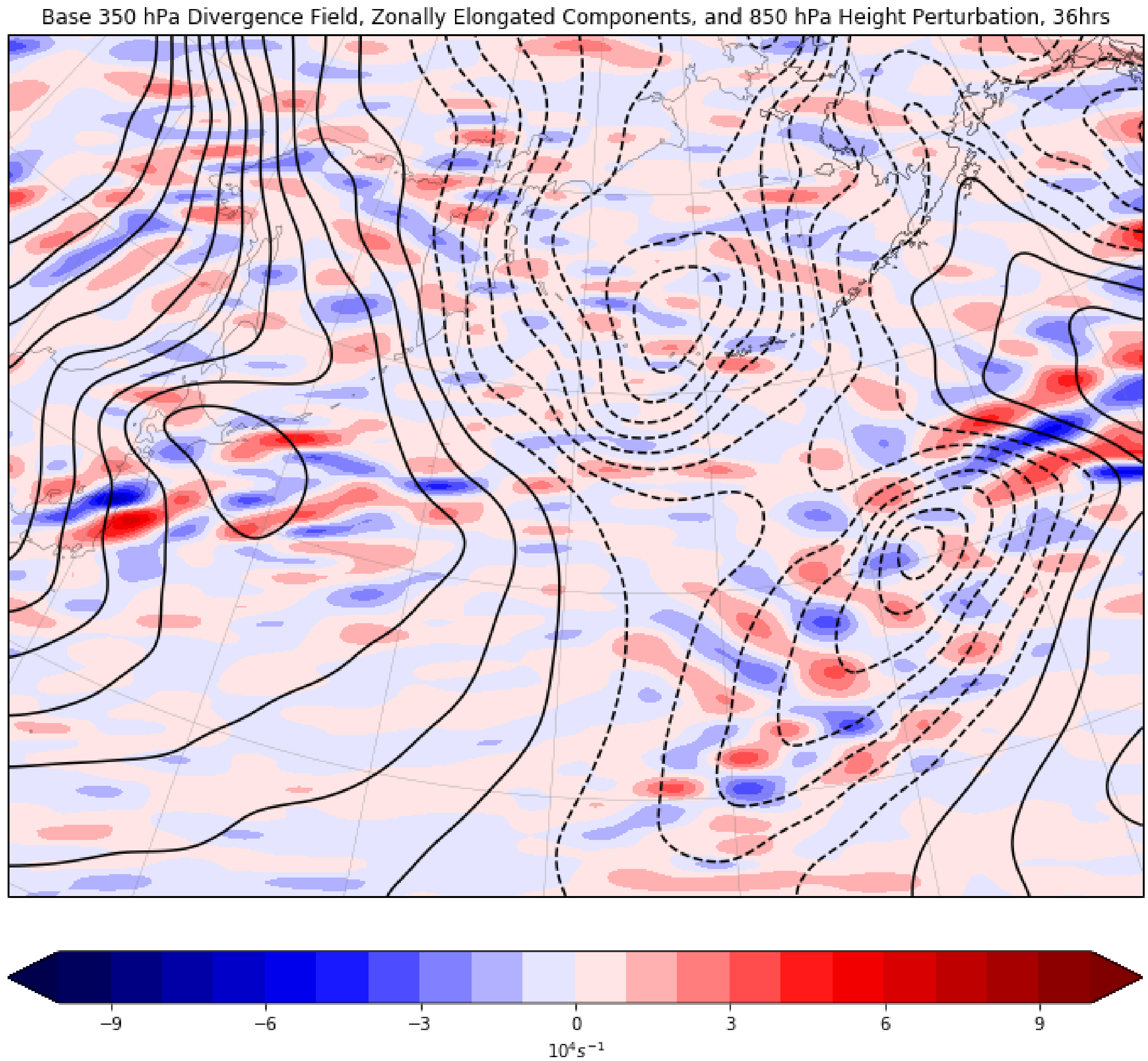

Figure 5.38: Case 1 Base 350 hPa Divergence (filled), Zonally Elongated Spectral Components, and 850 hPa Height Anomaly (contours) at 36 Hours. Intervals are 10^{-4} s^{-1} for divergence and 20 gpm for height.

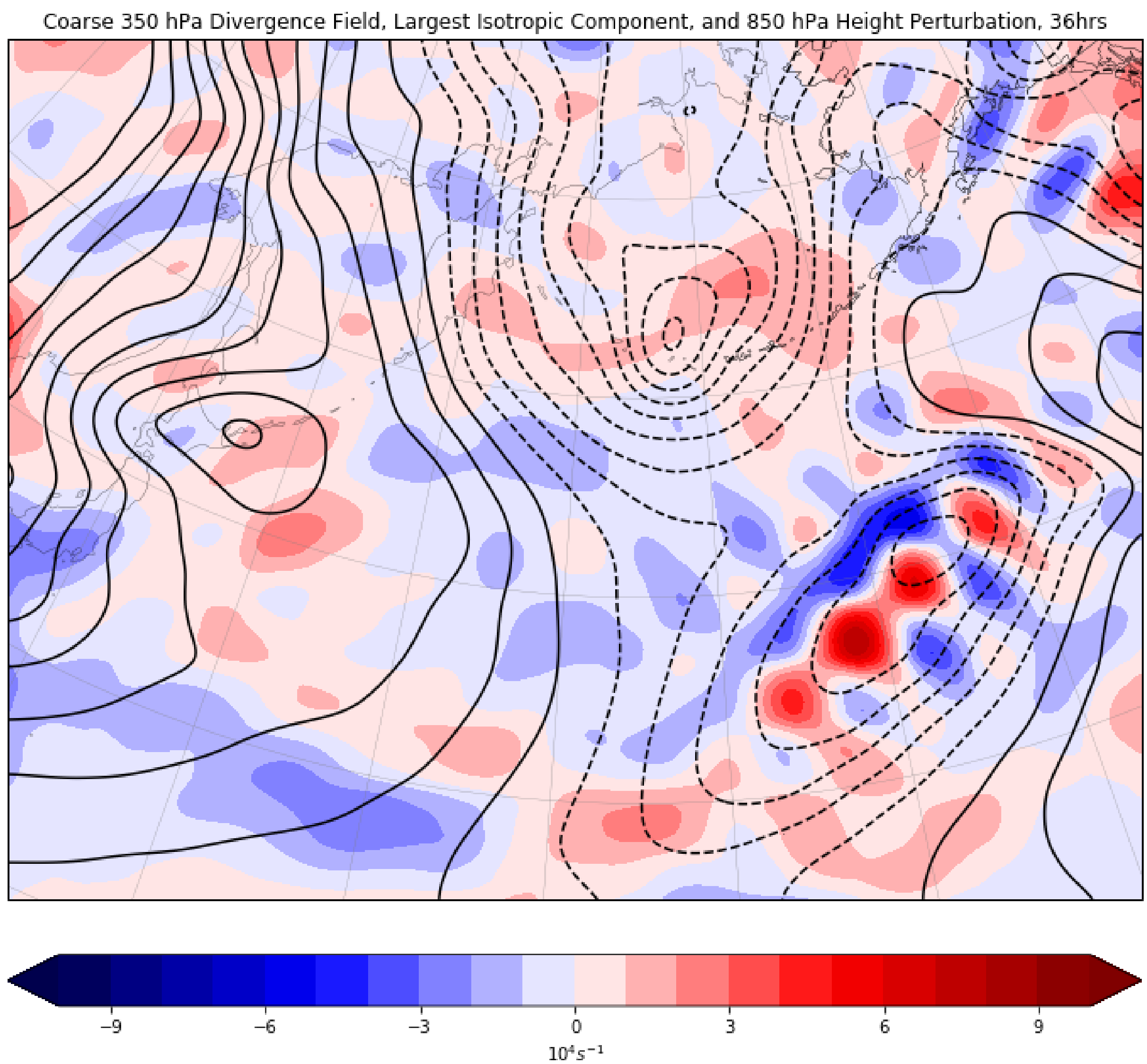

1271

1272 Figure 5.39: Case 1 Base 350 hPa Divergence (filled), Largest Isotropic Spectral Component, and 850 hPa

1273 Height Anomaly (contours) at 36 Hours. Intervals are 10^{-4} s^{-1} for divergence and 20 gpm for height.

1274

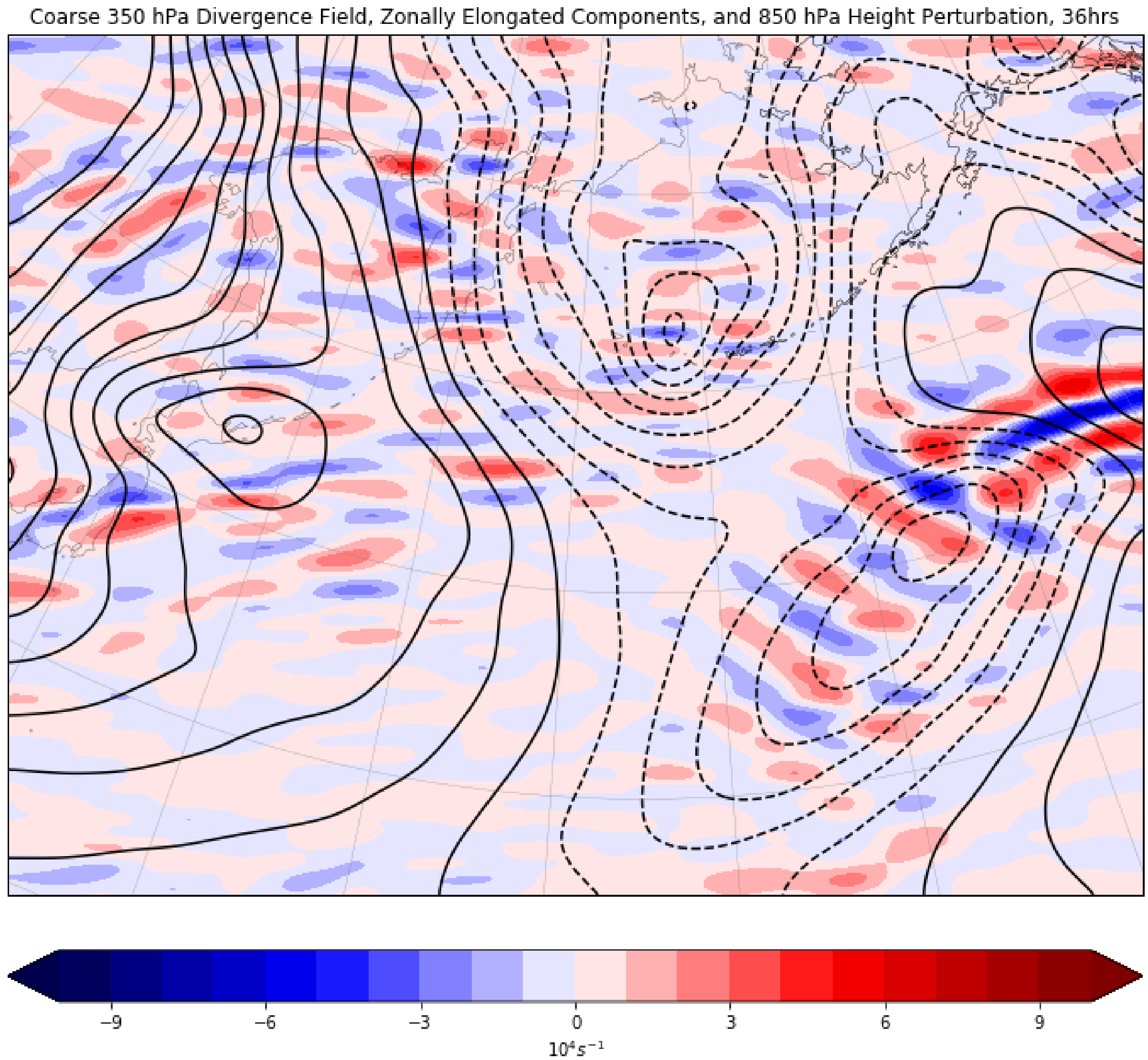

Figure 5.40: Case 1 Base 350 hPa Divergence (filled), Zonally Elongated Spectral Components, and 850 hPa Height Anomaly (contours) at 36 Hours. Intervals are 10^{-4} s^{-1} for divergence and 20 gpm for height.

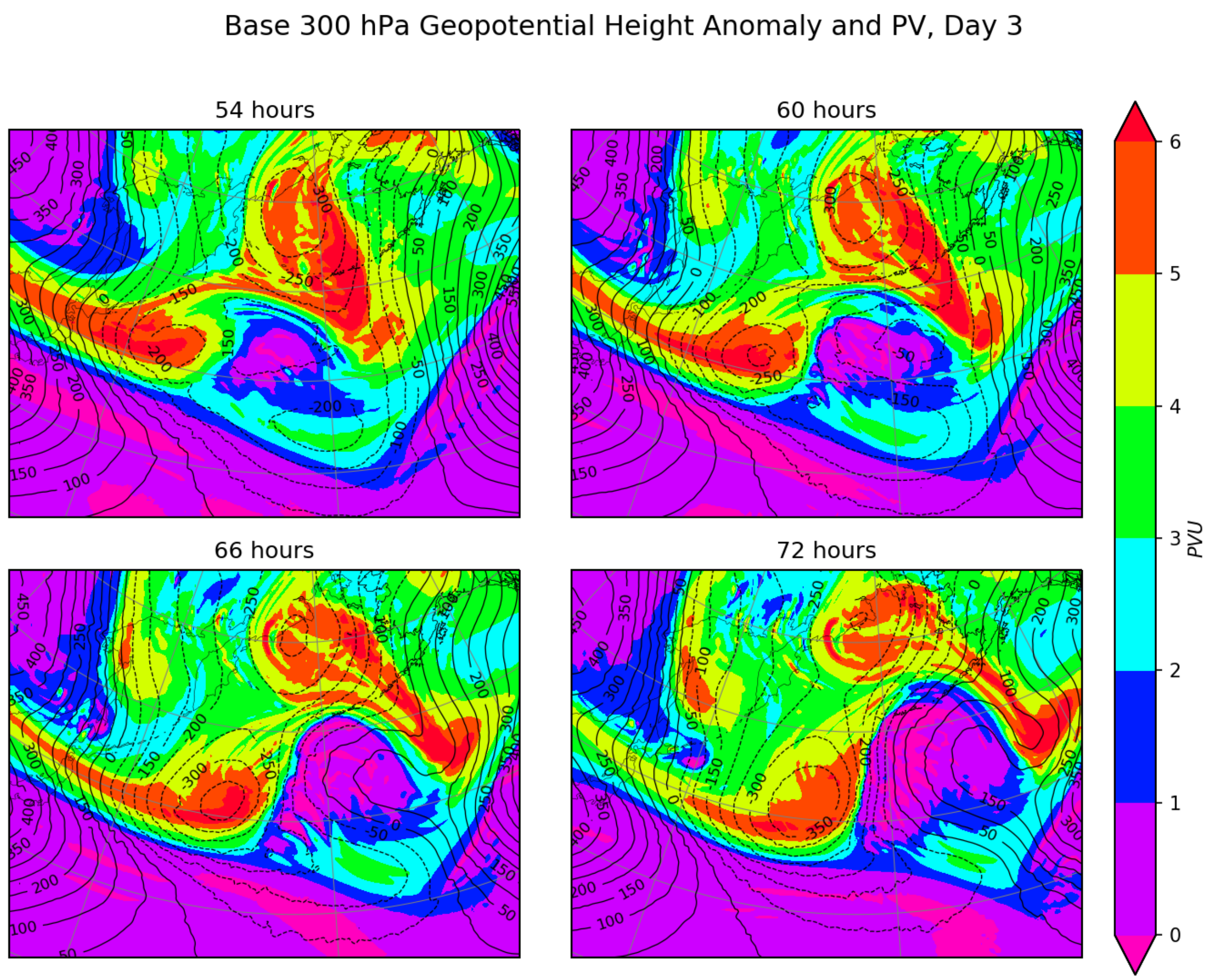

Figure 5.41: Case 1 Base 300 hPa Geopotential Height Anomaly and PV, Day 3. Contours are 50 gpm for height and 1 PVU for PV.

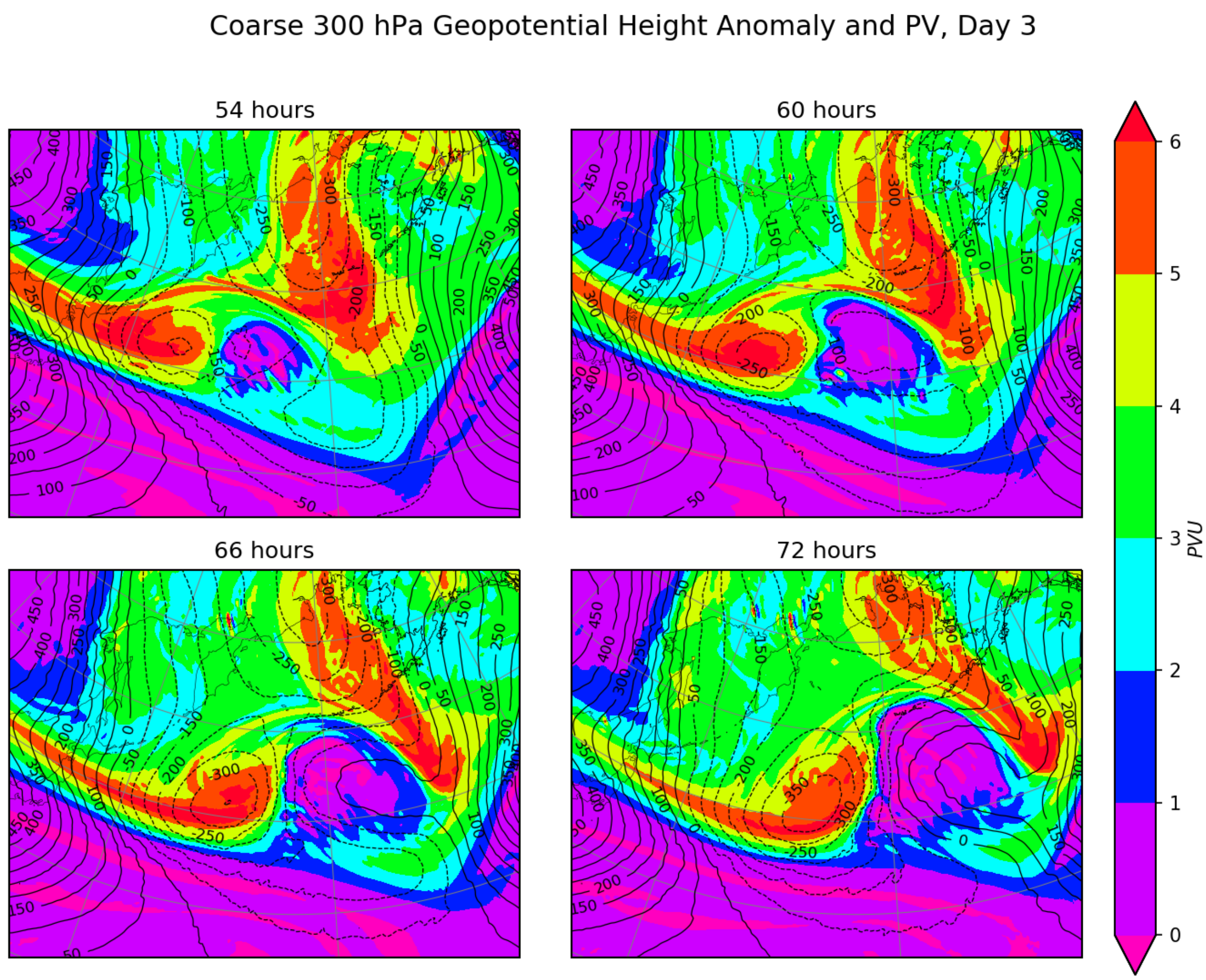

Figure 5.42: Case 1 Coarse 300 hPa Geopotential Height Anomaly and PV, Day 3. Contours are 50 gpm for height and 1 PVU for PV.

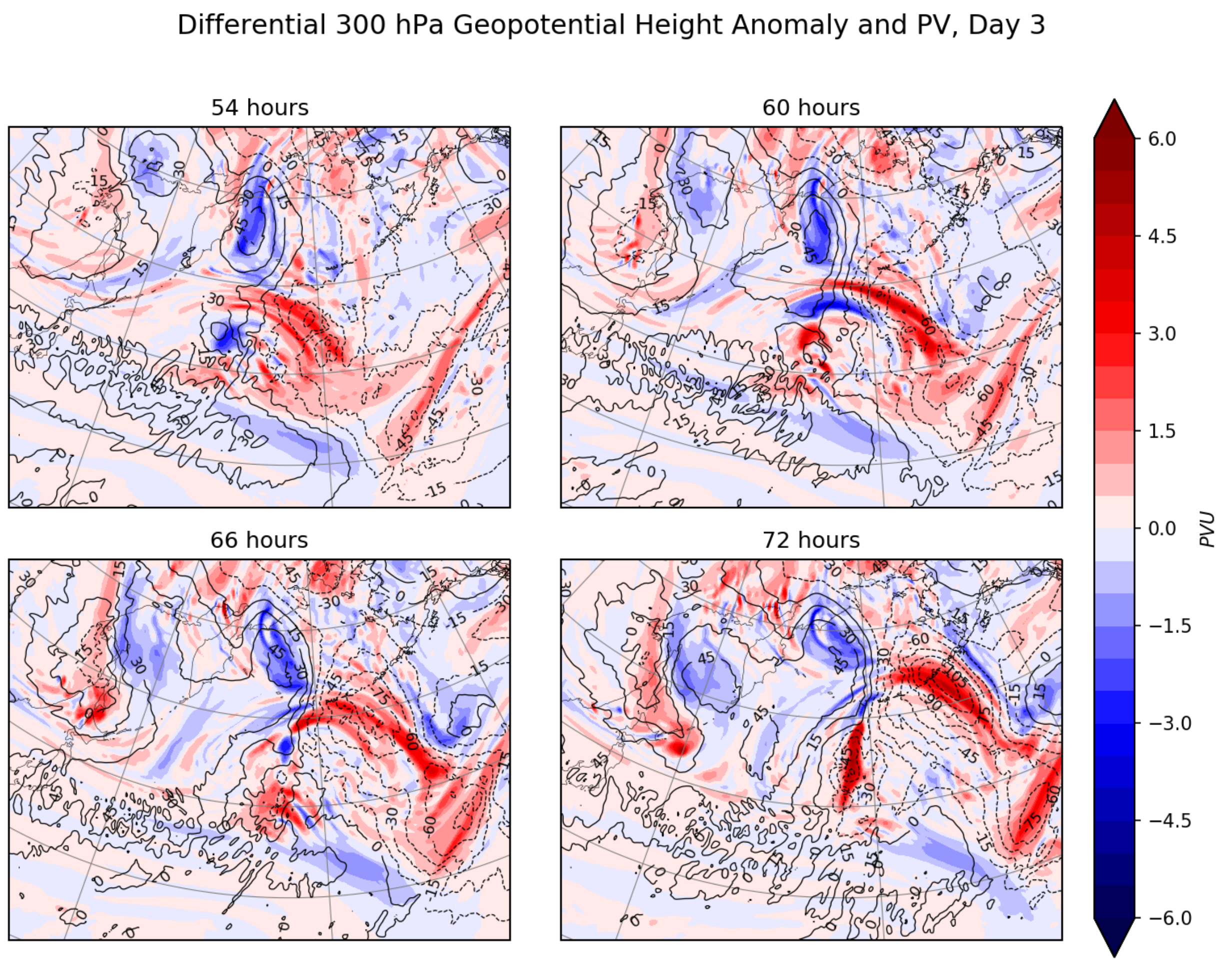

Figure 5.43: Case 1 Differential 300 hPa Geopotential Height Anomaly and PV, Day 3. Contours are 15 gpm for differential height and 0.5 PVU for PV.

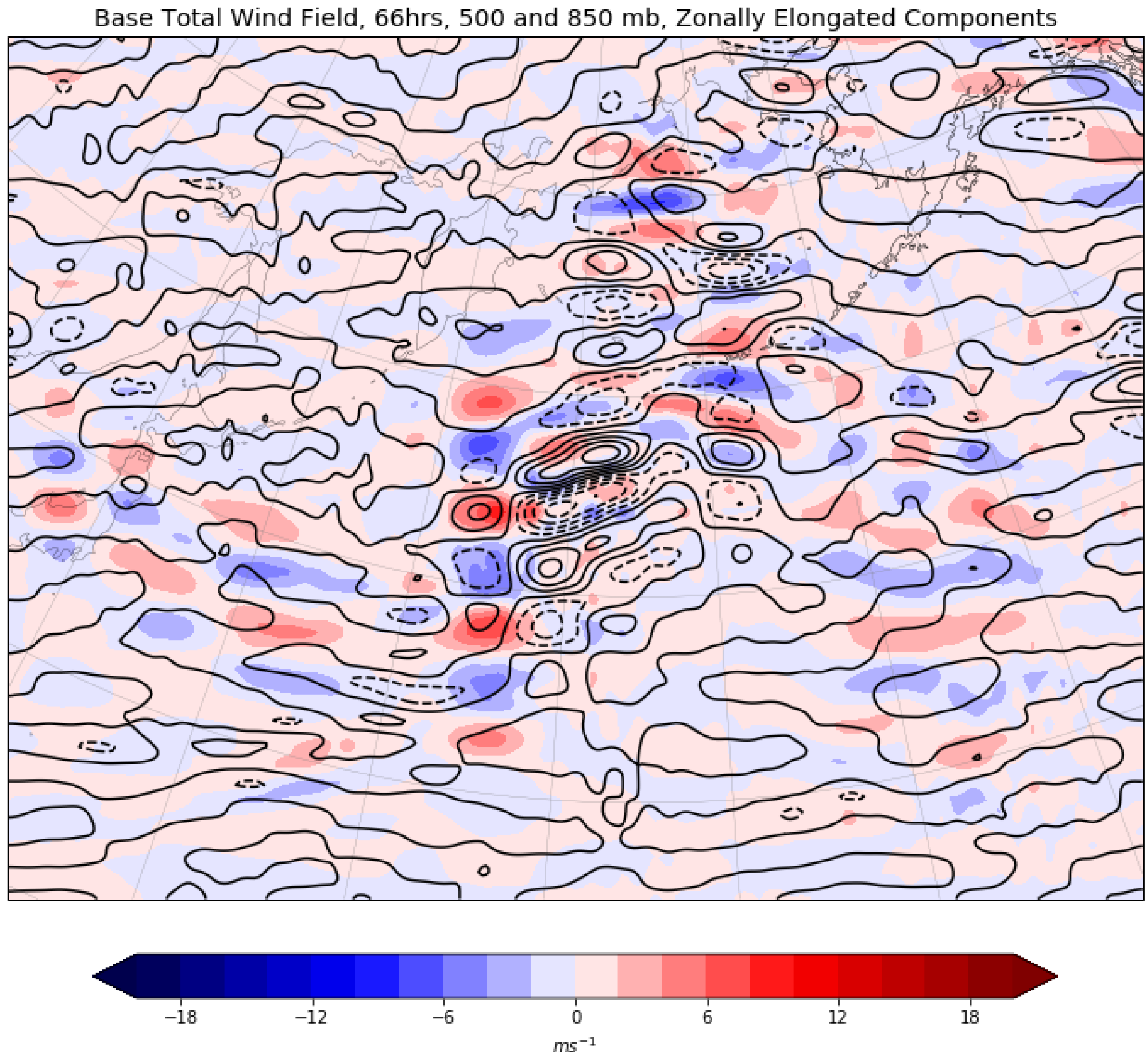

Figure 5.44: Case 1 Base Total Wind at 500 (filled) and 850 hPa (contours), Zonally Elongated Spectral Components. Contours are 2 ms^{-1}.

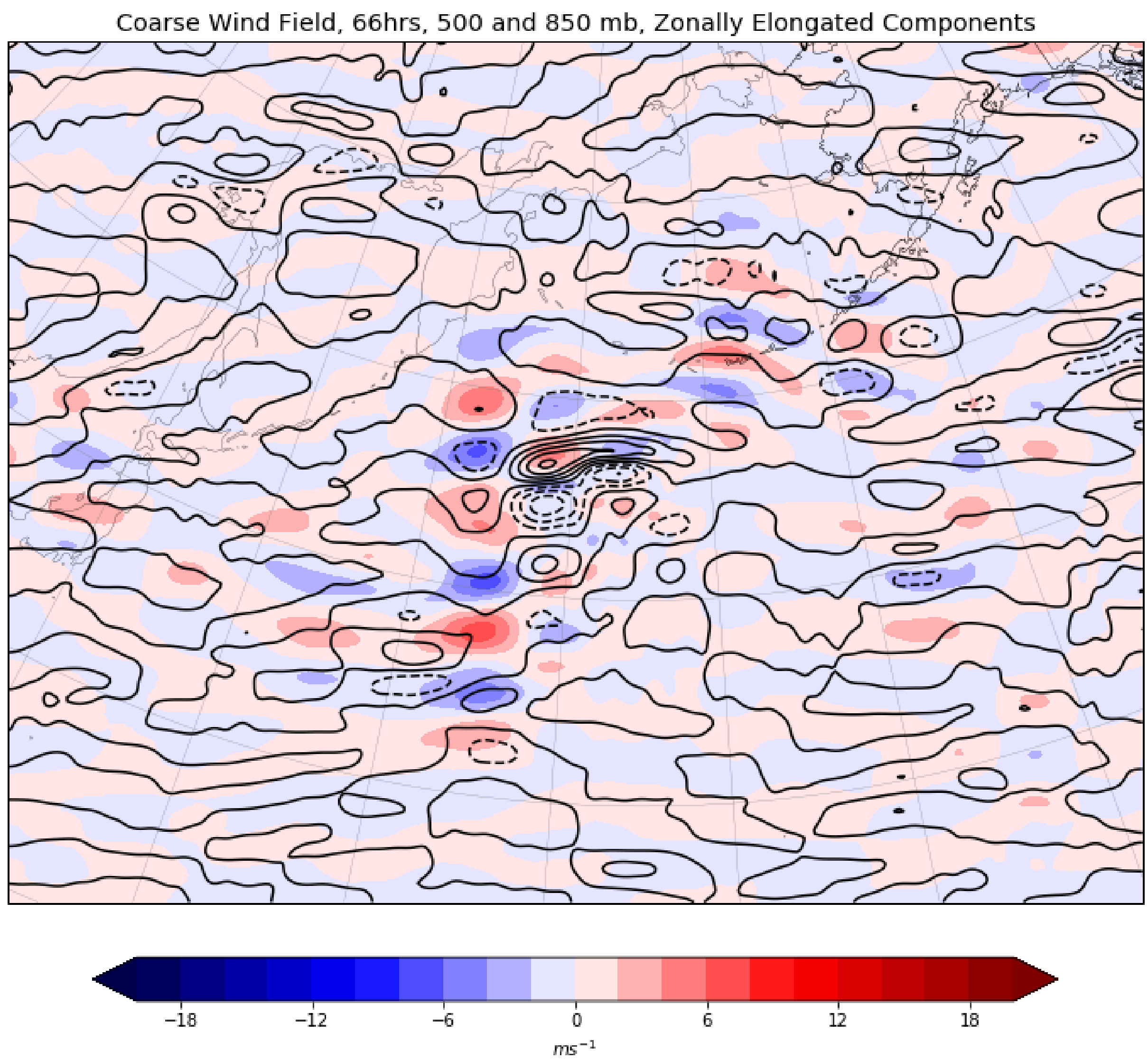

Figure 5.45: Case 1 Coarse Total Wind at 500 (filled) and 850 hPa (contours), Zonally Elongated Spectral Components. Contours are 2 ms^{-1}.

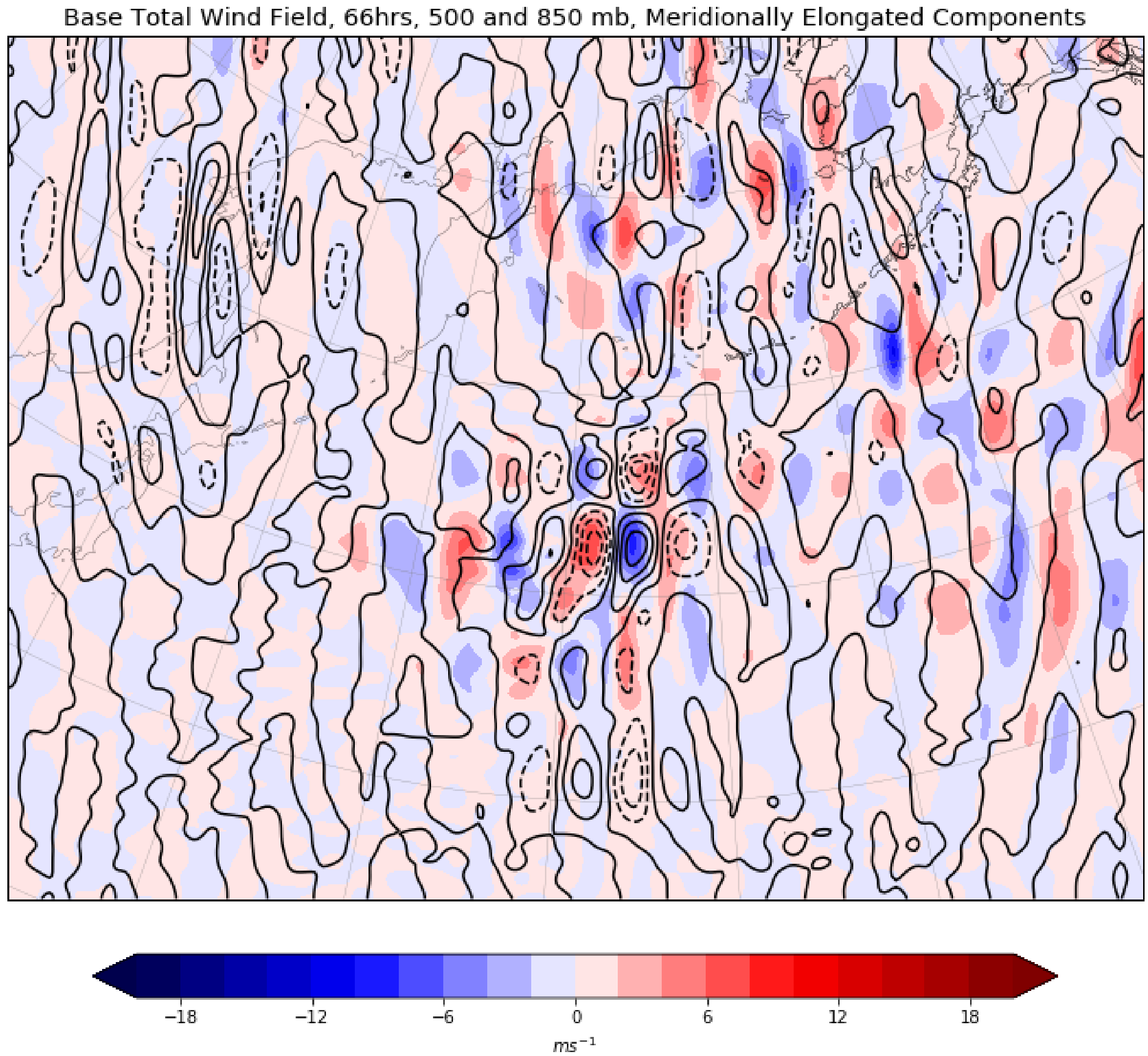

Figure 5.46: Case 1 Base Total Wind at 500 (filled) and 850 hPa (contours), Meridionally Elongated Spectral Components. Contours are 2 ms^{-1}.

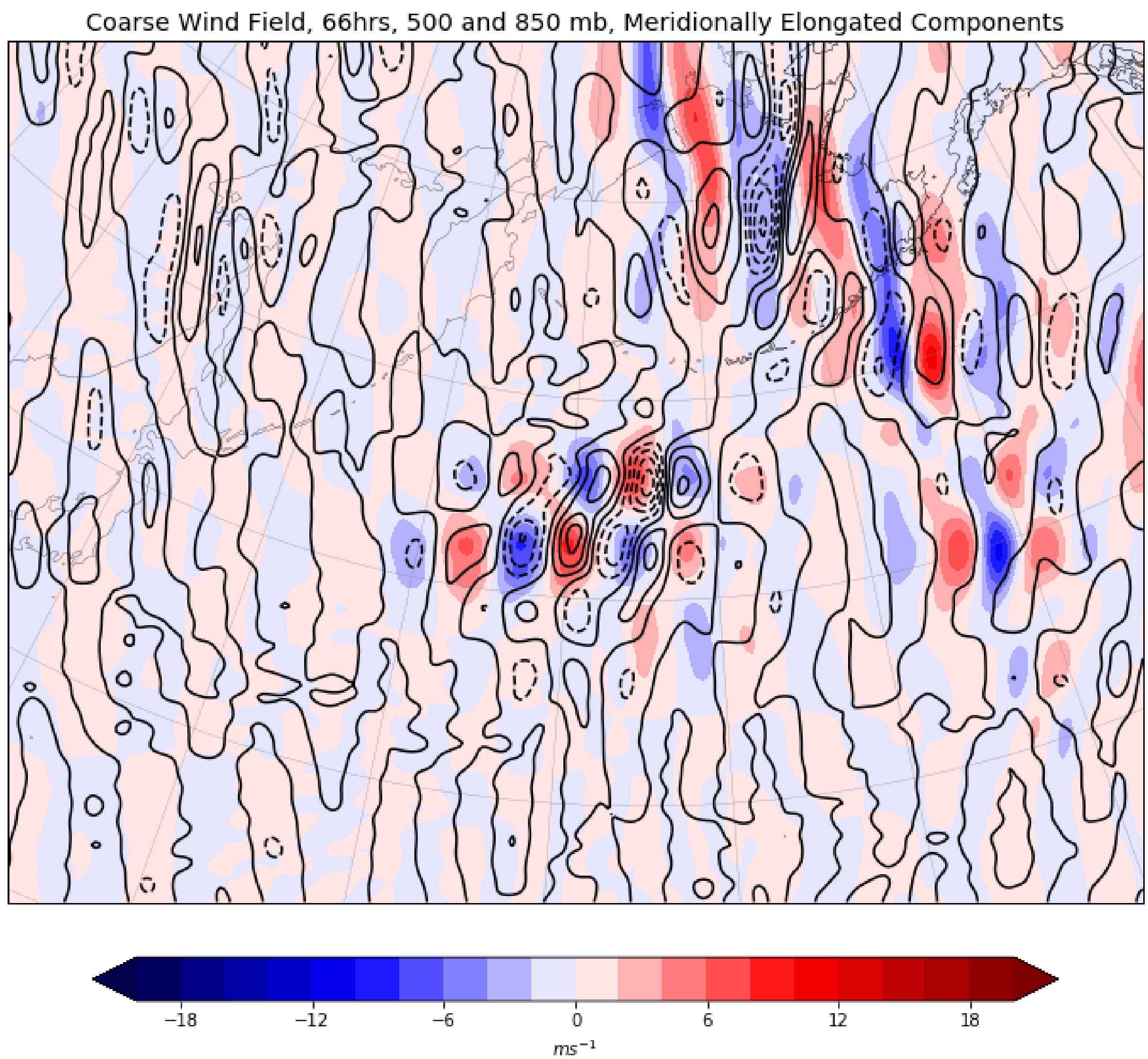

1303

1304 Figure 5.47: Case 1 Coarse Total Wind at 500 (filled) and 850 hPa (contours), Meridionally Elongated Spectral

1305 Components. Contours are 2 ms^{-1}.

1306

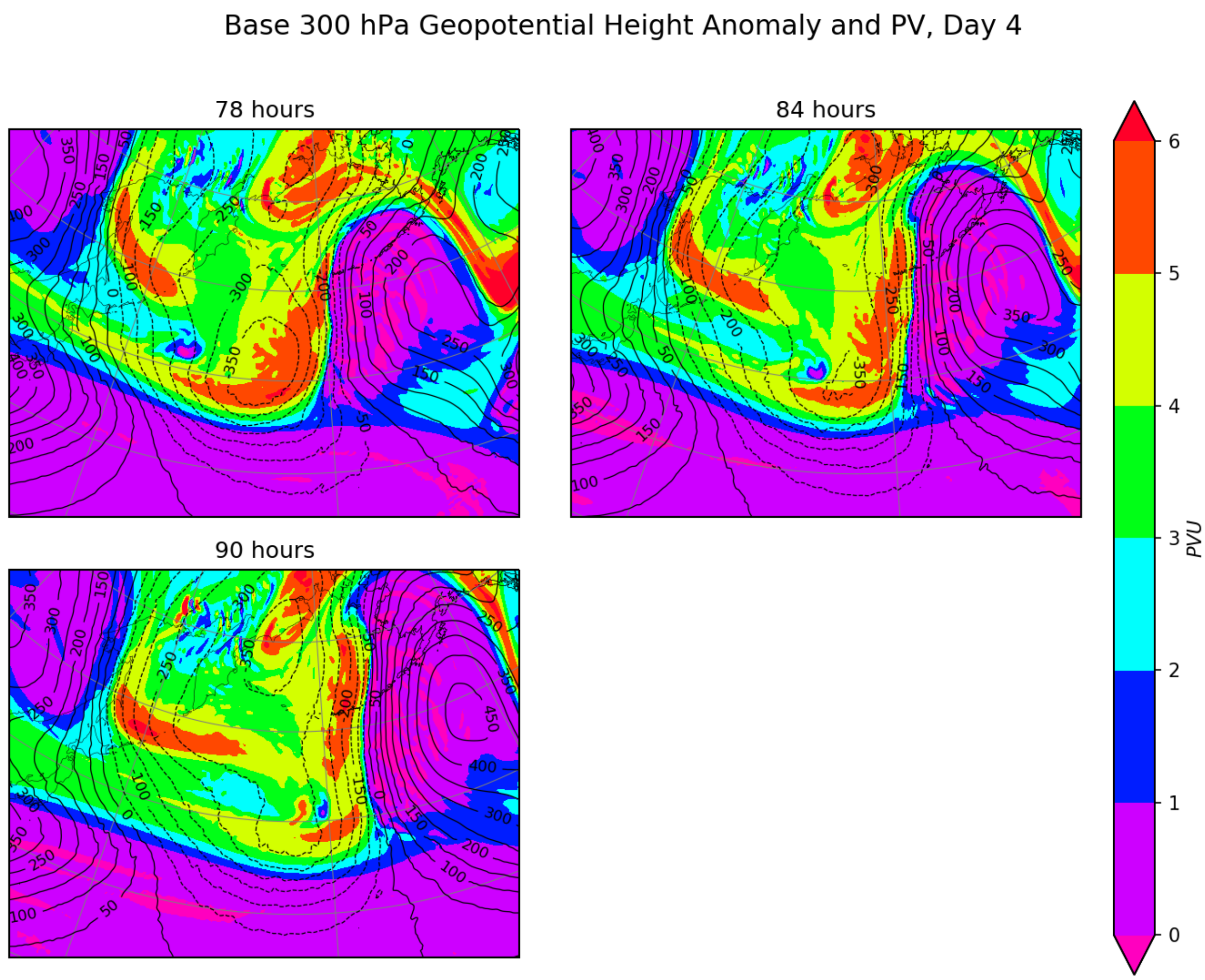

Figure 5.48: Case 1 Base 300 hPa Geopotential Height Anomaly and PV, Day 4. Contours are 50 gpm for height and 1 PVU. for PV

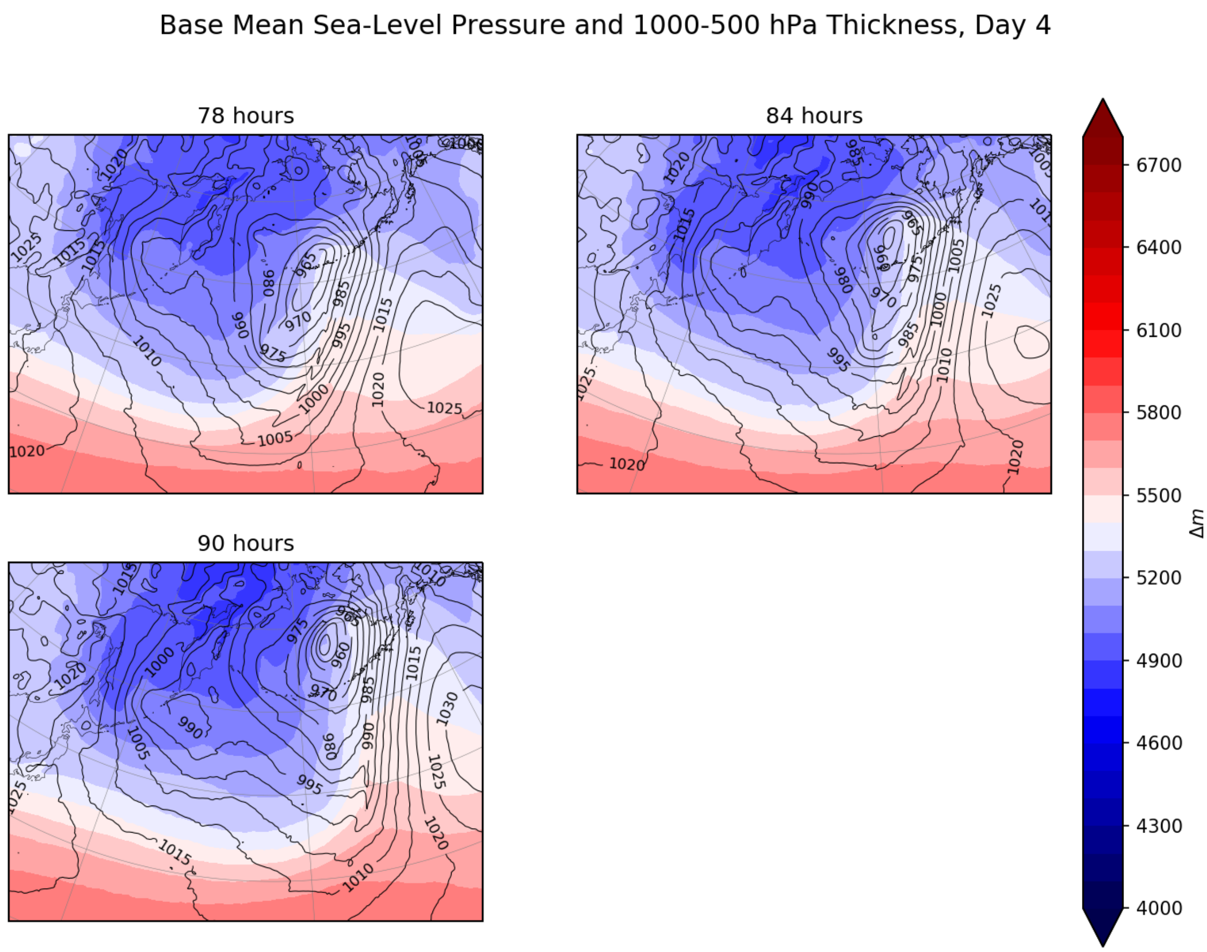

Figure 5.49: Case 1 Base Mean Sea-Level Pressure and 1000-500 hPa Thickness, Day 4. Contours are 5 hPa for pressure and 100 m for thickness.

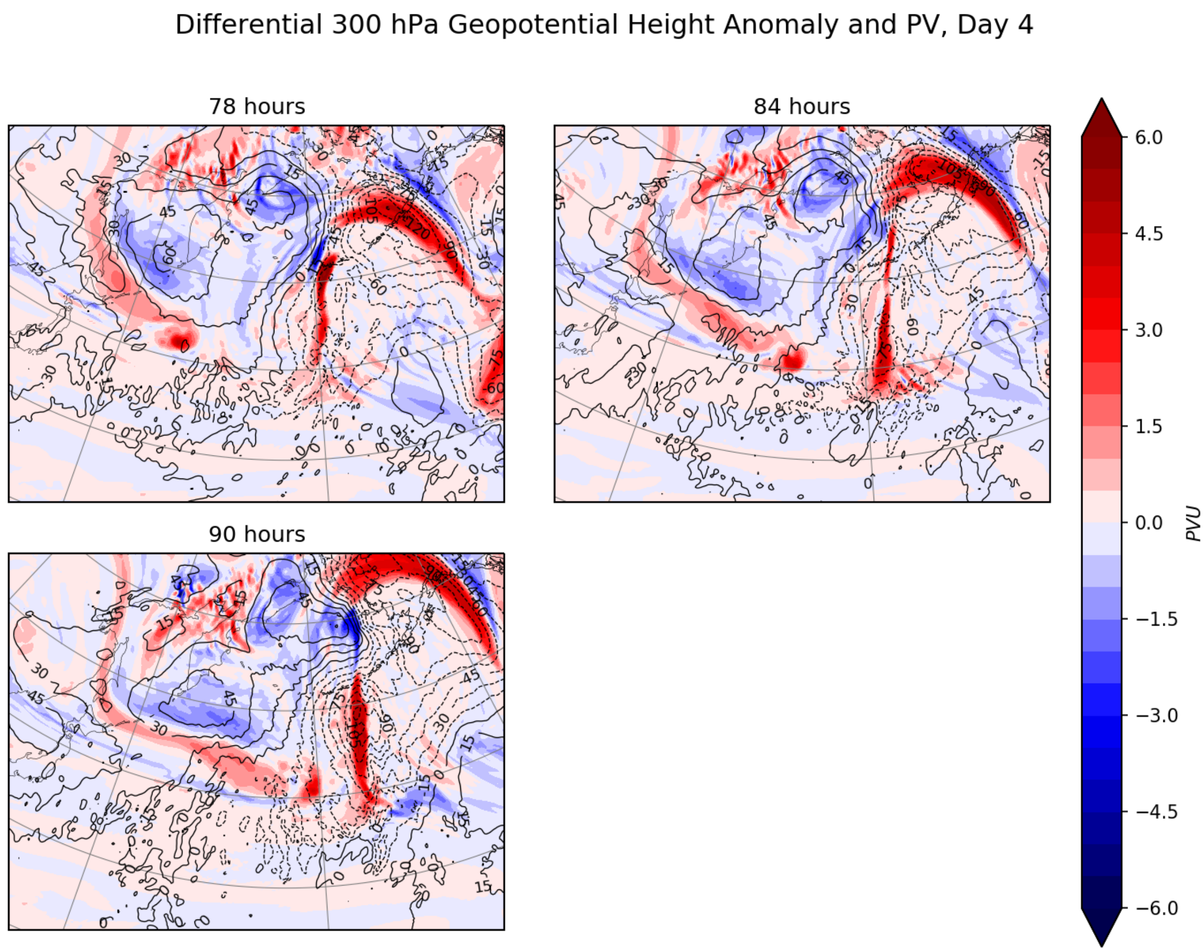

Figure 5.50: Case 1 Differential 300 hPa Geopotential Height Anomaly and PV, Day 4. Contours are 15 gpm for differential height and 0.5 PVU for differential PV.

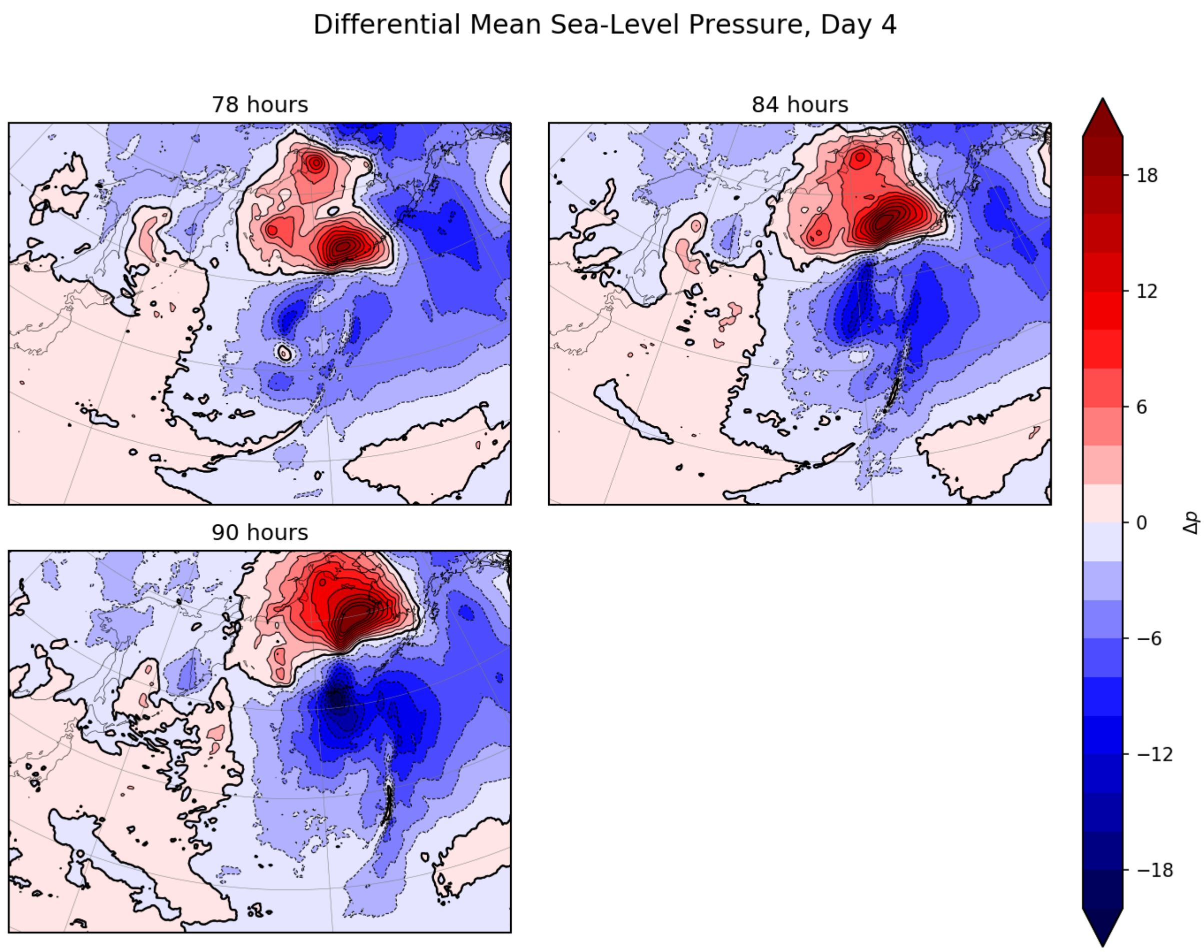

Figure 5.51: Case 1 Differential Mean Sea-Level Pressure, Day 4. Contour intervals are 2 hPa and the 0 hPa contour is bolded.

CHAPTER VI

CASE 2: APRIL 2014

While Chapter 5 provided a physical view of the energy cascade in both directions with a focus on direct causal mechanisms from constituent spatial bands, Chapters 6 and 7 will be focused more on the perturbations themselves and how the filtering affects their generation and propagation. Synoptic diagnosis will still be used for the framework of the chapters, but the conclusions will stem more from the statistics and mesoscale analysis than the synoptic.

6.1 Synoptic Diagnosis

Figure 6.1 depicts the 300 hPa geopotential height perturbations and PV field for the base simulation inner domain at its initialization and for the next three days at 12-hour intervals. The inner domain is dominated by a single, large-scale trough with an associated PV maximum over southern Canada. The PV trough has already broken by the time of the inner domain initialization, and as a result there is a separated PV maximum that extends equatorward into the Four Corners region. The southern extent of the PV anomaly is partially ejected from the central PV body and is still connected by a filament of PV through Wyoming. This filament and extrusion never completely separate from the main PV body, instead traveling around the geopotential height trough and re-entering the main body of the wave. The wave moves across eastern CONUS and becomes more strongly filamented due to deformation and anticyclonic breaking. The outer domain at 48 hours (Figure 6.2) shows the overall structure of the feature: a vortex-like geopotential height minimum with multiple filamented breaks along the outer edges—the southernmost extending into the inner domain and the westernmost moving toward it. By 78 hours (Figure 6.3), the height trough has reshaped into a broad height anomaly of -200 gpm over central CONUS with a latitudinal depth that extends to northern Mexico; the PV anomaly at this time is comprised of a combination of PV in the outer domain advecting back into the inner domain and new PV entering the domain from the Aleutian Islands. Figure 6.3 depicts the same fields as that of 6.1, but for the final 3 days of the simulation. As the new PV anomaly travels across CONUS, it too experiences distortion, eventually breaking cyclonically. The breaking is most prominent after 126 hours, at which point the PV debris has overturned clockwise about the height minimum over eastern CONUS. This is in contrast to Case 1, which is largely a single upper-level trough that exists in the inner domain for the entire simulation.

The 24-hourly base MSLP and 1000-500 hPa thickness (Figure 6.4, 6.5) shows that there are three low pressure systems that develop in the inner domain. A weak front is present over the Midwest at initialization, associated with the 300 hPa low, and propagates along with it over the course of the first day. A second low, an Alberta Clipper, moves in from western Canada after 30 hours and deepens concurrently with the second 300 hPa trough. This low remains in the inner domain for several days, moving across the Upper Midwest and exiting the inner domain toward the Canadian Shield after hour 78. The remnants of the upper-level, post-breaking PV debris help intensity a surface low after 102 hours, which pushes across the southern Appalachian Mountains by the end of the simulation. Such surface lows are common during the winter and early spring, and typically produce large swaths of thunderstorms that can inject energy into the atmosphere at small spatial scales.

6.2 Cluster Analysis

The k-means clusters for Case 2 are shown in Figure 6.6. Unlike Case 1, there is no cluster showing an energy state with both isotropic, synoptic scale wind perturbation energy and zonally elongated synoptic-scale energy; there is, however, one cluster—cluster four—which contains isotropic synoptic-scale and highly meridionally elongated synoptic energies. This is the only cluster that represents an above ensemble mean energy partition at the domain-wide synoptic scale. Cluster one is a good example of an excited cluster first mentioned in Chapter 5, where there is above ensemble mean partition energy most or all nodes. Cluster two is a low energy cluster, containing near-mean zonally elongated energy but well-below mean energy everywhere else. Cluster three is a near mean state, with mesoscale energy that is near the zonal mean, but is probably better identified as a lack of perturbation energy along the meridionally elongated synoptic scales than energy at the mesoscales. Cluster five is also near the mean state, but whereas cluster three has very weak meridionally elongated synoptic scale energy, cluster five has very weak zonally elongated synoptic scale energy. Finally, cluster six is a mesoscale-excited state, with higher than ensemble mean energy at all mesoscale nodes but lacking energy at the largest scales.

With these clusters in mind, we look first at the P_n^* time series for the base (Figure 6.7) and coarse (Figure 6.8) simulations. Before getting into the specific differences between the associated clusters for each simulation, there are a few trends in the energy partition plots that are worth noting—some expected and some not. First is that, like Case 1, there is a lack of small-scale energy in both the base and coarse simulations at initialization that is rapidly eliminated, and the coarse simulation small-scale nodes have less energy than their corresponding nodes in the base simulation. However, the energy partitions at initialization are not as far below the ensemble mean in Case 2 as in Case 1. The meridionally elongated nodes spend the first 2 days above the ensemble mean for both simulations. Both simulations experience a significant drop in node energy between 50 and 60 hours before all the nodes trend back up and peak around 100 hours. The two simulations then diverge strongly, with the base simulation experiencing another high amplitude peak before total decline in energy while the coarse just declines.

The base and coarse D_k are plotted in Figures 6.9 and 6.10, respectively. As expected, there is an overall reduction of total D_k during the first 6 hours or so in both models, and the coarse simulation D_k is larger than the base initially. Cluster two sees a large increase soon after initialization along with cluster three. This is consistent with both simulations spending most of the first 24 hours associated with clusters four, five, or six—all excited meridional clusters with weak zonally elongated perturbation energy. The simulations both start in a highly meridional post-breaking state, and a transition of perturbation energy from large-scale synoptic down to the meridionally elongated and isotropic mesoscales fits is expected.

Surprising, perhaps, is the fact that the coarse simulation is largely identical to the base simulation in terms of its associated clusters and D_k. Both see large reductions in cluster state four D_k around 30 hours and a minimum around 40 hours. Both experience a cluster transition to cluster two around 50 hours which peaks between 55 and 60 hours. It's not until hour 75—when the simulation energy state of the base simulation transitions to more closely resemble cluster five and the coarse simulation does not—that the cluster identifications differ for a prolonged period. This raises a couple of questions that bear investigation before looking into the simulation differences at 75 hours: does small-scale variability prior to hour 75 form or propagate similarly between both simulations, and how do differences in this variability produce the subsequent differing energy states, if they do?

We start by considering the column-integrated enstrophy. The integrated enstrophy for the base simulation at 42 hours during the first distortion minimum is shown in Figure 6.11. Most of the enstrophy is associated with the large-scale, deformed upper-level trough mentioned briefly in Section 6.1. Very small-scale enstrophy associated with the Rocky Mountains does not contribute strongly to the larger enstrophy envelopes. The coarse simulation at the same time is very similar, with the majority of its column-integrated enstrophy associated with the upper-level trough. Though the two simulations have a maximum in enstrophy in central Kentucky, the enstrophy in the coarse simulation extends farther south than in the base simulation. On the whole, however, the two are remarkably similar at this point and differential small-scale variability caused by the filter is limited to broadly weaker enstrophy in the coarse simulation.

During the transition between clusters five and three at 54 hours, the two simulations begin to differ in a minor way that will set up major differences in both their energy perturbations and dynamical states later in the simulations. The differential precipitation at 54 hours (Figure 6.12) shows a region over the Wyoming/South Dakota border where the coarse simulation precipitation is much higher. Persistent heavier precipitation in the coarse simulation results in destruction of PV aloft and the generation of a new PV gradient. The coarse simulation 300 hPa height and PV field (Figure 6.13) at 54 hours shows this: unlike the base simulation at 54 hours, the coarse simulation has developed a PV hole, and the advection of the nearby PV maximum is affected. Six hours later, more PV is drawn equatorward by the resulting flow than in the base simulation (Figure 6.13, 66 and 78 hours). Accumulation of PV along the tongue after 66 hours continues through the end of day three, where more PV is ejected out of the wave in the coarse simulation than the base.

The mesoscale variability is also impacted by the introduction of the PV hole at 54 hours. Figure 6.14 depicts the enstrophy of the two simulations at 60 hours. There is a strong maximum over Nebraska and South Dakota with a broad, curved region over the northern Great Plains. In the coarse simulation, the maximum is still along the Nebraska/South Dakota border, but the shape of the smoothed enstrophy is more discontinuous, as several local maxima are present that do not exist in the base simulation. An effect of the continued different precipitation patterns (Figure 6.15) is seen in the 500 hPa/vorticity difference fields (Figure 6.16), where most of the differences over the Northern Plains manifest at the smallest spatial scales. From this, we can say that differential development of precipitation patterns produced a small scall difference in the upper-level PV, which then lead to significant differences between the mesoscale variance of the two simulations and eventually the assignment to two different clusters.

Next, we look at hour 78, where the base simulation transitions to an energy state described by cluster five while the coarse simulation does not. The enstrophy at this time is shown in Figure 6.17. The base simulation has two major enstrophy maxima over Texas and Wisconsin and a weak enstrophy feature stretching down along the Rocky Mountains. The coarse simulation maxima are both farther west than in the base simulation. The shapes of the maxima and the various filaments in the coarse simulation are narrower and more zonally aligned in comparison to the base simulation as well. The 300 hPa waves are slightly out of phase (Figure 6.18), and the coarse simulation has a much deeper southern extent in its geopotential height minimum. It's seen that, broadly, the coarse simulation has less enstrophy than the base simulation, but it has larger peak enstrophy maxima. Like Case 1, the development of a new PV gradient is a direct consequence of the latent heat release, and in Case 2, regions of nonzero enstrophy preceded the development of heavy precipitation. The differences in the enstrophy maxima seem to be a significant enough trigger for differences in the two simulations' development.

The following 40 hours are defined by cluster states one and six, clusters that describe both simulations, but part of what we want to know now is why the coarse simulation does not experience two separate spikes in D_k and P_n^* as the base does. From Figure 6.18 we see there is a substantial difference in the southern extent of the 300 hPa trough and PV fields.

In the coarse simulation there is already wave breaking occurring, as evidenced by the ejection of PV material out of the wave (Figure 6.13); this ejection accounts for a large percentage of the southern half of the wave's PV. In both simulations, there is a broad region of convective rainfall across north Texas and Oklahoma at 102 hours (Figure 6.20) when the base simulation has been assigned cluster six again and the two simulations are coming down from their peaks in P_n^*, and so we look again to the enstrophy to see the differences in the small-scale variability. The base enstrophy at 102 hours (Figure 6.21) shows there is an enstrophy maximum aligning with the regions of maximum precipitation, with weaker bands of enstrophy aligned across the U.S./Canada border. The coarse simulation's enstrophy shows a larger enstrophy maximum equatorward than the base simulation, and the broad regions of enstrophy in the northern U.S. are significantly weaker. Twelve hours later (Figure 6.22) the base simulation maintains strong perturbations along the overturning PV gradient (Figure 6.19), with several regions of high column-integrated enstrophy within a broad region. The coarse simulation's enstrophy, by contrast, largely dissipates—the separation of the ejected vortical material from the wave prevents continued perturbation growth. Recalling the energy partition time series (Figs. 6.7 and 6.8), this is the cause of the lack of a second peak in perturbation energy in the coarse simulation. There is a stronger equatorward ejection of vortical material in the coarse simulation, which initially produces a strong enstrophy response. This coincides with convective precipitation occurring that is vertically aligned with the coarse 300 hPa PV vortex, and latent heat release underneath foments the diabatic destruction of the 300 hPa PV aloft. The remnants are overturning, which explains the increase in the zonally elongated energy partition nodes in the coarse simulation and the more rapid loss of total perturbation energy after breaking in the coarse simulation. Without a favorable upper- and lower-level tilt between the post-break remnants, the perturbation dissipates.

Eventually, the coarse simulation transitions into a state resembling cluster five after its southern enstrophy extrusion dissipates. It can be seen that there is still some energy at the smaller scales, but that energy is small compared to the base simulation. The base simulation does eventually transition to this energy state as well, but it occurs later and is only a temporary state as the base simulation quickly transitions over to a state described by cluster three. As mentioned in the brief synoptic discussion, the last days of the base simulation are defined by the filaments of vorticity and PV overturning, and the cluster three state most closely resembles the overturning effect as the simulation transitions from meridionally elongated, small-scale features to zonally elongated ones with weak energy compared to the ensemble mean. The coarse simulation, by comparison, undergoes vorticity ejection and overturning much earlier, and this signal is dominated by the energy partition described by cluster six. The two simulations end in different states as a result of the strong difference in their breaking.

Figures

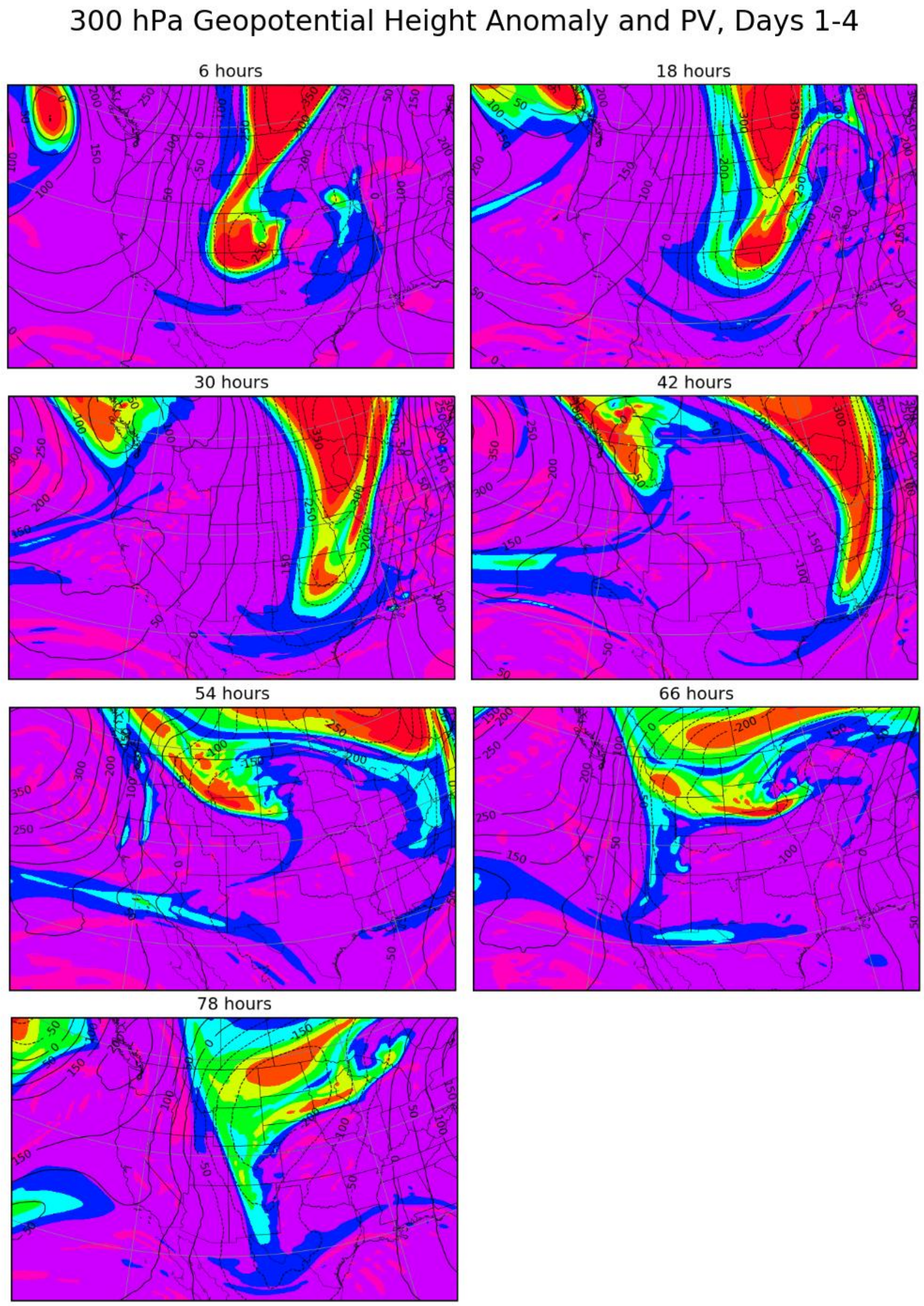

Figure 6.1: Case 2 Base 300 hPa Geopotential Height Anomaly and PV, Days 1-3. Contour intervals for PV are 1 PVU and 50 gpm for height anomaly.

300 hPa Outer Domain Geopotential Height Anomaly and PV, 48 Hours

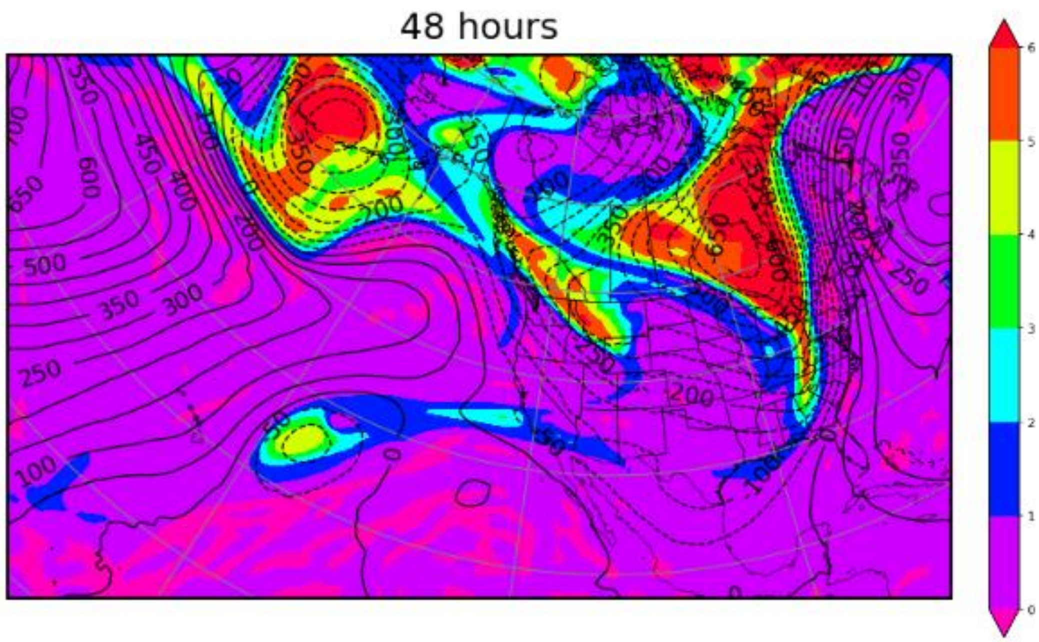

Figure 6.2: Case 2 Base 300 hPa Outer Domain Geopotential Height Anomaly and PV at 48 Hours. Contour intervals are 50 gpm for height and 1 PVU for PV.

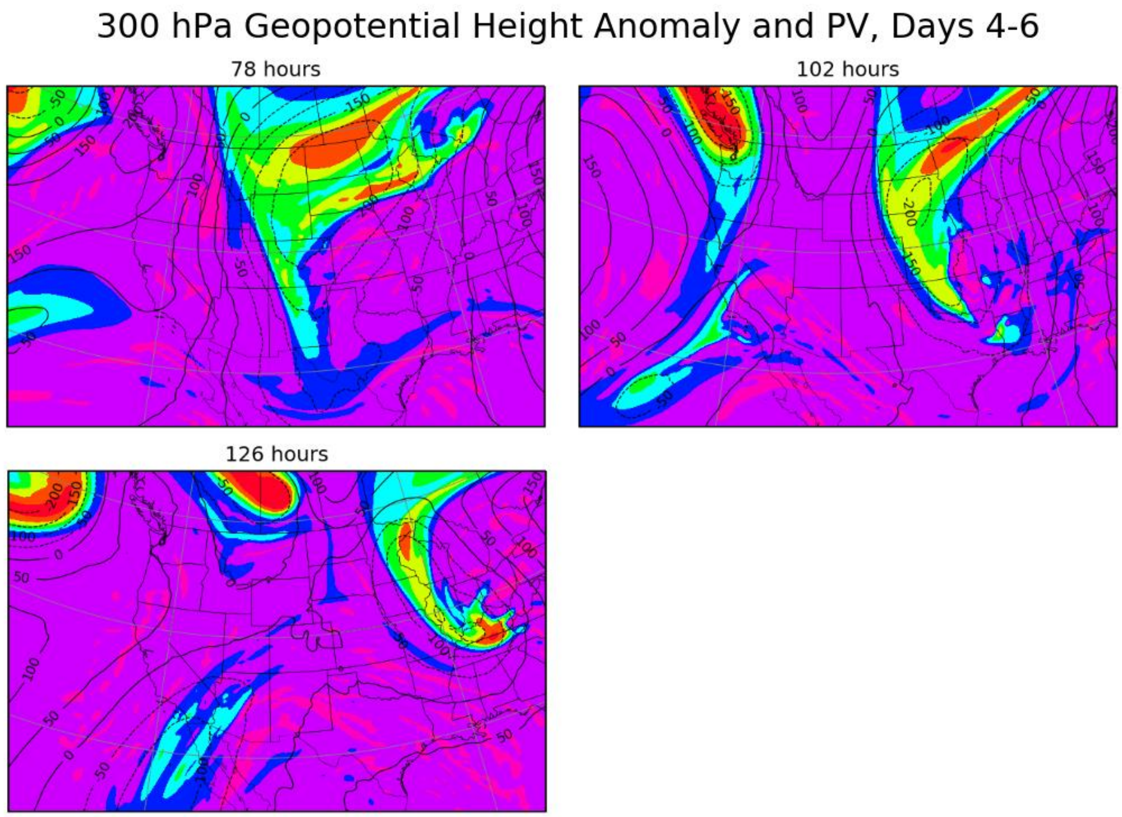

Figure 6.3: Case 2 Base 300 hPa Geopotential Height Anomaly and PV, Days 4-6. Contours are 50 gpm for height and 1 PVU for PV.

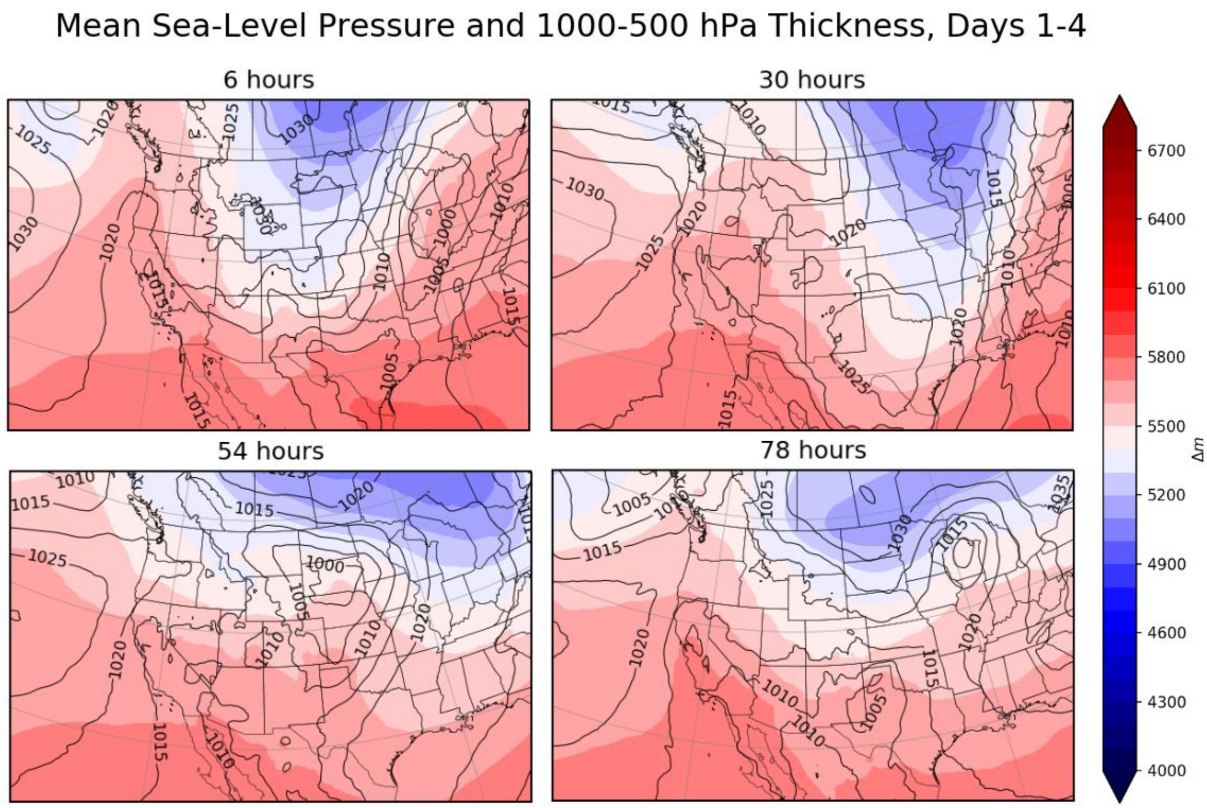

Figure 6.4: Case 2 Base Mean Sea-Level Pressure and 1000-500 hPa Thickness, Days 1-3. Contour intervals are 5 hPa for pressure and 100 meters for thickness. Blue contours are less than 5400 m.

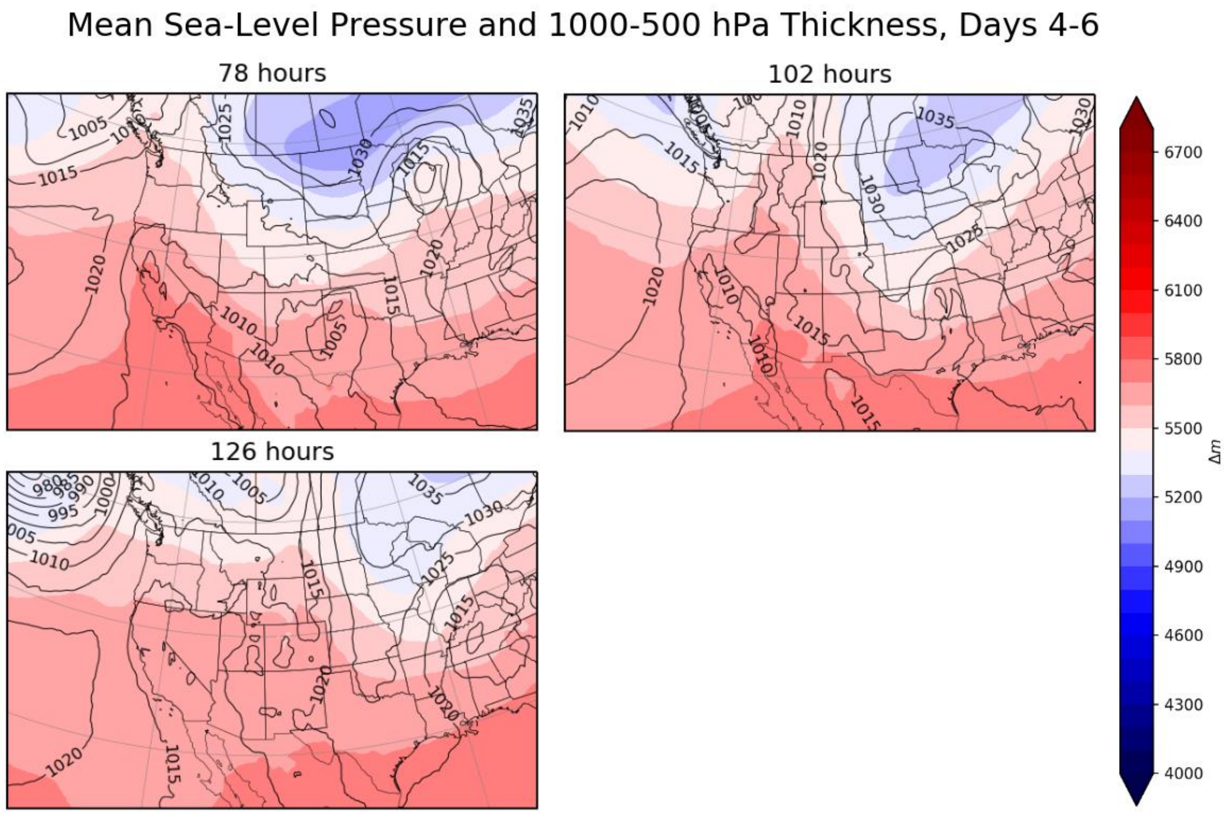

Figure 6.5: Case 2 Base Mean Sea-Level Pressure and 1000-500 hPa Thickness, Days 4-6. Contour intervals are 5 hPa for pressure and 100 m for thickness.

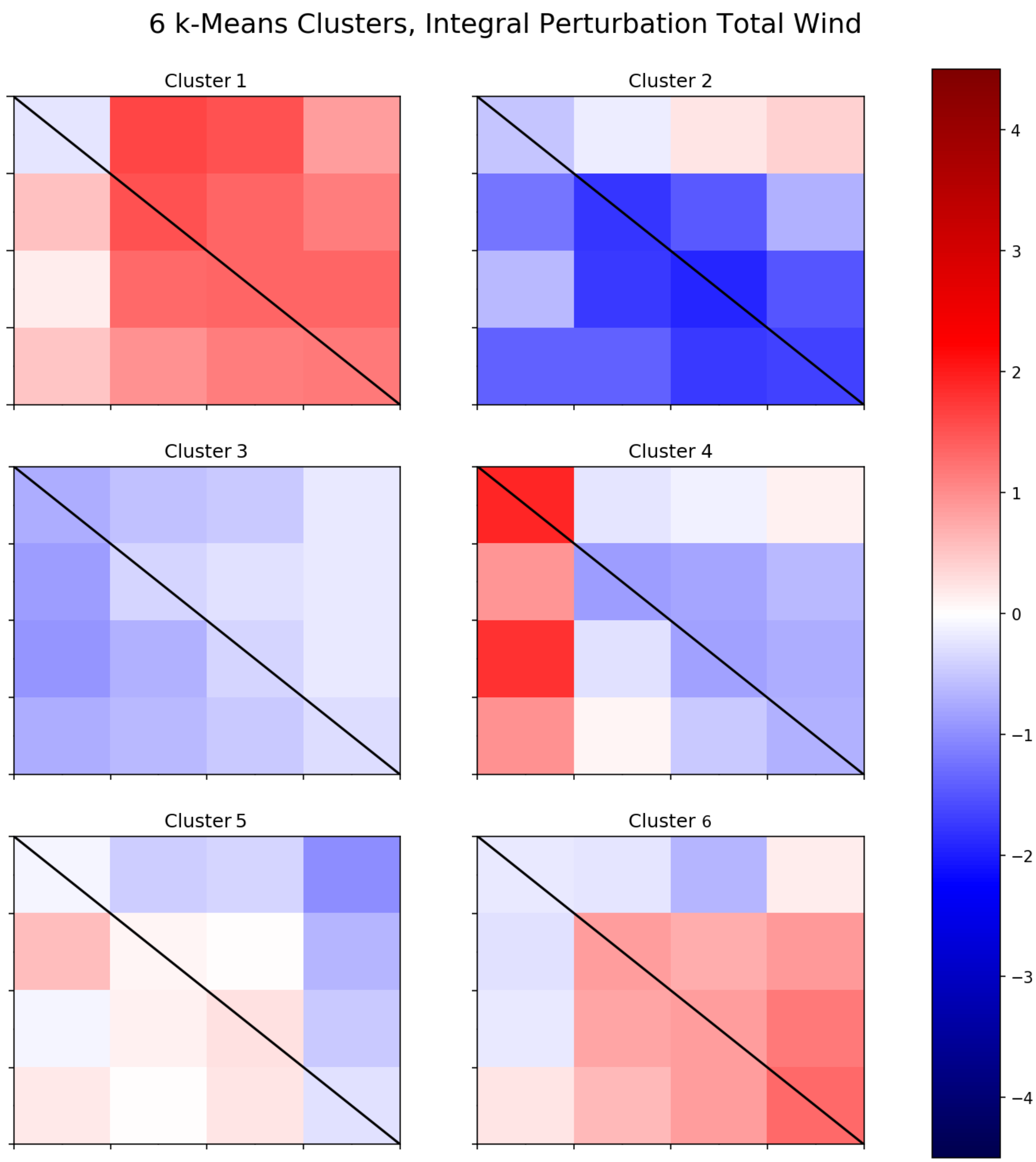

Figure 6.6: Case 2 k-means Cluster Centroids, Integral Perturbation Total Wind

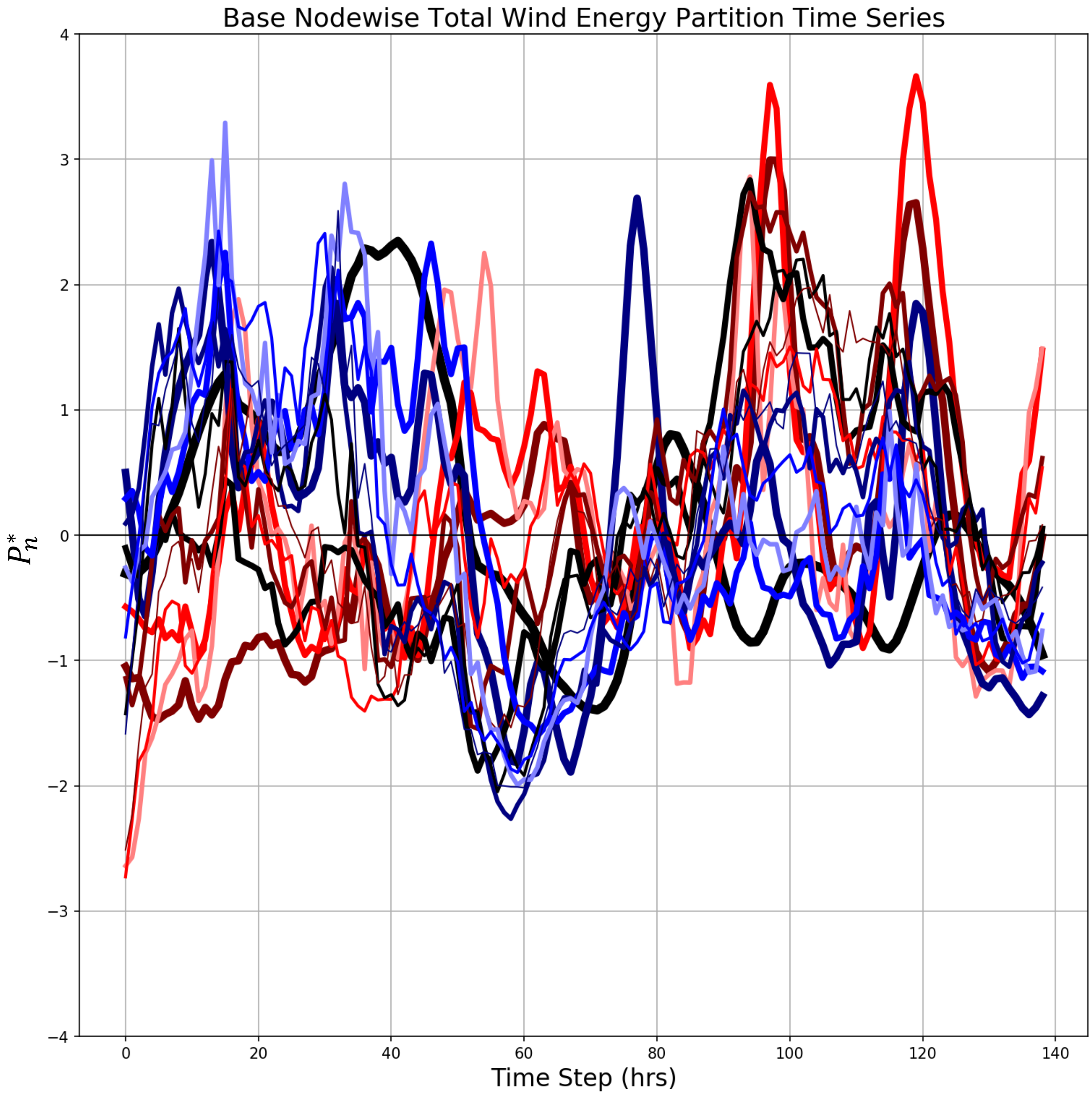

1549

1550 Figure 6.7: Case 2 Base Nodewise Total Wind Energy Partition Time Series

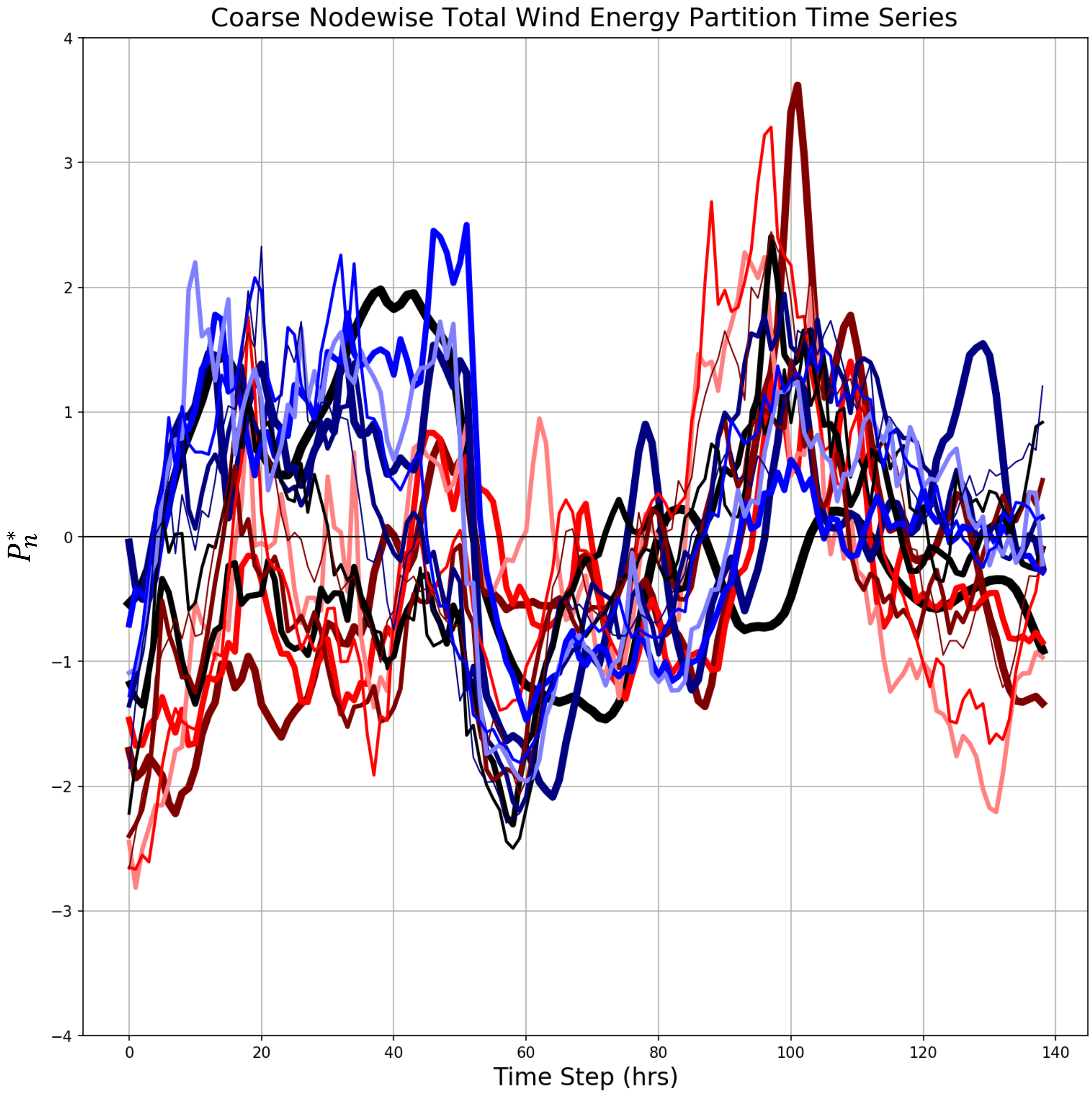

1551

1552 Figure 6.8: Case 2 Coarse Nodewise Total Wind Energy Partition Time Series

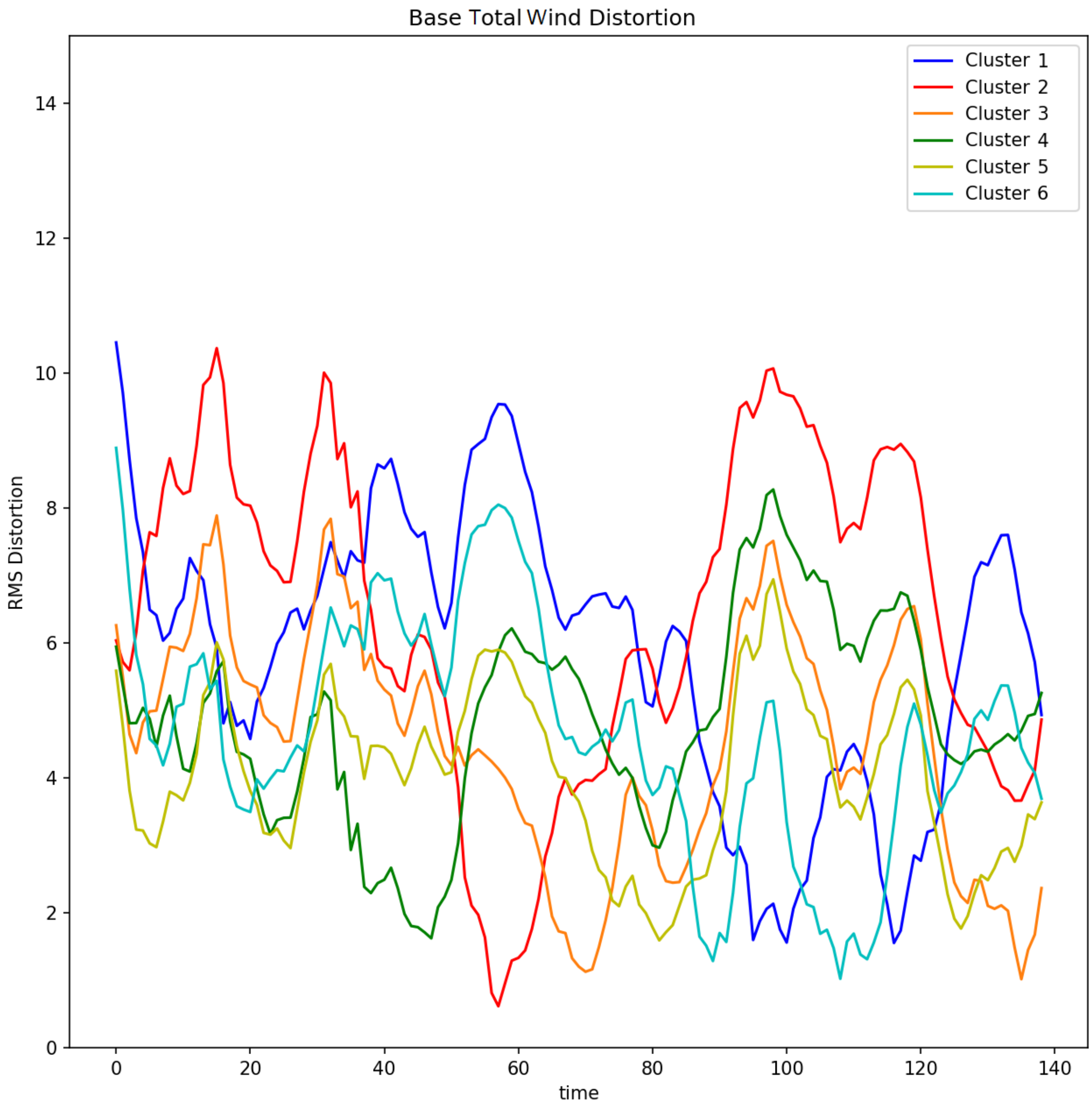

1553

1554 Figure 6.9: D_k for the Case 2 Base Simulation.

1555

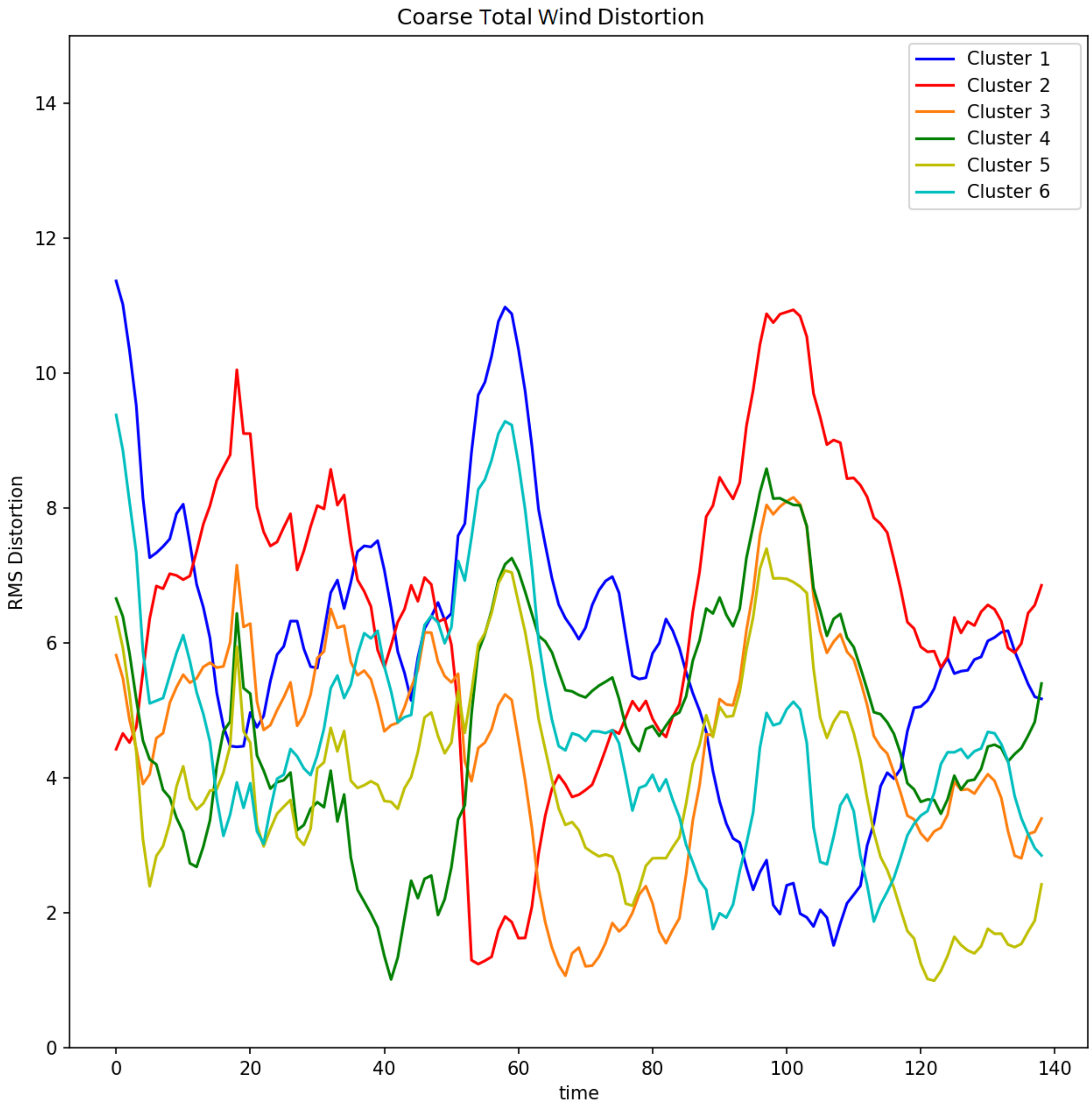

Figure 6.10: D_k for the Case 2 Coarse Simulation.

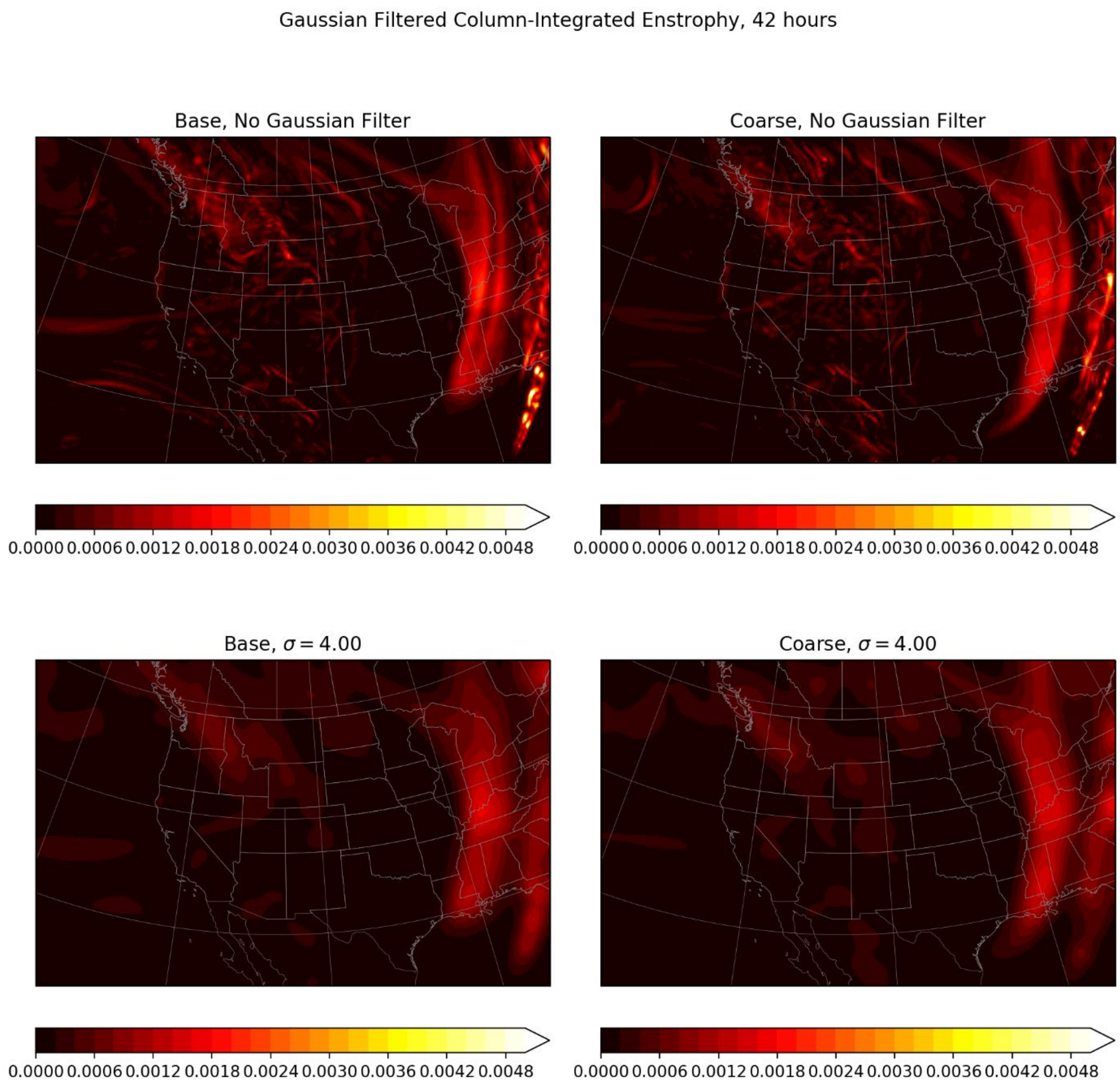

1559

1560 Figure 6.11: Case 2 Column-Integrated Enstrophy at 42 Hours. Contour intervals are $2x10^{-4}$ are hPa s^{-2}.

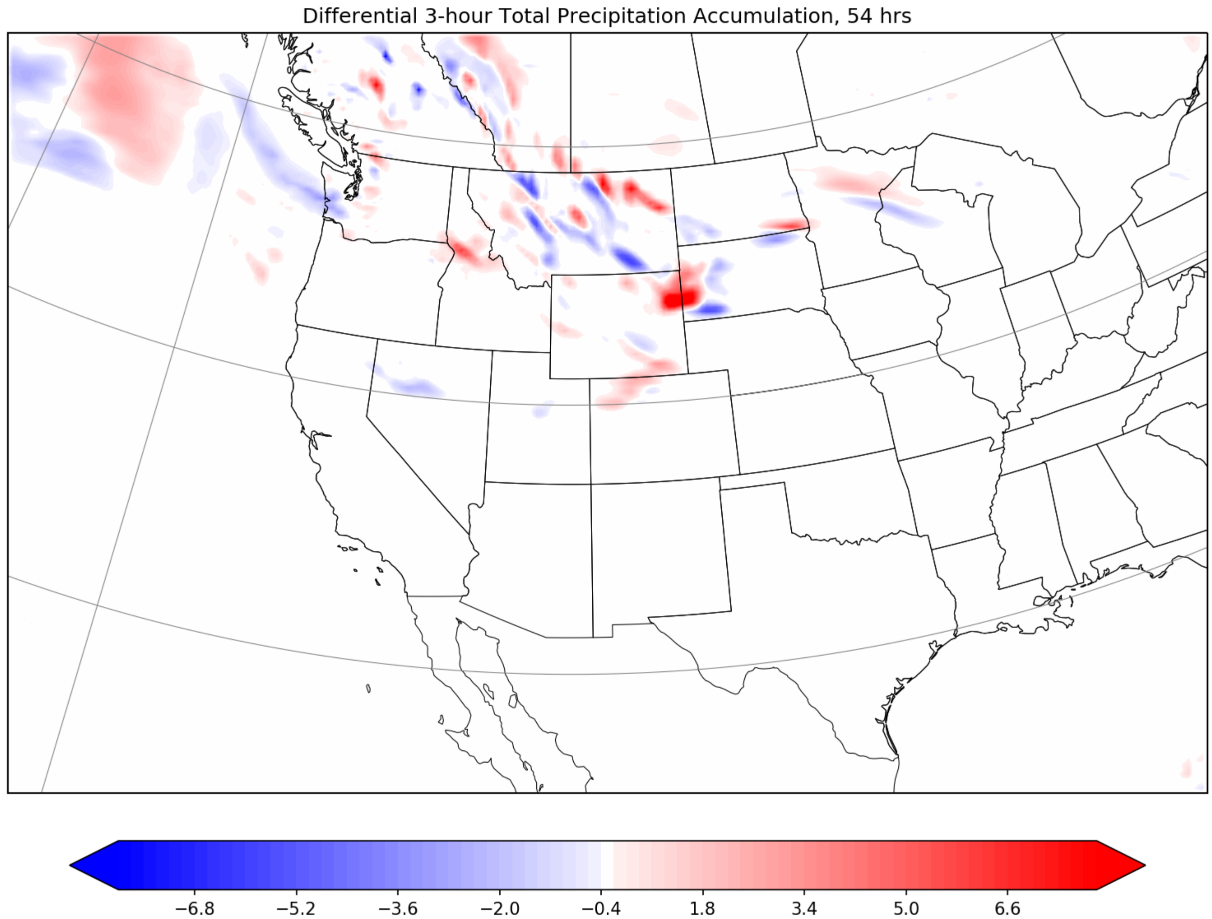

Figure 6.12: Case 2 Differential 3-hour Total Precipitation Accumulation at 54 Hours. Differential precipitation contours are 0.4 mm with the interval -0.4 to 0.4 appearing white.

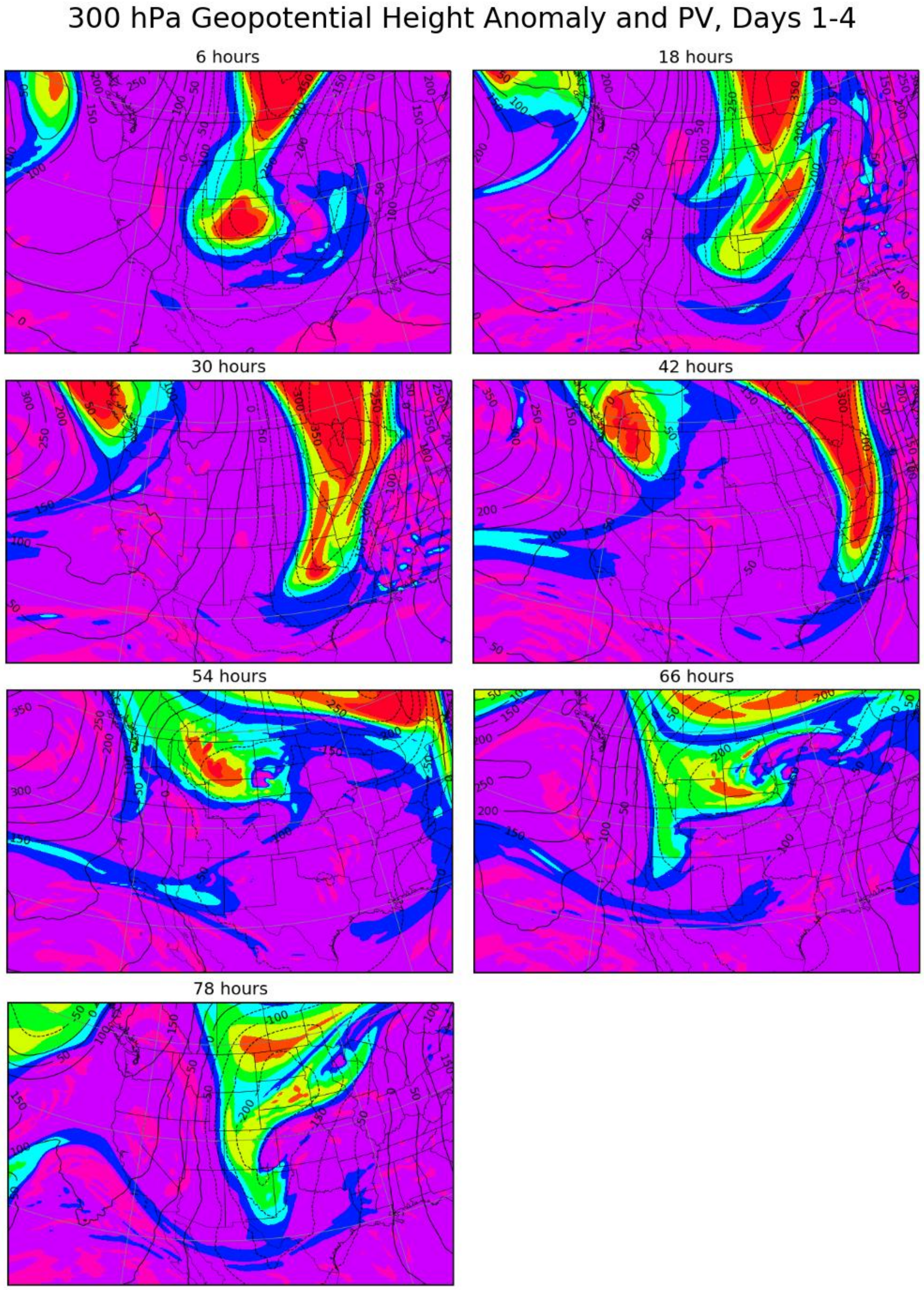

Figure 6.13: Case 2 Coarse 300 hPa Geopotential Height Anomaly and PV, Days 1-3. Contour intervals 50 gpm for height anomaly and 1 PVU for PV.

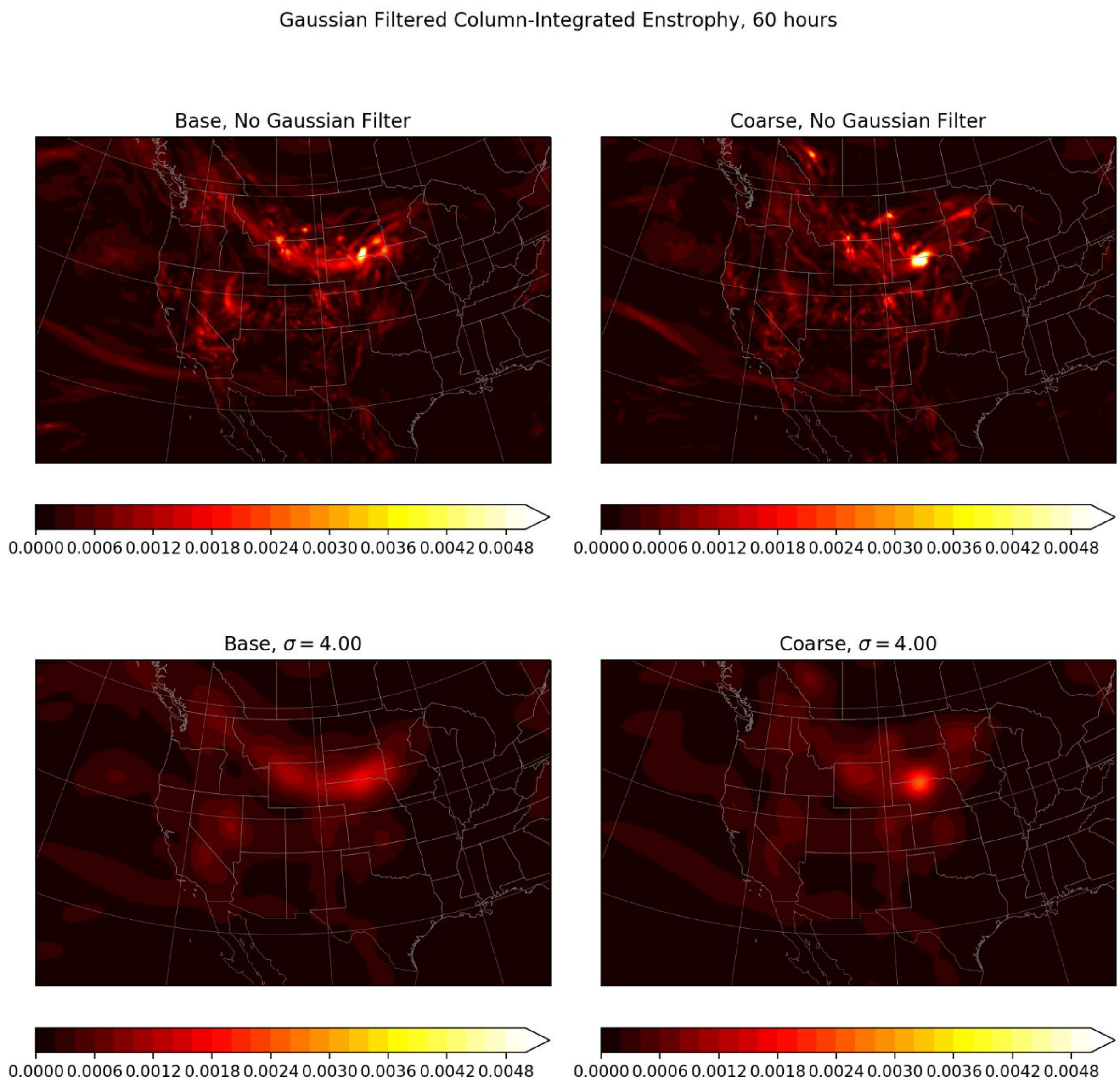

Figure 6.14: Case 2 Column-Integrated Enstrophy at 60 Hours. Contour intervals are $2x10^{-4}$ are hPa s^{-2}.

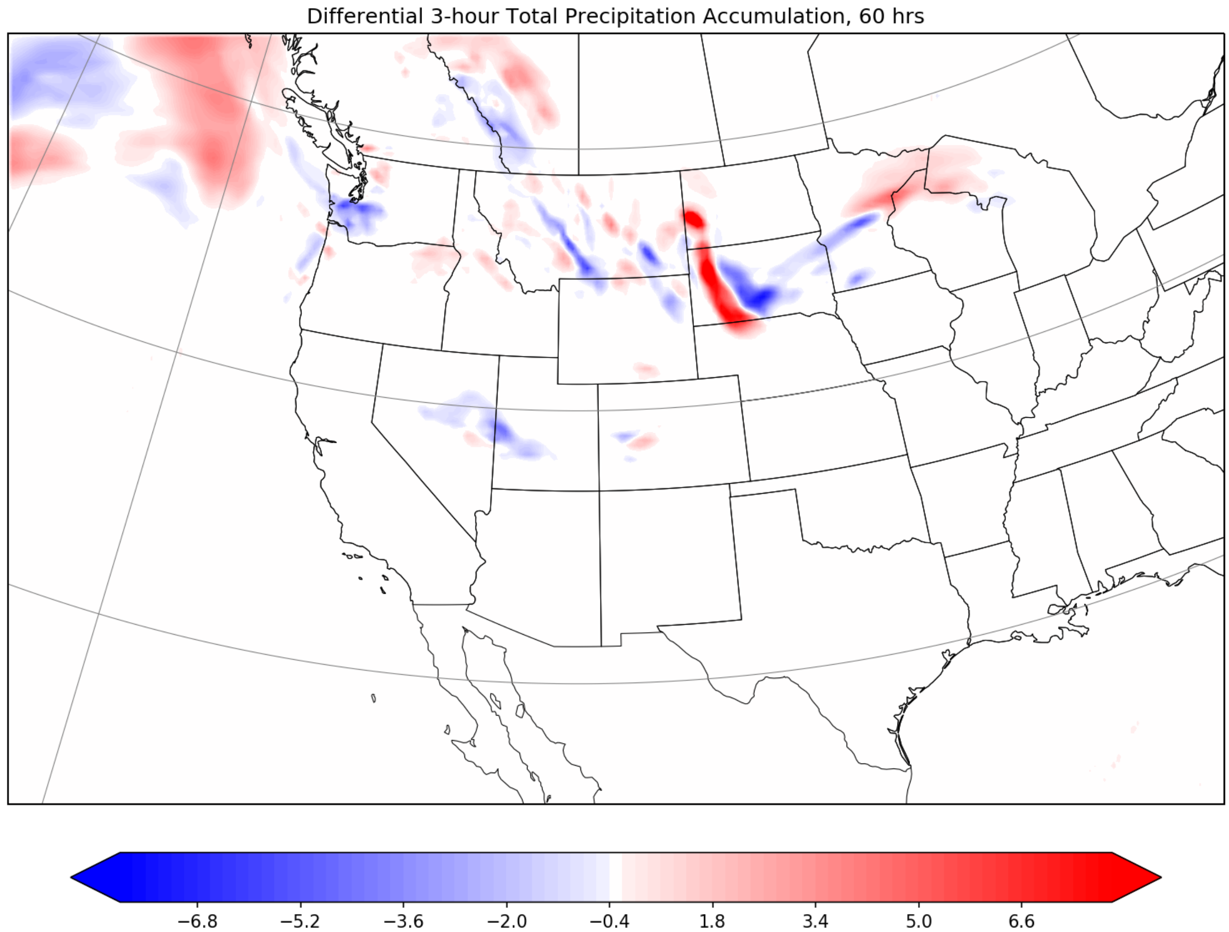

Figure 6.15: Case 2 Differential 3-Hour Total Precipitation Accumulation at 60 Hours. Differential precipitation contours are 0.4 mm with the interval -0.4 to 0.4 appearing white.

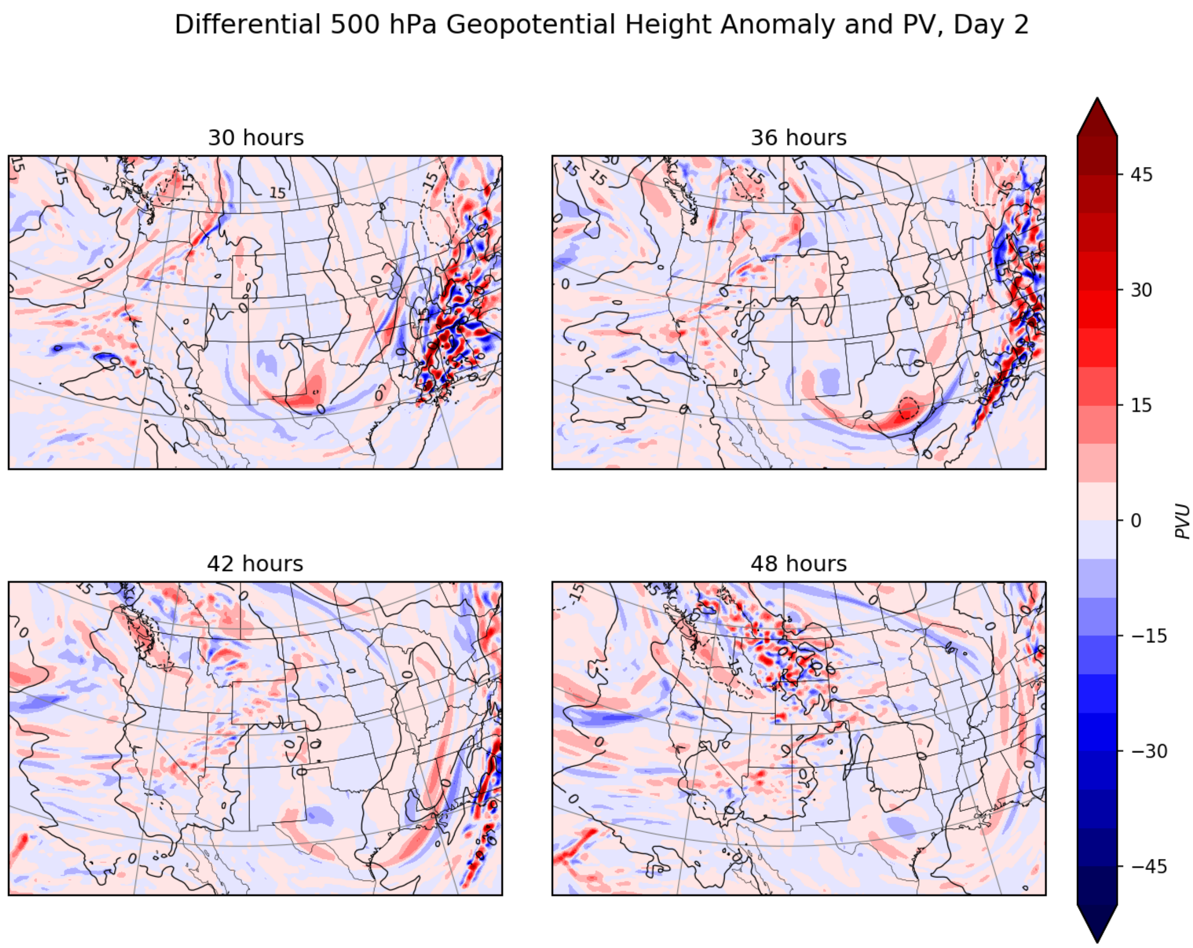

Figure 6.16: Case 2 Differential 500 hPa Geopotential Height Anomaly and Vorticity, Day 3. Contour intervals are 10^5 s^{-1}.

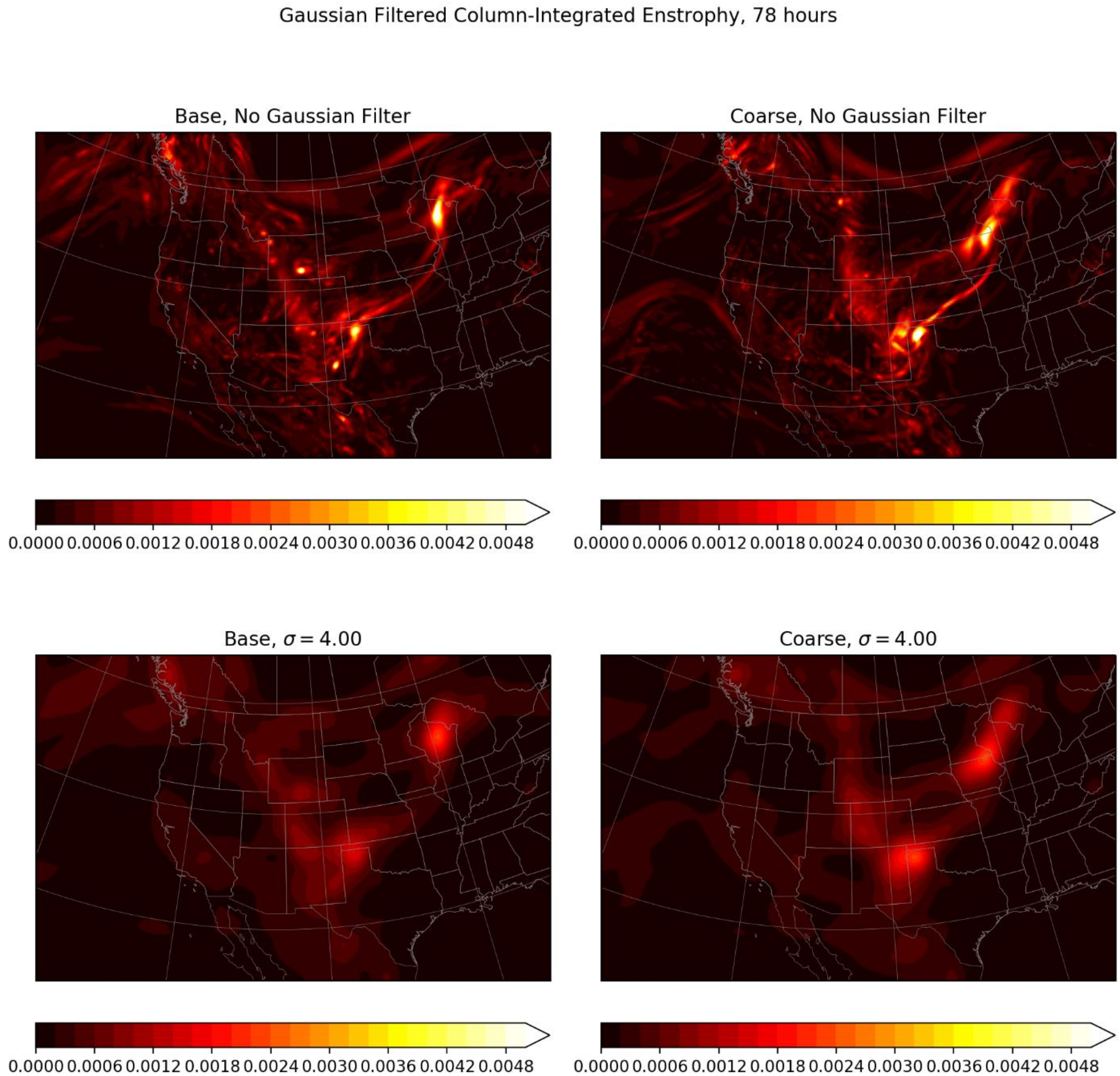

Figure 6.17: Case 2 Column-Integrated Enstrophy at 78 Hours. Contour intervals are $2x10^{-4}$ hPa s^{-1}.

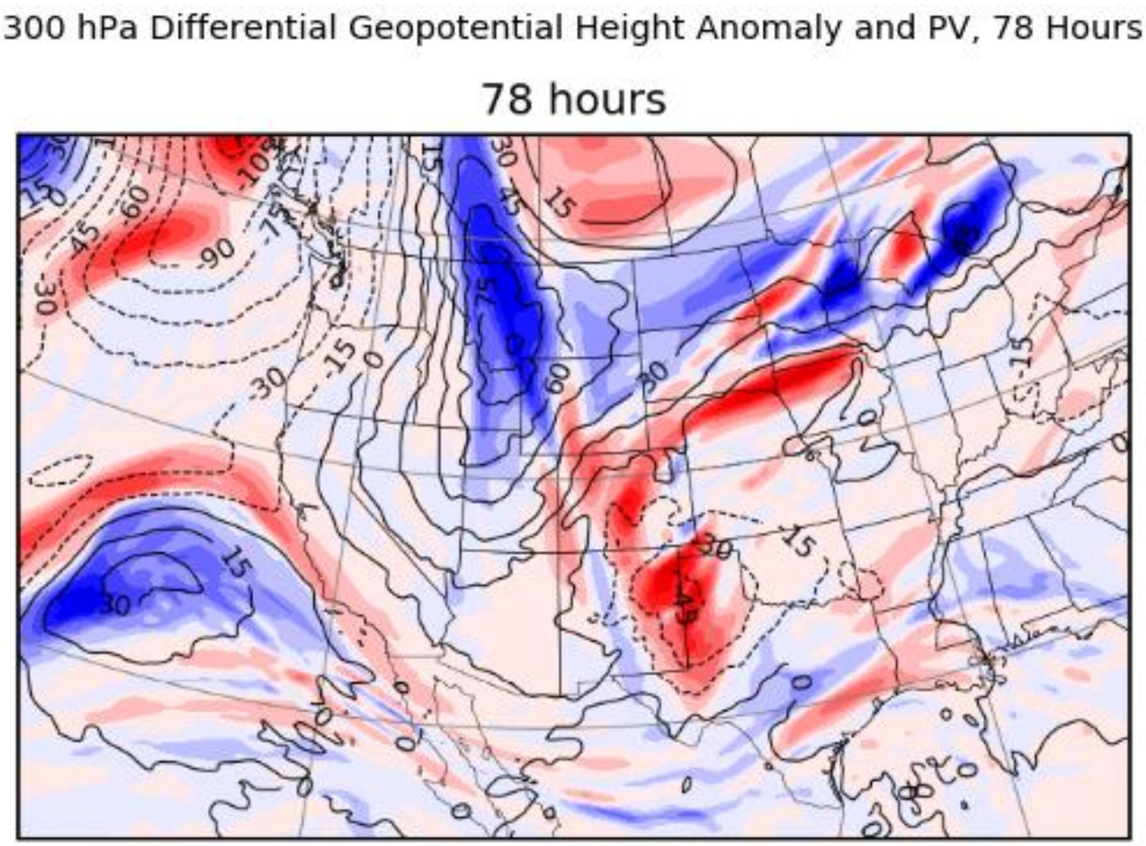

Figure 6.18: Case 2 Differential 300 hPa Geopotential Height Anomaly and PV at 78 Hours. Contour intervals are 15 gpm for differential height anomaly and 0.5 PVU for filled PV contours.

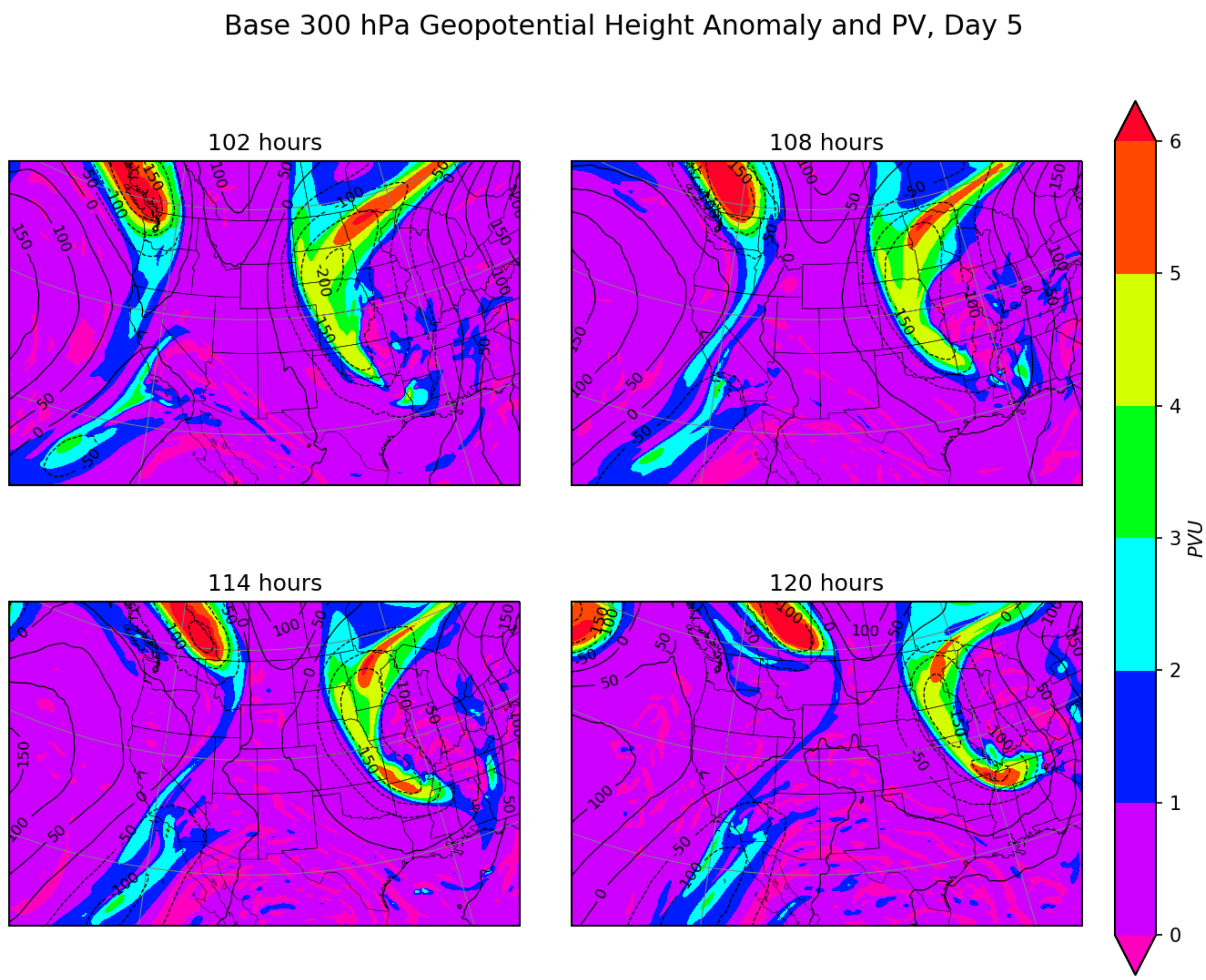

Figure 6.19: Case 2 Base 300 hPa Geopotential Height Anomaly and PV, Day 5. Contour intervals are 50 gpm for height and 1 PVU for PV.

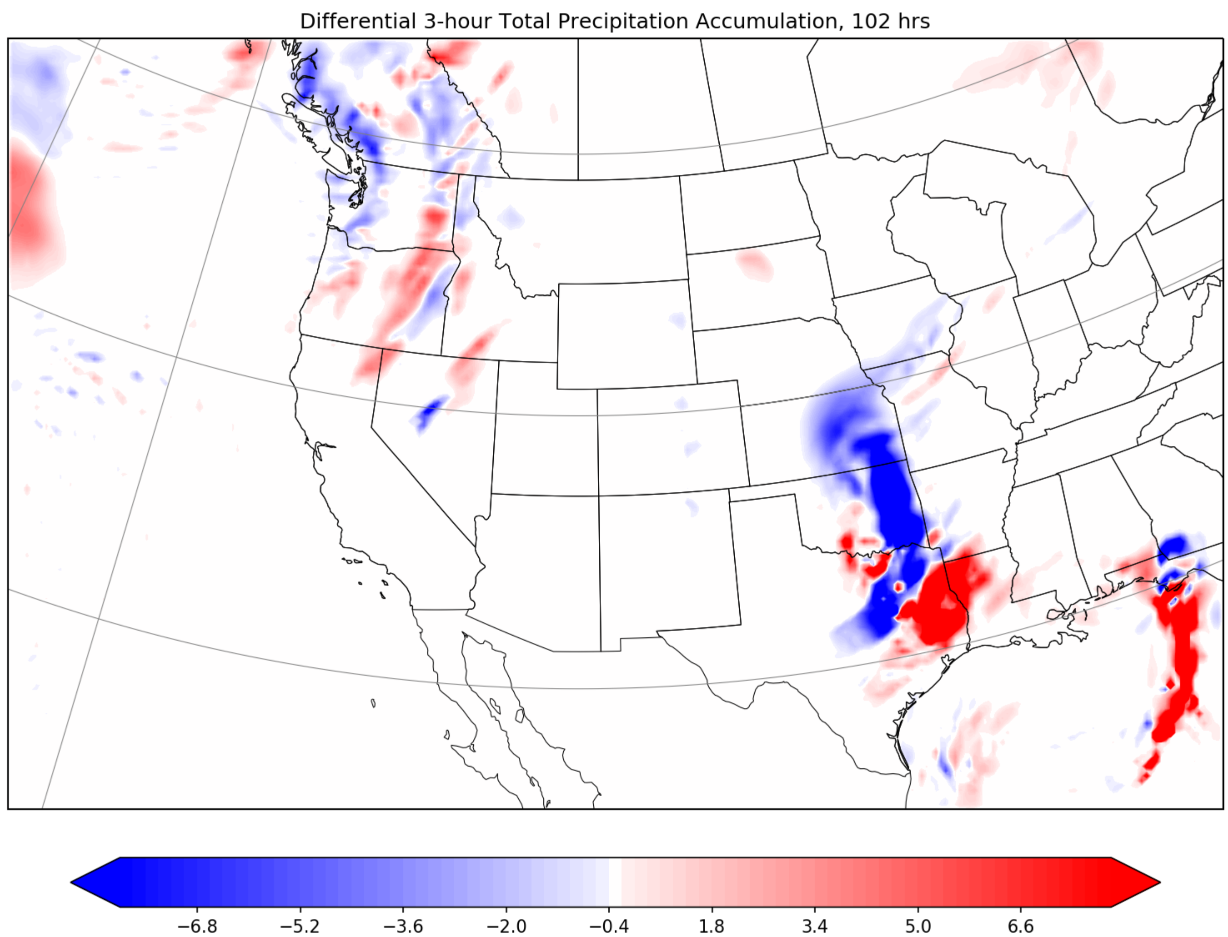

Figure 6.20: Case 2 Differential 3-Hour Total Precipitation Accumulation at 102 Hours. Differential precipitation contours are 0.4 mm with the interval -0.4 to 0.4 appearing white.

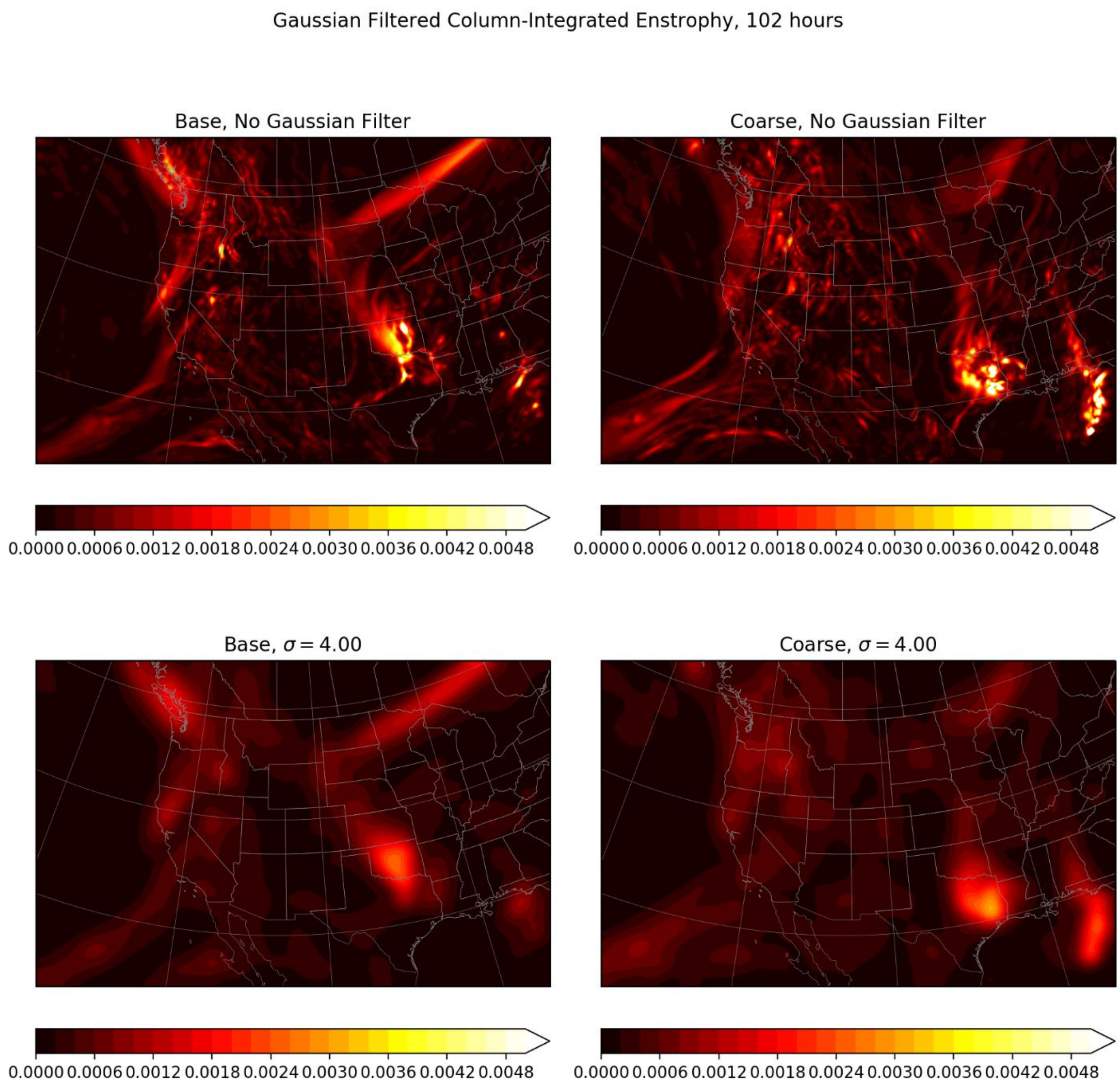

Figure 6.21: Case 2 Column-Integrated Enstrophy at 102 Hours. Contour intervals are $2x10^{-4}$ hPa s^{-1}.

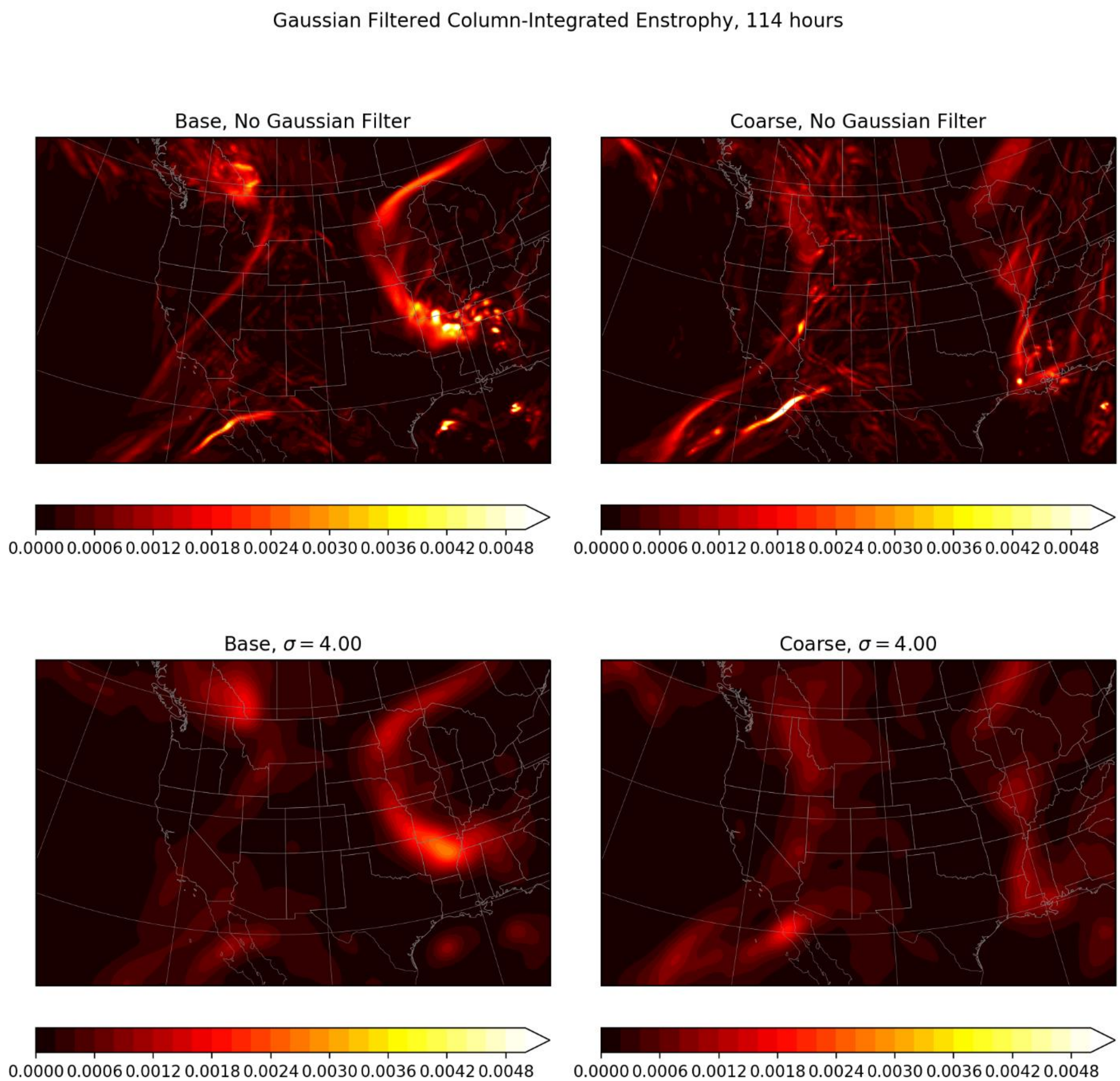

1597

1598 Figure 6.22: Case 2 Column-Integrated Enstrophy at 114 Hours. Contour intervals are $2x10^{-4}$ hPa s^{-1}.

1599

CHAPTER VII

CASE 3: DECEMBER 2014

7.1 Synoptic Diagnosis

Figure 7.1 depicts the 300 hPa geopotential height anomalies and PV for the first four days of the base simulation. At the inner domain initialization, there is a strong vortex positioned over the southwestern United States made up of a single potential vorticity structure that is connected to a large feature in Canada. Over the course of the first day, the vortex becomes increasingly deformed, with its upstream flank overturning with respect to longitude, becoming anticyclonically tilted, and breaking. This continues through the second day, with the PV maintaining its tilt but becoming further filamented and stretched as differential advection across the U.S. takes place. By 78 hours, the PV structure is little more than a ribbon on the downstream flank of a larger trough that has entered the inner domain and has spread over the majority of the central and western United States. During day 4 (Fig. 7.2), the larger trough over the U.S. experiences overturning. This overturning begins in the outer domain (Figure 7.3) and extends into the inner domain as the overturning becomes increasingly extreme. By 126 hours, the PV structure is strongly filamented. By the final day of the simulation, PV has separated from the main body of the trough and formed a vortex.

The MSLP for the base simulation for the first four days is shown in Figure 7.4. There is a weak frontal trough stretching across much of the central United States. This trough persists for several days, sliding across the country very slowly, narrowing over the course of the first 4 days while the 300 hPa PV anomaly narrows. Eventually, this low moves offshore, deepens, and migrates out of the domain. Afterward (Figure 7.5) it is replaced by high pressure that remains in place for the rest of the simulation.

7.2 Cluster Analysis

The clusters for Case 3 are shown in Figure 7.6. Clusters one and two are approximately oppositely aligned—cluster one showing above-average node energy where cluster two shows negative and vice versa. Cluster two is also one of two clusters with above mean domain-scale, isotropic energy, the other being cluster three. Cluster three is another example of an excited state cluster, where all nodes show above ensemble mean energy. Cluster four is close to the ensemble mean, where almost all node perturbation energy is near zero. Cluster six is a somewhat low energy node, where all the mesoscale nodes have energy partitions well-below the ensemble mean, but is probably more accurately described as a weak synoptic node, as the synoptic meridional nodes are near the ensemble mean and there is above mean energy at the zonally elongated synoptic nodes. Cluster five lacks large-scale or zonal synoptic energy but has meridional synoptic and weakly zonally elongated perturbation energy.

The energy partitions of the base and coarse simulations are shown in Figures 7.7 and 7.8, respectively. As with Cases 1 and 2, the coarse simulation begins with less P_n^* for all nodes than the base simulation. Also like Cases 1 and 2, the energy partition reflects the repopulation of small-scale flow constituents after initialization; Case 3 is closer to Case 2 in that there is a small increase in energy after initialization rather than the very large increase in Case 1. The mid-range meridionally elongated nodes see very little increase in energy at all after initialization, but this is consistent with the filtering because the base simulation experiences a net *reduction* in those nodes' energies. Beyond initialization, notable differences include hour 60, where the coarse simulation sees a much larger reduction in its domain-wide isotropic perturbations than the base simulation; between hours 80 and 100, where the coarse perturbation energies collectively drop below the ensemble mean while the base simulation energies form three groups of varying magnitudes; at hour 120 where the coarse simulation experiences a broad, collective increase of all node energies while the base simulation is much narrower and weaker; and beyond hour 140 where the zonally elongated nodes of the coarse simulation contain more perturbation energy than the base's equivalents.

At hour 60, the two simulations are assigned to the same cluster (see Figures 7.9 and 7.10 for the base and coarse D_k, respectively), having just transitioned from a state described by cluster five to one described by cluster one. The base simulation geopotential height anomalies and PV throughout day 3 are shown in Figure 7.11, and the difference fields between the coarse and base are shown in Figure 7.12. As with Cases 1 and 2, the 300 hPa PV experiences a phase difference between the two simulations of around 800 km. The column-integrated enstrophy at hour 60 (Figures 7.13) shows that the smoothed enstrophy of the two simulations' large-scale PV are very similar, but the base simulation enstrophy tends to be narrower; the enstrophy on the margins of the large-scale wave tends to be more zonal and in smaller regions (Figure 7.14). At 72 hours (Figure 7.15), the 300 hPa trough is overtaking the surface front, and both the coarse and base simulation enstrophy is diminishing. The coarse simulation has bands of precipitation across the Piedmont of Virginia and North Carolina, while the base simulation has most of its precipitation farther south in the southern Appalachians. The coarse simulation has more isolated, but stronger, enstrophy maxima while the base simulation has weaker enstrophy maxima but greater enstrophy over a broader area (Figure 7.16).

Between hours 80 and 100, the two simulations' energy partitions diverge, and subsequently the assigned cluster is different for each. The base simulation is described by cluster six, reaching a minimum D_k around 90 to 95 hours; the coarse simulation is described by cluster four at that same time. The enstrophy (Figure 7.17, smoothed differential Figure 7.18), and power spectrum ensemble temporal perturbation (Figure 7.19) at hour 96 shows that the both the base and coarse simulations have little above mean perturbation energy anywhere. The differential power spectrum (Figure 7.20) shows the coarse simulation has higher mesoscale perturbation energy but less elongated synoptic scale energy. The enstrophy suggests that there is a greater variety in the coarse mesoscale structure orientations, explaining the higher mesoscale perturbation energy and the lower synoptic perturbation energy.

From this point, there is little precipitation in Case 3, though the two simulation's cluster states still differ beyond 100 hours, so we need to try digging in to dry dynamics to see if it's possible they could be the cause. The base simulation 300 hPa kinematic deformation field at 90 hours (Figure 7.21) shows that the axes of dilatation along the PV discontinuity are oriented 45° across the PV discontinuity, indicating possible compression of the PV contours but little deformation of the broader PV wave. Axes of dilatation on the interior of the wave are small, also indicating weak deformation overall. The nonlinear deformation—the deformation caused by the level 4 approximation node only, because the smaller nodes do not project onto the scale of the trough—at 90 hours (Figure 7.22) shows that the perturbations are the largest component of deformation, so we can say that most of the deformation occurring at this point in the simulation is nonlinear. The coarse simulation has very similar axes of dilatation (Figure 7.23), and the differences between the two simulations are too small draw a distinct behavioral difference. There is likely no dynamical process driven by perturbations at this point in time that would result in changes to the PV wave shape.

Around 120 hours, there is a dramatic shift in every cluster D_k during which both simulations are in a state described by cluster three. Their 300 hPa PV troughs on day 5 (Figures 7.24 and 7.25) show that both have become stretched zonally, though the coarse simulation has stretched less than the base. The enstrophy at 108 hours (Figures 7.26) shows that the enstrophy maxima are at similar locations, though slightly displaced (Figure 7.27). Twelve hours later (Figure 7.28), the two maxima are farther apart (Figure 7.29), but they still largely occupy the same area, and their large-scale envelopes still overlap. The coarse simulation enstrophy maxima at both 114 and 120 hours are larger than the corresponding base simulation maxima, which follows from the differences in P_n^* (Figures 7.7 and 7.8). As there is little precipitation at this point within the trough in Case 3, the high amplitude spike in P_n^* can be viewed as an indicator of the forward energy cascade specifically. Case 2 showed that P_n^* would increase during wave breaking, but it did so in the context of vorticity ejection in the presence of moist dynamics. Case 3 shows that this spike will occur in the absence of moist dynamics, so the increase in energy at smaller scale is not from injection of kinetic energy from latent heat but from the turbulent cascade of kinetic energy.

The enstrophy at 144 hours (Figure 7.30) shows the coarse simulation vortex has been advected over 1000 km eastward, while the base simulation vortex has barely moved (Figure 7.31). Similar plots 12 hours later (Figure 7.32 and 7.33) show that the coarse simulation vortex has filamented and undergone zonal elongation, unlike the base simulation vortex which is still present over the western United States. The two simulations still occupy the same cluster state during this period—a consequence of the significant amount of filamentation they have both undergone over the past day and a half.

Unfortunately, this case yields less information about the role of subsynoptic flow components of flow on the synoptic scale than Cases 1 and 2. As there was a lack of meaningful latent heat release beyond the first 2 days and before the final day, there was no way for the small-scale flow components to project energy onto the synoptic scale. There is clearly *some* sensitivity to changes to the initial conditions, as the simulation states do diverge after 6 days, but there are too many possible factors to place a potential cause. The upstream ridge is significantly stronger in the base simulation, so upstream latent heat could be a cause of that difference as seen in Case 1. The upstream ridge is also large enough to extend beyond the northern boundary of the outer domain, so boundary effects are likely to play a part in the simulation differences as well. There is also the chaos of a dynamical system that can be the culprit. While it’s possible to characterize the differences between the simulations using P_n^* and D_k, it is not possible to make a strong conclusion as to why with the current experimental design.

Figures

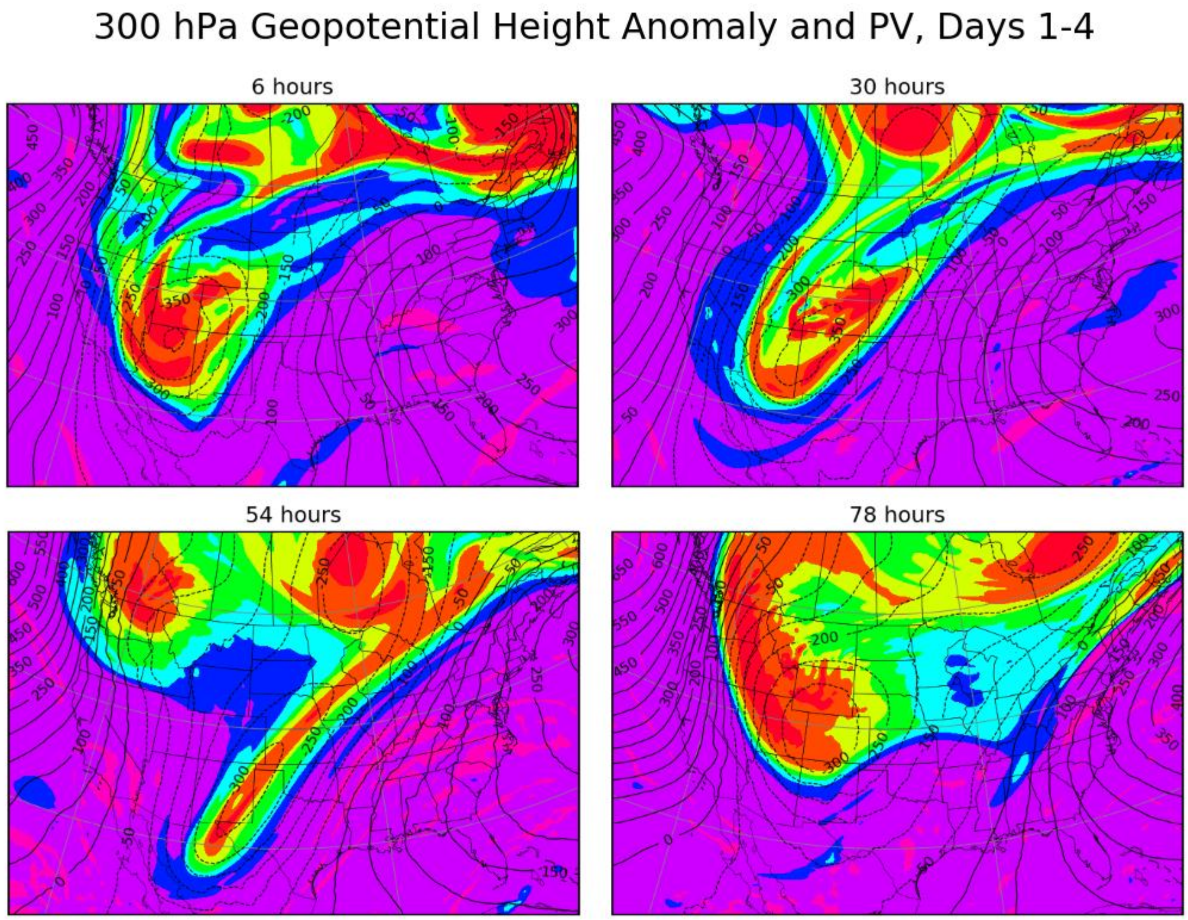

Figure 7.1: Case 3 Base 300 hPa Geopotential Height Anomaly and PV, Days 1-4. Contour intervals are 50 gpm for height anomaly and 1 PVU for PV.

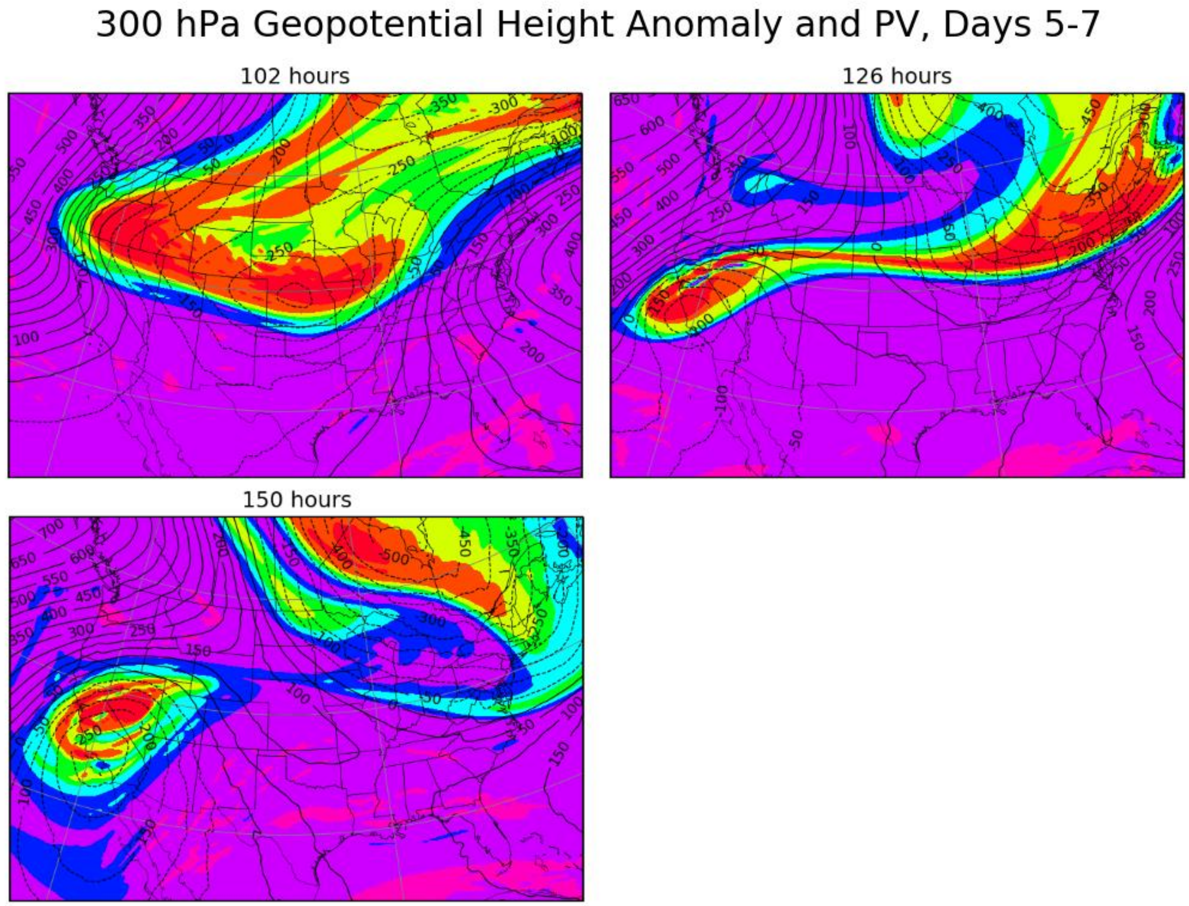

Figure 7.2: Case 3 Base 300 hPa Geopotential Height Anomaly and PV, Days 5-7. Contour intervals are 50 gpm for height anomaly and 1 PVU for PV.

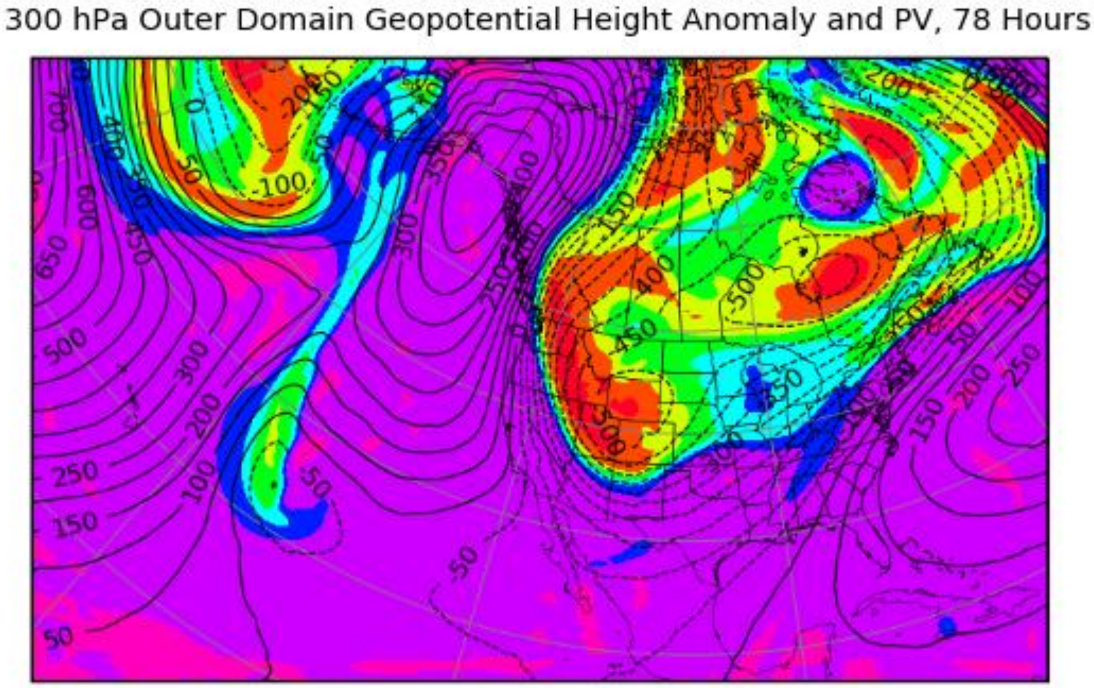

Figure 7.3: Case 3 Base 300 hPa Outer Domain Geopotential Height Anomaly and PV at 78 Hours. Contour intervals are 50 gpm for height anomaly and 1 PVU for PV (filled).

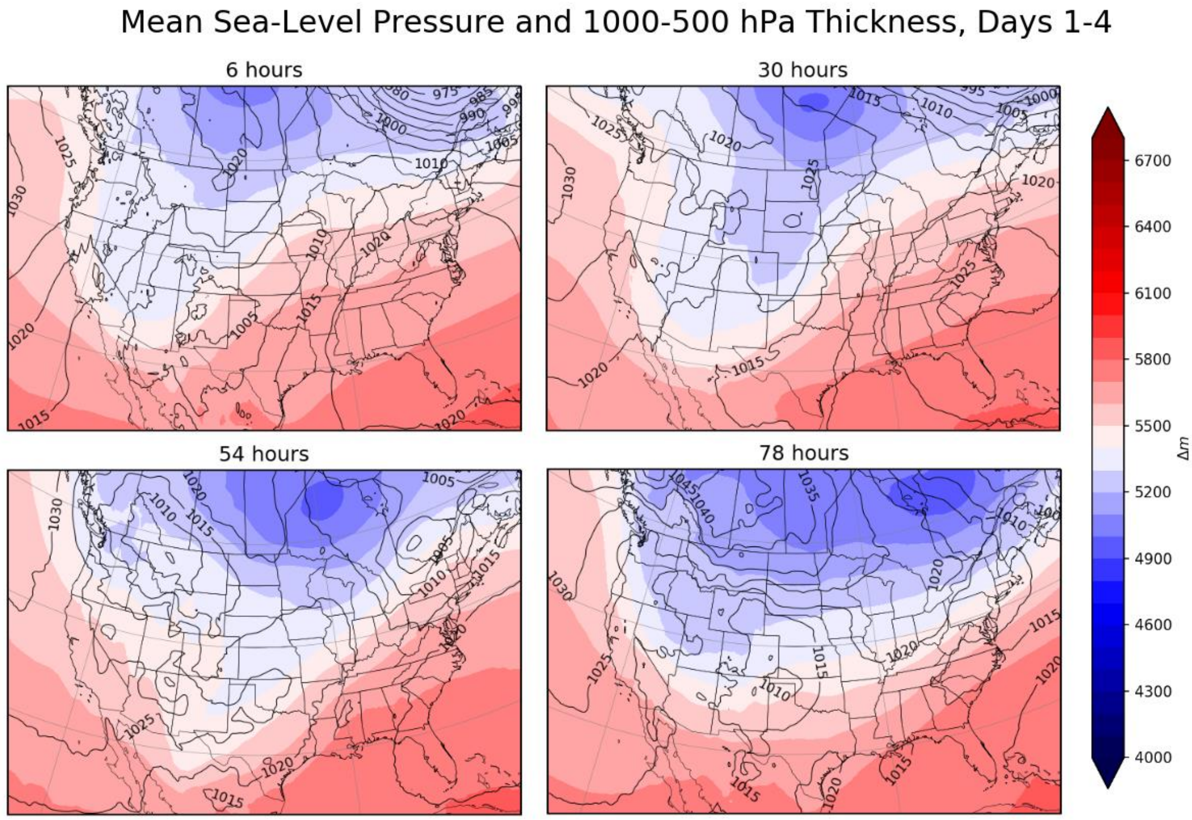

Figure 7.4: Case 3 Base Mean Sea-Level Pressure and 1000-500 hPa Thickness, Days 1-4. Contour intervals are 5 hPa for pressure and 100 meters for thickness. Blue contours are less than 5400 meters.

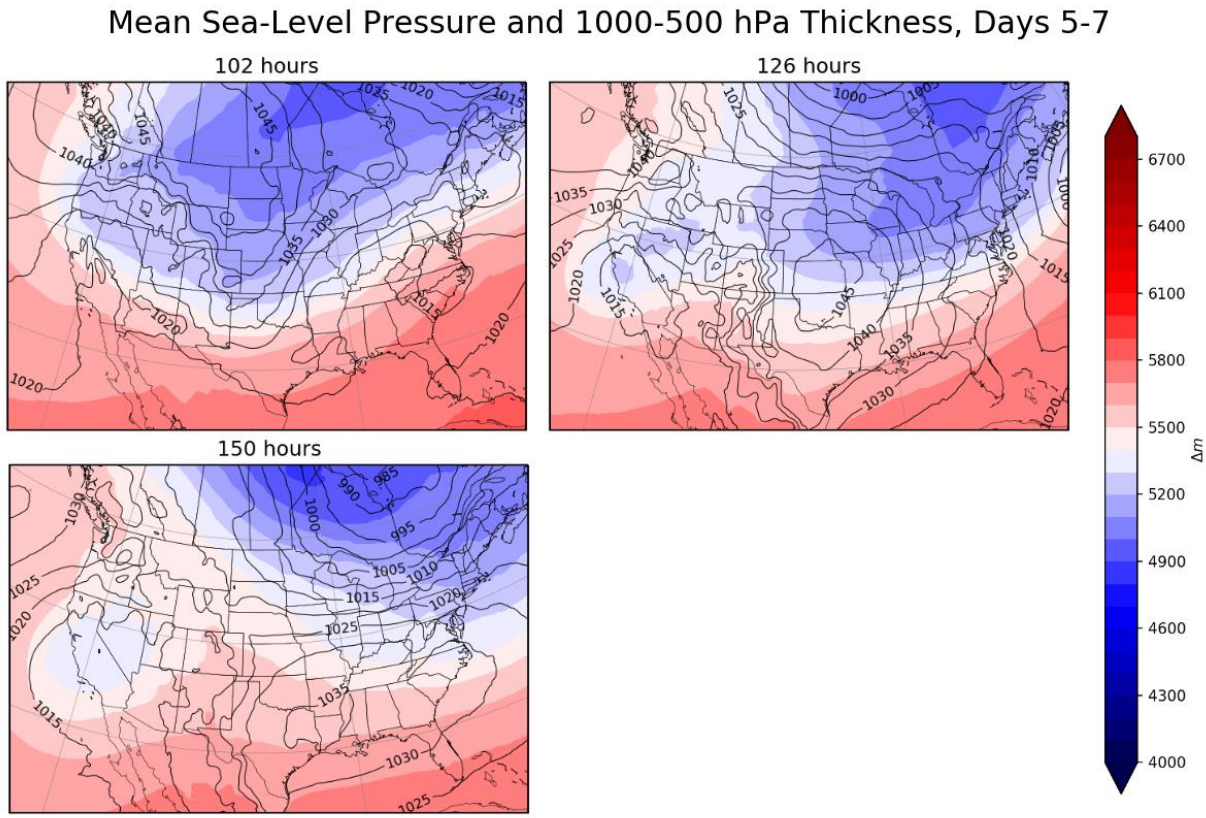

Figure 7.5: Case 3 Base Mean Sea-Level Pressure and 1000-500 hPa Thickness, Days 4-6. Contour intervals are 5 hPa for pressure and 100 meters for thickness. Blue contours are less than 5400 meters.

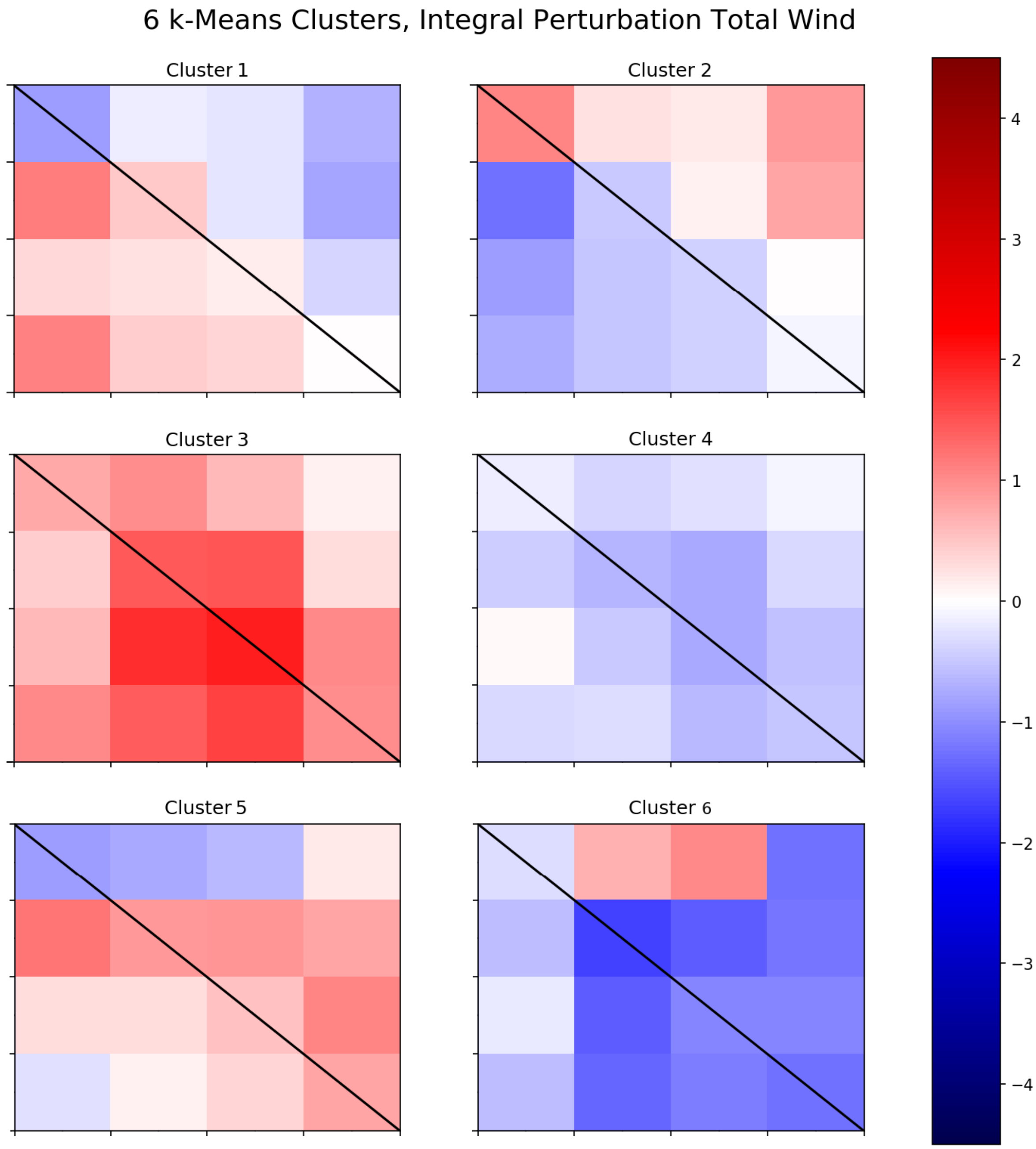

1765

1766 Figure 7.6: Case 3 k-Means Cluster Centroids, Integral Perturbation Total Wind.

1767

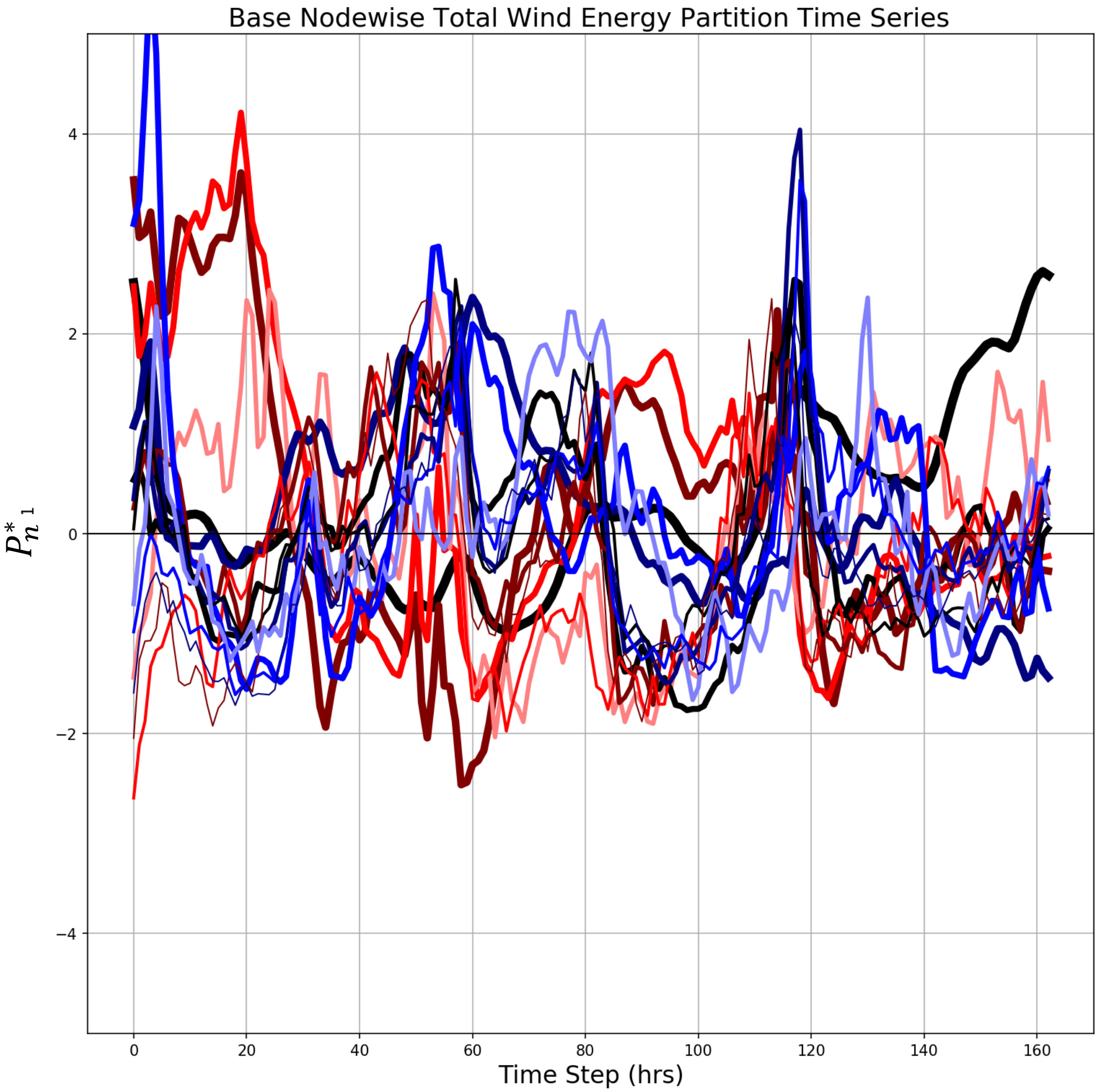

Figure 7.7: Case 3 Base Nodewise Total Wind Energy Partition Time Series.

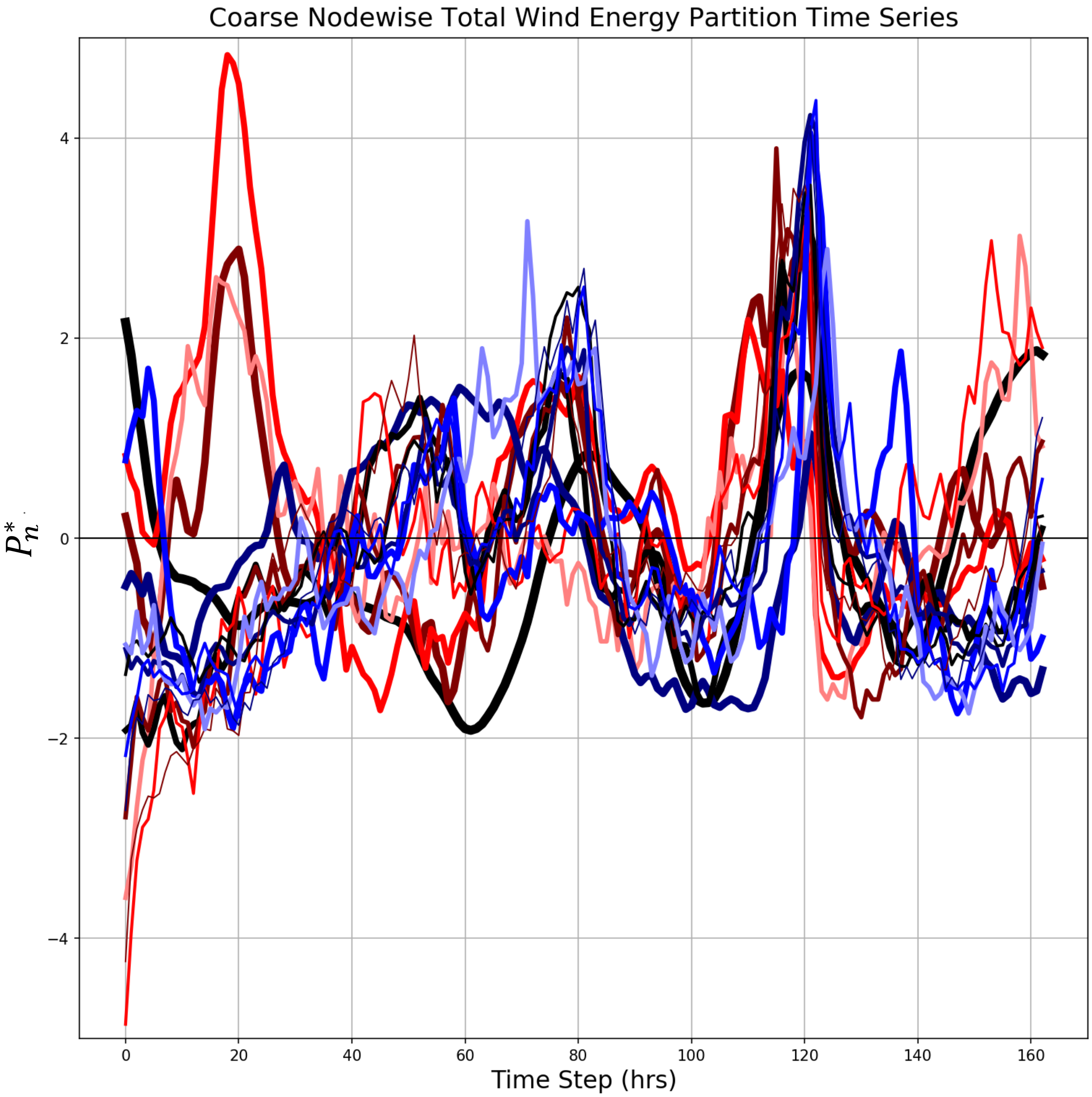

1772

1773 Figure 7.8: Case 3 Coarse Nodewise Total Wind Energy Partition Time Series.

1774

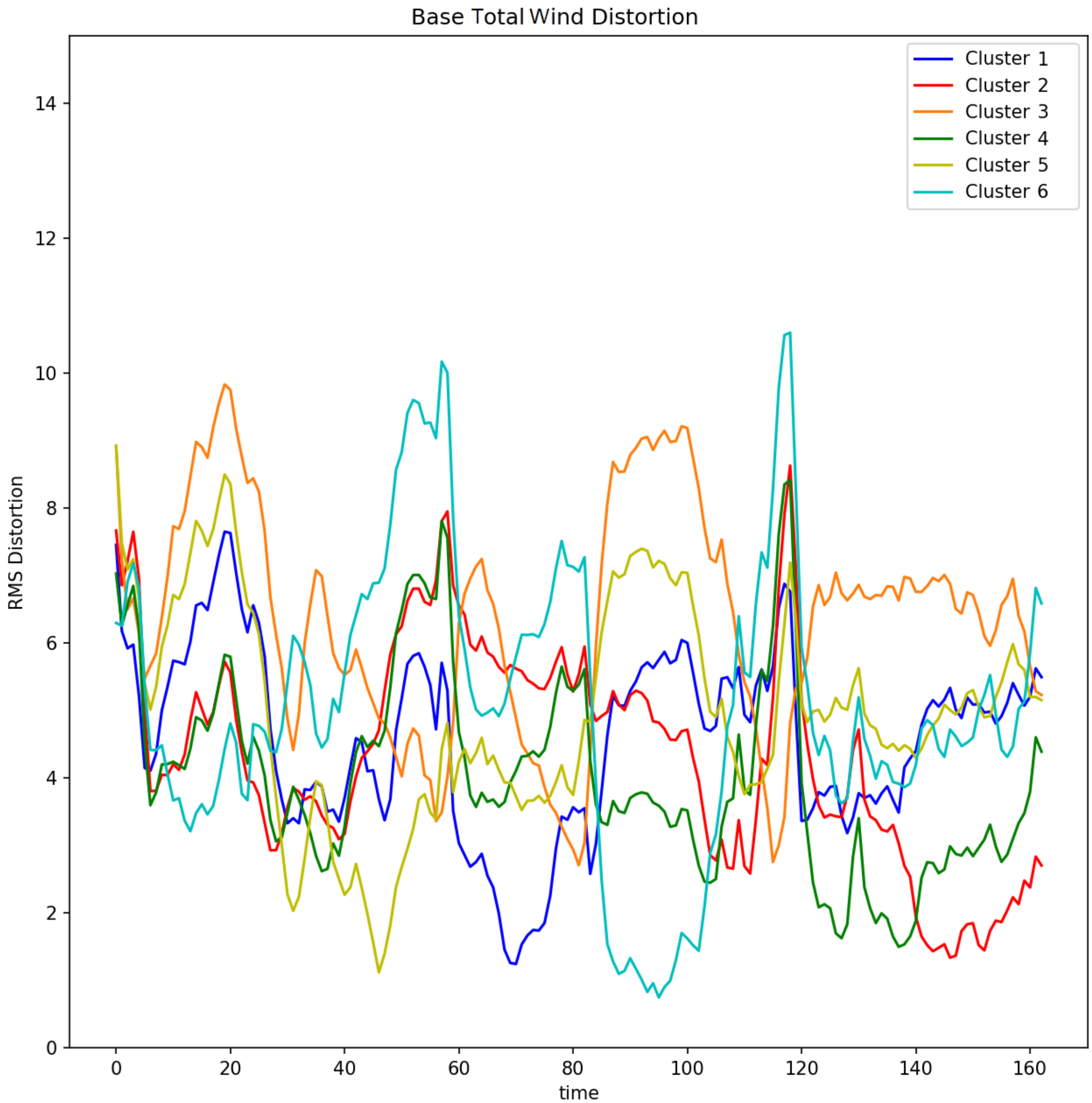

Figure 7.9: D_k of the Case 3 Base Simulation.

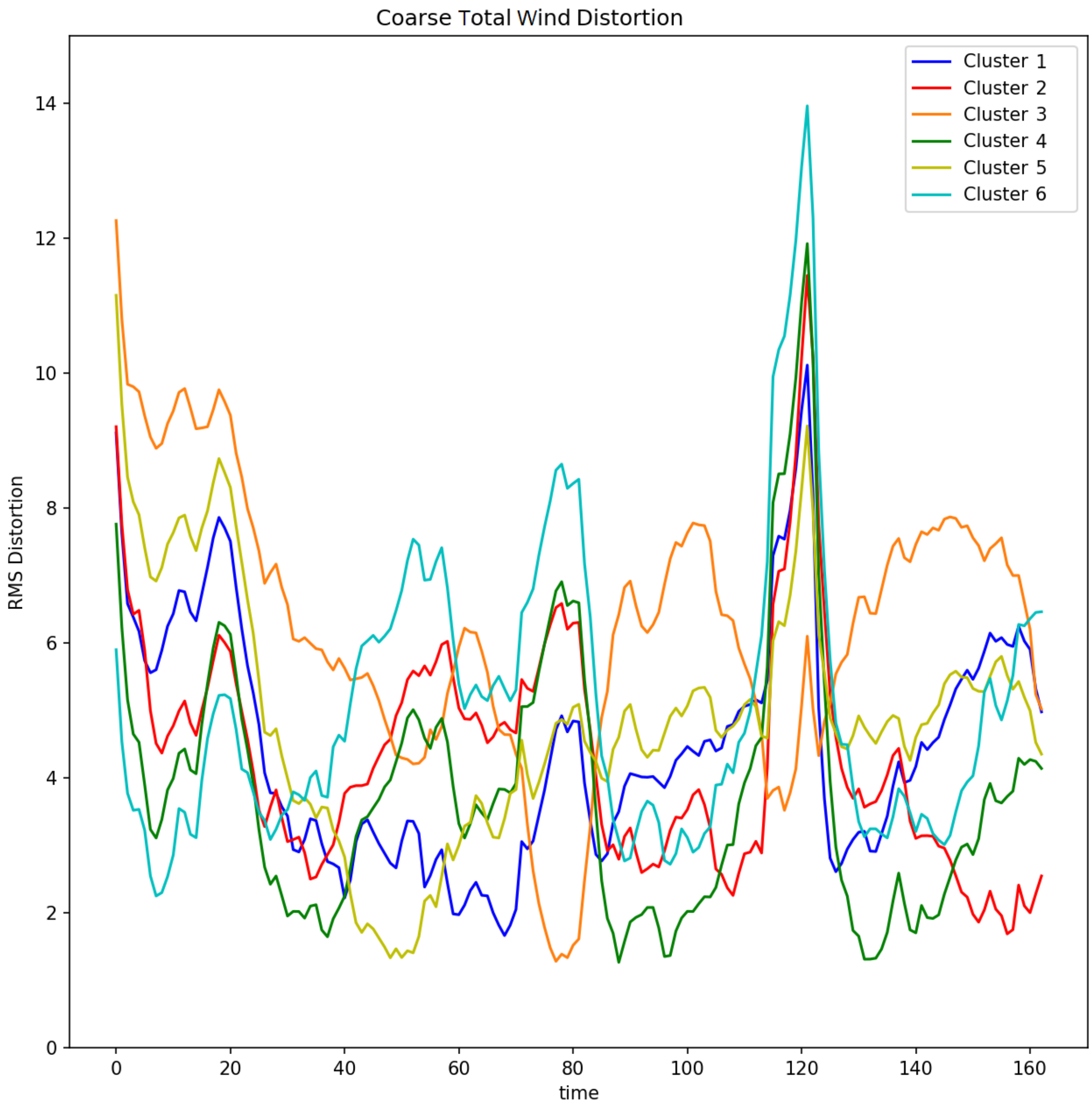

Figure 7.10: D_k of the Case 3 Coarse Simulation.

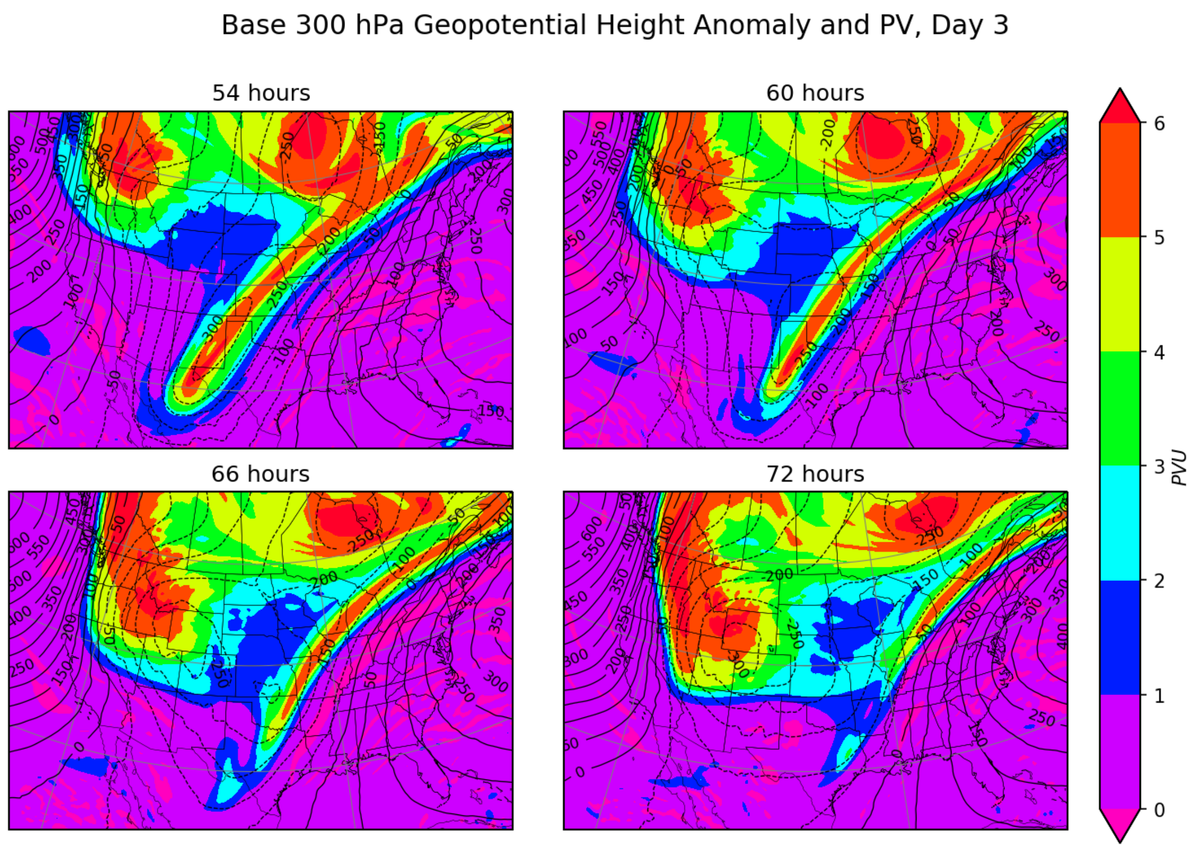

Figure 7.11: Case 3 Base 300 hPa Geopotential Height Anomaly and PV, Day 3. Contour intervals are 50 gpm for height and 1 PVU for PV.

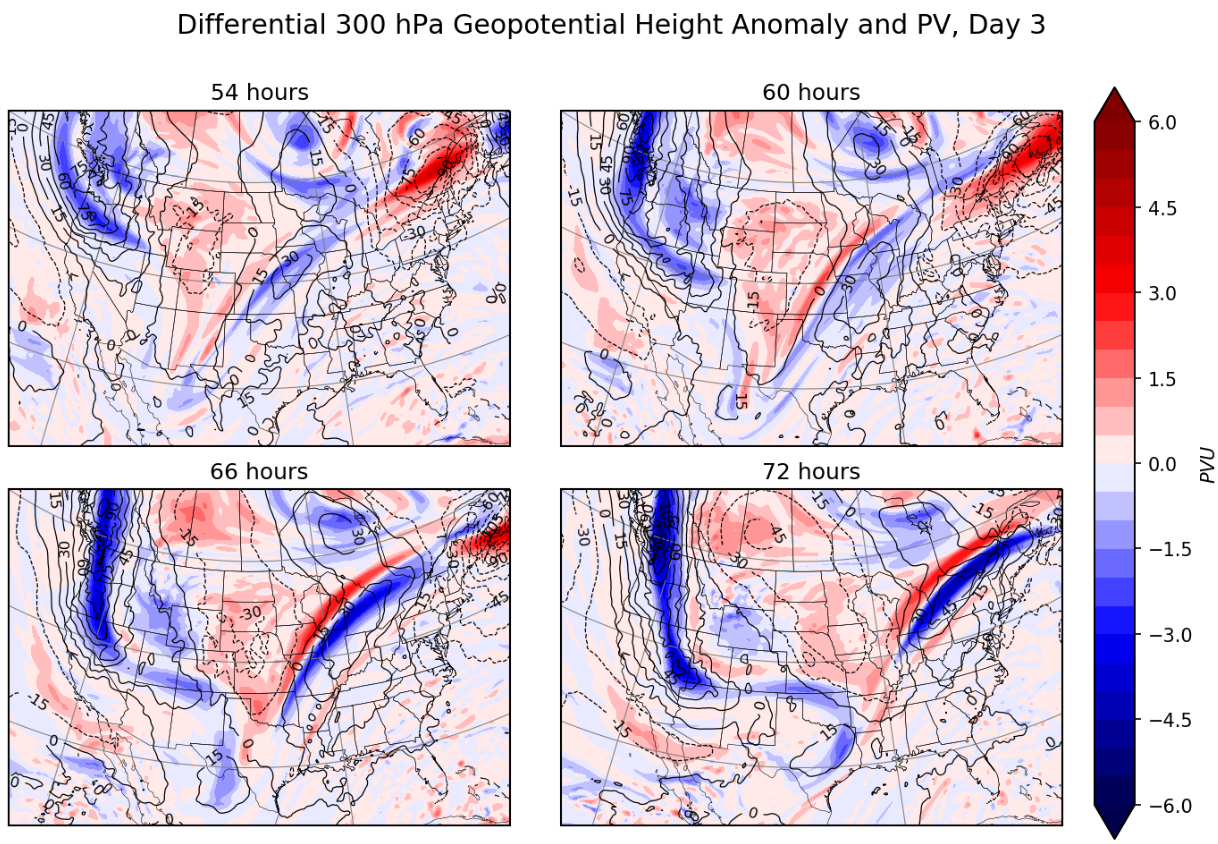

Figure 7.12: Case 3 Differential 300 hPa Geopotential Height Anomaly and PV, Day 3.

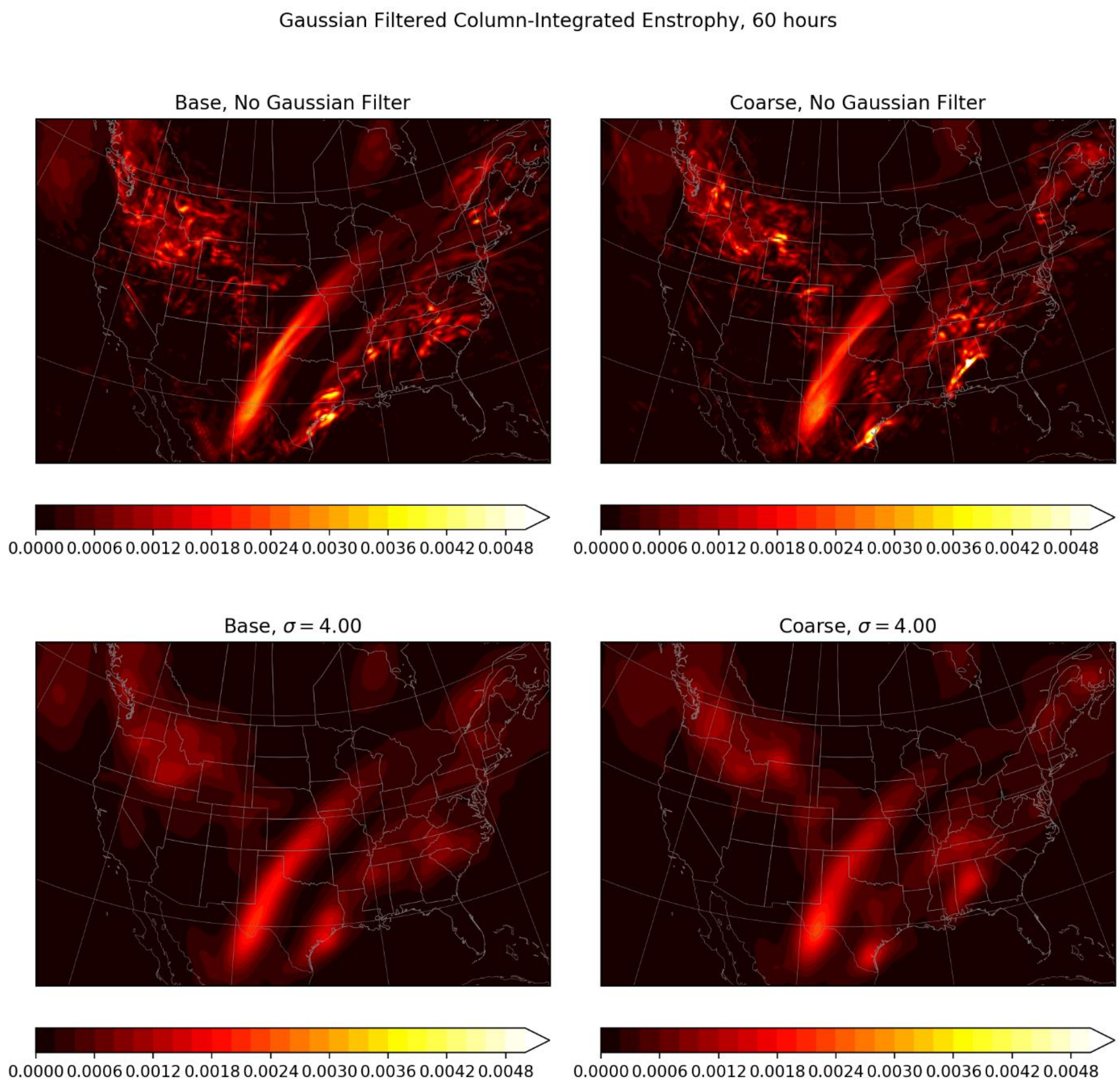

Figure 7.13: Case 3 Column-Integrated Enstrophy at 60 Hours. Contour intervals are $2x10^{-4}$ hPa s^{-1}.

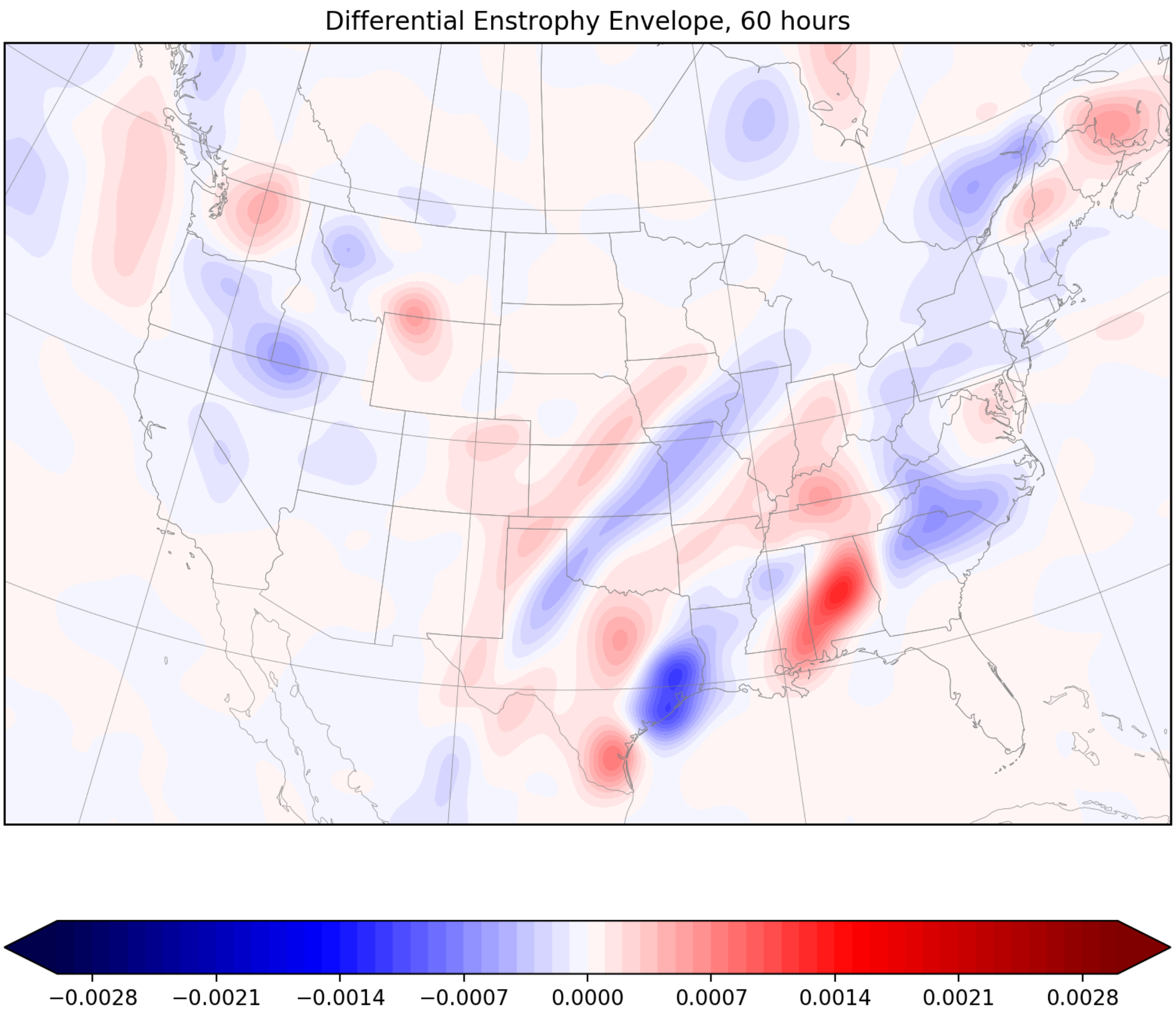

1791

1792 Figure 7.14: Case 3 Differential Enstrophy Envelope at 60 Hours. Contour intervals are 10^{-4} hPa s^{-1}.

1793

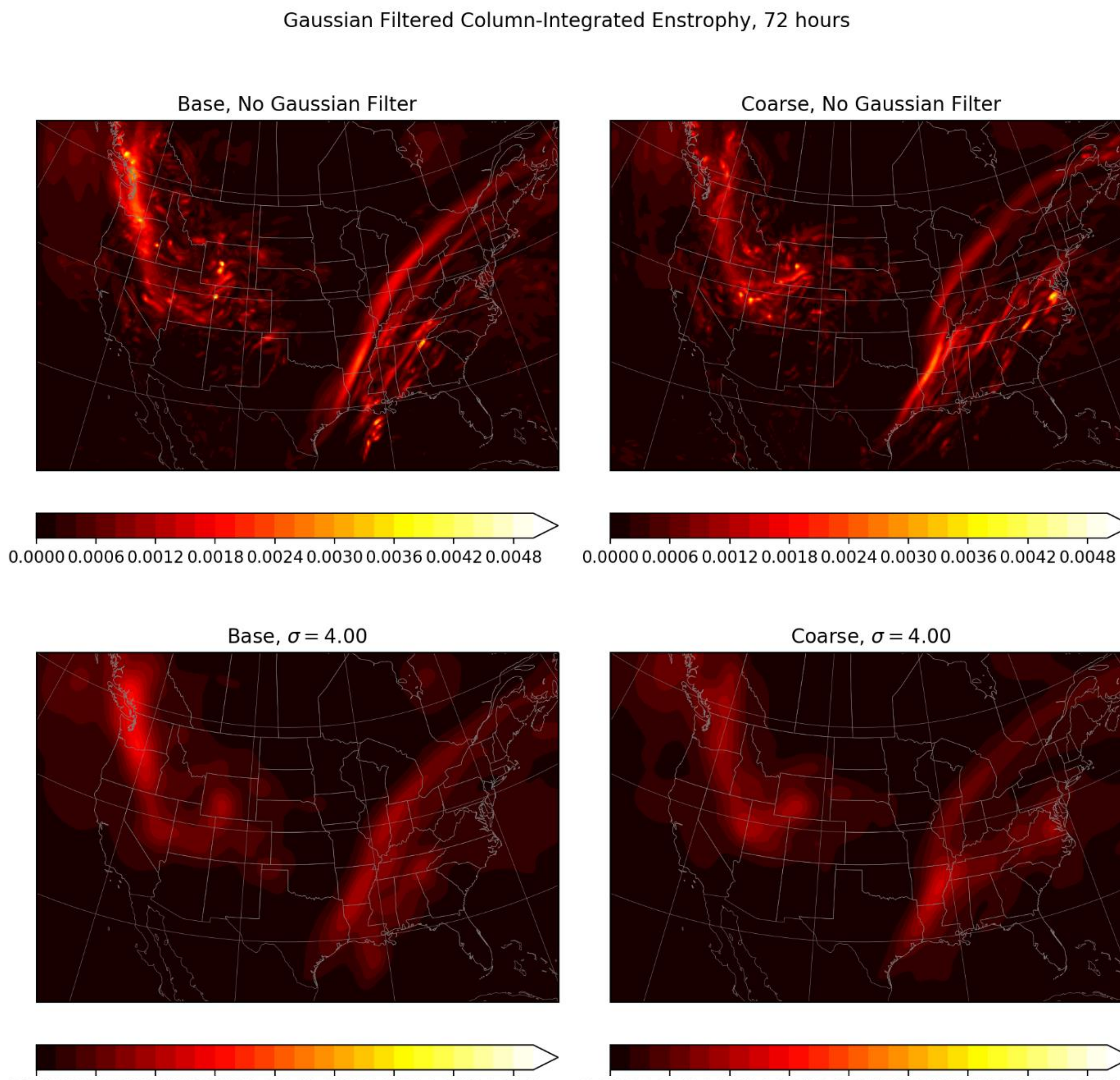

Figure 7.15: Case 3 Column-Integrated Enstrophy at 72 Hours. Contour intervals are $2x10^{-4}$ hPa s^{-1}.

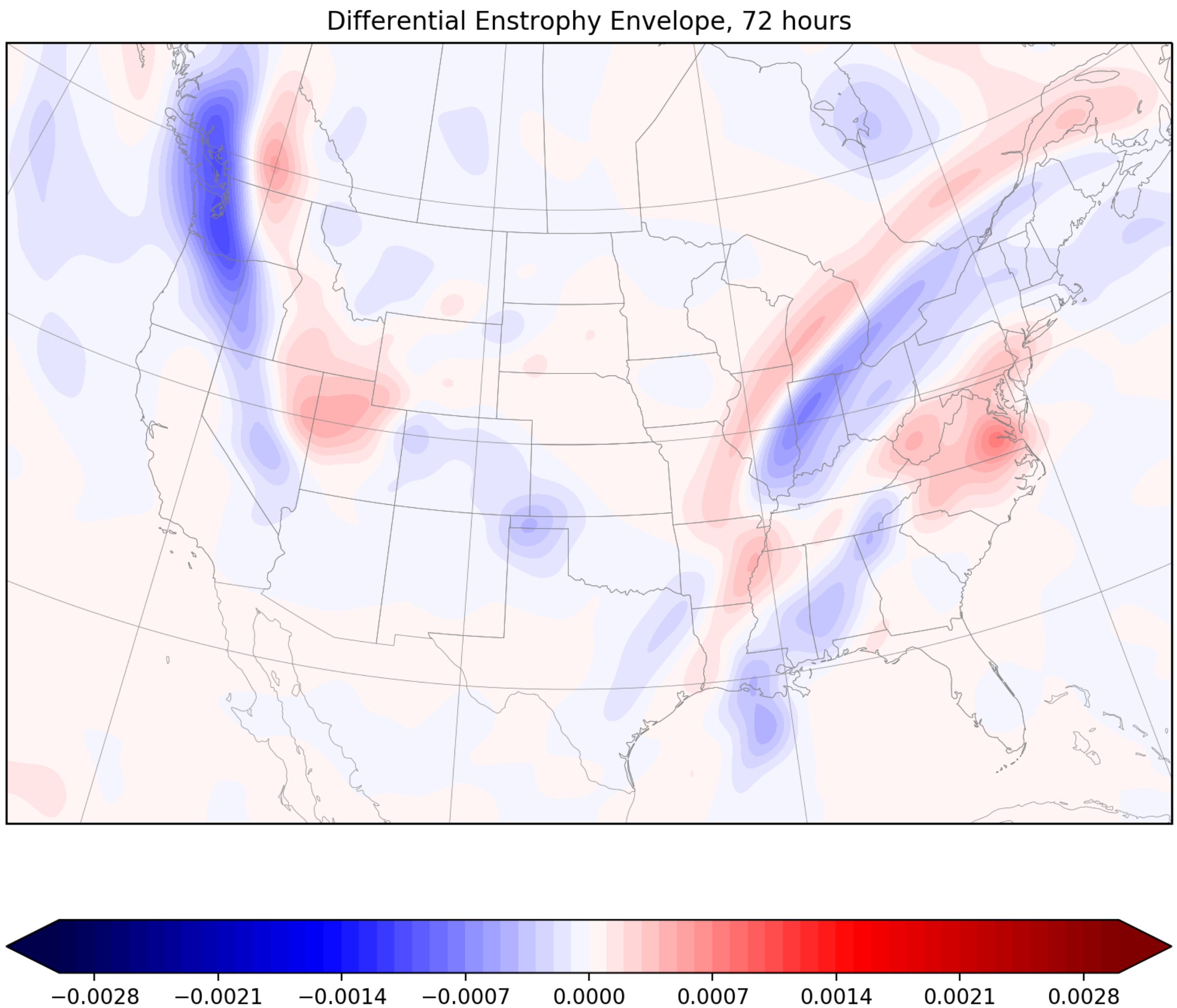

Figure 7.16: Case 3 Differential Enstrophy Envelope at 72 Hours. Contour intervals are 10^{-4} hPa s^{-1}.

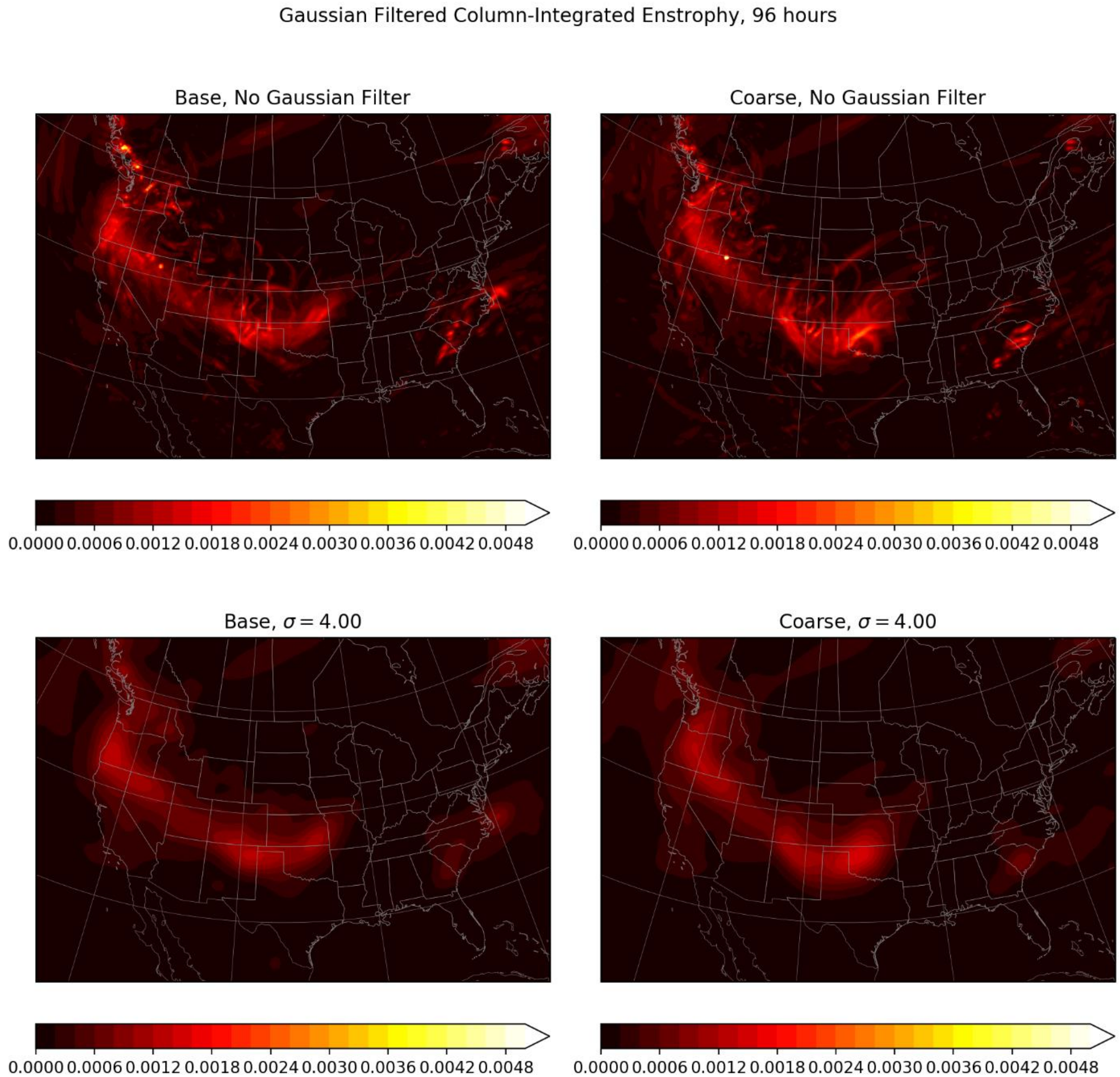

Figure 7.17: Case 3 Column-Integrated Enstrophy at 96 Hours. Contour intervals are 2x10^{-4} hPa s^{-1}.

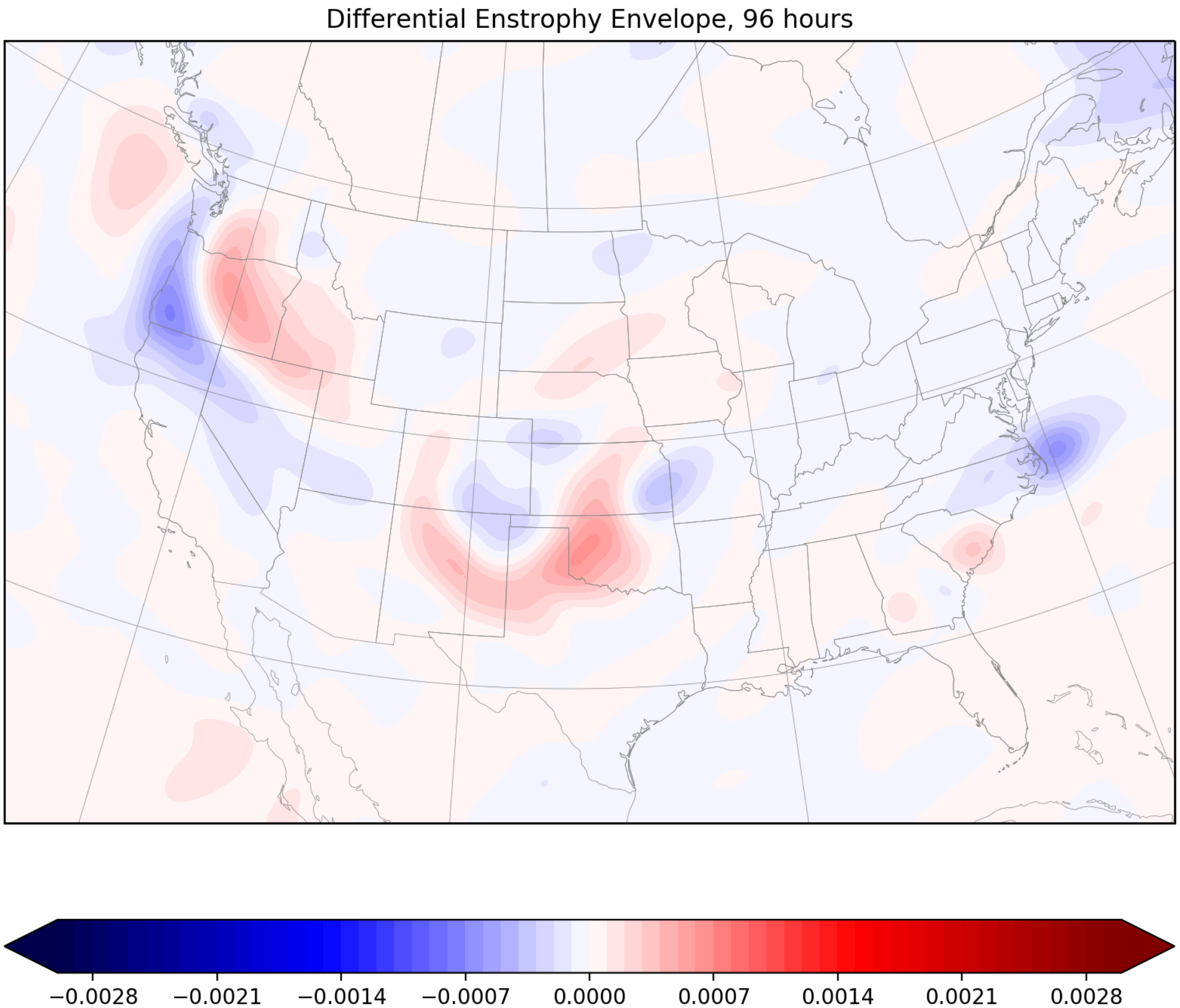

Figure 7.18: Case 3 Differential Enstrophy Envelope at 96 Hours. Contour intervals are 10^{-4} hPa s^{-1}.

1806

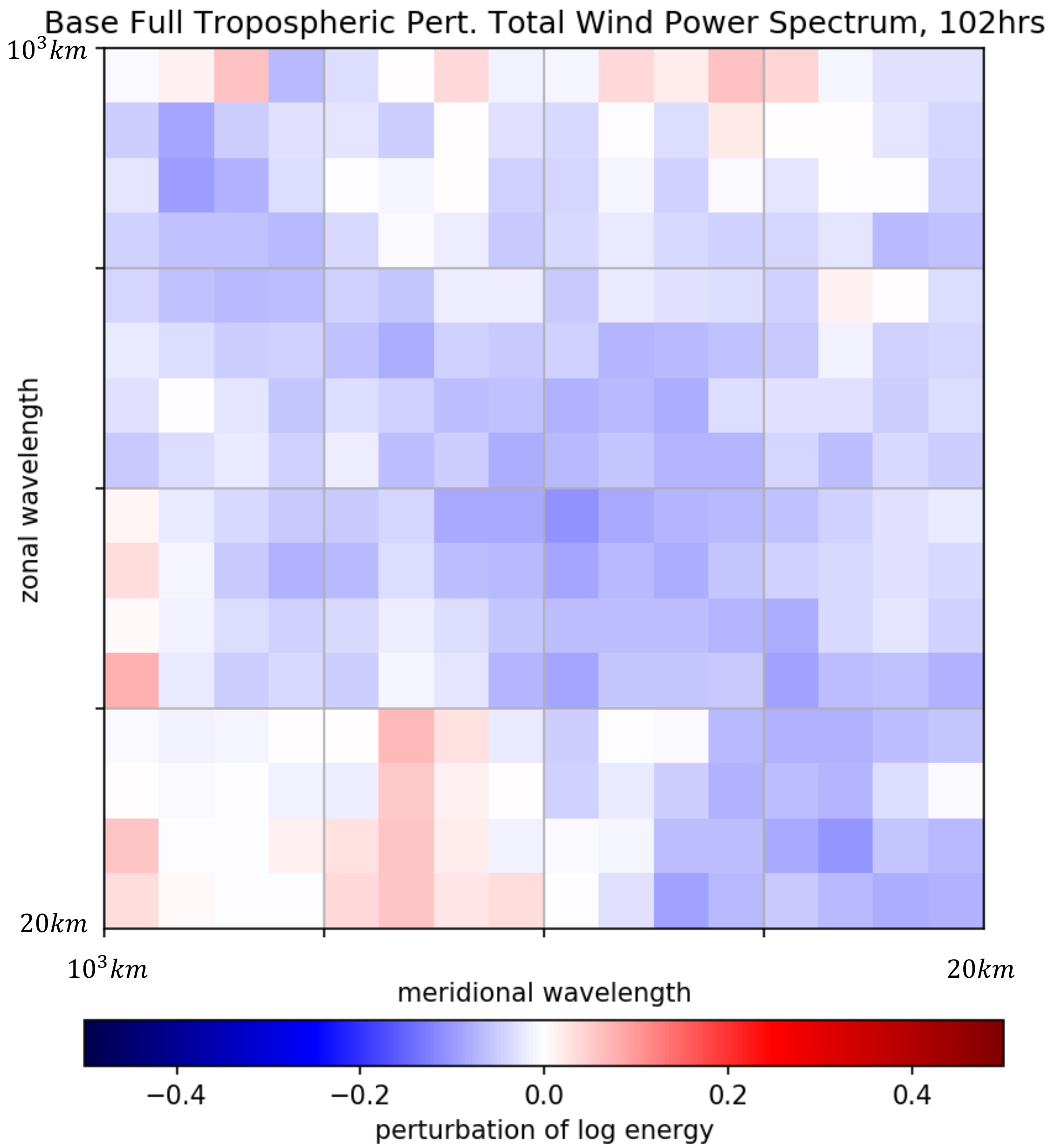

1807 Figure 7.19: Case 3 Base Full Troposphere Perturbation Total Wind Power Spectrum at 102 Hours.

1808

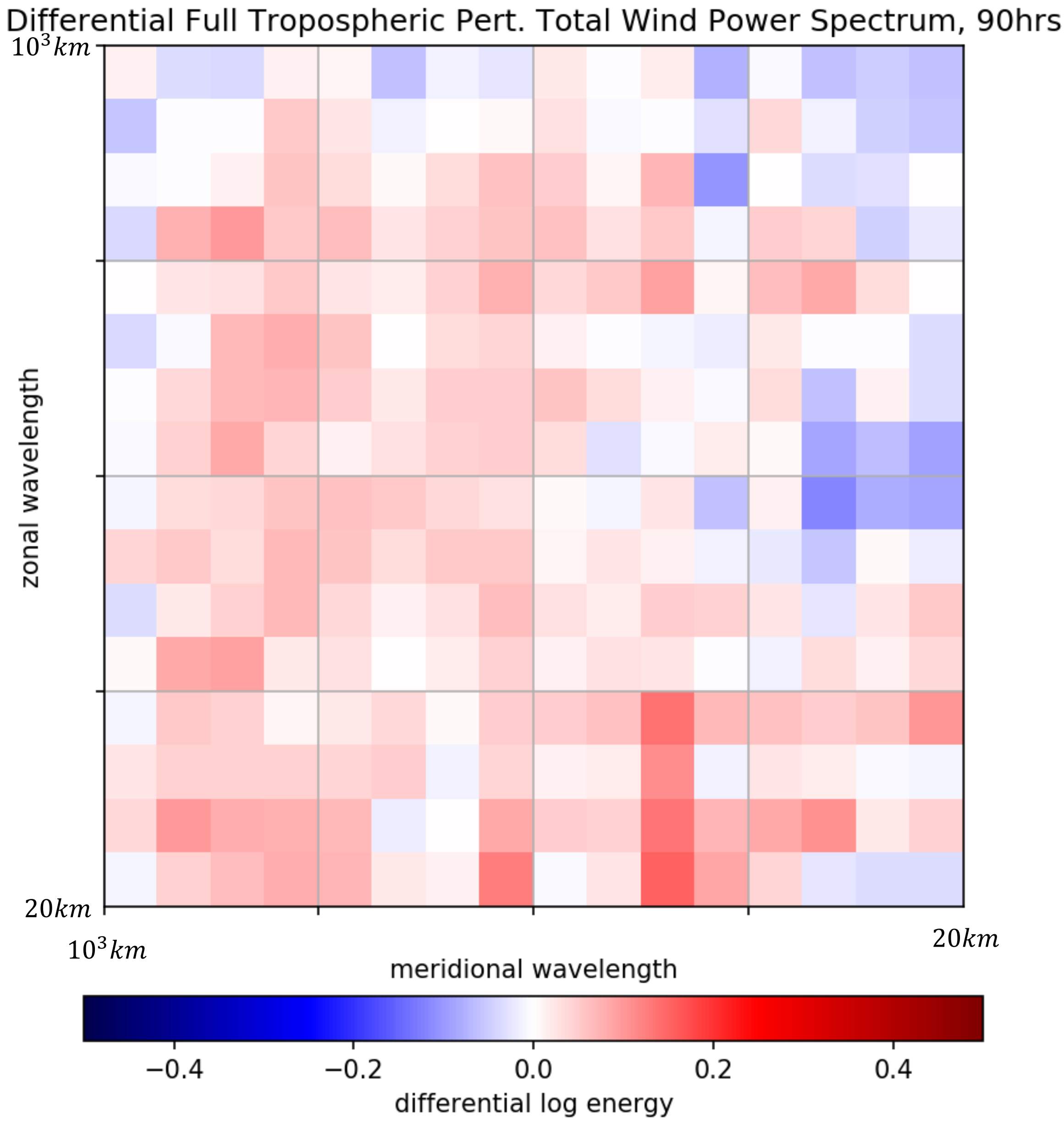

1809

1810 Figure 7.20: Case 3 Differential Full Tropospheric Perturbation Total Wind Power Spectrum at 102 Hours.

1811

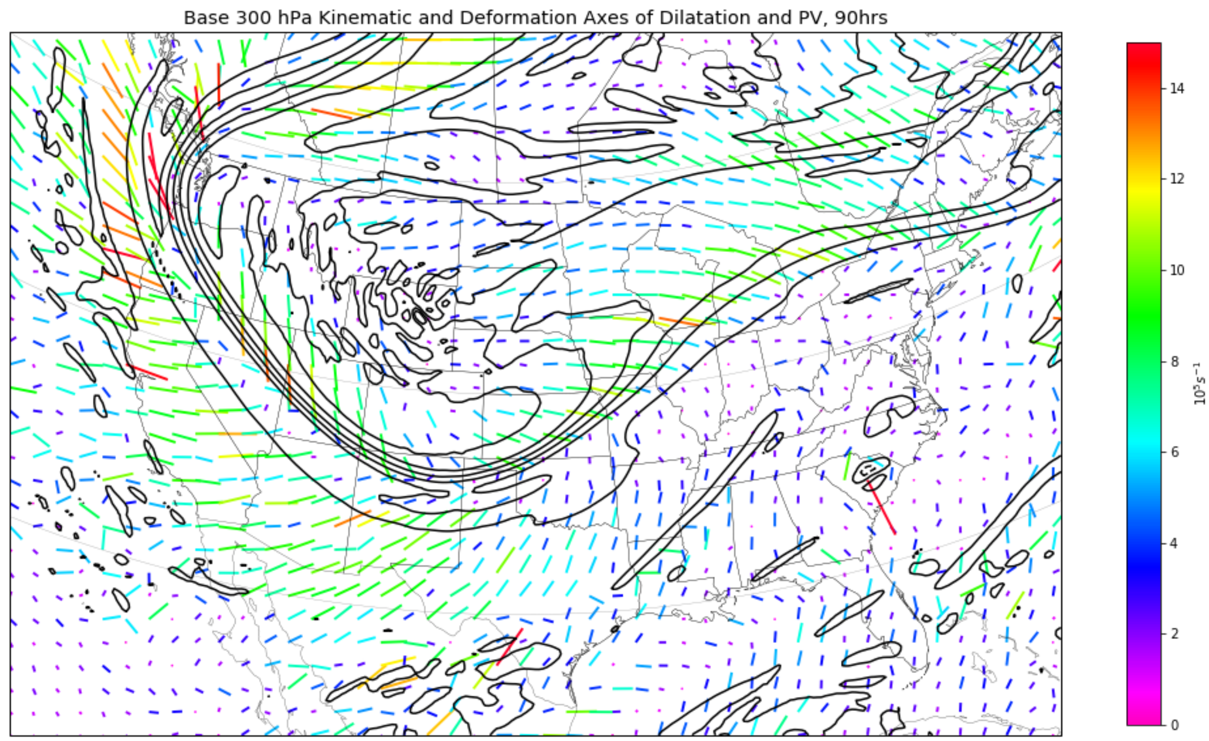

Figure 7.21: Case 3 Base 300 hPa Kinematic Deformation Axes of Dilatation and PV at 90 Hours. Units are 10^5 s^{-1}.

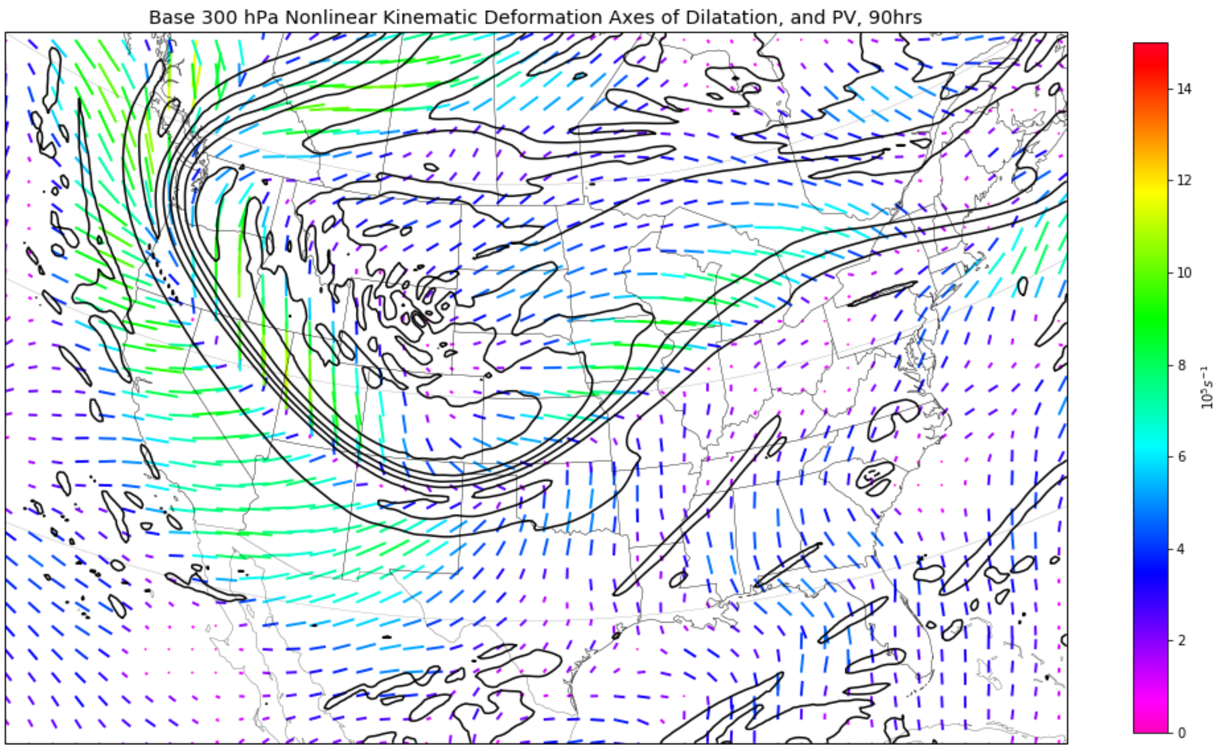

Figure 7.22: Case 3 Base 300 hPa Kinematic Deformation Axes of Dilatation, Nonlinear Component Only, and PV at 90 Hours. Units are 10^5 s^{-1}.

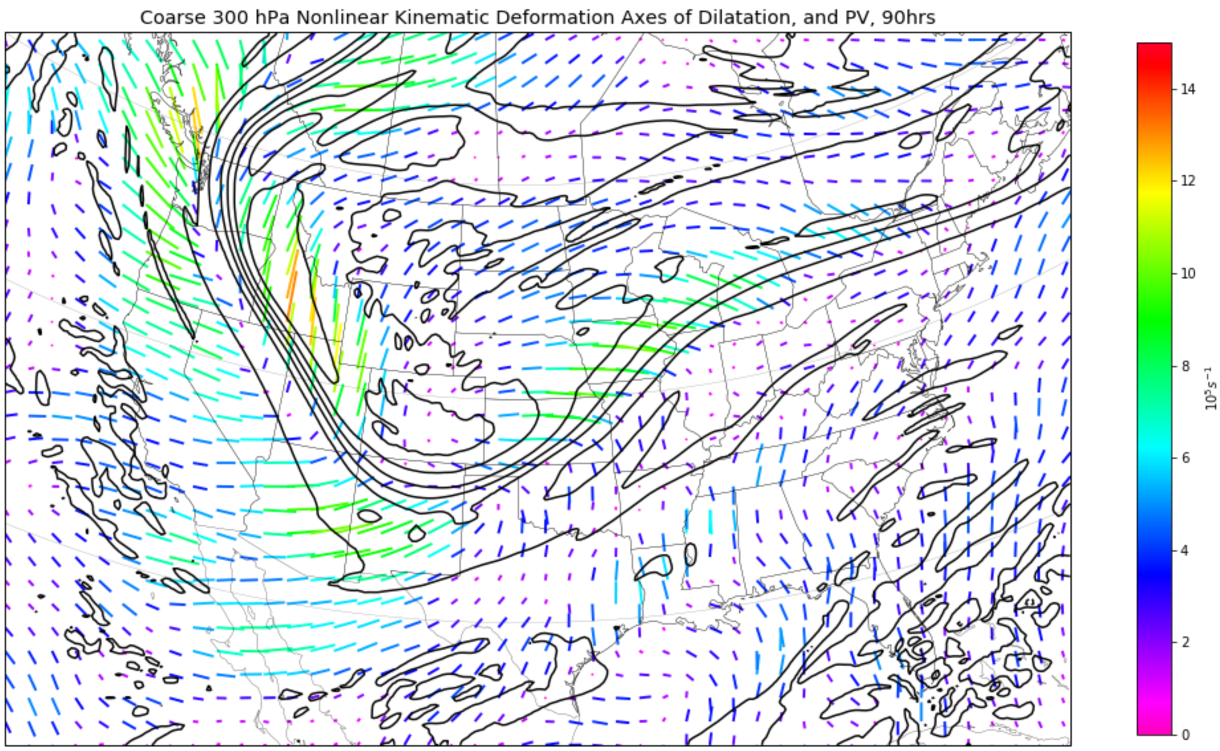

Figure 7.23: Case 3 Coarse 300 hPa Kinematic Deformation Axes of Dilatation, Nonlinear Component Only, and PV at 90 Hours. Units are 10^5 s^{-1}.

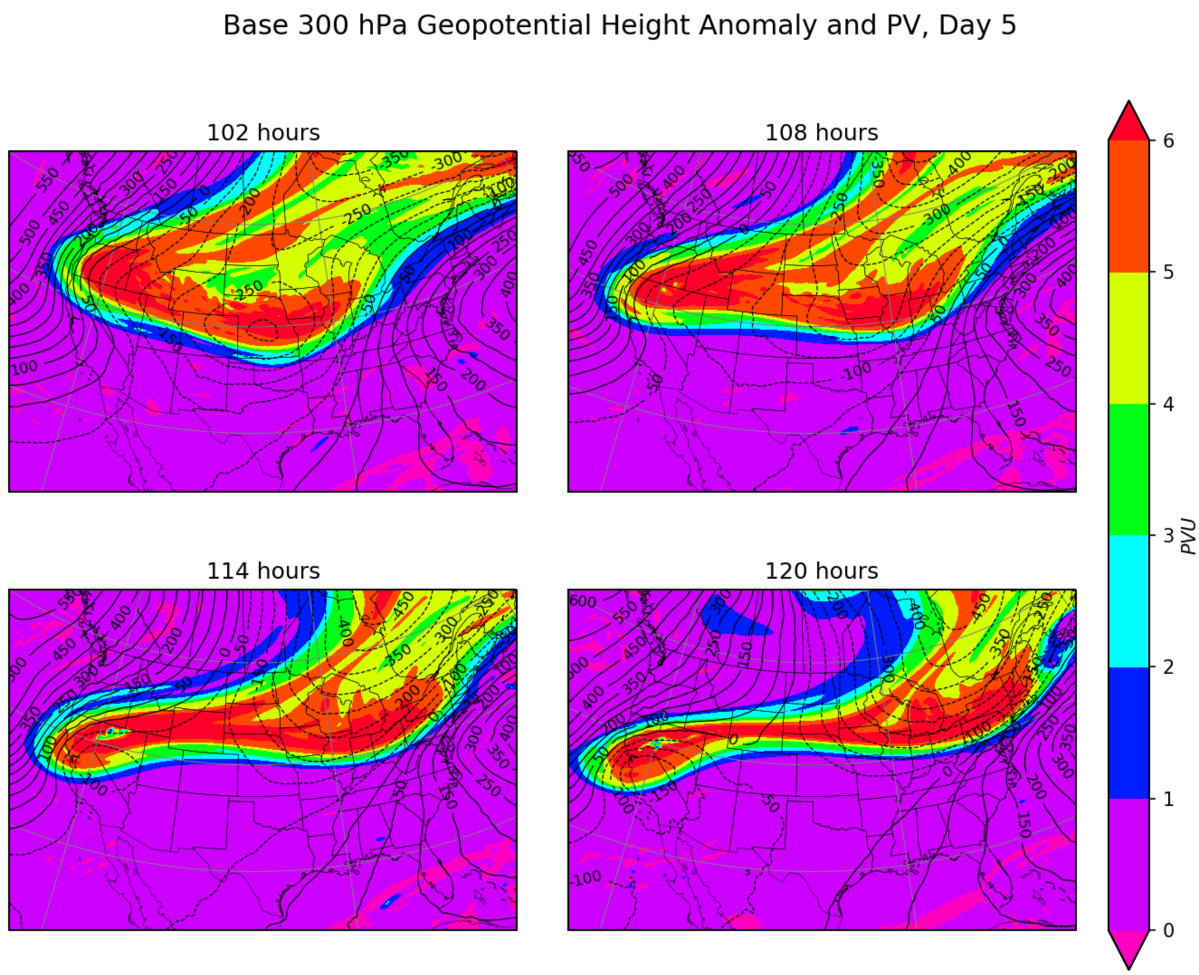

Figure 7.24: Case 3 Base 300 hPa Geopotential Height Anomaly and PV, Day 5. Contour intervals are 50 gpm for height anomaly and 1 PVU for PV.

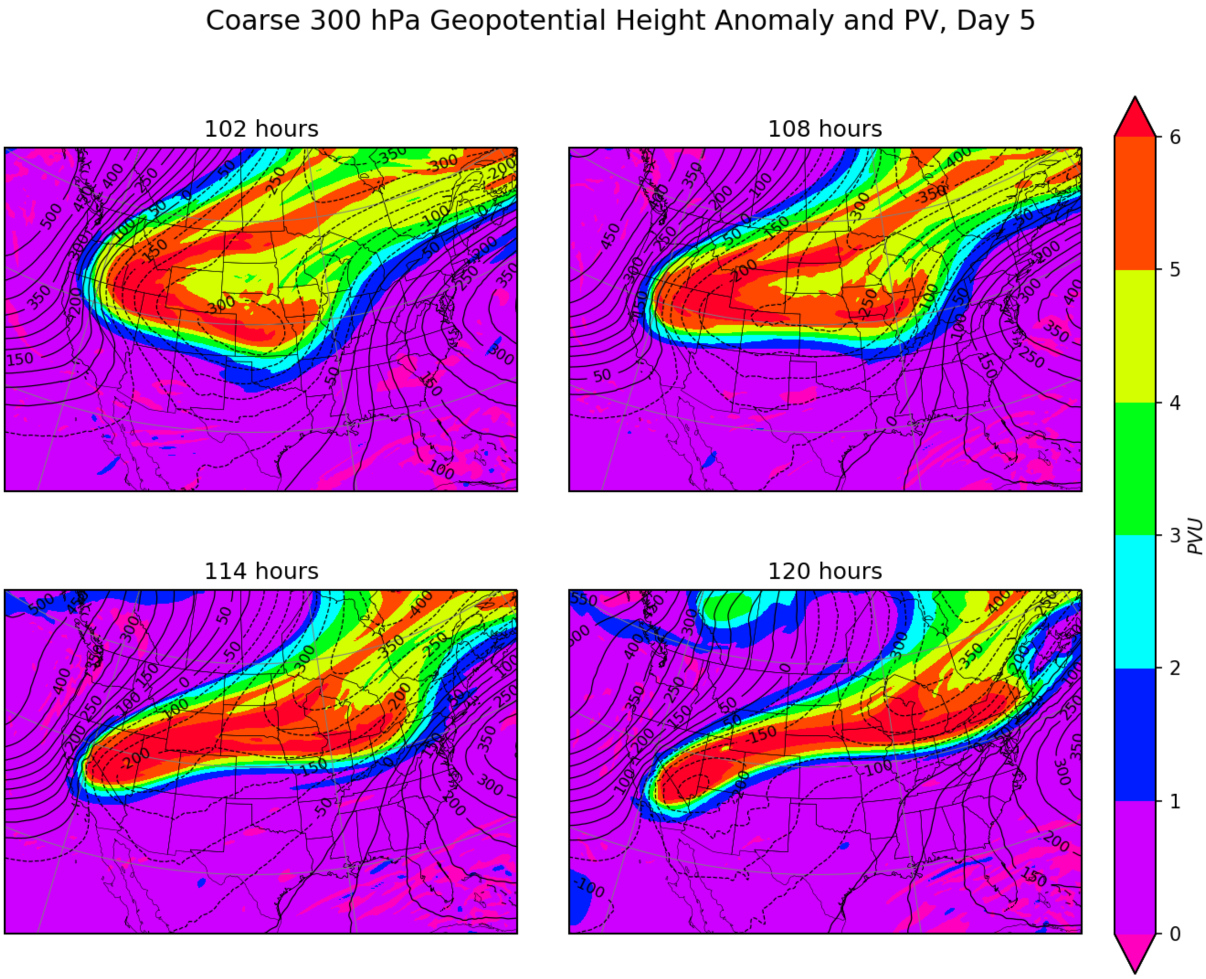

Figure 7.25: Case 3 Coarse 300 hPa Geopotential Height Anomaly and PV, Day 5. Contour intervals are 50 gpm for height anomaly and 1 PVU for PV.

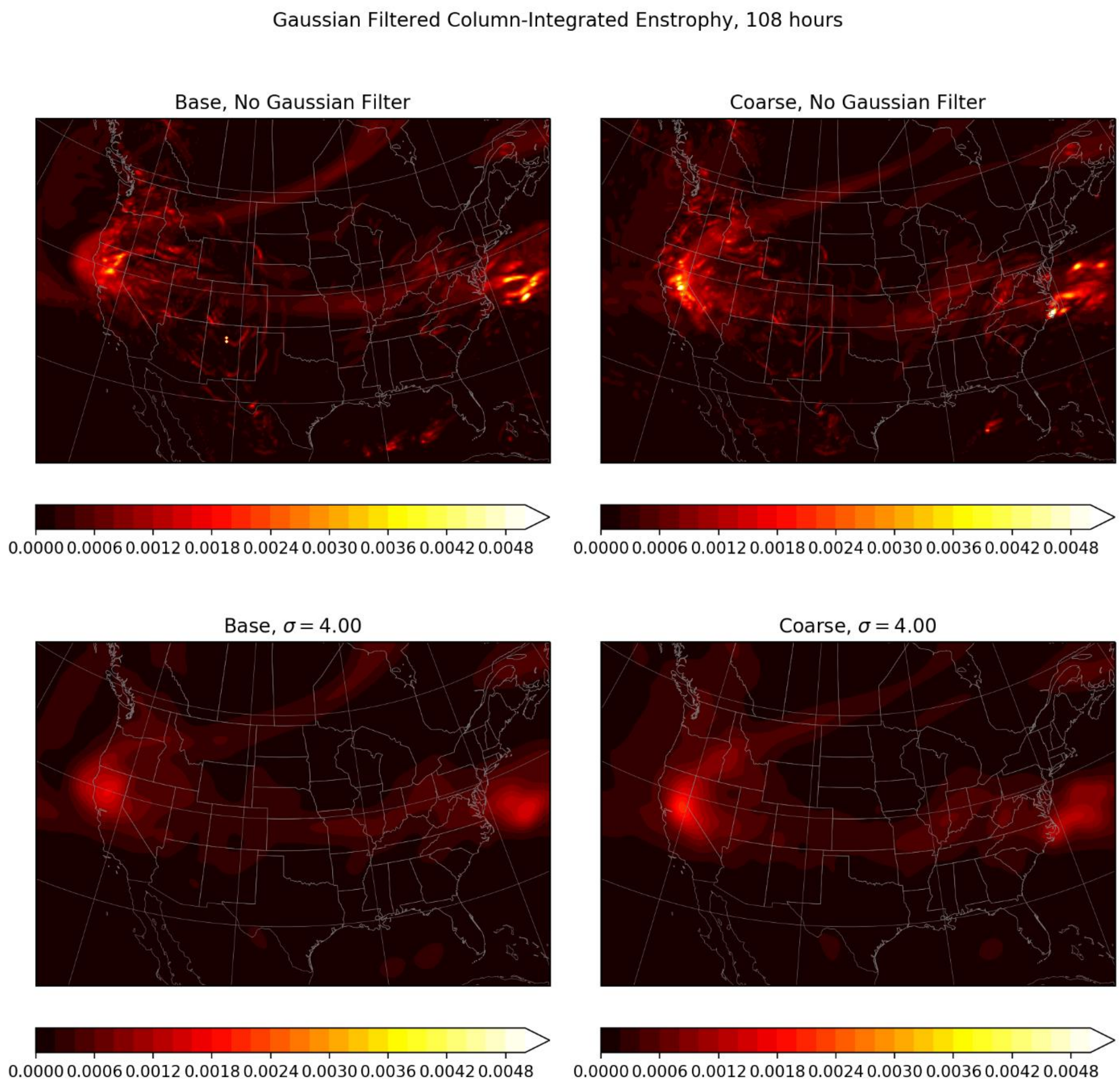

Figure 7.26: Case 3 Column-Integrated Enstrophy at 108 Hours. Contour intervals are $2x10^{-4}$ hPa s^{-1}.

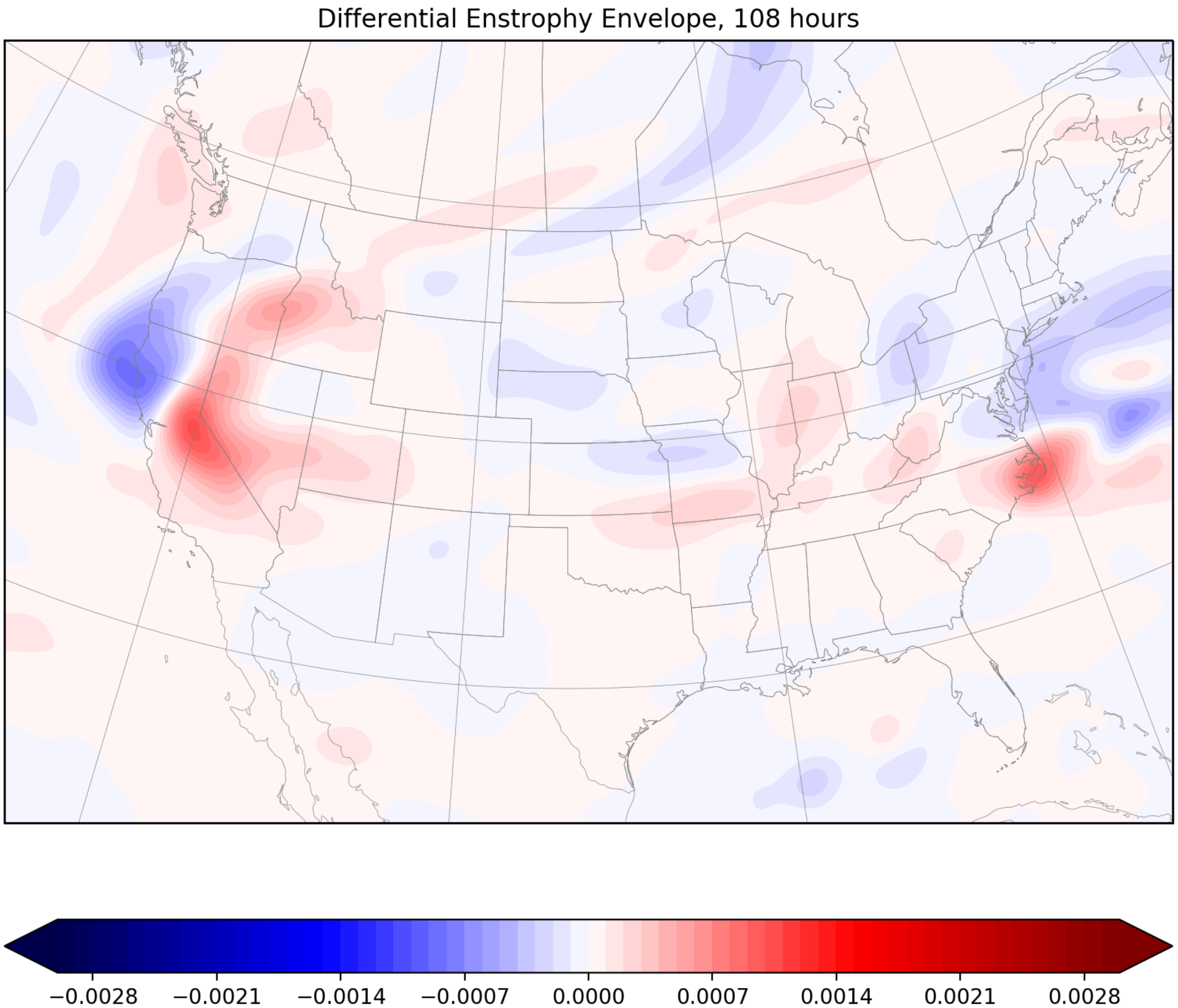

Figure 7.27: Case 3 Differential Enstrophy Envelope at 108 Hours. Contour intervals are 10^{-4} hPa s^{-1}.

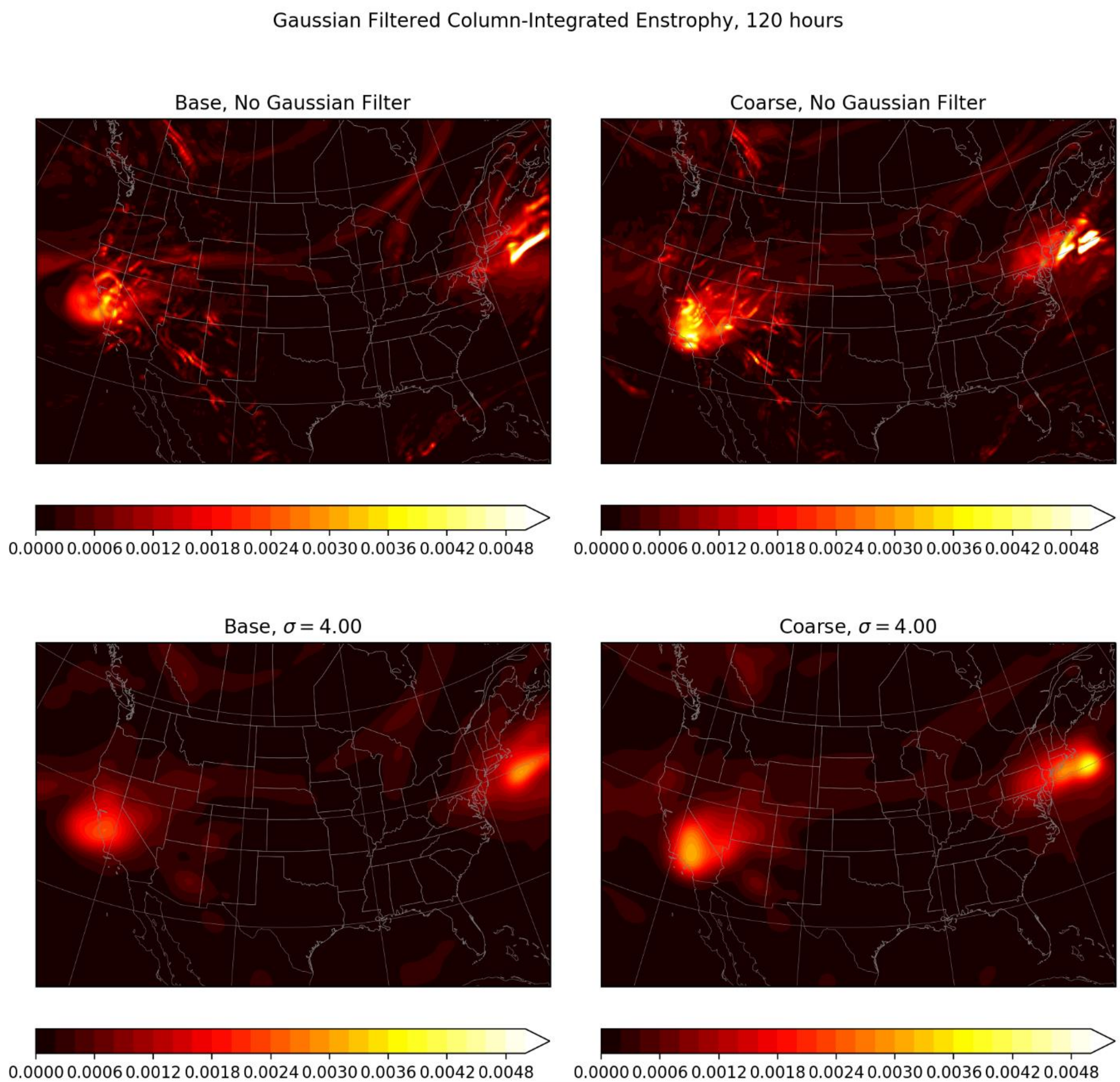

Figure 7.28: Case 3 Column-Integrated Enstrophy at 120 Hours. Contour intervals are 2×10^{-4} hPa s^{-1}.

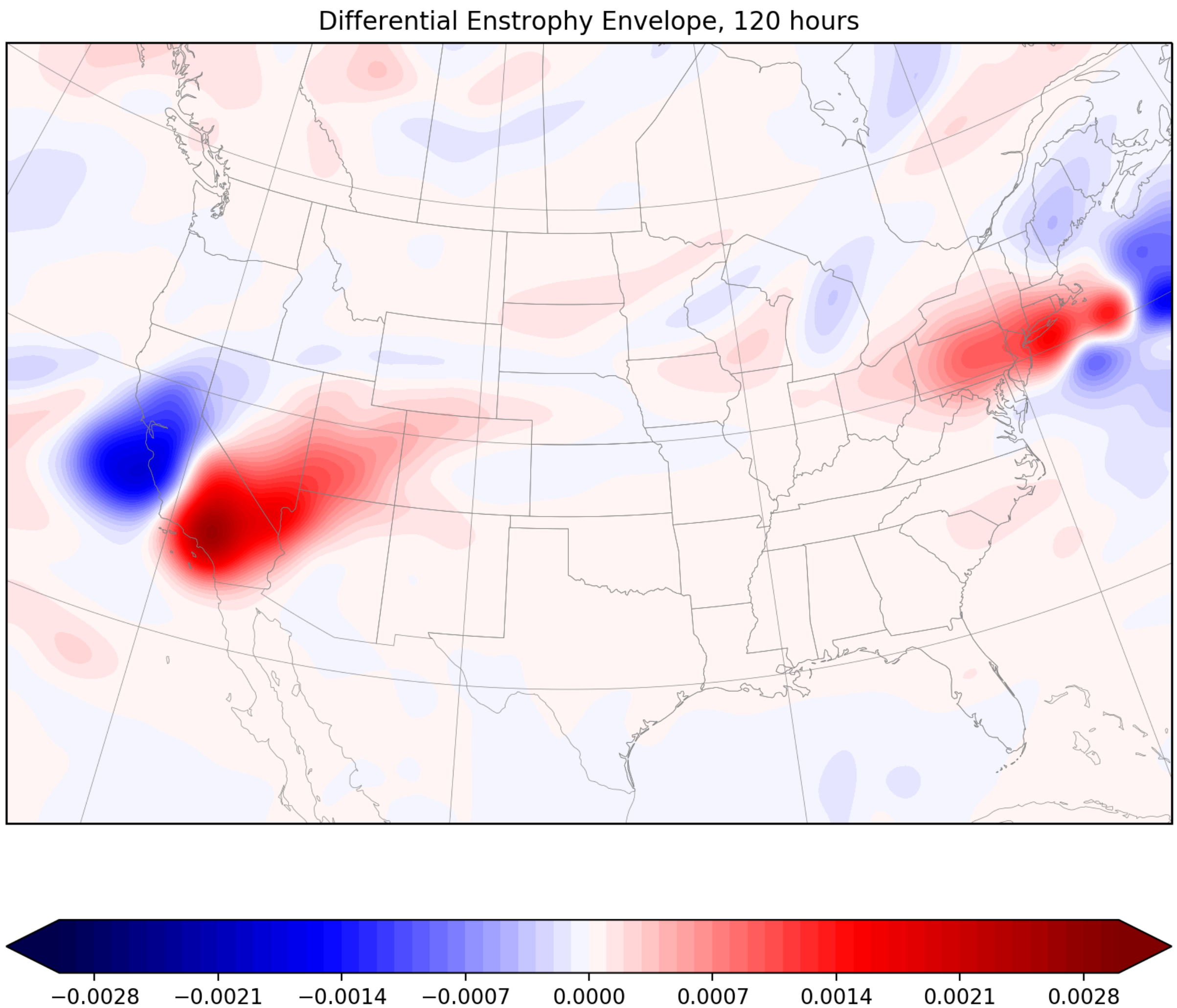

Figure 7.29: Case 3 Differential Enstrophy Envelope at 120 Hours. Contour intervals are 10^{-4} hPa s^{-1}.

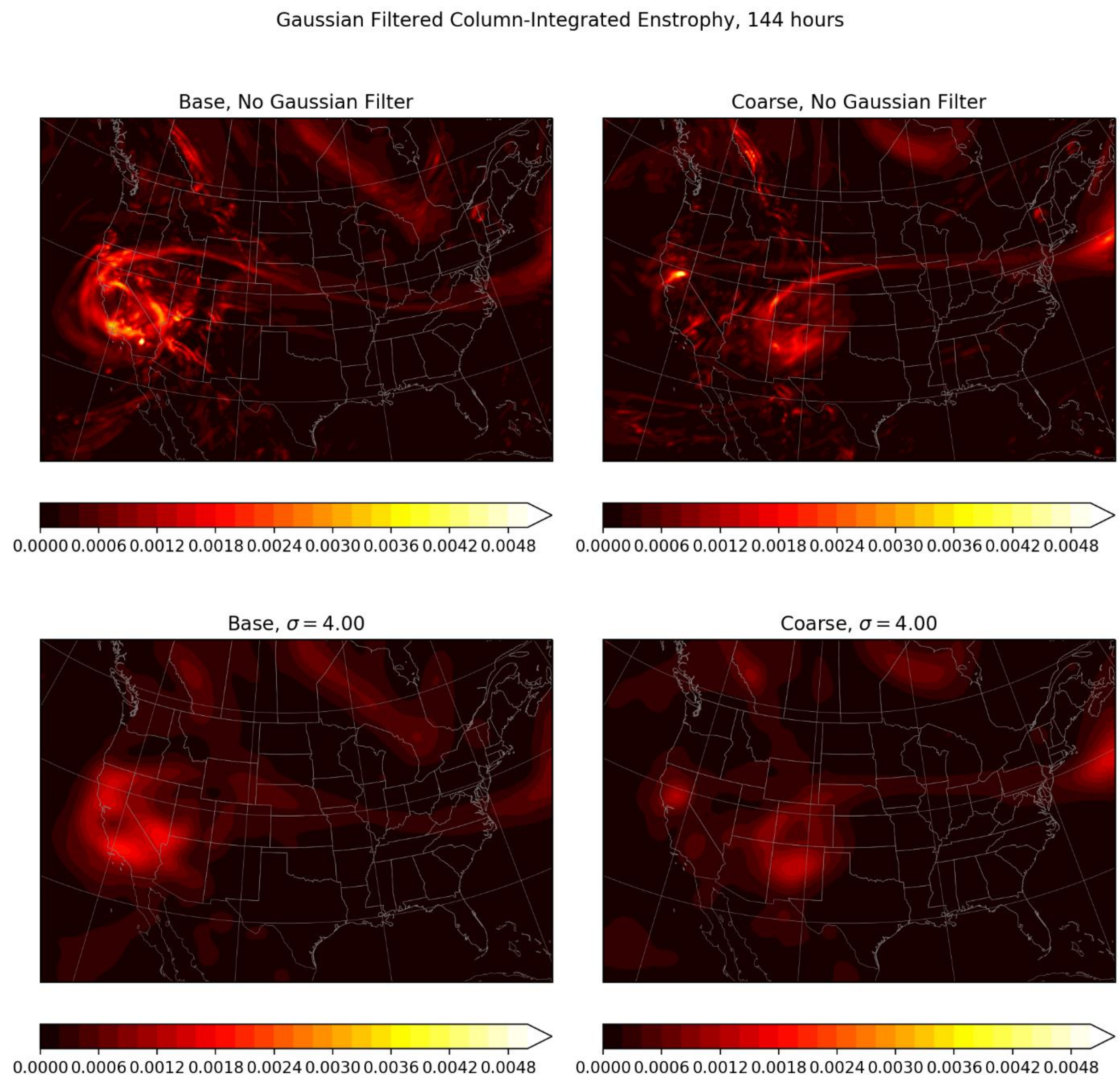

Figure 7.30: Case 3 Column-Integrated Enstrophy at 144 Hours. Contour intervals are $2x10^{-4}$ hPa s^{-1}.

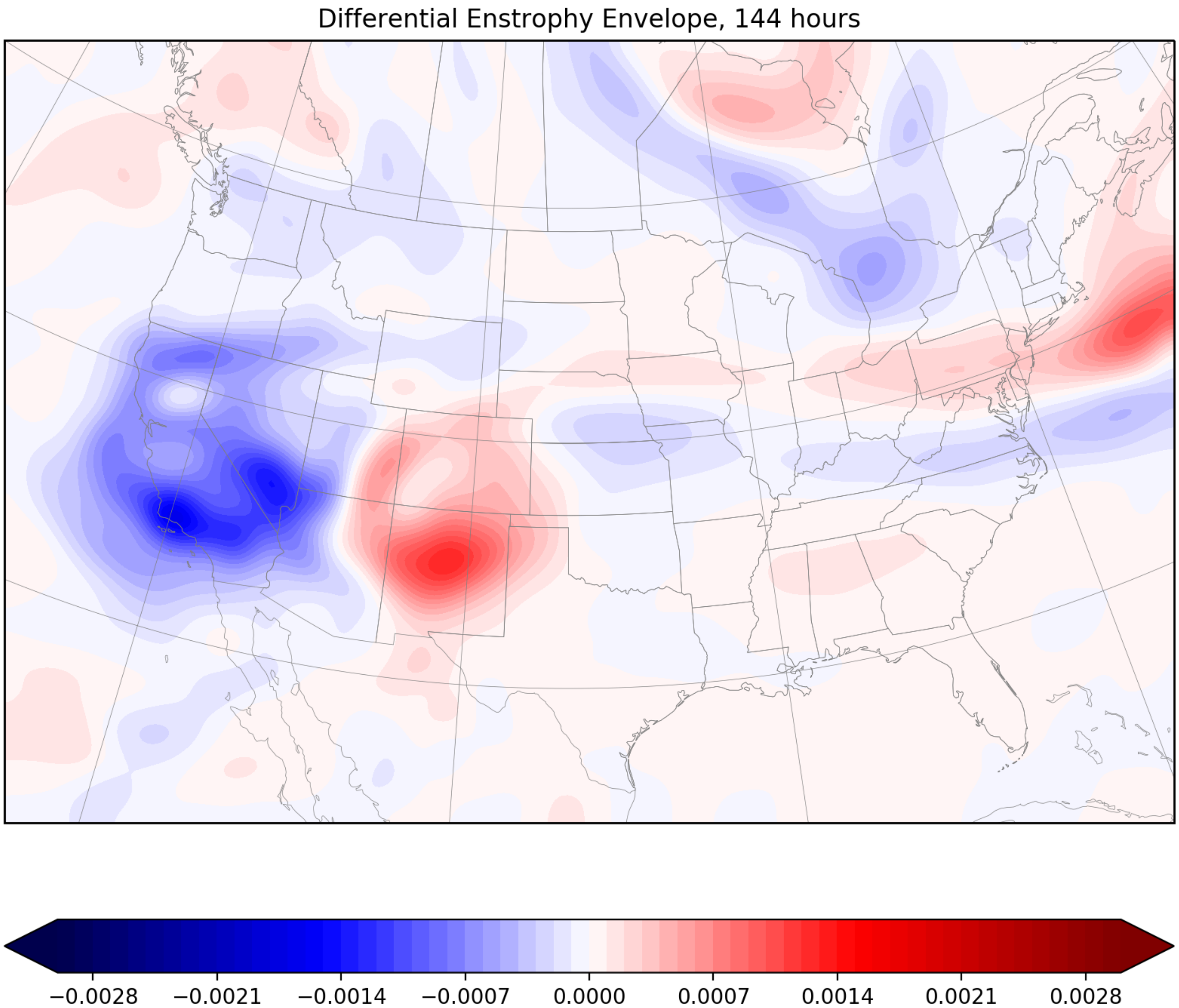

Figure 7.31 Case 3 Differential Enstrophy Envelope at 144 Hours. Contour intervals are 10^{-4} hPa s^{-1}.

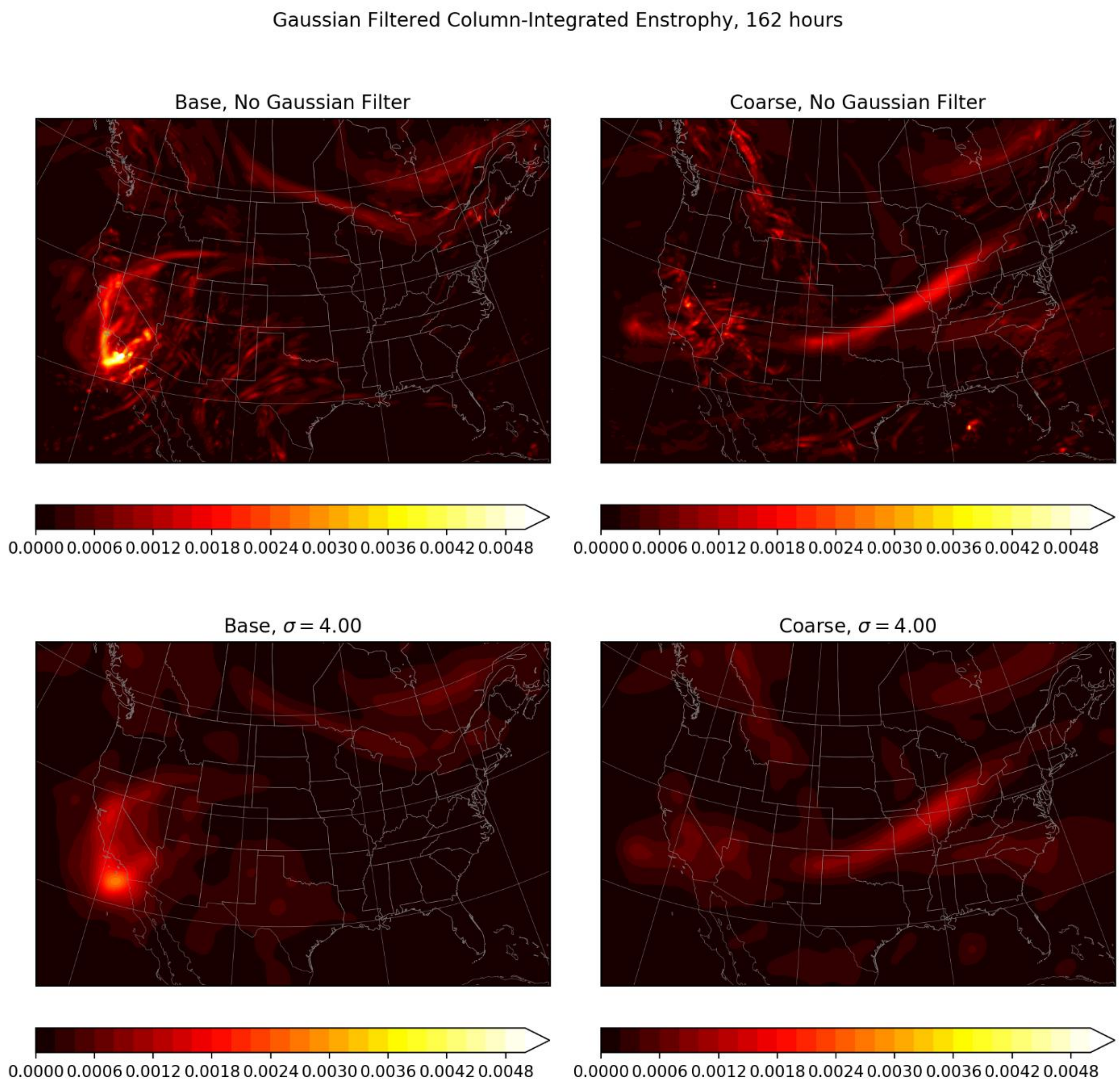

Figure 7.32: Case 3 Column-Integrated Enstrophy at 162 Hours. Contour intervals are $2x10^{-4}$ hPa s^{-1}.

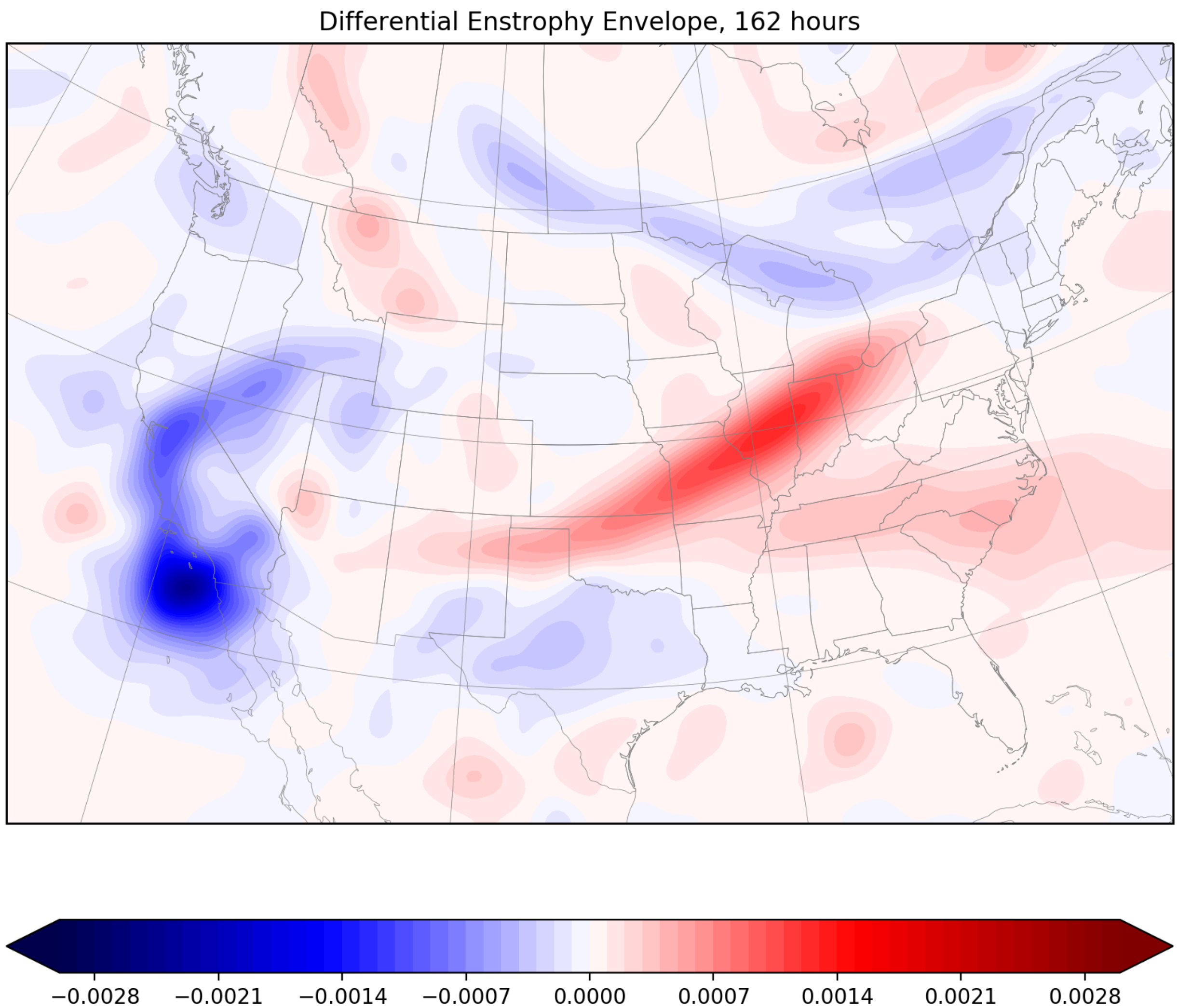

1852

1853 Figure 7.33: Case 3 Differential Enstrophy Envelope at 162 Hours. Contour intervals are 10^{-4} hPa s^{-1}.

1854

CHAPTER VIII

CONCLUSIONS

This study investigated the cascade of energy from subsynoptic scales to the synoptic scales through their influence on moist dynamics. Subsynoptic flow energy was suppressed using a two-dimensional wavelet filter algorithm with a filter threshold calculated using velocity potential variance. Pairs of WRF simulations of three case studies were carried out using standardized initial conditions for all three simulations. A combination of synoptic and statistical analysis was done on the simulation output to identify differences in small-scale variability and precipitation location and intensity that would generate changes to upper-level potential vorticity gradients.

The two-dimensional wavelet filter algorithm is a novel take on an existing algorithm in Azalinni et al. (2005), and is designed to remove a portion of the energy contained within the subsynoptic wavenumber band. Doing so results in synoptic velocity potential and stream function power being largely unchanged and a suppression of subsynoptic velocity potential and stream function power of 0.5 to 1 orders of magnitude at the largest subsynoptic scales to as much as 3 orders of magnitude at smaller scales. This results in a reduction in total tropospheric stream function variance of 1-2% and total tropospheric velocity potential variance of 2-6%. Variance reduction is larger at lower levels.

For added context, the suppression of energy by the wavelet filter and the evolution of energy during the early stages of the simulation run-time can be examined using a convention power spectrum (Errico 1985). We use a Fast Fourier Transform (FFT) algorithm for the computation of the power spectra. For the input data, the computation is carried out on the stream function and velocity potential mirrored across the poles—doing so removes the strong longitudinal trend without introducing false periodicity at the poles. For the simulation output, the spectrum is computed using the total kinetic energy of a square subset of the inner domain mirrored across both axes.

The two-dimensional and one-dimensional radial projection of the model input data's energy spectrum wavenumber space is shown in Figures 8.1 to 8.4. The magnitude of the reduction of power in both the stream function and velocity potential is consistent between the conventional spectra and the two-dimensional wavelet spectra of the Case 1 stream function and velocity potential pre- and post-filtering (Figures 4.5 to 4.8). The conventional spectra also show that the velocity potential sees a reduction in power at a lower subsynoptic wavenumber than the stream function. This is an explicit goal of the filter laid out in Chapter 3.2: removing constituents of the stream function that produce enstrophy but only weakly contribute to the kinetic energy of the mean flow. The conventional spectrum does a better job highlighting this successful aspect of the filter than the wavelet spectrum does due to the wavelet spectrum's binning. The conventional spectra demonstrate the efficacy of the newly designed wavelet filter and confirms the reduction of power of these variables at the desired scales. However, Figure 8.4 also shows an odd pattern in the velocity potential high wavenumber range that is not in the other conventional spectra nor in the wavelet spectra. This is caused by the false periodicity introduced in the coarse data by the wavelet filter near the poles (see Chapter 4). So the conventional spectra also demonstrate the need for further improvement on the application of wavelet filters on global geophysical data sets.

All cases shared some commonalities in the nodal distribution of their perturbation energy partitions and their trends through the simulations. Model spin-up is identifiable in the perturbation energy partition where, for the first 4-6 hours, there is a significant deficit in small-scale perturbation energy for both zonally and meridionally elongated nodes compared to later simulation times. The conventional spectrum, using Case 1 as a representative example (Figure 8.5), demonstrates this as well, despite there being artifacts in the wavenumber bands not resolvable by the outer domain. Filtering, as expected, introduces a further reduction of energy at subsynoptic scales, especially in the wavenumber band corresponding to the wavenumbers targeted by the filtering (Figure 8.6). The calculated power laws show the simulations are primarily resolving the energy injection wavenumbers, as the minimum grid resolution is too large to simulate much, if any, of the inertial subrange. During spin-there is a steady growth of power in the upper mesoscale wavenumber band (Figure 8.7) which agrees with the observed trends in the wavelet spectra and energy partitions. Suppression of subsynoptic energy in the coarse simulation results in the mid-range resolvable wavenumber energy being persistently weaker than the base simulation for around 24 hours (Figure 8.8). The delay in the production of small-scale energy foments a differential development of small-scale variability between the two simulations, as demonstrated by their differential enstrophy. This behavior can be identified in both the wavelet energy partitions and the conventional spectra.

Zonally elongated perturbations' kinetic energy is mostly found along the subtropical jet where the background zonal flow is the strongest. Meridionally elongated perturbations' kinetic energy is primarily in the northern mid-latitudes, but when there is strong perturbation growth along the subtropical jet, the zonal and meridional perturbation energy partitions tend to overlap. During wave amplification, there is a reduction in the energy of the largest zonally elongated perturbations and an increase in the energy of the largest meridionally elongated perturbations, as well as a reduction in the isotropic energy at the largest scales. The onset of high amplitude jet-stream waves results in a brief, rapid increase in all nodal kinetic energy save for the domain-scale isotropic scales.

Mesoscale and small-scale variability influences large-scale perturbations through the injection of energy via latent heat release and moist dynamics. Differences in the development of small-scale variability between the two simulations contributed to differences in precipitation patterns between the two simulations. It is not clear whether small-scale variability drives precipitation differences in these simulations or whether chaotic differences in simulation-parameterized precipitation drive the small-scale variability. Cases 1 and 2 suggest that it is the former, as broad areas of enhanced enstrophy frequently existed prior to the onset of precipitation-amplified variability. The locations where small-scale variability develops tend to be similar between simulations, so existing subsynoptic scale flow components may limit the spatial distributions of new small-scale variability.

Using assignment of cluster states via D_k is a convenient way to characterize the behaviors described above. When energy at subsynoptic scales is small and energy at synoptic scales tends to be large, some combination of synoptic isotropic and elongated perturbations' energy is always present in at least one cluster. As waves amplify, there is a transition to clusters with less energy in isotropic perturbations and increased energy in subsynoptic and mesoscale partitions. For Cases 2 and 3, rapid deepening that produces very large perturbation amplitudes results in the assignment to a cluster best described as an *excited state*, which precedes wave breaking and a transition to an assigned cluster that is strongly meridionally elongated; Case 1 does not see such strong perturbation amplitudes until near the end of the simulation, but it appears to have been about to undergo cyclonic wave breaking. Growth of high amplitude waves and their eventual breaking is a common example of the forward energy cascade, but energy partition cluster analysis shows that this process is not simply a cascade of energy downscale but a transformation across spatial orientations. A possible extension of this method would be to create prototypical cluster types, such as a large-scale zonal state, a large-scale meridional state, an excited state, etc., to form more generalized cluster assignments typifying various stages of cyclone life cycles.

Case 3 featured primarily dry dynamics. The moist dynamics in the early hours of the simulation agreed with the behaviors exhibited by the other two cases, namely that isolated hourly precipitation rates in the coarse simulation were higher than the base simulation, but the base simulation had broad regions of higher enstrophy on average. The moist dynamics, however, did not strongly influence the development of the simulated wave breaking, which was instead driven primarily by deformation by the largest perturbation scales. Differences between the two simulations were minimal prior to 126 hours, at which point the coarse simulation deformation ceased to cause filamentation. Case 3 suggests that, without a means of triggering moist dynamics, subsynoptic scale features do not cascade energy up to larger wavenumbers, as their amplitudes are too small to cause large differences in the atmospheric conditions that dictate the behavior of synoptic scale waves. This is in line with the existing body of research on the inertial subrange.

There is still much that is left unknown about the upscale cascade. We primarily focused on perturbation wind energy partitions, identifying their impacts upscale and how those changes altered moist dynamics and PV gradients, but one could easily center the analysis around PV instead, as it is developing PV gradients and anomalies that are impacted most directly by differential precipitation development. Additionally, most of the analysis identified isotropic upscale energy synoptically where possible, but all three cases have strong moist fronts, highly anisotropic sources of energy straddling the synoptic and mesoscales, that strongly impact the shape of large-scale perturbations. Changes to the small-scale atmospheric conditions influence frontogenesis.

Separating the role of small-scale variability on precipitation and the role of precipitation on small-scale variability is also an open problem. It’s difficult to determine how precipitation is influenced by suppressing subsynoptic and other small-scale components of flow, given how differences in precipitation between simulations can also be attributed to chaos. One possibility would be to determine the linearity of the response by adjusting the filter threshold to change how much energy is removed from the system to see whether the simulations diverge more or less quickly, if at all. Another possibility would be to examine the evolution of small-scale perturbations in dry simulations.

Figures

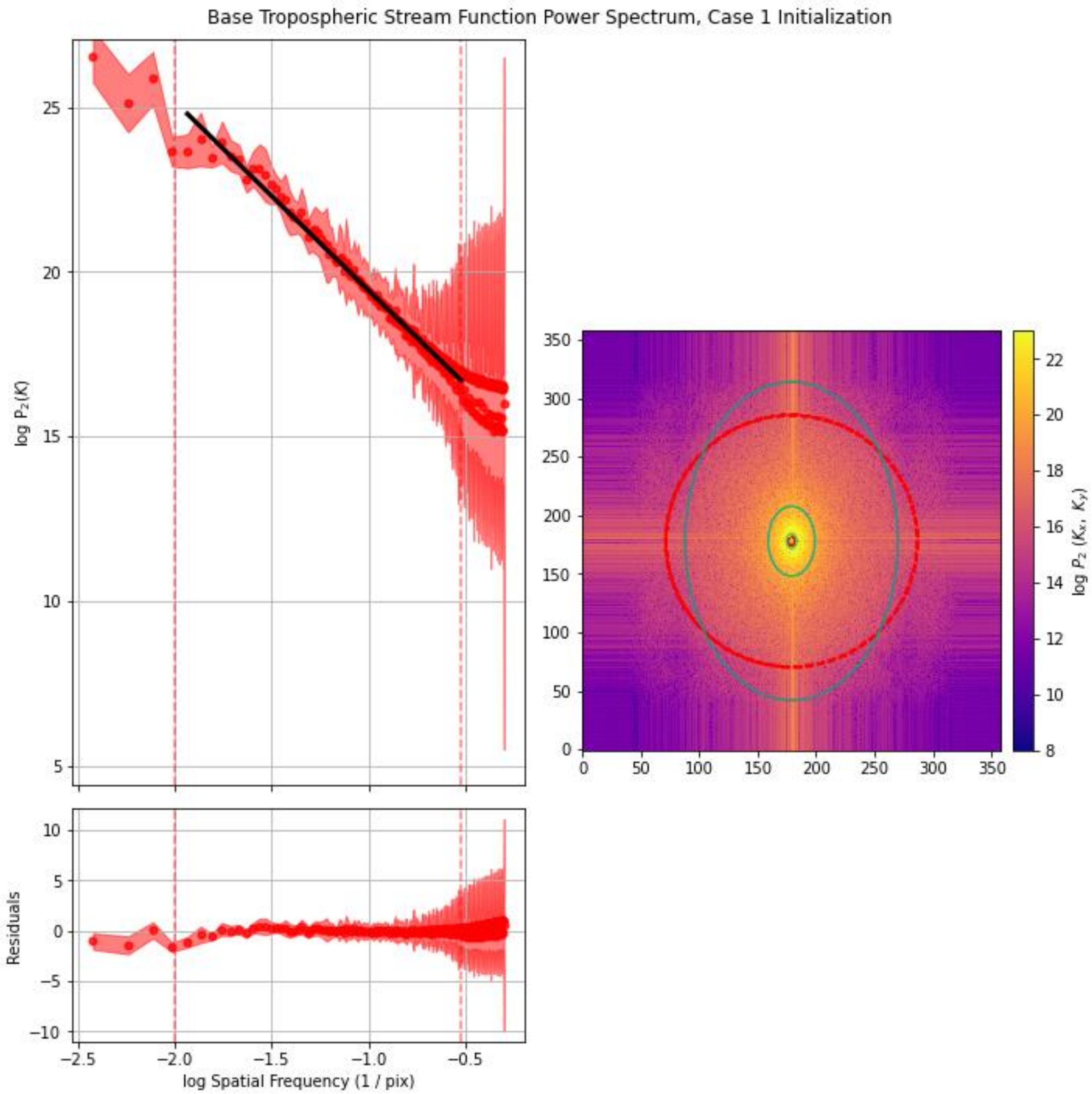

Figure 8.1: Fast Fourier Transform (FFT) Two-Dimensional (right) and Projected One-Dimensional (top left) Power Spectra for the Case 1 Initialization Time Base Stream Function. The two-dimensional color contours are the log10 of the power of the spatial wavenumbers. Both y-axes of the one-dimensional plots are log10 of the power and projection uncertainty, respectively, and the x-axis is the log of 1/pixels, where 1 pixel is 1 degree latitude or longitude. The synoptic scale cut-off is at approximately -1.0 on the x-axis at the equator, shifting toward -1.5 with higher latitude.

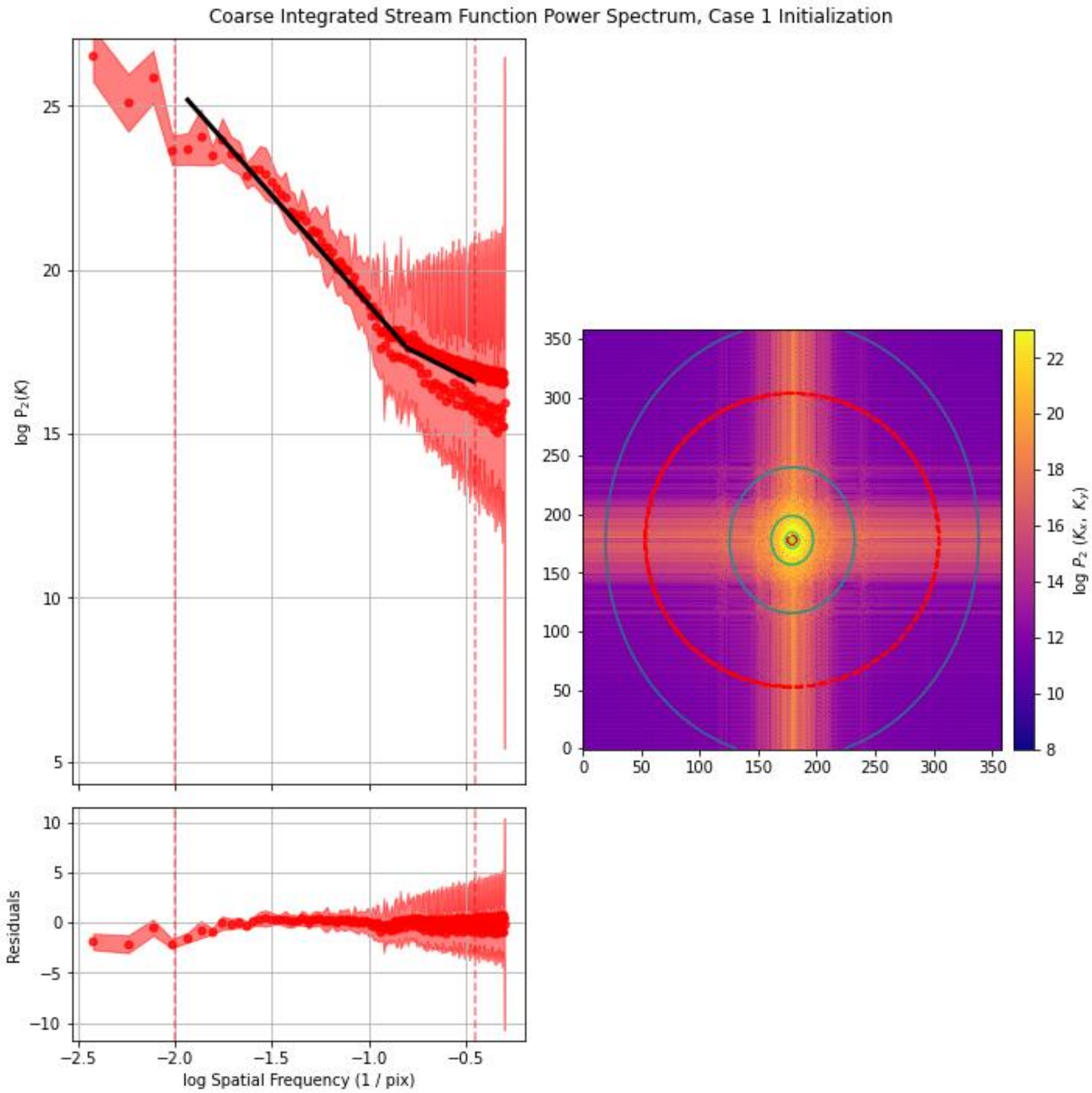

Figure 8.2: FFT Two-Dimensional (right) and Projected One-Dimensional (top left) Power Spectra for the Case 1 Initialization Coarse Stream Function. Axes and contours are the same as Figure 8.1.

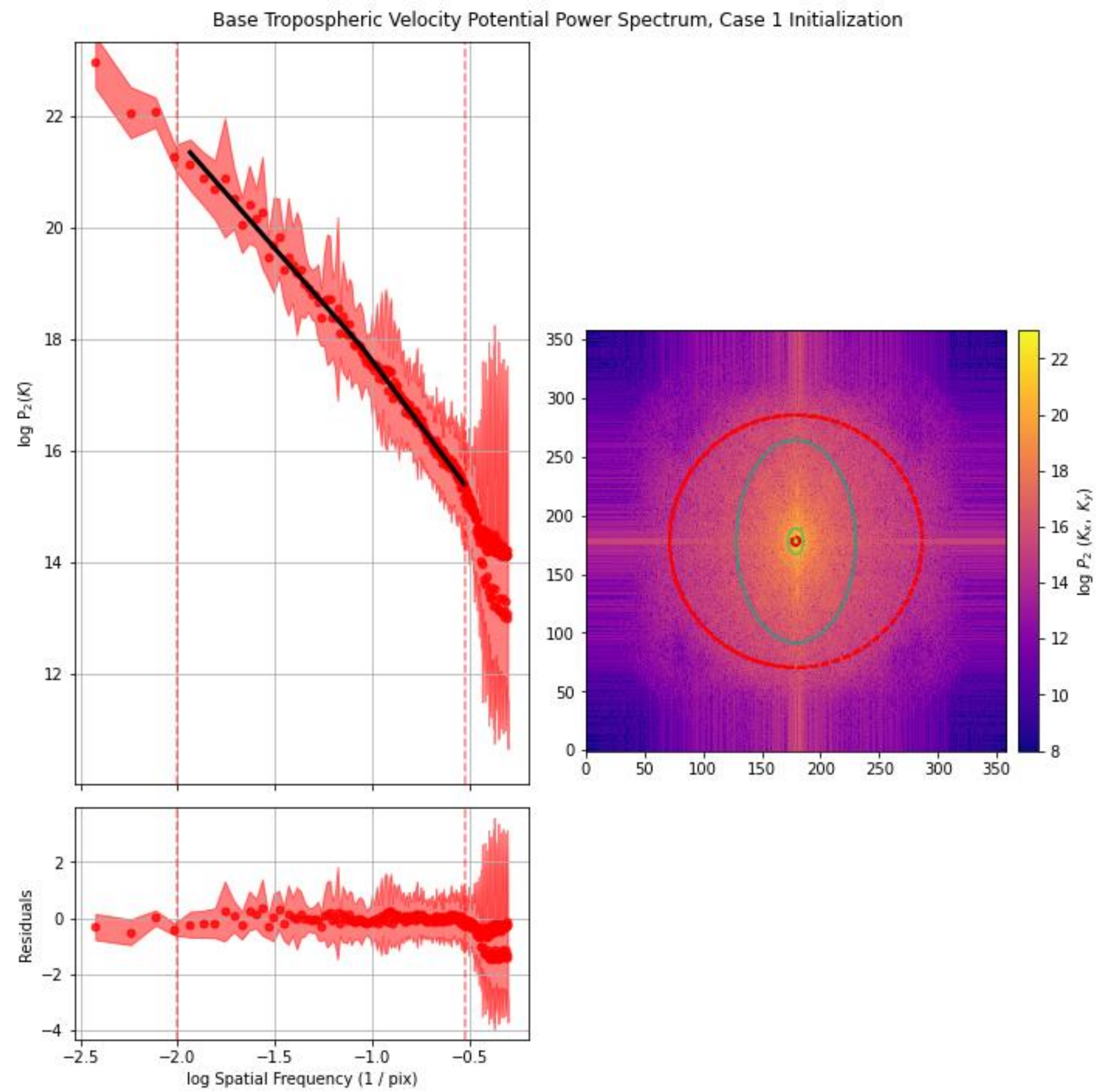

Figure 8.3: FFT Two-Dimensional (right) and Projected One-Dimensional (top left) Power Spectra for the Case 1 Initialization Time Base Velocity Potential. Axes and contours are the same as Figure 8.1.

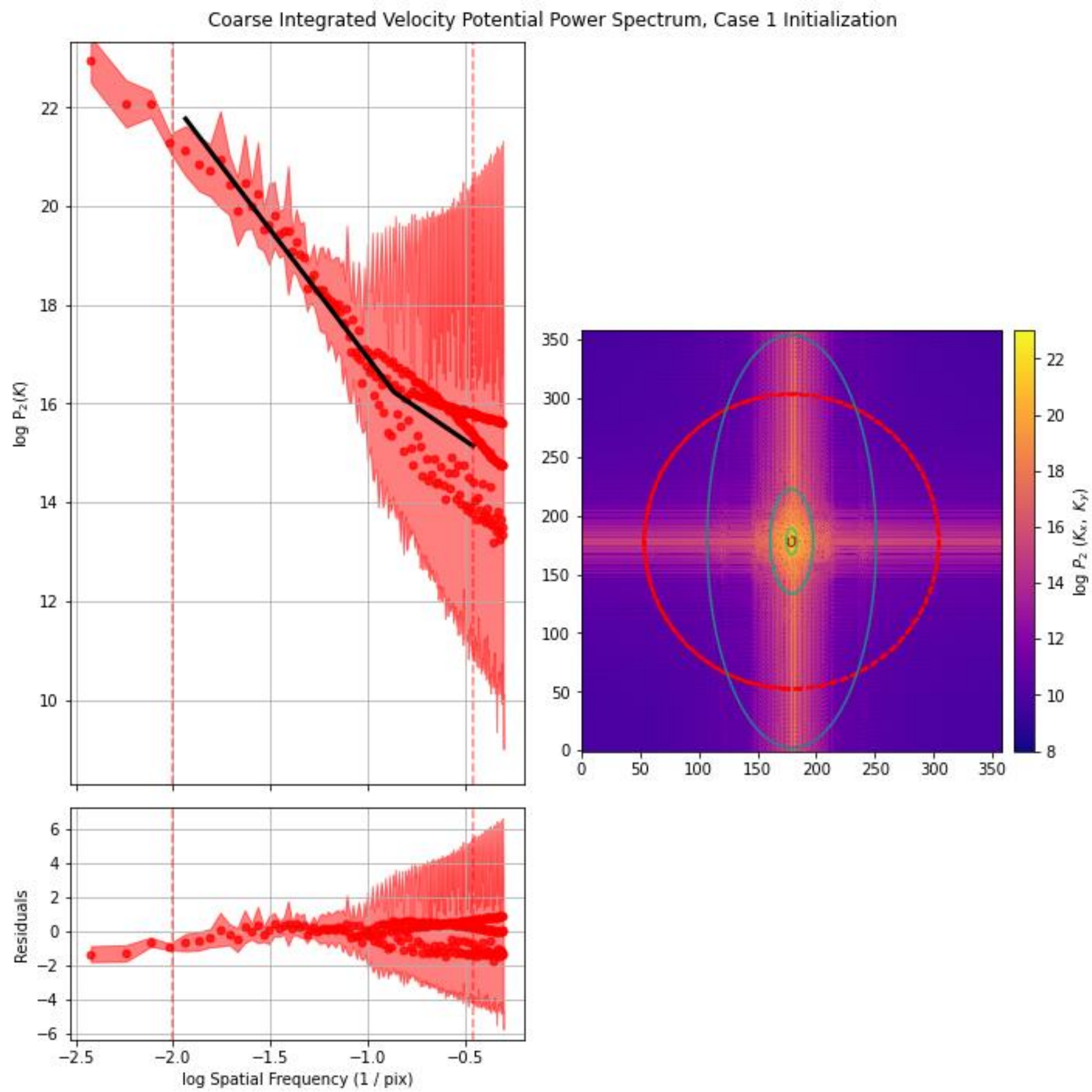

Figure 8.4: FFT Two-Dimensional (right) and Projected One-Dimensional (top left) Power Spectra for the Case 1 Initialization Coarse Stream Function. Axes and contours are the same as Figure 8.1.

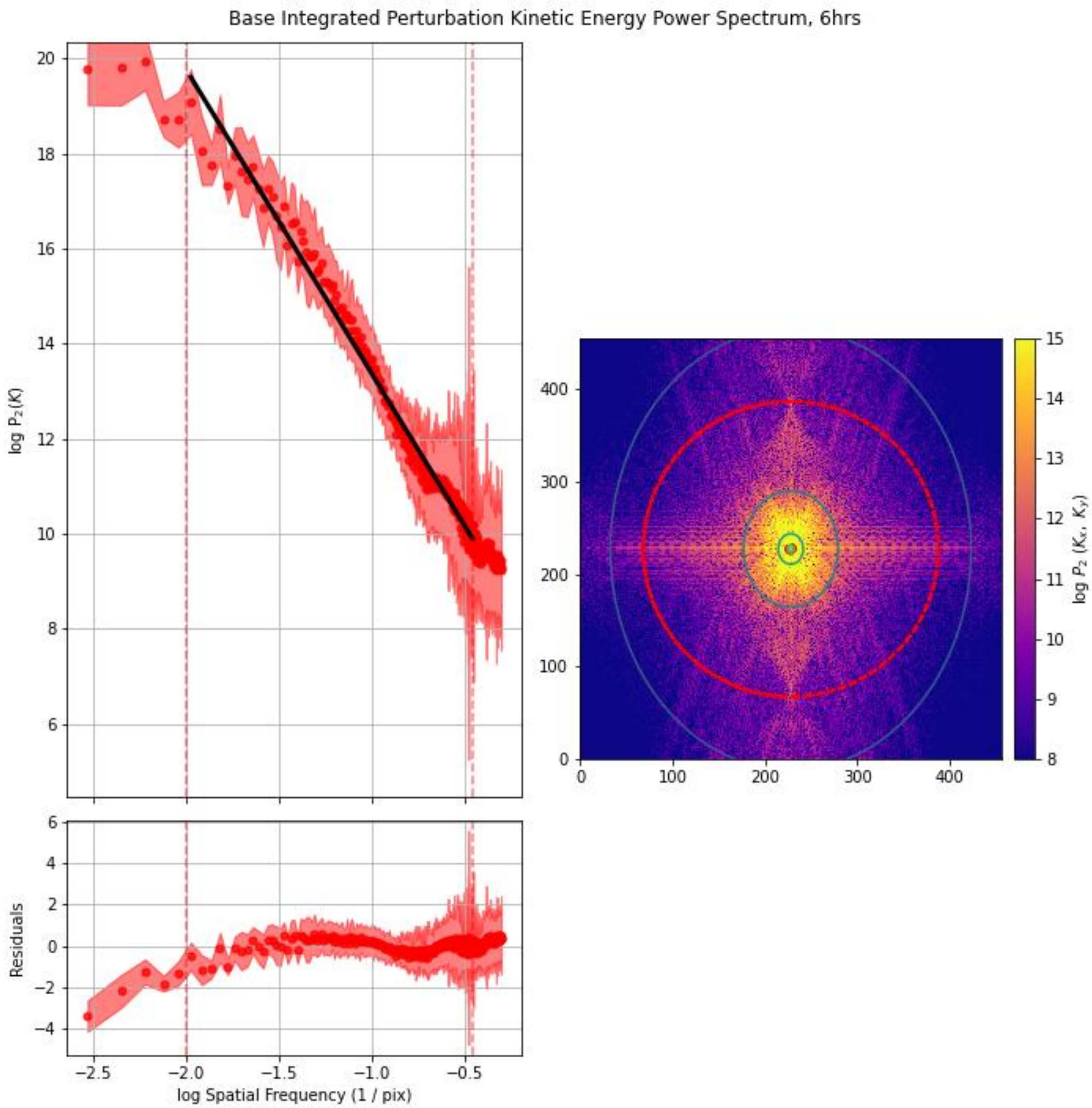

2020

2021 Figure 8.5: FFT Two-Dimensional (right) and Projected One-Dimensional (top left) Power Spectra for the

2022 Case 1 Base Kinetic Energy at 6 Hours. Pixels in the x-axis of the one-dimensional transform are now 20 km,

2023 the same Δx as the simulation grid spacing. Contour intervals and axes are the same as those of Figure 8.1.

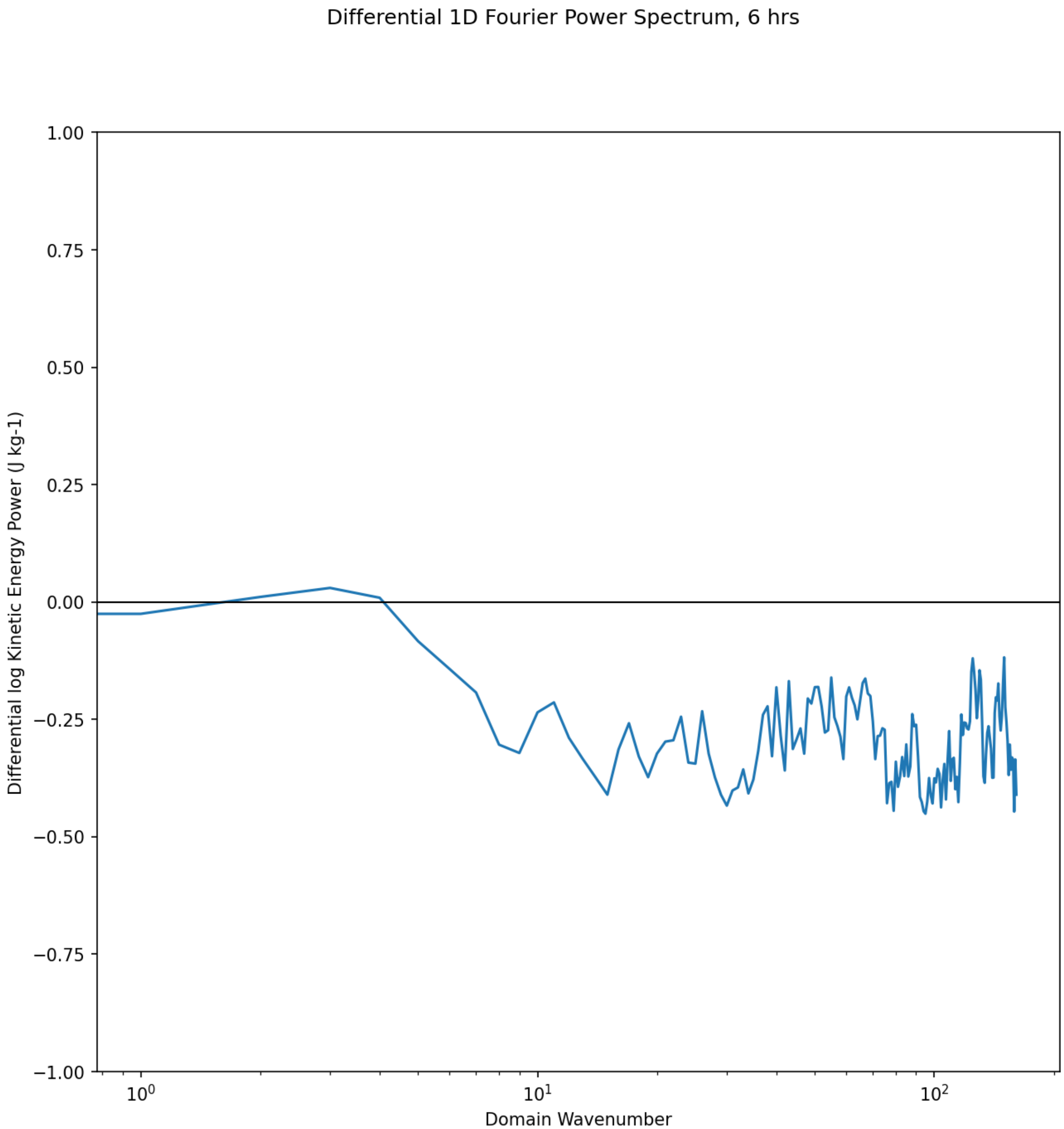

Figure 8.6: Case 1 Differential Kinetic Energy 1D Fourier Power Spectrum at 6 Hours. Positive values indicate greater energy in the coarse simulation.

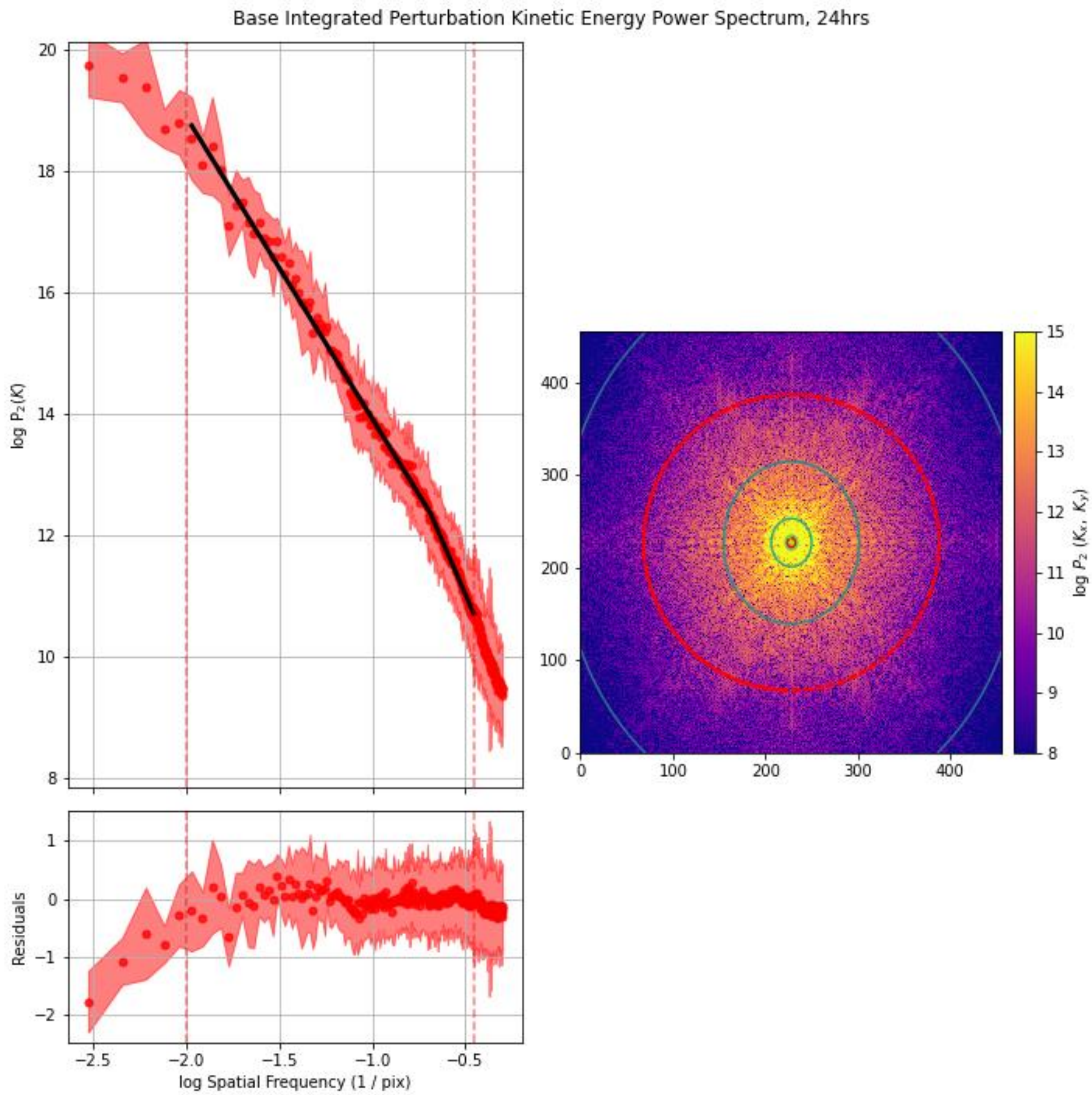

Figure 8.7: FFT Two-Dimensional (right) and Projected One-Dimensional (top left) Power Spectra for the Case 1 Base Kinetic Energy at 24 Hours. Contour intervals and axes are the same as those of Figure 8.1.

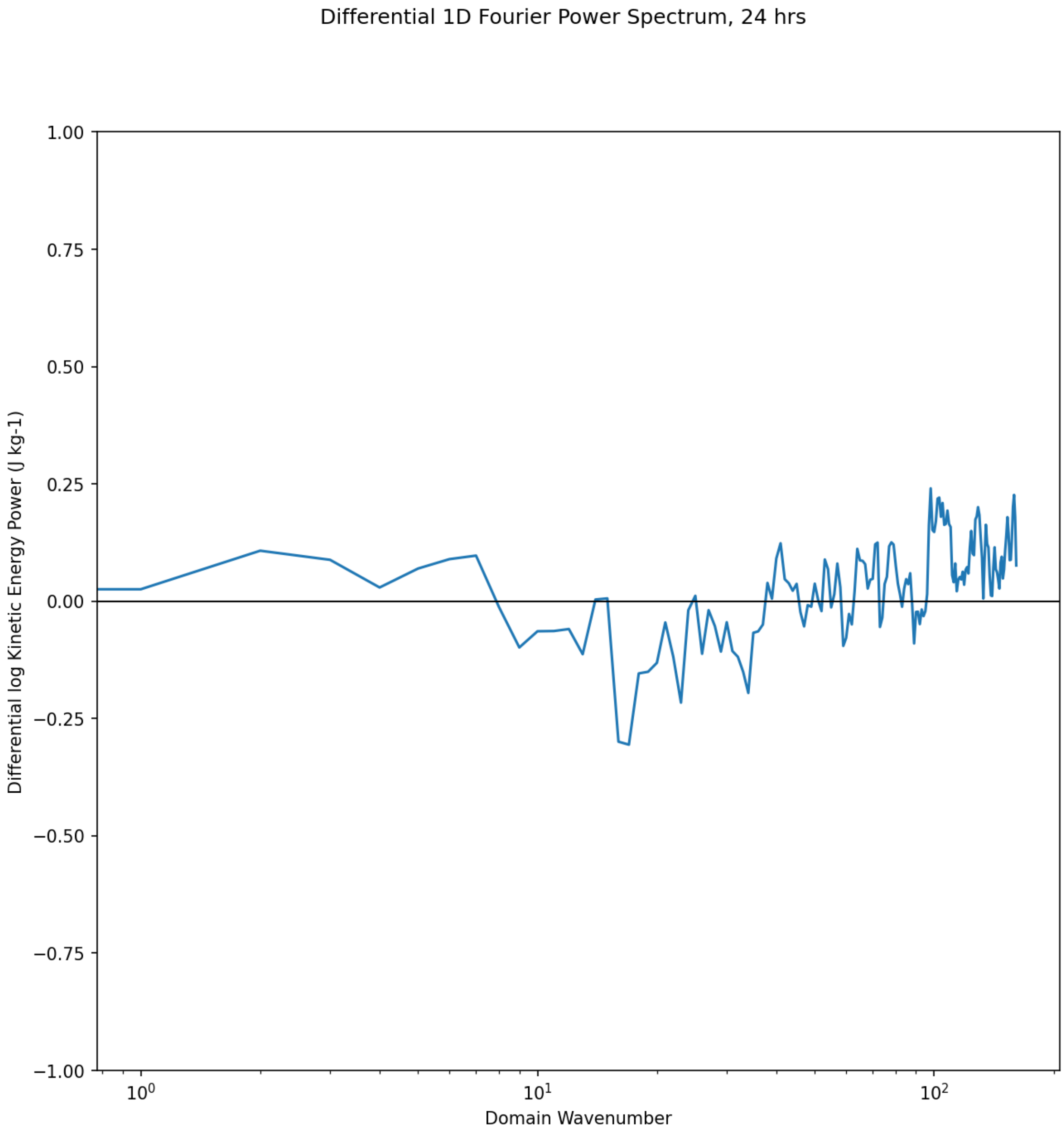

Figure 8.8: Case 1 Differential 1D Kinetic Energy Fourier Power Spectrum at 24 Hours.

CITATIONS

Augier, P. and E., Lindborg, 2013: A new formulation of the spectral energy budget of the atmosphere, with application to two high-resolution general circulation models. *J. Atmos. Sci.*, **70**, 2293-2308.

Azzalini, A., M. Farge, and K. Schneider, 2005: Nonlinear wavelet thresholding: A recursive method to determine the optimal denoising threshold. *Appl. Comput. Harmonic Anal.*, **18,** 177-185.

Blatter, C., 1998: *Wavelets: A primer*. A. K. Peters, LTD., 200 pp.

Charney, J. G., 1972: Geostrophic turbulence. *J. Atmos. Sci*., 28, 1067-1095.

Daubechies, I., 1988: Orthonormal basis of compactly supported wavelets. *Comm. Pure Appl. Math.* **16**, 909-996.

Errico, R. M, 1985: Spectra computed from a limited area grid. *Mon. Wea. Rev.*, **113**, 1554-1562.

Eschenroeder, A. Q., 1964: Intensification of turbulence by Chemical Heat Release. *Phys. of Fluids*, **7**, 1735-1743.

Farge, M., 1992: Wavelet transforms and their applications to turbulence. *Annu. Rev. Fluid Mech.*, **24**, 395-457.

—, Schneider, and N. Kevlahan, 1999: Non-Gaussianity and coherent vortex simulation for two-dimensional turbulence using an adaptive orthogonal wavelet basis. *Phys. Fluids*., **11**, 2187-2201.

Gage, K. S., 1979: Evidence for a $k^{-5/3}$ Law Inertial Range in Mesoscale Two-Dimensional Turbulence. *J. Atmos. Sci.*, **36**, 1950-1954.

Grell, G. A. and Freitas, S. R., 2014: A scale and aerosol aware stochastic convective parameterization for weather and air quality modeling, *Atmos. Chem. Phys.*, **14**, 5233-5250, doi:10.5194/acp-14-5233-2014.

Hamilton, K., Y. O. Takahashi, and W. Ohfuchi, 2008: Mesoscale spectrum of atmospheric motions investigated in a very fine resolution global general circulation model. *J. Geophys. Res.*, **113**, 19 pp.

Hong, S.–Y., J. Dudhia, and S.–H. Chen, 2004: A revised approach to ice microphysical processes for the bulk parameterization of clouds and precipitation. *Mon. Wea. Rev.*, **132**, 103–120.

Hong, S.–Y., Y. Noh, and J. Dudhia, 2006: A new vertical diffusion package with an explicit treatment of entrainment processes. *Mon. Wea. Rev.*, **134**, 2318–2341.

Jaberi, F. A. and C. K. Mednia, 1998: Effects of heat of reaction on homogeneous compressible turbulence. *J. Sci. Comp.*, **13**, 201-228.

Jimenez, P. A., J. Dudhia, J. F. Gonzalez–Rouco, J. Navarro, J. P. Montavez, and E. Garcia–Bustamante, 2012: A revised scheme for the WRF surface layer formulation. *Mon. Wea. Rev.,* **140**, 898–918.

Kolmogorov, A. N.,1941: The local structure of turbulence in incompressible viscous fluid for very large Reynolds numbers. *Doklady Akademii Nauk SSSR*, **30**, 299–303.

Lee G, G. R., F. Wasilewski, K. Wohlfahrt, A. O'Leary, H. Nahrstaedt, and Contributors, 2006: "PyWavelets - Wavelet Transforms in Python", 2006-, https://github.com/PyWavelets/pywt.

Lilly, D. K., 1983: Stratified turbulence and the mesoscale variability of the atmosphere. *J. Atmos. Sci.*, **40**, 749-761.

Lindborg, E., 2006: The energy cascade in a strongly stratified fluid. *J. Fluid Mech.*, **550**, 207-242.

Liu, Y., X. S. Liang, and R. H. Weisberg, 2007: Rectification of the Bias in the Wavelet Power Spectrum. *J. Atmos. Ocean. Tech.*, **24**, 2093-2102.

Livescu, D., F. A. Jaberi, and C. K. Mednia, 2001: The effects of heat release on the energy exchange in reacting turbulent shear flow. *J. Fluid Mech.*, **450**, 35-66.

—, 2004: Small scale structure of homogeneous turbulent shear flow. *Phys. of Fluids*, **16**, 2864-2876.

Lorenz, E. N., 1960: Maximum simplification of the dynamic equations. *Tellus*, **12**, 243-254.

Mallat, S., 1989: A theory for multiresolution signal decomposition: the wavelet representation. *IEEE PAMI*. **2**, 674-693.

Martius, O., C. Schwierz, and H. C. Davies, 2007: Breaking Waves at the Tropopause in the Wintertime Northern Hemisphere: Climatological Analyses of the Orientation and the Theoretical LC1/2 Classification. *J. Atmos. Sci.*, **64**, 2576-2592.

Merilees, P. E. and H. Warn, 1975: On energy and enstrophy exchanges in two-dimensional non-divergent flow. *J. Fluid Mech*., **69**, 625-630.

Meyer, Y., 1990: *Wavelets and operators*. Cambridge University Press, 233 pp.

Misiti, M., Y. Misiti, G. Oppenheim, and J.-M. Poggi, 2007: *Wavelets and their applications*. ISTE LTD, 330 pp.

Nastrom, G. D. and K S. Gage, 1985: A climatology of atmospheric wavenumber spectra of wind and temperature observed by commercial aircraft. *J. Atmos. Sci.*, **42**, 950-960.

National Centers for Environmental Prediction/National Weather Service/NOAA/U.S. Department of Commerce, 2000: NCEP FNL Operational Model Global Tropospheric Analyses, continuing from July 1999. Research Data Archive at the National Center for Atmospheric Research, Computational and Information Systems Laboratory, Boulder, CO. [Available online at https://doi.org/10.5065/D6M043C6.]

Plu, M., P. Arbogast, and A. Joly, 2008: A wavelet representation of synoptic-scale coherent structures. *J. Atmos. Sci*., **64**, 3116-3138.

Pouquet, A. and R. Marino, 2013: Geophysical Turbulence and the Duality of the Energy Flow Across Scales. *Phys. Rev. Lett.*, **111**.

Tewari, M., F. Chen, W. Wang, J. Dudhia, M. A. LeMone, K. Mitchell, M. Ek, G. Gayno, J. Wegiel, and R. H. Cuenca, 2004: Implementation and verification of the unified NOAH land surface model in the WRF model. *20th conference on weather analysis and forecasting/16th conference on numerical weather prediction*, pp. 11–15.

Tung, K. K. and W. W. Orlando, 2002: The k^{-3} and $k^{-5/3}$ energy spectrum of atmosphere turbulence: Quasigeostrophic two-level model simulation. *J. Atmos. Sci*., **60**, 824-835.

Waite, M. L. and C. Snyder, 2012: Mesoscale Energy Spectra of Moist Baroclinic Waves. *J. Atmos. Sci.*, **70**, 1242-1256.

Yano, J. I., P. Bechtold, J.-L. Redelsperger, and F. Guichard, 2004: Wavelet compressed representation of deep moist convection. *Mon. Wea. Rev*., **130**, 1697-1722.